Asymptotic Theory of Transonic Wind Tunnel Wall Interference

N. D. Malmuth, C. C. Wu, H. Jafroudi,
R. Mclachlan, J. D. Cole, and R. Sahu

Rockwell International Science Center
1049 Camino Dos Rios
Thousand Oaks, CA 91360

December 1991

Final Report for Period March 30, 1984 through July 30, 1990

**ARNOLD ENGINEERING DEVELOPMENT CENTER
ARNOLD AIR FORCE BASE, TENNESSEE
AIR FORCE SYSTEMS COMMAND
UNITED STATES AIR FORCE**

This report has been reviewed by the Office of Public Affairs (PA) and is releasable to the National Technical Information Service (NTIS). At NTIS, it will be available to the general public, including foreign nations.

APPROVAL STATEMENT

This report has been reviewed and approved.

Mark S. Briski

MARK S. BRISKI, Capt, USAF
Directorate of Technology
Deputy for Operations

FOR THE COMMANDER

Keith L. Kushman

KEITH L. KUSHMAN
Director of Technology
Deputy for Operations

REPORT DOCUMENTATION PAGE

Public reporting burden for this collection of information is estimated to average 1 hour per response, including the time for reviewing instructions, searching existing data sources, gathering and maintaining the data needed, and completing and reviewing the collection of information. Send comments regarding this burden estimate or any other aspect of this collection of information, including suggestions for reducing this burden, to Washington Headquarters Services, Directorate for Information Operations and Reports, 1215 Jefferson Davis Highway, Suite 1204, Arlington, VA 22202-4302, and to the Office of Management and Budget, Paperwork Reduction Project (0704-0188), Washington, DC 20503

1. AGENCY USE ONLY (Leave blank)	2. REPORT DATE December 1991	3. REPORT TYPE AND DATES COVERED Final - Mar. 30, 1984 - July 30, 1990

4. TITLE AND SUBTITLE	5. FUNDING NUMBERS
Asymptotic Theory of Transonic Wind Tunnel Wall Interference Study	PE 65807F

6. AUTHOR(S)
Malmuth, N. D., Wu, C. C., Jafroudi, H., Mclachlan, R., Cole, J. D., and Sahu, R., Rockwell International Science Center

7. PERFORMING ORGANIZATION NAME(S) AND ADDRESS(ES)	8. PERFORMING ORGANIZATION REPORT NUMBER
Rockwell International Science Center 1049 Camino Dos Rios Thousand Oaks, CA 91360	AEDC-TR-91-24

9. SPONSORING/MONITORING AGENCY NAMES(S) AND ADDRESS(ES)	10. SPONSORING/MONITORING AGENCY REPORT NUMBER
Arnold Engineering Development Center/DOT Air Force Systems Command Arnold Air Force Base, TN 37389-5000	

11. SUPPLEMENTARY NOTES

Available in Defense Technical Information Center (DTIC).

12a. DISTRIBUTION/AVAILABILITY STATEMENT	12b. DISTRIBUTION CODE
Approved for public release; distribution is unlimited.	

13. ABSTRACT (Maximum 200 words)

Two limiting cases are considered related to transonic wall interference. For the first corresponding to slender airplanes, an area rule for interference holds in which the interference of the complete airplane can be obtained from that of its equivalent body of revolution. For large wall height, the slender case exhibits an asymptotic triple deck structure consisting of a cross flow-dominated zone near the model, a weakly perturbed free-field mid field which has a linear multipole far field for solid and free-jet wall conditions. Nonclassical, experimentally determined pressure conditions prescribed on a cylindrical interface lead to a "tube vortex" far field. For a high aspect ratio second case, the interference is driven by the imaging effect of the interface on the projection of the trailing vortex system in the Trefftz plane. This gives a downwash correction to a near-field nonlinear lifting line flow. Slightly subsonic free-stream conditions give a spike-like interference flow field due to the shock movement for both limiting cases. Computer codes written to treat these cases, as well as the underlying numerical methods, are described. Approaches integrating the asymptotics with measurement to augment Wall Interference Assessment/Correction (WIAC) procedures are outlined.

14. SUBJECT TERMS			15. NUMBER OF PAGES 229
transonic flow tunnels	perturbation theory	fluid dynamics	
asymptotic series	numerical analysis		16. PRICE CODE
transonic flow	aerodynamics		

17. SECURITY CLASSIFICATION OF REPORT UNCLASSIFIED	18. SECURITY CLASSIFICATION OF THIS PAGE UNCLASSIFIED	19. SECURITY CLASSIFICATION OF ABSTRACT UNCLASSIFIED	20. LIMITATION OF ABSTRACT Same as Report

COMPUTER GENERATED

PREFACE

This report constitutes the final report of the Air Force contract F40600-84-C0010, Asymptotic Theory of Transonic Wind Tunnel Wall Interference Study. This effort was conducted under the sponsorship of Arnold Engineering Development Center (AEDC), Air Force Systems Command (AFSC), Arnold Air Force Base, Tennessee 37389. Dr. Keith Kushman and Captain Mark Briski, USAF, were the AEDC technical representatives for the contract. The manuscript was submitted for publication on August 1, 1990. Editorial comments were provided by J. Erickson and W. Sickles of Calspan. Reproducibles used in the publication of this report were supplied by the authors. AEDC has neither edited nor altered this manuscript.

TABLE OF CONTENTS

LIST OF ILLUSTRATIONS

LIST OF TABLES

1. INTRODUCTION

For the foreseeable future, the wind tunnel will continue to be a vital tool in the development of atmospheric vehicles. In the application of data from such facilities to obtain aircraft performance predictions, wall effects must be accounted for. Procedures to treat subsonic wall interference have received considerable attention. A view of existing technology for this speed regime can be obtained from Refs. 1–3. By contrast, the methodology for the transonic case is much less developed since it gives rise to a particularly difficult environment. Some problem areas that contribute to the inaccuracy of transonic wall interference assessment have been summarized by Kemp in Ref. 4. These are:

1. Nonlinearity of the governing equation at supercritical flow conditions.

2. Nonlinearity of ventilated wall cross flow boundary conditions and difficulties in predicting or measuring them.

3. Wind tunnel geometry features, such as finite ventilated wall length, diffuser entry, and presence of a wake survey rake and its support.

4. Boundary layer on tunnel side walls, which causes the flow to deviate from two-dimensional test conditions when they are desired.

In addition to these, other viscous effects such as shock–boundary layer interactions are relevant to interference assessment considerations. Regarding Items 1–4, sidewall boundary layers have received attention by Barnwell in Ref. 5. Crossflow boundary conditions and wall boundary condition simulations have been treated in Refs. 6 and 7.

To deal with the nonlinear effects, computational procedures have to be utilized to treat the interaction of the test article with the walls. Some of these are applied to "classical" boundary conditions simulating the latter. As a concurrent approach, techniques incorporating measurements on control surfaces of flow quantities such as the pressure and velocity components are gaining acceptance. Refs. 8–14 illustrate different concepts using this approach for subsonic and transonic ranges. Discussions of related issues are contained in Refs. 15 and 16.

In addition to the utility of purely numerical large–scale computationally intensive methods for transonic wall correction prediction, there is a need for approaches that can reduce the number of input parameters necessary to compute the correction, shed light on the physics of the wall interference phenomena, simplify the necessary computations, and be generalized in three dimensions, as well as unsteady flows. Asymptotic procedures such as those described in Refs. 17–20 provide such advantages. Furthermore, they can stimulate valuable interactions with the other methods previously mentioned to suggest possible improvements, as well as deriving beneficial features from them.

The crucial importance of understanding transonic wall interference and developing simplified computationally non–intensive models has also occurred in developing drag estimates based on a computational nonlinear area rule algorithm developed at the Rockwell

Science Center. Figure 1 from Ref. 21 shows the sizeable impact of wall interference characterization in accurately predicting the drag rise of wing–body combinations. In the figure, various classical models for the wall interaction are compared to approximation of the slotted wall condition corresponding to a slot parameter of approximately $\frac{1}{4}$. It is seen that a dramatic improvement in the agreement of theory and experiment can be obtained with the proper wall simulation.

Because of the importance of obtaining simplified procedures for transonic wall interference predictions for three–dimensional models and adaptive wall applications such as those described in Refs. 22–28, the Rockwell International Science Center team conducted an effort for Arnold Engineering Development Center (AEDC) under Air Force Contract No. F40600–82–C0005 to develop three–dimensional extensions of its two–dimensional asymptotic theory of transonic wall interference, described in Ref. 20. Out of this program, Rockwell developed theories for low and high aspect ratio configurations. From the effort summarized in Ref. 29, which was restricted to an analytical investigation, a formulation for the numerical treatment of the low aspect ratio case was obtained. A partial development of the high aspect ratio theory was also obtained and is described in Ref. 29.

On the basis of this study, a follow–on program has been conducted under the contract, "Asymptotic Theory of Transonic Wind Tunnel Wall Interference". This effort was sponsored by AEDC under Contract F40600–84–C0010. One objective of the program was to fully develop the high aspect ratio theoretical wall interference model for solid wall and pressure specified boundary conditions (Task 2.0). Another was to numerically implement both the slender and high aspect ratio theories in the form of computer codes, (Tasks 1.0 and 3.0, respectively).

Based on discussions with AEDC and Calspan personnel during the program, the contract was modified to perform additional studies regarding the application of the asymptotic methods to Wind Tunnel Interference/Assessment Correction (WIAC) procedures in which computational and analytical techniques for interference prediction are augmented with the use of appropriate experimental measurements (Task 4.0). The original thrust of this effort was to combine the asymptotic theory with momentum theorems to obtain more information on the nature of the interference. However, on the basis of the results obtained in the theoretical and computational phases of the work, it became evident that the information from the momentum theorems were naturally present in the asymptotic developments and that the emphasis should be on exploiting the latter to develop new and improved WIAC techniques. This motivated the formulation of two Asymptotic Integrated with Measurement (AIM) techniques in the contract. They are in line with the high aspect ratio and slender configuration models developed. For the slender case typifying compact fighter and missile test articles, additional theoretical analyses beyond the original Statement of Work were performed to devise asymptotic models of the wall interference when pressure boundary conditions are prescribed on a wall or interface. This led to a new triple deck model of the interference flow field.

This report summarizes the work conducted under Tasks 1.0–4.0. Section 2 describes the theoretical and computational studies conducted under Task 1.0 as well as the supplementary activity related to the pressure interface condition for slender bodies. In Section 3,

SC83-24478

ZERO LIFT
WAVE DRAG
COEFFICIENT

C_D

WING-BODY TESTED

EXPERIMENT-(NACA TN 3872)

O WING A

□ CORRECTED FOR
INTERFERENCE

NONLINEAR AREA RULE CODE

FREE AIR ——·——
HARD WALL ———
FREE JET ————
SLOTTED WALL ··········

$(\phi + c\phi\,\widetilde{\,r\,} = 0)$, c = 1/4

0.020

0.016

0.012

0.008

0.004

0

0.6   0.7   0.8   0.9   1.0   1.1   1.2   1.3   1.4

MACH NUMBER, M
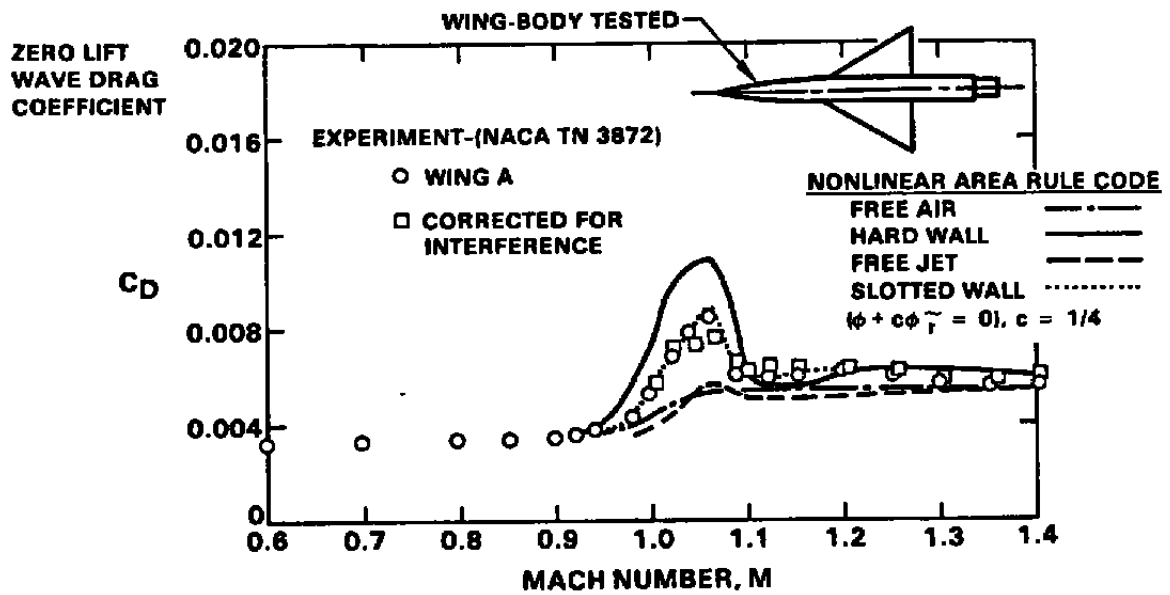
Fig. 1. Comparison of computational Area Rule with experiment.

3

the investigations conducted under Tasks 2.0 and 3.0 are discussed. The AIM concepts are detailed in Section 4. Numerical procedures as well as structure of the codes are outlined in Sections 2 and 3. This information will complement User's Guides for both confined slender and high aspect ratio configuration codes which will be released in the near future. Results for both slender and high aspect ratio limiting cases are presented. In Sections 5 and 6, conclusions and recommendations for future work are provided.

2. CONFINED SLENDER CONFIGURATIONS

In what follows, the flow over a slender airplane model in a circular wind tunnel test section will be considered. The main contractual activity in this phase was to computationally solve the wall interference problem (P1) derived in Ref. 29. A schematic of the arrangement is shown in Fig. 2. The interference problem derived in Ref. 29 is associated with free jet and solid wall boundary conditions imposed on an interface control surface (shown in phantom in Fig. 2). For this purpose, a secondary limit of a large test section radius within the primary Karman Guderley transonic small disturbance limit was used. Only subsonic freestreams are considered in the analysis. In Ref. 29, the flow was shown to have a "triple deck" structure. These decks or zones are shown schematically in Fig. 2.

Near the axis of symmetry of an equivalent body of revolution having the same streamwise distribution of cross-sectional area as the complete airplane (axis layer), lateral gradients dominate. In Ref. 29, the equivalent body was shown to simulate the interference of the complete airplane (Area Rule for Interference). Within a "central layer", if α, the angle of attack, and the characteristic thickness, δ, are such that $\alpha/\delta = O(1)$, as $\delta \to 0$, the flow is nearly axisymmetric and can be characterized as a nonlinear line source. Asymptotic representations for the central and axis layers were derived in which the first order terms are those associated with the unconfined flow. The second order corrections of these regions are due to the wall effects. A third region denoted as the wall layer was identified, where the assumption of small wall perturbations is invalid. Here, other simplifications apply which represent the slender airplane as a multipole reflected in the walls.

It was shown that the effect of the walls on the flow field is deduced by solving the second order problem for the central layer. This consists of the equation of motion, hereinafter referred to as the "variational equation", subject to boundary conditions devised from matching the wall and axis layers.

In the next section, prior to considering the computational solution of the problem P1, some extension of the concepts of Ref. 29 will be applied to a generalization of P1 to handle pressure boundary conditions. The numerical solution of this problem was not attempted within the contractual effort.

2.1 Treatment of Pressure Specified Interface Boundary Conditions

In what follows, the flow structure in the region close to the interface, hereinafter called the wall layer, will be determined for pressure data specified on the interface. This provides a modified far field for the variational problem from those appropriate to free jet and solid wall conditions. The wall layer as well as the other flow regions have been identified in Fig. 2 of Ref. 29 and the inset of Fig. 2. Although the pressure boundary condition theory was called out as a contractual requirement in connection only with the high aspect ratio code associated with Task 3.0, the contractor deemed it useful to develop a corresponding theory for the slender body code written under Task 1.0 in the Work Statement of the contract. This software presently handles solid wall boundary

conditions. The formulation of the computational problem for pressure specified boundary conditions will be given in which the free jet conditions are a special case. This discussion in this section will be restricted to axially symmetric pressure data on the interface. This limitation will be removed in a subsequent section.

Referring to Fig. 2, the orientation of a slender model as related to a cylindrical control surface delineated in the figure is shown. The set up is similar to that described in Ref. 29. However, a pressure boundary condition is to be specified on the cylindrical interface S_C. These pressures are assumed to be obtained by suitable measurements such as from static probes and rails. The pressure distribution is also considered to be an arbitrary function of the streamwise coordinate x and in a later section the angle variable θ. Such distributions can be associated with the following effects:

- Wall boundary layers

- Noncircular cross section walls such as octagonal and rectangular test sections

- Yaw

- Asymmetric control surface deflections.

Moreover, the pressure specified formulation is relevant to the two variable method, adaptive wall applications, and our recently developed combined asymptotic and experimental interference prediction (AIM) method.

2.1.1 KG Theory

For a self–contained account, some of the analytical developments which are common to the solid wall analysis will be repeated here. The viewpoint will be similar to the solid wall case, i.e., a secondary approximation of large radius h of the control surface (shown schematically in Fig. 2) within the basic approximations of the Karman Guderley (KG) small disturbance model. Thus, the body is represented as the surface

$$r = \delta F(x, \theta) \quad , \qquad (2-1)$$

within the coordinate system indicated in Fig. 2, with $\delta =$ the characteristic thickness ratio, and overbars representing dimensional quantities.

The asymptotic expansion of the velocity potential Φ in terms of the freestream speed U is

$$\frac{\Phi}{U} = \bar{x} + \delta^2 \phi(x, \bar{r}, \theta; K, H, A) + \cdots \quad , \qquad (2-2)$$

which holds for the KG outer limit,

$$x, \bar{r} = \delta r, \theta, K = \left(1 - M_\infty^2\right)/\delta^2, H = h\delta/c, A = \alpha/\delta \text{ fixed as } \delta \to 0, \qquad (2-3)$$

where $M_\infty =$ freestream Mach number, $K =$ KG similarity parameter, $H =$ scaled height of control surface, $A =$ incidence parameter. For $(2-3)$, the ideas of Ref. 29 and the pressure formula valid on the interface,

$$C_p = -2\delta^2 \phi_x \qquad (2-4)$$

give the following (primary) KG formulation:

6

2.1.2 Problem Q:

$$(K - (\gamma + 1)\phi_x)\phi_{xx} + \frac{1}{\tilde{r}}(\tilde{r}\phi_{\tilde{r}})_{\tilde{r}} + \frac{1}{\tilde{r}^2}\phi_{\theta\theta} = 0 \qquad (2-5a)$$

$$\lim_{\tilde{r}\to 0}\tilde{r}\phi_{\tilde{r}} = \frac{S'(x)}{2\pi} \quad , \quad 0 < x < 1 \qquad (2-5b)$$

$$\phi_{\tilde{r}}(x,0) = 0 \quad , \quad x > 1 \qquad (2-5c)$$

$$\phi_x(x,H,\theta) = f_x(x,\theta;H) = -C_p/2\delta^2 \qquad (2-5d)$$

$$\phi(x,H,\theta) = f(x,\theta;H) \qquad (2-5d')$$

Here, $S(x)$ = streamwise area progression of the test article, $\overline{S}(\overline{x})$ = dimensional cross sectional area, $\overline{x}$ = dimensional coordinate in freestream direction, and $S(x) = \overline{S}(\overline{x})/\delta^2 L^2$, where L is the body length. Problem Q above represents a generalization of those discussed in Ref. 29 because of the fully three–dimensional nature of the equation of motion $(2-5a)$ and in accord with the previous remarks, the more general nature of the external conditions. The latter are given by either $(2-5d)$ or $(2-5d')$.

2.1.3 Large H Theory

The secondary expansions associated with $H \to \infty$ will now be considered. It is anticipated that the structure of the various layers, i.e., Axis, Central, and Wall layers shown in Fig. 2, will resemble those for solid walls. Accordingly, these representations are:

2.1.4 Central Layer

$$\phi = \phi_0(x,\tilde{r}) + \mu_{1/2}(H)\phi_{1/2}(x,\tilde{r},\theta) + \mu_1(H)\phi_1(x,\tilde{r},\theta) + \cdots \qquad (2-6a)$$

$$K = K_0^* + \nu_1(H)K_1^* + \cdots \qquad (2-6b)$$

$$A = A_0 + \kappa_1(H)A_1 + \cdots \qquad (2-6c)$$

which hold in the central limit

$$x,\tilde{r} \text{ fixed as } H \to \infty \quad .$$

These lead to the following generalized hierarchy of approximate equations:

2.1.5 Free Field Approximation

$$(K_0^* - (\gamma + 1)\phi_{0_x})\phi_{0_{xx}} + \frac{1}{\tilde{r}}(\tilde{r}\phi_{0_{\tilde{r}}})_{\tilde{r}} = 0 \qquad (2-7a)$$

2.1.6 Variational Equations

$$(K_0^* - (\gamma + 1)\phi_{0_x})\phi_{1/2_{xx}} - (\gamma + 1)\phi_{0_{xx}}\phi_{1/2_x} + \frac{1}{\tilde{r}}(\tilde{r}\phi_{1/2_{\tilde{r}}})_{\tilde{r}} + \frac{1}{\tilde{r}^2}\phi_{1/2_{\theta\theta}} = 0 \qquad (2-7b)$$

Fig. 2. Control surface in tunnel.

$$\left(K_0^* - (\gamma+1)\phi_{0_x}\right)\phi_{1_{xx}} - (\gamma+1)\phi_{1_x}\phi_{0_{xx}} + \frac{1}{\tilde{r}}\left(\tilde{r}\phi_{1_{\tilde{r}}}\right)_{\tilde{r}} + \frac{1}{\tilde{r}^2}\phi_{1_{\theta\theta}} = -K_1^*\phi_{0_{xx}} \qquad (2-7c)$$

where $\nu_1(H) = \mu_1(H)$ to keep the forcing term in $(2-7c)$, and to address the possibility of adjusting K_1^* as a Mach number correction to achieve interference-free flow. The significant complication of Eqs. $(2-7b)$ and $(2-7c)$ over their solid wall counterparts is the presence of the terms involving θ derivatives. On the other hand, a substantial simplification from the Problem Q is the allowability of factorization and superposition due to the linearity of these equations. As will be seen, the angular dependence of the far fields for these problems involve simple factors such as $\cos\theta$, $\cos 2\theta$, etc. It is envisioned that this dependence can be factored out, e.g., by allowing $\phi_1 = \tilde{\phi}_1(x,\tilde{r})\cos\theta$, which gives a two-dimensional equation for $\tilde{\phi}_1$. Also to be confirmed by matching is the assertion that the far field for ϕ_0 has a similar structure to that given in Ref. 29.

2.1.7 Wall Layer

The appropriate representation is assumed to be

$$\phi = \epsilon_0(H)\varphi_0(x^\dagger, r^\dagger, \theta) + \epsilon_{1/2}(H)\varphi_{1/2} + \epsilon_1\varphi_1 + \cdots \quad , \qquad (2-8a)$$

for the wall layer limit,

$$x^\dagger = x/H \quad , \quad r^\dagger = \tilde{r}/H \quad , \quad \text{fixed as } H \to \infty \quad . \qquad (2-8b)$$

Substitution of $(2-8a)$ into the KG formulation gives

$$O(\epsilon_0) : L[\varphi_0] = 0 \qquad (2-9a)$$

$$O(\epsilon_{1/2}) : L[\varphi_{1/2}] \qquad (2-9b)$$

$$O(\epsilon_1, \epsilon_0^2/H) : L[\varphi_1] = \left((\gamma+1)\varphi_{0_{x^\dagger}} - K_1^*\right)\varphi_{0_{x^\dagger x^\dagger}} \quad , \qquad (2-9c)$$

where

$$L \equiv K_0^*\frac{\partial}{\partial x^\dagger} + \Delta_T^\dagger \quad , \quad \Delta_T \equiv \frac{1}{r^\dagger}\frac{\partial}{\partial r^\dagger}\left(r^\dagger\frac{\partial}{\partial r^\dagger}\right) + \frac{1}{r^{\dagger 2}}\frac{\partial^2}{\partial\theta^2} \quad .$$

2.1.8 Behavior of φ_0 near Origin

As in the solid wall case, if $R^\dagger = \sqrt{\left(\frac{x}{K_0^*}\right)^2 + \tilde{r}^2/H}$, the source-like behavior,

$$\varphi_0 \simeq \frac{S(1)}{\sqrt{K_0^*}}\left\{-\frac{1}{4\pi R^\dagger} + \cdots\right\} \quad , \qquad (2-10)$$

is anticipated.

From $(2-5d')$, the similarity form,

$$f(x,\theta;H) = \frac{1}{H}f(x^\dagger,\theta) \qquad (2-11)$$

9

is appropriate, and leads to the boundary conditions

$$\varphi_0(x^\dagger, 1, \theta) = f(x^\dagger, \theta) = f(x^\dagger, \theta + 2\pi) \qquad (2-12a)$$

$$\varphi_{1/2,1}(x^\dagger, 1, \theta) = 0 \quad . \qquad (2-12b)$$

If

$$\Delta^\dagger = \frac{\partial}{\partial x^\dagger} + \frac{1}{r^\dagger}\frac{\partial}{\partial r^\dagger}\left(r^\dagger\frac{\delta}{\partial r^\dagger}\right) + \frac{1}{r^{\dagger^2}}\frac{\partial^2}{\partial \theta^2}$$

$$X^\dagger = x^\dagger / \sqrt{K_0^*} \quad .$$

Then $(2-10)$ implies

$$\Delta^\dagger \varphi_0 = \frac{S(1)}{\sqrt{K_0^*}}\delta(x^\dagger)\cdot\frac{\delta^+(r^\dagger)}{2\pi r^{\dagger^2}} \quad . \qquad (2-13)$$

With the following exponential Fourier transform pair

$$\overline{\varphi}_0 = \int_{-\infty}^{\infty} e^{-ikX^\dagger}\varphi_0 dX^\dagger$$

$$\varphi_0 = \frac{1}{2\pi}\int_{-\infty}^{\infty} e^{ikX^\dagger}\overline{\varphi}_0 dk \quad ,$$

the boundary value problem for $\overline{\varphi}_0$ corresponding to $(2-10)$, $(2-12a)$ and $(2-13)$ is

$$L\overline{\varphi}_0 = \left(\Delta_T^\dagger - k^2\right)\overline{\varphi}_0 = 0 \qquad (2-14a)$$

$$\lim_{r^\dagger \to 0} r^\dagger \frac{d\overline{\varphi}_0}{dr^\dagger} = \frac{1}{2\pi}\frac{S(1)}{\sqrt{K_0^*}} \qquad (2-14b)$$

$$\overline{\varphi}_0(1, \theta) = \overline{f}(\theta, k) = \overline{f}(\theta + 2\pi, k) \quad . \qquad (2-14c)$$

In contrast to the solid wall case, the decomposition of the solution into the fundamental solution M_0 and a part M_1 that is bounded at $X = \pm\infty$ as indicated in Eqs. (12) of Ref. 29 is not required since with the Dirichlet conditions, there can be mass flow through the interface to eliminate the solid wall source flow division at upstream and downstream infinity. The eigenfunction expansion solving $(2-14)$ is

$$\overline{\varphi}_0 = A_0 K_0(kr^\dagger) + B_0 I_0(kr^\dagger) + \sum_{n=1}^{\infty} I_n(kr^\dagger)\{B_n \cos n\theta + C_n \sin n\theta\} \quad , \qquad (2-15)$$

where K_0 and I_n are Bessel functions, the periodicity condition in $(2-14c)$ has been used to determine the eigenvalues $\lambda_n = n$, $n = 0, 1, 2, \cdots$, and $(2-14b)$ has been utilized to eliminate the K_n for $n > 0$.

10

Application of $(2 - 14c)$ and inversion gives finally,

$$
\varphi_0 = \frac{1}{\pi^2} \int_0^\infty \cos kX^\dagger dk \left\{ \frac{S(1)}{\sqrt{K_0^*}} \left[\frac{I_0(kr^\dagger)}{I_0(k)} K_0(k) - K_0(kr^\dagger) \right] \right.
$$
$$
\left. + \frac{I_0(kr^\dagger)}{I_0(k)} \int_0^{2\pi} \overline{f}(\theta, k) d\theta \right\}
$$
$$
+ \frac{2}{\pi^2} \sum_{n=1}^\infty \int_0^\infty \cos kX^\dagger \frac{I_n(kr^\dagger)}{I_n(k)} dk \int_0^{2\pi} \overline{f}(\theta', k) \cos n(\theta - \theta') d\theta' \quad .
$$

$$(2 - 16)$$

The integrals in $(2 - 16)$ are convergent since the Bessel ratios decay exponentially as $k \to \infty$ and are analytic as $k \to 0$.

As indicated previously, for the analysis in this section, the θ variation will be suppressed. This may be realistic for many practical applications for nearly circular test sections and interfaces in the intermediate region of slender body theory discussed in Ref. 30. For convenience, the f distribution has been assumed symmetric in X, i.e., $f(X) = f(-X)$, to obtain $(2 - 16)$.* Therein, the exponential transforms have been expressed in terms of cosine integrals. The analysis can be readily generalized to handle unsymmetrical f distributions.

2.1.9 Asymptotic Representation of $(2 - 16)$ as $R^\dagger \to 0$

To obtain the required representation, the following integrals are considered:

$$
\mathcal{I}_1 = \int_0^\infty \cos kX^\dagger \frac{I_0(kr^\dagger)}{I_0(k)} dk \int_0^{2\pi} \overline{f}(\theta, k) d\theta \qquad (2 - 17a)
$$

$$
\mathcal{I}_2 = \int_0^\infty \left\{ \frac{I_0(kr^\dagger) K_0(k)}{I_0(k)} - K_0(kr^\dagger) \right\} \cos kX^\dagger dk \qquad (2 - 17b)
$$

$$
\mathcal{I}_3 = \sum_{n=1}^\infty \int_0^\infty \cos kX^\dagger \frac{I_n(kr^\dagger)}{I_n(k)} dk \int_0^{2\pi} \overline{f}(\theta', k) \cos n(\theta - \theta') d\theta' \quad . \qquad (2 - 17c)
$$

Consistent with the assumption of axisymmetric interface pressures, $\mathcal{I}_3$ will not be considered here. By approximating $I_0(kr^\dagger)$ and $\cos kX^\dagger$ as $R^\dagger \to 0$, and term by term integration of the series obtained, the following approximation for φ_0 results:

$$
\varphi_0 = -\frac{S(1)}{4\pi\sqrt{K_0^*}R^\dagger} + (\mathcal{A}_0 + \mathcal{B}_0) + (\mathcal{C}_0 + \mathcal{D}_0) R^{\dagger^2} P_2(\cos \omega)
$$
$$
+ O\left(R^{\dagger^3}\right)
$$

$$(2 - 18a)$$

---

* This restriction will be removed in Section 2.2.

where

$$A_0 = \frac{S(1)}{\sqrt{K_0^*}\pi^2} \int_0^\infty \frac{K_0(k)dk}{I_0(k)} \qquad (2-18b)$$

$$B_0 = \frac{1}{\pi} \int_0^\infty \frac{dk}{I_0(k)} \int_0^\infty f(X^\dagger) \cos kX^\dagger dX \qquad (2-18c)$$

$$C_0 = -\frac{1}{\pi} \int_0^\infty \frac{k^2 dk}{I_0(k)} \int_0^\infty f(X^\dagger) \cos kX^\dagger dX^\dagger \qquad (2-18d)$$

$$D_0 = \frac{-S(1)}{2\pi^2 \sqrt{K_0^*}} \int_0^\infty \frac{k^2 K_0(k)}{I_0(k)} dk \quad . \qquad (2-18e)$$

Here, ω is the scaled analogue of the polar angle defined in Fig. 2 i.e., $\omega = \cos^{-1} X^\dagger / R^\dagger$ and $P_2(\cos\omega)$ is a Legendre polynomial.

The constants given in $(2-18b)$–$(2-18e)$ are all given by convergent integrals. In particular, B_0 converges if $\overline{f}(k)$ is bounded as $|k| \to \infty$, and even under milder conditions on $\overline{f}$. This results from the potent exponential decay of I_0. No problem is encountered as $k \to 0$ since the integrand is analytic at that point.

The terms involving B_0 and C_0 give the effect of the pressure boundary condition.

2.1.10 Matching

For purposes of matching, the following asymptotic approximations for the wall layer and central region are appropriate:

$$\frac{\Phi_{central}}{U} = x + \delta^2 \left\{ \frac{A_0}{R} + \frac{B_0 \cos\omega}{R^2} + \frac{C_0}{R^3}(\cos 3\omega - \cos\omega) + \frac{A}{\sqrt{K_0^*}R^3} P_2(\cos\omega) \right\}$$
$$+ \mu_{1/2}(H)\phi_{1/2} + \mu_1\left(\alpha_0 R^2 P_2(\cos\omega) + \alpha_1 R\cos\omega + \alpha_2\right) + \cdots \qquad (2-19)$$
$$\text{as } R \to \infty$$

$$\frac{\Phi_{wall}}{U} = x + \delta^2 \left\{ \epsilon_0 \frac{S(1)}{\sqrt{K_0^*}} \left[-\frac{1}{4\pi R^\dagger} + (A_0 + B_0) + (C_0 + D_0)R^{\dagger^2} P_2(\cos\omega) + \cdots \right] \right\}$$
$$+ \epsilon_{1/2}B_0 \cos\omega \left[\frac{1}{R^{\dagger^2}} + (C_0 + D_0)R^\dagger \right]$$
$$+ \epsilon_1 \left\{ C\left[-\frac{P_2(\cos\omega)}{R^{\dagger^2}} + C_0 + D_0 \right] + \frac{C_0}{R^{\dagger^3}}(\cos 3\omega - \cos\omega) \right\}$$
$$+ \cdots \quad , \qquad \text{as } R^\dagger \to 0$$
$$(2-20)$$

where A_0, B_0, C_0, and $\underline{A}$ are constants that have been previously defined in Ref. 29 with a corrected value for C_0 being $\frac{(\gamma+1)S^2(1)}{108\pi^2 K_0^{5/2}}$.

Preliminary matching considerations govern the selection of the various elements comprising $(2-19)$ and $(2-20)$. The ϕ_1 coefficient of μ_1 represents a harmonic solution of $(2-7c)$. The response to the nonlinear forcing terms $(\gamma+1)\phi_{0_x}\phi_{1_{xx}}$ and $(\gamma+1)\phi_{1_x}\phi_{0_{xx}}$ are decaying terms as $R\to\infty$ that are higher order to the order of the matching and can be neglected. Regarding $(2-20)$, $\varphi_{1/2}$ and φ_1, the coefficients of $\epsilon_{1/2}$ and ϵ_1, respectively, consist partially of $X^\dagger$ derivatives of φ_0, such that the multipole expansion has primary singularities which are source, doublet, and quadrupole forms with their appropriate reflections. Thus, the reflection of the doublet is an X derivative of the sources, and the quadrupole has the same relationship to the doublet.

For matching Eqs. $(2-19)$ and $(2-20)$ are written in the intermediate variable

$$R_\eta = \frac{R}{\eta} \qquad (2-21)$$

which is held fixed as $H\to\infty$. The gauge function η is an order class intermediate between 1 and H as $H\to\infty$. This is expressed symbolically as

$$1 << \eta(H) << H \quad . \qquad (2-22)$$

Thus, $\frac{1}{\eta(H)}\to 0$ as $H\to\infty$, and $\frac{\eta}{H}\to 0$ as $H\to\infty$. For axial symmetry of the interface pressures, the matching process is almost identical to that discussed in Ref. 29. The only difference will be the redefinition of certain constants associated with the streamwise integrals of the specified pressure data as well as the switchback terms. For understanding of basic issues related to the extension to non–axisymmetric interface pressures, the matching is diagrammed in Fig. 3.

Referring to the figure, the various labeled terms denoted by the circles give the following matchings:

$① \leftrightarrow ①'$ $\Rightarrow A_0 = -\dfrac{S(1)}{4\pi\sqrt{K_0^*}}$, $\epsilon_0 = \frac{1}{H}$

$② \leftrightarrow ④.1'$ $\Rightarrow \epsilon_{1/2} = \frac{1}{H^2}$

$③ \leftrightarrow ⑤.3'$ matched

$④ \leftrightarrow ⑤.1'$ $\Rightarrow \epsilon_1 = \frac{1}{H^3}$, $C = -\dfrac{A}{\sqrt{K_0^*}}$

$⑤ \leftrightarrow ②'$ $\Rightarrow \mu_{1/2} = \frac{1}{H}$, $\phi_{1/2} = \mathcal{A}_0 + \mathcal{B}_0$

$⑥.1 \leftrightarrow ③'$ $\Rightarrow \mu_1 = \frac{1}{H^3}$, $\alpha_0 = \mathcal{C}_0 + \mathcal{D}_0$

$⑥.2 \leftrightarrow ④.2'$ $\Rightarrow \alpha_1 = B_0\alpha_0$

$⑥.3 \leftrightarrow ⑤.2'$ $\Rightarrow \alpha_2 = \alpha_0 C \quad .$

As will be seen in the next section, the non–axially symmetric case requires additional terms in the wall, central, and axis layers to deal with the effect of the higher harmonics.

Fig. 3. Matching of central and wall regions for axially symmetric interface pressures.

The matching of the central layer and the axis layer proceeds along similar lines to that given in Ref. 29. All that is required is the essential result for the boundary condition, which is

$$\phi_{1_r}(x,0) = 0 \quad . \tag{2-23}$$

The expression for the interference pressure remains the same as that given in Ref. 29. However, there is an implicit dependence on the interface pressure data through the far field influence of the terms involving the constants B_0 and C_0 defined in $(2-18c)$ and $(2-18d)$. Also, the flux of streamwise momentum of the interference field through the interface must be considered in the calculation of the interference drag. The implicit dependence on the interface pressure data is shown in the following altered problem P1 denoted P2 for the interference potential in the central region ϕ_1.

<u>P2:</u>

$$[K_0^* - (\gamma+1)\phi_{0_x}]\,\phi_{1_{xx}} - (\gamma+1)\phi_{0_x}\phi_{1_x} + \frac{1}{\tilde{r}}(\tilde{r}\phi_{1_r})_{\tilde{r}} = -K_1^*\phi_{0_{xx}} \tag{2-24a}$$

$$\phi_{1_r}(x,0) = 0 \tag{2-24b}$$

$$\phi_1 \simeq \alpha_0 R^2 P_2(\cos\omega) + \alpha_1 R \cos\omega + \alpha_2 \quad \text{as } R \to \infty \tag{2-24c}$$

where

$$\alpha_0 = C_0 + \mathcal{D}_0 \tag{2-24d}$$

$$\alpha_1 = B_0\alpha_0 \tag{2-24e}$$

$$\alpha_2 = -\frac{8\pi b_0 A}{\sqrt{K_0^*}} = \alpha_0 C \quad . \tag{2-24f}$$

For the free jet case, $C_0 = 0$ in $(2-24d)$ and $B_0 = 0$ in Fig. 3. Solid wall conditions are modeled by making $\alpha_0 = b_0' = b_0 S(1)/\sqrt{K_0^*}$, with $\alpha_1 = 8\pi B_0 b_0$, with $b_0 = .063409^*$.

<u>2.1.11   Discussion</u>

Because of the relationship of P1 to P2, the computational algorithm which has been developed for the solid wall case can be used to solve P2 with corrections of the indicated constants and the post–processing subroutine DRAG1 to account for the flux of streamwise momentum through the interface. Note here that the effect of α_2 in $(2-24c)$ can be neglected.

---

* The determination of this value is discussed in Section 2.12.

2.2 Generalization to Angular and Unsymmetrical Variations

Summary

In this section, the pressure boundary condition asymptotic analysis given in Section 2.1 is extended to handle angular interface and unsymmetrical variations of measured pressure.

Central Layer

With the generalized angular variation at the interface, $(2-6a)$ is anticipated to be modified as

$$\phi = \phi_0(x,\tilde{r}) + \mu_{1/2}(H)\phi_{1/2}(x,\tilde{r},\theta) + \mu_{3/4}(H)\phi_{3/4}(x,\tilde{r},\theta) + \mu_1(H)\phi_1(x,\tilde{r},\theta) + \cdots \quad (2-25)$$

As compared to $(2-6a)$, $(2-25)$ contains an extra term (indicated by 3/4 subscripts). This insertion is required by matching considerations associated with the more general class of interface pressure distributions involving angular and asymmetric streamwise variations.

The analysis and results are such that Eqs. $(2-3)$ to $(2-6)$ remain unchanged. Reflecting the more general interface distribution the expression for φ_0 becomes

$$\varphi_0 = \frac{S(1)}{4\pi^2\sqrt{K_0^*}}\left(\tilde{Q}_1 - \tilde{Q}_2\right) + \frac{Q_0}{4\pi^2} + \frac{1}{2\pi^2}\sum_{n=1}^{\infty}(Q_n\cos n\theta + P_n\sin n\theta) \quad (2-26a)$$

where

$$\tilde{Q}_1 = \int_{-\infty}^{\infty}\frac{I_0\left(kr^\dagger\right)K_0(k)}{I_0(k)}e^{ikX^\dagger}dk \quad (2-26b)$$

$$\tilde{Q}_2 = \int_{-\infty}^{\infty}K_0\left(kr^\dagger\right)e^{ikX^\dagger}dk \quad (2-26c)$$

$$Q_n = \int_{-\infty}^{\infty}e^{ikX^\dagger}\frac{I_n\left(kr^\dagger\right)}{I_n(k)}dk\int_0^{2\pi}\overline{f}(\theta,k)\cos n\theta d\theta \quad (2-26d)$$

$$P_n = \int_{-\infty}^{\infty}e^{ikX^\dagger}\frac{I_n\left(kr^\dagger\right)}{I_n(k)}dk\int_0^{2\pi}\overline{f}(\theta,k)\sin n\theta d\theta \quad . \quad (2-26e)$$

Upon expanding the integrands in $(2-26)$ for small R, and with considerable algebraic manipulation, the asymptotic expansions of the integrals can be obtained. The methodology exemplified in Ref. 29 involves expansion of the Bessel functions for small $r^\dagger$ and the $e^{ikX^\dagger}$ kernel for small $X^\dagger$ and gives a series that can be integrated term by term. These integrals are convergent for the ray limits $\left(R^\dagger \to 0, \theta \text{ fixed}\right)$ of interest.

Collecting results, the desired expansion of φ_0 is

$$\varphi_0 = \frac{\mathcal{A}_{00}}{R^\dagger} + \mathcal{A}_0 + \mathcal{B}_0 + \mathcal{A}_{01}X^\dagger$$

$$+ \underbrace{\mathcal{E}_0 r^\dagger \cos\theta}_{y} + \underbrace{\mathcal{F}_0 r^\dagger \sin\theta}_{z} + X^\dagger \left(\underbrace{\mathcal{E}_{01} r^\dagger \cos\theta}_{X^\dagger y} + \underbrace{\mathcal{F}_{01} r^\dagger \sin\theta}_{X^\dagger z} \right) \qquad (2-27a)$$

$$\underbrace{\mathcal{G}_0 r^\dagger \cos 2\theta}_{y^2 - z^2} + \underbrace{\mathcal{H}_0 r^{\dagger^2} \sin 2\theta}_{yz}$$

$$(\mathcal{C}_0 + \mathcal{D}_0)\, R^{\dagger^2} P_2(\cos\omega) + \cdots$$

where the terms shown under those in $(2-27a)$ are listed to indicate their correspondence with spherical harmonics and the spherical coordinates are as shown in Fig. 4.

SC50443

Fig. 4. Spherical coordinates.

From the asymptotic expansions, the constants in $(2-27a)$ are:

$$\mathcal{A}_{00} = -\frac{S(1)}{4\pi\sqrt{K_0^*}} \qquad (2-27b)$$

$$\mathcal{A}_0 = \frac{S(1)}{2\pi^2\sqrt{K_0^*}} \int_0^\infty \frac{K_0(k)}{I_0(k)} dk \quad , \quad \mathcal{B}_0 = \frac{1}{4\pi^2} \int_{-\infty}^\infty \frac{dk}{I_0(k)} \int_0^{2\pi} \overline{f_R}(\theta, k) d\theta \qquad (2-27c)$$

$$\mathcal{A}_{01} = \frac{1}{4\pi^2} \int_{-\infty}^\infty \frac{k\,dk}{I_0(k)} \int_0^{2\pi} \overline{f_I}(\theta, k) dk \qquad (2-27d)$$

17

$$\mathcal{E}_0 = \frac{1}{4\pi^2} Re\ i \int_{-\infty}^{\infty} \frac{k^2 dk}{I_1(k)} \int_0^{2\pi} \overline{f} \cos\theta d\theta \quad , \quad \overline{\mathcal{F}}_0 = \frac{1}{4\pi^2} Re \int_{-\infty}^{\infty} \frac{k dk}{I_1(k)} \int_0^{2\pi} \overline{f} \sin\theta d\theta$$

$$(2-27e)$$

$$\mathcal{E}_{01} = \frac{1}{4\pi^2} Re\ i \int_{-\infty}^{\infty} \frac{k^2 dk}{I_1(k)} \int_0^{2\pi} \overline{f} \cos\theta d\theta \quad , \quad \overline{\mathcal{F}}_{01} = \frac{1}{4\pi^2} Re\ i \int_{-\infty}^{\infty} \frac{k^2 dk}{I_1(k)} \int_0^{2\pi} \overline{f} \sin\theta d\theta$$

$$(2-27f)$$

$$\mathcal{C}_0 = -\frac{S(1)}{4\pi^2 \sqrt{K_0^*}} \int_0^{\infty} \frac{k^2 K_0(k)}{I_0(k)} dk \quad , \quad \mathcal{D}_0 = -\frac{1}{8\pi^2} \int_{-\infty}^{\infty} \frac{k^2 dk}{I_0(k)} \int_0^{2\pi} \overline{f_R} d\theta \qquad (2-27g)$$

$$\mathcal{G}_0 = \frac{1}{4\pi^2} Re \int_{-\infty}^{\infty} \frac{k^2 dk}{I_2(k)} \int_0^{2\pi} \overline{f} \cos 2\theta d\theta \quad , \quad \mathcal{H}_0 = -\frac{1}{4\pi^2} Re \int_{-\infty}^{\infty} \frac{k^2 dk}{I_2(k)} \int_0^{2\pi} \overline{f} \sin 2\theta d\theta$$

$$(2-27h)$$

<u>Matching</u>

Using the intermediate limit described in Section 2.1.10, matching of the central and wall regions is schematically indicated in Fig. 5 in which both representations are written in terms of the intermediate variable R_η defined in Section 2.1.10. It should be noted that nonlinear effects are associated with Poisson equation forcing terms such as $\phi_{1_z}\phi_{0_{zz}}$ in $(2-7c)$. The Poisson form is associated with $R \to \infty$ ray limit of the central region flow. In Fig. 4, $\Omega^{(1)}$ is a particular solution of the equation

$$\frac{1}{\sin\omega}\left(\frac{d}{d\omega}\sin\omega\frac{d\Omega^{(1)}}{d\omega}\right) + \frac{\Omega^{(1)}}{\sin^2\omega} = \cos\omega \qquad (2-28a)$$

and $\Omega^{(2)}$ is the solution of

$$\frac{1}{\sin\omega}\left(\frac{d}{d\omega}\sin\omega\frac{d\Omega^{(2)}}{d\omega}\right) + \frac{\Omega^{(2)}}{\sin^2\omega} = \frac{3P_3(\cos\omega) + 2P_1(\cos\omega)}{5} \qquad . \qquad (2-28b)$$

As indicated in Section 2.1.10, the matching of the central and axis layers proceeds along similar lines to that discussed in Ref. 29.

All that is required is the essential result for the boundary condition, which is

$$\phi_{1_r}(x,0) = 0 \qquad .$$

The expression for the interference pressure remains the same as that given in Ref. 29. However, there is an implicit dependence on the interface pressure data through the far field influence of the terms involving the constants defined in $(2-27c)$ to $(2-27h)$. Also, the flux of streamwise momentum of the interference field through the interface must be considered in the calculation of the interference drag. The implicit dependence on the interface pressure data is shown in the following altered problem P1 denoted P2 for the interference potential in the central region ϕ_1.

PRESSURES SPECIFIED ON INTERFACE

$$\frac{\Phi_{central}}{U} = x + \delta^2 \left\{ \left[\left[\frac{A_0}{\eta R_\eta} + \frac{B_0 \cos\omega}{\eta^2 R_\eta^2} + \frac{C_0}{\eta^3 R_\eta^3}(\cos 3\omega - \cos\omega) + \frac{A_0}{\sqrt{K_0^2}\eta^3 R^3} P_3(\cos\omega) \right] \right. \right.$$

$$+ \frac{1}{H}a_{1/4} + \frac{1}{H^2}\left[A_{01}\eta R_\eta \cos\omega + \mathcal{E}_{01}\eta R_\eta \sin\omega\cos\theta + \mathcal{F}_{01}\eta R_\eta \sin\omega\sin\theta + a_{1/4} + \frac{P_2(\cos\omega)}{3\eta R_\eta} \right]$$

$$+ \frac{1}{H^3}\left[\overline{A_0}\eta^2 R_\eta^2 P_2(\cos\omega) + \overline{A_1}\eta R_\eta\cos\omega + \overline{A_2} + \eta^2 R_\eta^2\cos\omega\sin\omega(\mathcal{E}_{01}\cos\theta + \mathcal{F}_{01}\sin\theta) \right.$$

$$+ \overline{A_3}\eta R_\eta\sin\omega\sin\theta + \eta^2 R_\eta^2\sin^2\omega(\overline{A_5}\cos 2\theta + \overline{A_7}\sin 2\theta) + \overline{A_6}\eta R_\eta\sin\omega\cos\theta$$

$$\left. \left. + \alpha\Omega^{(1)}(\omega) + \Omega^{(2)}(\omega)[\beta\cos\theta + \gamma\sin\theta] \right] \right\} = x + \delta^2\phi_{central}$$

$$\frac{\Phi_{wall}}{U} = x + \delta^2 \left\{ \frac{1}{H}\left[\frac{S(1)}{4\pi\frac{\eta R_\eta}{H}} + \overline{A_0 + B_0} + A_0\frac{\eta R_\eta}{H}\cos\omega + (C_0 + D_0)\frac{\eta^2 R_\eta^2}{H^2}P_2(\cos\omega) \right. \right.$$

$$+ \frac{\eta R_\eta}{H}\sin\omega(\mathcal{E}_0\cos\theta + \mathcal{F}_0\sin\theta) + \frac{\eta^2 R_\eta^2}{H^2}\sin^2\omega(\mathcal{G}_0\cos 2\theta + 2\mathcal{H}_0\sin 2\theta)$$

$$\left. + \frac{\eta^2 R_\eta^2}{H^2}\cos\omega\sin\omega(\mathcal{E}_{01}\cos\theta + \mathcal{F}_{01}\sin\theta) \right]$$

$$+ \frac{1}{H^2}B\left[\frac{\cos\omega}{\eta^2 R_\eta^2} + 2(C_1 + D_0)\frac{\eta R_\eta}{H}\cos\omega + \frac{\eta R_\eta}{H}\sin\omega(\mathcal{E}_{01}\cos\theta + \mathcal{F}_{01}\sin\theta) + A_{01} \right]$$

$$+ \frac{1}{H^3}\left[C\left(-\frac{1}{2\pi}\frac{P_2(\cos\omega)}{\frac{\eta^2 R_\eta^2}{H^2}} + 2C_1 \right) + \frac{C_0}{\frac{\eta^3 R_\eta^3}{H^3}}(\cos 3\omega - \cos\omega) + \frac{CP_3(\cos\omega)}{\frac{\eta R_\eta}{H}} \right.$$

$$\left. \left. + \frac{a_{01}a_{00}P_2(\cos\omega)}{\frac{\eta R_\eta}{H}} - 2a_{00}(C_0 + D_0)\Omega^{(1)}(\omega) + \Omega^{(2)}(\mathcal{E}_{01}\cos\theta + 2\mathcal{F}_{01}\sin\theta) \right] \right\} = x + \delta^2\phi_{wall}$$

Fig. 5. General case of matching of central region and wall layers.

19

P2:

$$[K_0^* - (\gamma + 1)\phi_{0_x}]\phi_{1_{xx}} - (\gamma + 1)\phi_{0_x}\phi_{1_x} + \frac{1}{\bar{r}}(\bar{r}\phi_{1_r})_{\bar{r}} = -K_1^*\phi_{0_{xx}} \qquad (2-29a)$$

$$\phi_{1_r}(x,0) = 0 \qquad (2-29b)$$

$$\phi_1 \simeq R^2 \left\{ \overline{\mathcal{A}_0} P_2(\cos\omega) + \cos\omega\sin\omega \left(\overbrace{\overline{\mathcal{E}_{01}}\cos\theta + \overline{\mathcal{F}_{01}}\sin\theta}^{①} \right) \right.$$

$$\left. + \sin^2\omega \left(\overbrace{\overline{\mathcal{A}_3}\cos 2\theta + \overline{\mathcal{A}_4}\sin 2\theta}^{②} \right) \right\}$$

$$+ R \left\{ \overline{\mathcal{A}_1}\cos\omega + \sin\omega \left(\overbrace{\overline{\mathcal{A}_5}\sin\theta + \overline{\mathcal{A}_6}\cos\theta}^{③} \right) \right\} \qquad (2-29c)$$

$$+ \mathcal{A}_2 + \cdots \quad \text{as } R \to \infty$$

where by Fig. 5, with B and C defined in Ref. 29

$$\overline{\mathcal{A}_0} = \mathcal{C}_0 + \mathcal{D}_0 \qquad (2-29d)$$

$$\overline{\mathcal{A}_1} = 2B\overline{\mathcal{A}_0} \qquad (2-29e)$$

$$\overline{\mathcal{A}_2} = 2CC_1 = 2B(\mathcal{C}_0 + \mathcal{D}_0) \qquad (2-29f)$$

$$\overline{\mathcal{A}_3} = \mathcal{G}_0 \qquad (2-29g)$$

$$\overline{\mathcal{A}_4} = \mathcal{H}_0 \qquad (2-29h)$$

$$\overline{\mathcal{A}_5} = \overline{\mathcal{F}_{01}} \qquad (2-29i)$$

$$\overline{\mathcal{A}_6} = \mathcal{E}_{01} \quad . \qquad (2-29j)$$

2.2.1 Discussion

The problem $(2-29a)$–$(2-29c)$ is the generalization of the Problem P2 given in Section 2.1.10 *accounting for asymmetries in the streamwise distribution of the interface pressures as well as angular θ variations*. These effects are given by the terms marked as ①
– ③ in $(2-29c)$. They represent averages of the early harmonics *which to this order is all that the far field is sensitive to*. The specialization to the free jet case is obtained by setting $\mathcal{D}_0 = g_0 = \mathcal{H}_0 = \mathcal{E}_{01} = \overline{\mathcal{F}}_{01} = 0$ in Eqs. $(2-29)$.

2.3 Shock Jump Conditions

An important element to be considered in the numerical solution of the Problem P1 referred to in the previous sections is the satisfaction of the shock jump conditions. For

the free field case, these relations are satisfied by the divergence or conservation form of the Karman Guderley small disturbance equation. These give the Rankine Hugoniot jump conditions. They are satisfied using type sensitive shock capturing schemes such as those originally developed by Murman and Cole in Ref. 31. On the other hand, the wall interference corrections related to the Problem P1 have to be satisfied by use of explicit relations. These have been derived for the high aspect ratio transonic lifting line theory formulated in Ref. 32. These relations will be derived for axisymmetric flow in this section.

Referring to Fig. 6, conditions across the shock front denoted as S will be discussed. This surface is given by

$$S = x - g(\tilde{r}) = 0 \quad , \tag{2-30}$$

where $\tilde{r} = \delta r$, and consistent with the Problem P1 delineated in Ref. 29, axial symmetry is assumed. The Problem P1 describes the wall interference flow away from the walls on the axis of symmetry of a cylindrical test section. The velocity potential in this zone, denoted by Φ, is given by the asymptotic expansion

SC84-29502

Fig. 6. Orientation of shock surfaces.

$$\frac{\Phi}{U} = x + \delta^2 \left\{ \phi_0(x,\tilde{r}) + \frac{a_0'}{H} + \frac{1}{H^3}\phi_1(x,\tilde{r}) + \cdots \right\} \quad , \tag{2-31}$$

where U is the freestream speed, the ϕ_i are perturbation potentials, a_0' is a constant, H is the wall height in units of the body length, and δ is the confined body's thickness ratio. The secondary expansion in the braces in $(2-31)$ is an approximation for the perturbation potential ϕ which is governed by the Karman Guderley transonic small disturbance equation $(2-5a)$, with $\frac{\partial}{\partial\theta}$ assumed zero.

Equation $(2-5a)$ can be written in the divergence form,

$$L\{\phi\} \equiv \left\{ K\phi_x - \frac{\gamma+1}{2}\phi_x^2 \right\}_x + \frac{1}{\tilde{r}}(\tilde{r}\phi_{\tilde{r}})_{\tilde{r}} = 0 \quad , \tag{2-32}$$

21

where subscripts denote partial differentiation. Denoting the transverse velocity vector as $\vec{v} = v\vec{1}_{\tilde{r}}$, $(v = \phi_{\tilde{r}})$, the $\tilde{r}$ derivative term in $(2-32)$ can be written as $\tilde{\nabla} \cdot \vec{v}$, where $\tilde{\nabla} \cdot$ is the cross flow divergence.

The integral form of $(2-32)$, applied to the infinitesimal thickness $(= \epsilon)$ volume V shown in Fig. 6 is

$$\int\int_V L\{\phi\} 2\pi\tilde{r}\, d\tilde{r}\, dx = 0 \quad ,$$

and the divergence theorem gives rise to the flux form

$$\int_S \left\{ \left[Ku - \frac{\gamma+1}{2}u^2 \right] + [\vec{v}] \cdot \frac{\vec{n}}{\delta} \right\} 2\pi\tilde{r}\, d\tilde{r} = 0 \quad , \tag{2-33}$$

where $[f] \equiv \lim_{\epsilon \to 0} \{f(x, g+\epsilon) - f(x, g-\epsilon)\}$, $u = \phi_x$, and $\vec{n}$ is a unit vector normal to S. Since $(2-33)$ holds for an arbitrary area, the integrand must be zero,

$$\left[Ku - \frac{\gamma+1}{2}u^2 \right] + [\vec{v}] \cdot \frac{\vec{n}}{\delta} = 0 \quad . \tag{2-34}$$

Now

$$\vec{n} = \frac{\nabla S}{|\nabla S|} = \frac{\vec{i} - \delta g'(\tilde{r})\vec{1}_{\tilde{r}}}{\sqrt{1 + \mathcal{O}(\delta^2)}} \quad , \tag{2-35}$$

where $\vec{i}$ is the unit vector in the x direction and $\vec{1}_{\tilde{r}}$ that in the $\tilde{r}$ direction. Substituting into $(2-34)$, this gives

$$\left[Ku - \frac{\gamma+1}{2}u^2 \right] - g'[v] = 0 \quad . \tag{2-34'}$$

By virtue of conservation of tangential momentum across the shock, the perturbation of the velocity vector $\vec{q}$ is normal to the shock surface. This perturbation velocity is given by

$$\frac{\vec{q} - U\vec{i}}{U} = \delta^2 u\vec{i} + \delta^3 v\vec{1}_{\tilde{r}} \quad .$$

On the basis of tangential momentum conservation,

$$(\vec{q} - U\vec{i}) \times \nabla S = 0 \quad ,$$

which gives

$$[v] = -[u]g'(\tilde{r}) \quad . \tag{2-35}$$

Eliminating g' from $(2-34')$ using $(2-35)$ gives

$$\left[Ku - \frac{(\gamma+1)}{2}u^2 \right][u] + [v]^2 = 0 \quad . \tag{2-36}$$

Since tangential momentum is conserved, the tangential velocity component to the shock is continuous across it. Upon tangential integration, and disposing of an unessential constant, the following relation is obtained

$$[\phi] = 0 \quad . \tag{2-37}$$

Equations $(2-36)$ and $(2-37)$ lead upon substitution of the asymptotics into the jump relations for the approximate quantities appearing in $(2-31)$. To obtain a determinate set of quantities, the shock's representation is assumed to be in the same form as that for ϕ, i.e.,

$$g = g_0(\tilde{r}) + \frac{1}{H}g_{1/2}(\tilde{r}) + \frac{1}{H^3}g_1 + \cdots \quad . \tag{2-38}$$

Denoting f as a quantity of interest which has the same asymptotic form as ϕ, on the basis of $(2-38)$ and Taylor's expansion,

$$
\begin{aligned}
f(x,g) =& f_0(x,g_0) + \frac{1}{H}\big(f_{1/2}(x,g_0) + g_{1/2}f_{0_g}(x,g_0)\big) \\
&+ \frac{g_{1/2}^2}{H^2}f_{0_{gg}}(x,g_0) + \frac{1}{H^3}\big(f_1(x,g_0) + g_1 f_{0_g}(x,g_0)\big) \\
&+ \cdots \quad .
\end{aligned}
\tag{2-39}
$$

By virtue of $(2-39)$, substitution of the expansion $(2-31)$ into $(2-36)$ gives the approximate shock relations which are:

$$O(1) \; : \; \left[\left(K - \frac{\gamma+1}{2}u_0\right)u_0\right] + [v_0]^2 = 0 \tag{2-40a}$$

$$
\begin{aligned}
[u_1]\left[Ku_0 - \frac{\gamma+1}{2}u_0^2\right] &+ [u_0]\left[(K - (\gamma+1)u_0)u_1\right] \\
&+ 2[v_0][v_1] = -g_1\bigg\{ [u_0]\left[(k - (\gamma+1)u_0)u_{0_g}\right] \\
&+ \left[Ku_0 - \frac{\gamma+1}{2}u_0^2\right][u_{0_g}] \\
&+ 2[v_0][v_{0_g}] \bigg\}
\end{aligned}
\tag{2-40b}
$$

where $u_i \equiv \phi_{i_g}$ and $v_i \equiv \phi_{i_r}$, where i is equal to $0,1$. The quantity $g_{1/2}$ can be shown to vanish on the basis of $(2-37)$ which with $(2-39)$ leads to the additional set of relations:

$$O(1) \; : \; [\phi_0] = 0 \tag{2-41a}$$

$$O(H^{-3}) \; : \; [\phi_1] = -g_1[\phi_{0_g}] \quad . \tag{2-41b}$$

It should be noted that the $O(H^{-1})$, $O(H^{-2})$ equations obtained in the process leading to Eqs. $(2-40)$ are vacuous.

Equations $(2 - 40)$ and a vorticity relationship to be derived in the next section complete the formulation necessary for the computational solution.

2.4 Shock Conservation Laws for Wall Correction Flow

In addition to the jump relations derived in Section 2.3, a useful conservation law can be derived for use in the numerical solutions. In analogy to the free field large aspect ratio case discussed in Ref. 32, this law will be obtained using the divergence theorem. Considering the region shown in Fig. 7, the divergence form of $(2-7c)$ (with $\frac{\partial}{\partial \theta} = 0$ and dropping the stars on the K's) is

$$\left\{ K_1 \phi_{0_x} + K_0 \phi_{1_x} - (\gamma + 1)\phi_{0_x}\phi_{1_x} \right\}_x + \frac{1}{\tilde{r}}(\tilde{r}\phi_{1_{\tilde{r}}})_{\tilde{r}} = 0 \quad ,$$

or

$$\hat{\nabla} \cdot \left(K_1 \phi_{0_x} + K_0 \phi_{1_x} - (\gamma + 1)\phi_{0_x}\phi_{1_x}, K_0 \phi_{1_{\tilde{r}}} \right) = 0 \quad , \qquad (2-42)$$

where $\hat{\nabla}\cdot$ refers to the divergence operator in the $x, \hat{r}$ coordinate system in which $\hat{r} = \sqrt{K_0}\tilde{r}$. From $(2-42)$,

$$\int\int_S (K_1 \phi_{0_x} - w\phi_{1_x}, K_0\phi_{1_{\tilde{r}}}) \cdot \vec{n} dS \quad ,$$

where $w \equiv (\gamma + 1)\phi_{0_x} - K_0$, S represents the surface of revolution consisting of the sphere S_R, $R = R_0$, the cut S_B around $\hat{r} = 0$, S_0 around the shock or shocks, and $\vec{n}$ is the unit normal to the shock surface.

Now, since $\phi_{1_{\tilde{r}}}(x, 0) = 0$,

$$\int\int_{S_B} = \int\int \phi_{1_{\tilde{r}}} \cdot \vec{1}_{\tilde{r}} dx = 0 \quad ,$$

where $\vec{1}_{\tilde{r}}$ is the unit vector in the $\hat{r}$ direction. Also, $\int\int_{S_R}$ can be shown to vanish to the order of approximation considered by virtue of Eq. (20b) in Ref. 29. From the previous section, with the first approximation of the shock shape given by

$$X = G_0(\tilde{r})$$

$$\frac{[\phi_{0_{\tilde{r}}}]}{[\phi_{0_x}]} = -G_0'(\tilde{r}) \quad , $$

where $[\quad]$ denotes the jump of the indicated quantity across the shocks and

$$\vec{n} = \frac{\vec{\imath} - G_0'(\hat{r})\vec{1}_{\tilde{r}}}{\sqrt{1 + G_0'^2(\hat{r})}} \quad , $$

the desired conservation law is

$$\int_{S_0} \left\{ K_1 [\phi_{0_x}] - [w\phi_{1_x}] - \frac{[\phi_{0_{\tilde{r}}}][\phi_{1_{\tilde{r}}}]}{[\phi_{0_x}]} \right\} d\tilde{r} = 0 \quad , \qquad (2-43)$$

Fig. 7. Regions appropriate to shock conservation laws.

where S_0 is the shock surface.

2.5   Regularization of the Problem for the Correction Potential ϕ_1

To avoid the singularity at ∞, the problem P1 in Ref. 29 is transformed by subtracting off the far field for ϕ_1. Accordingly, the variable $\hat{\phi}_1$ is introduced in P1, where

$$\hat{\phi}_1 = \phi_1 - \phi_{FF} \quad . \qquad (2-44)$$

Here,

$$M\left[\phi_1\right] \equiv \left(K_0 - (\gamma+1)\phi_{0_x}\right)\phi_{1_{xx}} - (\gamma+1)\phi_{0_{xx}}\phi_{1_x} + \frac{1}{\tilde{r}}(\tilde{r}\phi_{1_{\tilde{r}}})_{\tilde{r}} = -K_1\phi_{0_{xx}} \quad (2-45a)$$

and

$$\lim_{\tilde{r}\to 0} \phi_{1_{\tilde{r}}} = 0 \quad . \qquad (2-45b)$$

Noting that (for solid walls)

$$\phi_1 \simeq \phi_{FF} = b_0'\tilde{R}^2 P_2(\cos\omega) + 8\pi b_0' B_0\tilde{R}\cos\omega \qquad (2-45c)$$

as

$$\tilde{R} = \sqrt{\frac{x^2}{K_0^2} + \tilde{r}^2} \to \infty$$

and

$$\phi_{FF} = b_0'\left(X^2 - \frac{\tilde{r}^2}{2}\right) + 8\pi b_0 B_0 X \quad , \qquad (2-46)$$

where

$$b_0' = \frac{S(1)}{\sqrt{K_0}}b_0$$

$$4\pi B_0 = -S(1) + \int_0^1 S(x)dx + \pi(\gamma+1)\int_{-\infty}^{\infty} dx \int_0^{\infty} \tilde{r}^2\phi_{0_x}^2 d\tilde{r}$$

$$\omega = \text{polar angle defined in Fig. 1}$$
$$S(x) = \text{model cross sectional area}$$
$$R = \text{polar radius defined in Fig. 1} \quad .$$

From $(2-44)$ and $(2-46)$, $(2-45a)$ and $(2-45b)$ become

$$M\left[\hat{\phi}_1\right] = \frac{2(\gamma+1)\phi_{0_x}b_0'}{K_0} + \phi_{0_{xx}}\left\{(\gamma+1)\left(\frac{2b_0'x}{K_0} + \frac{8\pi b_0 B_0}{\sqrt{K_0}}\right) - K_1\right\} \quad (2-47a)$$

$$\lim_{\tilde{r}\to 0} \hat{\phi}_{1_{\tilde{r}}} = 0 \qquad (2-47b)$$

$$\hat{\phi}_1 \to 0 \text{ as } \tilde{R} \to \infty \qquad (2-47c)$$

where $\tilde{R} = \delta R$.

The slender body interference code will use the regularized form represented by Equations $(2 - 47)$.

2.6 Basic Code Modules

Figures 8 show flow charts which give an overview of the interaction of the functional modules to be used in the design of the wall interference code under Task 1.0. The preprocessor ATF sets up the grid and inputs other parameters through the subroutines INITIA, INPUT. The input geometry data is read in from the disk file. The solver STINT25 has primary subprograms denoted as RELAX1, OUTFNL, SONIC, DRAG1 used to solve the zeroth order flow problem and RELAXV1, OUTFNL1, and DRAG1 for the variational problem for $\dot{\phi}_1$. RELAX1 and RELAXV1 are modules which respectively are the principal successive line overrelaxation routines which serve the purpose of solving the tridiagonal system for the free field and the interference problems. The tridiagonal solver is denoted as TRID. RELAX1 and RELAXV1 include special treatment of far field, internal, boundary, and shock points with appropriate type sensitive switches. SONIC determines subsonic and supersonic zones, and OUTFNL and OUTFNL1 provide the basic flow and interference pressure fields as well as the quantities g_i defined in Ref. 29 necessary to compute free field and interference drags. These are computed in DRAG and DRAG1, respectively. The relationship of the flow solving modules is shown in Figs. 8.

2.7 Upstream and Downstream Far Fields

For slender test articles that are sting mounted inside solid walls, the flow at great distances from the model behaves as a confined source in accord with the analyses given in the previous sections. Referring to the cylindrical coordinate system indicated in Fig. 9, far field behaviors were worked out in certain "ray limits" in which if $R = \sqrt{x^2 + \tilde{r}^2}$ and $\cos\omega = x/R$, $R \to 0$ for θ fixed. The case $\omega = 0$, or π, i.e., $x \to \pm\infty$ however is degenerate and requires special treatment and had not been analyzed.

For a properly posed numerical simulation of the finite height case, the structure of this flow must be properly modeled. This can be achieved using the Divergence Theorem.

If x is the usual dimensionless coordinate in the freestream direction depicted in Fig. 9, then the transonic small disturbance formulation gives the following equation of motion

$$\Delta\phi \equiv \phi_{XX} + \frac{1}{\tilde{r}}(\tilde{r}\phi_{\tilde{r}})_{\tilde{r}} = \frac{(\gamma + 1)}{\sqrt{K}}\phi_X\phi_{XX} \qquad (2 - 48)$$

where $K = (1 - M_\infty^2)/\delta^2$, M_∞ = freestream Mach number, ϕ is the perturbation potential, and $X = x/\sqrt{K}$. The slender body boundary condition is

$$\lim_{\tilde{r}\to 0} \tilde{r}\frac{\partial\phi}{\partial\tilde{r}} = \frac{S'(x)}{2\pi} \quad , \qquad (2 - 49)$$

where $S(x)$ is the cross sectional area distribution for $0 \leq x \leq 1$, and $S'(x)$ is without great loss of generality assumed zero for $1 \leq x \leq \infty$, (constant diameter sting).

Fig. 8. Flow chart for preprocessor and solver.

Fig. 8. Flow chart for preprocessor and solver (continued). N in the notation STINTN denotes the Nth version of the main driver.

SC 0951-CS

Fig. 8. Flow chart for preprocessor and solver (concluded).

A control cylinder is considered consisting of the walls (S_H), an internal surface bounding the model near the axis, (S_ϵ), and the inflow and outflow faces $(S_{-\infty})$ and S_∞, respectively. Accounting for the impermeability of the walls expressed as

$$\left.\frac{\partial\phi}{\partial\tilde{r}}\right|_{\tilde{r}=H} = 0 \quad , \tag{2-50}$$
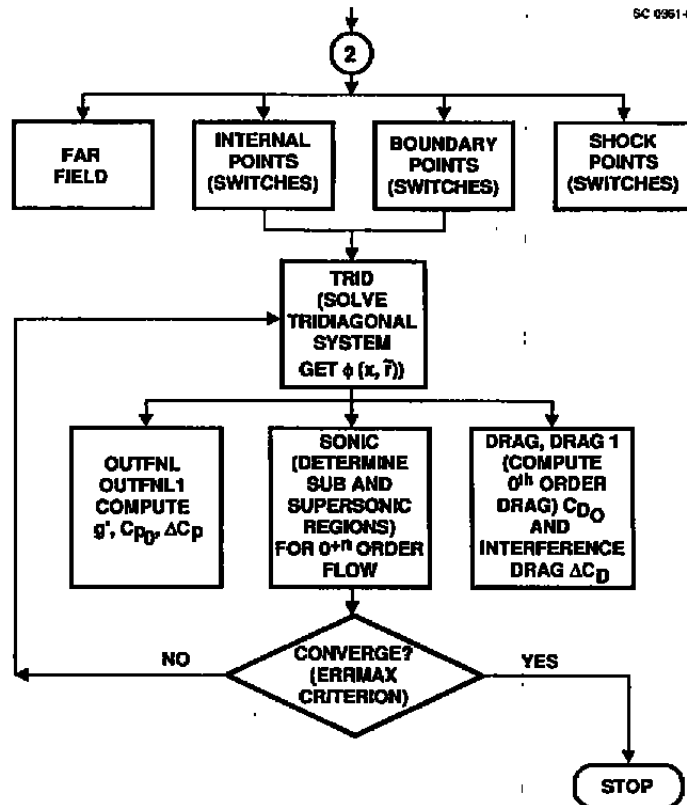
the divergence theorem when applied to $(2-48)$ gives

$$\int\int_V\int \triangle\phi\, dV = \int\int_{S_\epsilon+S_H+S_\infty+S_{-\infty}} \frac{\partial\phi}{\partial n} dS = 2\pi\int_0^H \tilde{r}d\tilde{r}\int_{-\infty}^\infty \left\{ \frac{(\gamma+1)}{2\sqrt{K}}\cdot\frac{\partial}{\partial X}(\phi_X^2) \right\} dX, \tag{2-51}$$

where V denotes the volume of the control cylinder. Evaluating the terms in $(2-51)$,

$$\int_{S_\epsilon}\frac{\partial\phi}{\partial n}dS = \lim_{\tilde{r}\to 0}\int_0^{2\pi} d\theta\int_0^\infty \frac{\partial\phi}{\partial\tilde{r}}\tilde{r}dX = 2\pi\int_0^\infty \frac{S'(x)}{2\pi}dX = S(1) \quad . \tag{2-52}$$

From $(2-50)$,

$$\int_{S_H}\frac{\partial\phi}{\partial n}\bigg|_{\tilde{r}=H} dS = 0 \quad . \tag{2-53}$$

For a slender configuration, we assert that as in the subsonic case, the lift effect produces a Trefftz plane $(x=\infty)$ flow component that can be represented as an infinitesimal span vortex pair reflected in the walls. This pair is the Trefftz plane projection of the trailing vortex system from the body. Superposed on this flow is an outflow due to the source effect. A similar outflow occurs at $x=-\infty$. Accordingly, we are led to the asymptotic inflow and outflow conditions

$$\phi \simeq C_{FF}x + f(\tilde{y},\tilde{z}) \quad \text{as } x\to\infty \tag{2-54a}$$

$$\begin{pmatrix} \tilde{y} = \tilde{r}\sin\theta \\ \tilde{z} = \tilde{r}\cos\theta \end{pmatrix}$$

$$\phi \simeq -C_{FF}x \quad \text{as } x\to -\infty \quad , \tag{2-54b}$$

where $f(\tilde{y},\tilde{z})$ is related to the lift, and the constant factor C_{FF} appears in the manner indicated in order to preserve the anticipated symmetry of the apparent source flow from the sting-mounted, finite base area model. In this connection, it is important to note that Eqs. $(2-54)$ are exact solutions to the nonlinear small disturbance equation $(2-48)$. This is true even for $f(\tilde{y},\tilde{z})$, since it satisfies cross flow Laplace's equation. It should be noted that the inflow and outflow conditions to be specified at $x=\pm\infty$ are independent of the form of f.

From $(2-54)$, it is clear then that

$$\int\int_{S_\infty+S_{-\infty}} \frac{\partial\phi}{\partial n}dS = 2\pi C_{FF}H^2 \quad . \tag{2-55}$$

31

Fig. 9. Model confined by solid cylindrical walls and control volume.

The last term to be evaluated in (2 − 51) is the right hand side, which is

$$2\pi \int_0^H \tilde{r}\,d\tilde{r} \int_{-\infty}^{\infty} \frac{(\gamma+1)}{2\sqrt{K}} \frac{\partial}{\partial X}\left(\phi_X^2\right) dX = \frac{(\gamma+1)}{2\sqrt{K}} \int_0^H \tilde{r}\left\{\phi_X^2(\infty,\tilde{r}) - \phi_X^2(-\infty,\tilde{r})\right\} d\tilde{r}$$

which vanishes by virtue of (2 − 54), as a milder condition of symmetry of the axial component of the far upstream and downstream flow. From this, as well as (2 − 51) to (2 − 55), it follows that the inflow and outflow conditions are,

$$\phi_x \simeq \pm \frac{S(1)}{2\pi H^2} \qquad \text{as } x \to \pm\infty \quad , \tag{2-56}$$

i.e., the apparent source strength is proportional to the body base area. Equation (2−56) is used in the numerical simulation of the flow field.

A complete asymptotic expansion based on the eigenfunction expansion for a confined point source given in Ref. 29 can be used to obtain refinement of (2 − 56) and treat the transonic case. From Green's theorem and the properties of the Green's function G, the perturbation potential ϕ in the confined incompressible solid wall circular cross section case is

$$\phi = \frac{1}{2\pi H^2} \int_0^1 |x - \xi| S'(\xi)d\xi + \frac{1}{2\pi H^2} \int_0^1 S'(\xi) \sum_n \frac{e^{-\lambda_n|x-\xi|}}{\lambda_n} \frac{J_0\left(\lambda_n r\right)}{\left[J_0(\lambda_n H)\right]^2} d\xi,$$

where the summation is over the eigenvalues λ_n which solve the following secular equation

$$J_1\left(\lambda_n H\right) = 0 \quad .$$

Thus,

$$\lambda_1 H = 3.8317$$
$$\lambda_2 H \doteq 10.1734$$
$$\lambda_3 H = 13.3237$$
$$\vdots$$

From these eigenvalues, it is clear that for moderate H, the confined flow decays much more rapidly upstream and downstream than the free field, with the former demonstrating exponential relaxation to the freestream and the latter, algebraic behavior.

Based on these considerations, and extension to compressible flow which introduces a nonlinear volume source the expression for the asymptotic upstream and downstream behavior is

$$\phi \doteq \frac{1}{2\pi H^2} \left\{ \frac{(\pm x \mp 1)S(1)}{K} + V \pm \frac{(\gamma+1)\pi}{K} \int_0^H \tilde{r}d\tilde{r} \int_{-\infty}^{\infty} \phi_{0_s}^2 dx \right\}$$
$$+ \text{TST} \quad \text{as} \quad x \to \pm\infty \qquad (2-56')$$

where TST = exponentially small terms which are

$$O\left(e^{-\frac{3.83}{H}|x|}\right) \quad \text{as} \quad |x| \to \infty$$

$$V = \int_0^1 S(x)dx \quad .$$

The last term in $(2-56')$ represents the average kinetic energy of the horizontal perturbation of the flow.

2.8 Difference Equations for the Wall Interference Correction Potential

A successive line overrelaxation (SLOR) algorithm for the large height correction potential has been coded. The initial approach is to use modifications of type sensitive switches developed by Murman and Cole[31], and pseudo–time operators devised by Jameson[33] as well as generalizations of the procedures developed in Ref. 34. Results to be discussed for the full nonlinear finite height theory algorithm show good convergence for transonic Mach numbers.

The basic code modules to treat this problem have been flow charted in Fig. 8. Principal modules are RELAX1 and RELAXV1 which are used to solve the discretized form of Eqs. $(2-47)$ by nonlinear iteration and SLOR. Some highlights of our approach will now be outlined.

Applying the SLOR approach to Eqs. $(2-47)$, the discretized form is

$$2\left\{ (1-\mu_{ij})(COEF_0)_{ij} \left(\frac{\hat{\phi}_{i+1} - \omega^{-1}\phi_i^+ - (1-\omega^{-1})\hat{\phi}_i}{x_{i+1} - x_i} - \frac{\omega^{-1}\hat{\phi}_i + (1-\omega^{-1})\hat{\phi}_i - \hat{\phi}_{i-1}^+}{x_i - x_{i-1}} \right) \right.$$

$$\left. + \mu_{i-1,j} \left(\frac{\hat{\phi}_i^+ - \hat{\phi}_i - \hat{\phi}_{i-1}^+}{x_i - x_{i-1}} - \frac{\hat{\phi}_{i-1} - \hat{\phi}_{i-2} - \hat{\phi}_i^+}{x_{i-1} - x_{i-2}} \right) \right\} / (x_{i+1} - x_{i-1})$$

$$- (\gamma+1)(\phi_{0_{xx}})_{ij} \left\{ \frac{\hat{\phi}_i^+ - \hat{\phi}_{i-1}^+}{x_i - x_{i-1}} \right\}$$

$$+ \left(\frac{1}{(\tilde{r})_j (\tilde{r}_{j+1} - \tilde{r}_{j-1})} \right) \left\{ \left(\frac{\tilde{r}_{j+1} + \tilde{r}_j}{\tilde{r}_{j+1} - \tilde{r}_j} \right) \left(\hat{\phi}_{j+1}^+ - \hat{\phi}_j^+ \right) \right.$$

$$\left. - \left(\frac{\tilde{r}_j - \tilde{r}_{j-1}}{\tilde{r}_{j+1} - \tilde{r}_{j-1}} \right) \left(\hat{\phi}_j^+ - \hat{\phi}_{j-1}^+ \right) \right\} = RHS_{ij}$$

$$(2-57a)$$

$$(RHS)_{ij} = \left\{ \frac{2(\gamma+1)\phi_{0_x} b_0'}{K_0} + \phi_{0_{xx}} \left((\gamma+1)\left(\frac{2b_0' x}{K_0} + \frac{8\pi b_0 B_0}{\sqrt{K_0}} \right) - K_1 \right) \right\}_{ij} , \quad (2-57b)$$

$$(COEF_0)_{ij} = (K_0 - (\gamma+1)\phi_{0_x})_{ij} \qquad (2-57c)$$

and

$$\mu_{ij} = \begin{cases} 0, & \text{for } COEF_{0_{ij}} > 0 \text{ (subsonic flow)} \\ 1, & \text{for } COEF_{0_{ij}} \le 0 \text{ (supersonic flow)} \end{cases} . \qquad (2-57d)$$

Here, $(RHS)_{ij}$ is the discretization of the forcing terms in $(2-47a)$, ω is a relaxation parameter chosen such that $1 \le \omega \le 2$, the plus superscripts signify current values, the quantities without plus subscripts denote values from the previous sweep through the flow field, quantities with i subscript only, have j suppressed, and j subscripted entities have i suppressed. The structure of $(2-57)$ is similar to that for the free field dominant and finite height (fully nonlinear) problems with the following exceptions:

1) For the nonlinear problems, a factor analogous to $COEF_0$, $COEF$ appears, involving the actual dependent variables rather than a known quantity, giving a nonlinear difference equation rather than the linear form $(2-11)$.

2) Eq. $(2-57a)$ contains a first order linear contribution and a right hand side $(RHS)_{ij}$ absent in the nonlinear free field and finite H problem.

3) Artificial damping has been used for the nonlinear problem but may not be required for the linear one.

4) $(COEF)_0$ by its nature is frozen in pseudo-time, whereas $COEF$ is constantly being updated using time linearization with ϕ_x given by its value at the previous sweep (time level).

5) Additional boundaries associated with the zeroth order shocks are required in the $\hat{\phi}$ problem across which the perturbation shock conditions need to be satisfied.

Note, for bodies with pointed tails, Eq. $(2-57b)$ specializes to

$$(\text{RHS})_{ij} = 8\pi b_0 B_0(\gamma + 1)(\phi_{0_{xx}})_{ij} \quad . \tag{2-57b'}$$

The tridiagonal system for $\hat{\phi}_j$ is then

$$B_j \hat{\phi}_{j-1} + D_j \hat{\phi}_j + A_j \hat{\phi}_{j+1} = C_j \quad , \quad j = 2, 3, \cdots, \text{JMAX} - 1 \tag{2-58a}$$

$$D_j = -2 \left\{ (1 - \mu_{ij}) \left(\frac{\text{COEF}_0}{\omega} \right)_{ij} \left(\frac{1}{x_{i+1} - x_i} + \frac{1}{x_i - x_{i-1}} \right) \right.$$
$$\left. - \mu_{i-1,j} (\text{COEF}_0)_{i-1,j} \left(\frac{1}{x_i - x_{i-1}} + \frac{1}{x_{i-1} - x_{i-2}} \right) \right\} / (x_{i+1} - x_{i-1}) \tag{2-58b}$$

$$- \frac{(\gamma + 1)(\phi_{0_{xx}})_{ij}}{x_i - x_{i-1}} - \frac{1}{\tilde{r}_j (\tilde{r}_{j+1} - \tilde{r}_{j-1})} \left\{ \frac{\tilde{r}_{j+1} + \tilde{r}_j}{\tilde{r}_{j+1} + \tilde{r}_j} + \frac{\tilde{r}_j + \tilde{r}_{j-1}}{\tilde{r}_j - \tilde{r}_{j-1}} \right\} \quad .$$

$$B_j = \frac{1}{\tilde{r}_j (\tilde{r}_{j+1} - \tilde{r}_{j-1})} \left(\frac{\tilde{r}_j + \tilde{r}_{j-1}}{\tilde{r}_j - \tilde{r}_{j-1}} \right) \tag{2-58c}$$

$$A_j = \frac{1}{\tilde{r}_j (\tilde{r}_{j+1} - \tilde{r}_{j-1})} \left(\frac{\tilde{r}_{j+1} + \tilde{r}_j}{\tilde{r}_j - \tilde{r}_{j-1}} \right) \tag{2-58d}$$

$$C_j = -2 \left\{ (1 - \mu_{ij})(\text{COEF}_0)_{ij} \left(\frac{\hat{\phi}_{i+1} - (1 - \omega^{-1})\hat{\phi}_i}{x_{i+1} - x_i} - \frac{(1 - \omega^{-1})\phi_i - \hat{\phi}_{i-1}^+}{x_i - x_{i-1}} \right) \right.$$
$$\left. - \mu_{i-1,j} \left(\frac{\hat{\phi}_i + \hat{\phi}_{i-1}^+}{x_i - x_{i-1}} + \frac{\hat{\phi}_{i-1}^+ - \hat{\phi}_{i-2}}{x_{i-1} - x_{i-2}} \right) \right\} - (\gamma + 1)(\phi_{0_{xx}})_{ij} \left\{ \frac{\hat{\phi}_{i-1}^+}{x_i - x_{i-1}} \right\} + (\text{RHS})_{ij}$$
$$\tag{2-58e}$$

At the body, $j = 2$, and the previously indicated boundary condition, $\phi_{1_r} = 0$ implies

$$D_2 = D_2^{j > 2} + \frac{1}{r_2 r_3} \tag{2-59a}$$

$$B_2 = 0 \quad . \tag{2-59b}$$

Also, A_2 and C_2 take their specialized values at $\tilde{r} = \tilde{r}_2$ (with $\tilde{r}_1 = 0$).

In $(2-58)$ and $(2-59)$, the μ_{ij} are designed to provide the necessary type sensitive switching and implementation of Murman's shock point operator defined in Ref. 35. This behavior is essential not only for the zeroth order solution but the variational one as well.

Subsequent sections will describe the scheme of shock fitting that interacts with the difference equations $(2-58)$ and $(2-59)$.

2.9 Finite Height Application of Zeroth Order Code

As indication of an application of the zeroth order part of STINT25 calculated by RELAX1, an equivalent body of revolution representative of a transonic/supersonic

blended wing fighter configuration was computed in a solid wall wind tunnel. The cross sectional area progression of the model is indicated in Fig. 10 which shows curvature changes associated with such geometrical features as wing–body intersections, canopies, and inlets. One purpose of this study was to explore aspects of the application of the code to realistic airplane geometries.

Fig. 10. Area distribution of blended wing fighter configuration.

As an indication of the flow environment for subsequent wall interference studies, Fig. 11 shows the pattern of isoMachs over the configuration associated with Fig. 10 in a free field at $M_\infty = .95$. These results could be practically obtained using the nonlinear analogue of the difference method associated with Eqs. (2–57)–(2–59) on a VAX computer in a CPU limited Fast Batch or interactive environment. The grid utilized 194 points in the x direction with uniform spacing over the body and logarithmic stretching ahead and behind. In the $\bar{r}$ direction, a similar geometric progression spacing was used with

50 points. Nominal convergence* typically was achieved between 500 to 1500 sweeps, with more sweeps required at the higher transonic Mach numbers.

Fig. 11. IsoMachs over blended wing configuration in free field, $M_\infty = .95$.

The complexity of the flow structure evident in Fig. 11 is to be associated with the multiple inflection points of the area progression and the possibility for envelopes to form in the steeply inclined wave system. In Fig. 11, a shock is formed near about $\frac{2}{3}$ of the body length from such an envelope process.

Figures 12 and 13 illustrate the Mach number and surface pressure distributions at the same freestream Mach number for the free field environment and a solid wall confined case. To obtain a nominal simulation of the free field, the upper computational boundary $j =$ JMAX was placed at $H \simeq 1.3$ and homogeneous Dirichlet conditions were imposed there. Homogeneous Neumann inflow and outflow conditions at $x = \pm\infty$ were also prescribed. For the solid wall simulation, $H \simeq 0.66$ was utilized. Homogeneous Neumann conditions were used at $j =$ JMAX and Eq. (2 − 9) applied at $x = \pm\infty$.

---

* Defined as $\max_{\substack{1 \leq i < IMAX \\ 1 \leq j \leq JMAX}} |\phi_{ij}^+ - \phi_{ij}| = 10^{-5}$.

Fig. 12. Finite height solid wall interference effect at $M_\infty = .95$ on blended fighter configuration equivalent body — Mach number distribution over body.

Fig. 13. Finite height solid wall interference effect at $M_\infty = .95$ on blended fighter configuration equivalent body — surface pressures.

From the figures and in accord with simple one–dimensional gasdynamic reasoning, the constrictive effect of the solid walls is to exaggerate the effect of stream tube area changes associated with body area changes.

An experimental validation was performed of the 0th order solver RELAX1 based on one of the variable blockage ratio tests of a blunt nosed model (B-3) in the Langley 8 and 16 foot tunnels, reported in Ref. 36. The test section was slotted and slatted as well as octagonal in shape. For such a blunt body which locally violates small disturbance theory, the agreement with the data is surprisingly excellent as shown in Fig. 14. For this comparison, the special improved accuracy boundary discretization procedure described in the next section was used. The quality of the comparison is believed to be partially attributable to this improvement.

2.10 Improved Accuracy Procedures for Numerical Treatment of Body Boundary Conditions

In the finite wall height application of the code, the interference pressures are computed as the difference between the confined and free field pressures. The numerical truncation error is a larger percentage of this difference than of either of the former quantities. This fact puts a greater demand on numerical accuracy than has been stressed in state of the art codes. Accordingly, all error sources were evaluated. Some items considered within an incompressible and subsonic framework were:

1. Accurate treatment of boundary conditions on axis of equivalent body.

2. Proper application of upstream and downstream far fields.

3. Need for double precision on shorter word length computers such as the VAX to handle high frequency errors propagating on fine grids for large iteration counts.

4. Treatment of nose and tail singularities.

The techniques apply directly to the transonic case. Moreover, study of subsonic flows is particularly useful because of the availability of closed form analytical solutions to check the numerics.

The second of Figs. 8 shows the subroutine RELAX1, which solves the tridiagonal system representing a discretized approximation of the transonic small disturbance partial differential equation of motion (TSDE) $(2 - 5a)$. It contains a special procedure which deals with the boundary conditions. These are satisfied by incorporating the condition of flow tangency at the body into the discretization of the vertical perturbation velocity flux gradient. In the nonlinear difference equation for the free field flow $(2 - 57a)$, this corresponds to an approximation fulfilling the role of the terms in the braces on the left hand side near the equivalent body of revolution (EBR) line of symmetry, (x axis). One scheme employed is associated with Eqs. $(2 - 59a)$ and $(2 - 59b)$.

Figure 15 is a schematic representation of the nodes relevant to the boundary points. In the finite height case, this treatment is made more difficult because the perturbation potential is logarithmically singular as the scaled radial coordinate tends to zero. Existing

Fig. 14. Validation of RELAX1 code against Couch experiment, B–3 body, $M = .99$.

free field codes familiar to us do not properly deal with this singularity. Whereas this limitation may be of moderate consequence to the prediction of free and confined pressures, in accord with the previous remarks, it is absolutely crucial to the treatment of interference pressures and testing of the variational equation solver. Accordingly, attention was given to the development of a scheme that accounts for the singularity in the boundary treatment.

Fig. 15. Nodes in vicinity of axis.

Referring to Fig. 15, the discretization of the third term,

$$T \equiv \frac{1}{\tilde{r}}(\tilde{r}\phi_{0_r})_{\tilde{r}} \,,$$

(2 − 60)

in the TSDE will now be discussed. This is the vertical flux gradient previously indicated. Shown in the figure are the first 3 (j) vertical node points as well as $\frac{1}{2}$ node points. If $\tilde{r}_j, j = 1, 2, \cdots, JMAX$ represent the j mesh points,

$$r_{j+1/2} = (r_{j+1} + r_j)/2 \,,$$

(2 − 61)

we consider (dropping the subscript zero on ϕ and the tildes on r), the discretized version of $T \equiv T_j$, given by

$$T_j = \left\{ \frac{1}{r}(r\phi_r)_r \right\}_j \,.$$

(2 − 62)

Using the half node points in the vicinity of the x axis

$$T_2 = \frac{1}{r_2} \frac{(r\phi_r)_{5/2} - (r\phi_r)_{3/2}}{r_{5/2} - r_{3/2}} \,.$$

(2 − 63)

42

The essential new idea is that a "regularized" version $\hat{\phi}$ of the perturbation velocity potential ϕ is introduced, where

$$\hat{\phi} = \phi - \frac{S'(x)}{2\pi} \ln r$$

(2 − 64)

$S'(x) =$ streamwise (x) derivative of the EBR area progression.

The logarithmic singularity is represented by the second term in $(2 - 64)$. Numerical differentiation of ϕ in the r direction is then accomplished by differentiating ϕ as the sum of a numerical approximation of its regular part and an analytical evaluation of the logarithmically singular component. The truncation error which would have normally become large due to the infinity on the axis will be substantially reduced using the differentiation of the linear polynomial representing the bounded quantity $\hat{\phi}$.

In accord with these ideas, the terms in $(2 - 63)$ can be evaluated as follows:

$$(r\phi_r)_{5/2} = \frac{(r_3 + r_2)}{2} \left\{ \frac{\hat{\phi}_3 - \hat{\phi}_2}{r_3 - r_2} + \frac{S'(x)}{2\pi(r_3 + r_2)/2} \right\} = \frac{(r_3 + r_2)}{2} \left(\frac{\hat{\phi}_3 - \hat{\phi}_2}{r_3 - r_2} \right) + \frac{S'(x)}{2\pi}$$

$$= \frac{(r_3 + r_2)}{2} \left\{ \frac{\phi_3 - \phi_2 - \frac{S'(x)}{2\pi} \ln r_3/r_2}{r_3 - r_2} \right\} + \frac{S'(x)}{2\pi}$$

(2 − 65a)

$$(r\phi_r)_{3/2} = r_{3/2} \left\{ \hat{\phi}_r \Big|_{3/2} + \frac{S'(x)}{2\pi r_{3/2}} \right\} = r_{3/2} \hat{\phi}_r \Big|_{3/2} + \frac{S'(x)}{2\pi}$$

$$= \frac{(r_2 + r_1)}{2} \left\{ \frac{\phi_2 - \frac{S'(x)}{2\pi} \ln r_2 - g(x)}{r_2 - r_1} \right\} + \frac{S'(x)}{2\pi}$$

(2 − 65b)

where the fact that

$$\phi \simeq \frac{S'(x)}{2\pi} \ln r + g(x) + \cdots$$

(2 − 66)

has been used in $(2 - 65b)$. Noting that $r_1 = 0$, and collecting results,

$$T_2 = \frac{(r_3 + r_2)}{r_2} \left[\frac{\hat{\phi}_3 - \hat{\phi}_2 - \frac{S'(x)}{2\pi} \ln r_3/r_2}{r_3 - r_2} \right]$$

$$- \frac{1}{r_3} \left[\hat{\phi}_2 - \frac{S'(x)}{2\pi} \ln r_2 - g(x) \right]$$

(2 − 67)

Accordingly, the tridiagonal system discretizing TSDE

$$B_j \hat{\phi}_{j-1} + D_j \hat{\phi}_j + A_j \hat{\phi}_{j+1} = C_j \quad , \quad j = 1, 2, \cdots, JMAX$$

at $j = 2$, has in accord with $(2 - 67)$,

$$B_2 = 0 \tag{2 − 68a}$$

$$A_2 = A_j^{j>2} \big|_{j=2} \tag{2 − 68b}$$

$$D_2 = D_j^{j>2} \big|_{j=2} \tag{2 − 68c}$$

$$C_2 = C_j^{j>2} \big|_{j=2} + \frac{1}{2\pi r_2 r_3} \left\{ \frac{S'(x)}{2\pi} \left[\frac{r_3 + r_2}{r_3 - r_2} \ln \frac{r_3}{r_2} - \ln r_2 \right] - g(x) \right\}. \tag{2 − 68d}$$

In the computational implementation, $g(x)$ is initialized as zero and then updated each iteration using $(2-66)$. For $(2-68d)$, $g(x)$ is "time linearized" from the previous iteration without relaxation. As an additional refinement, it is useful to note that the three dots in $(2-66)$

$$= \frac{S'''(x)}{2\pi} \left(\frac{r^2 \ln r}{4} - \frac{r^2}{4} \right)$$

in incompressible and subsonic Prandtl Glauert flow, and is an $O(S'''(x)r^2 \ln^2 r)$ expression at transonic Mach numbers. The updated g is computed using linear extrapolation as

$$g(x) = \dot{\phi}_3 - \frac{r_3}{r_3 r_2} \left(\dot{\phi}_3 - \dot{\phi}_2 \right). \tag{2-69}$$

Numerical experiments show that this produces results equally acceptable to those from an asymptotic approximation based on previously mentioned higher order terms proportional to $S'''(x)$ when $S'''(x)$ is known analytically. For tabular $S(x)$ input, the linear form $(2-69)$ is preferred due to significant errors possible in obtaining $S'''(x)$.

This scheme was applied to treat incompressible flow over a parabolic arc of revolution body, in the free field and confined by solid walls. The normalized radius F which is given by

$$F(x) = 2x(1-x) \qquad (0 \leq x \leq 1) \tag{2-70a}$$

gives the cross sectional area,

$$S(x) = \pi F^2 = 4\pi x^2 (1 - 2x + x^2) \quad . \tag{2-70b}$$

Thus

$$S'(x) = 8\pi(x - 3x^2 + 2x^3) \quad . \tag{2-70c}$$

Now, in the free field,

$$g(x) = \frac{S'(x)}{4\pi} \ln \frac{1}{4x(1-x)} - \frac{1}{4\pi} \int_0^1 \frac{S'(\xi) - S'(x)}{|x - \xi|} d\xi \quad , \tag{2-71}$$

which for $(2-70a)$ specializes to

$$g(x) = 2x(1 - 3x + 2x^2) \ln \frac{1}{4x(1-x)} + \frac{44}{3}x^3 - 22x^2 + 8x - \frac{1}{3} \tag{2-72a}$$

$$g'(x) = 2\left(1 - 6x + 6x^2\right) \{3 - \ln 4x(1-x)\} + 6\left(1 - 6x + 6x^2\right) \quad . \tag{2-72b}$$

The corresponding confined solution is given in Ref. 37.

2.10.1 Results

Figure 16 gives a comparison of VAX 11/780 application of the finite height code run in the free field to the exact solution represented by $(2-70a)$. The vertical $(\bar{r})$ grid was developed with logarithmic clustering. The clustering parameter SA provides a uniform

2.1.2 Problem Q:

$$\left(K - (\gamma + 1)\phi_x\right)\phi_{xx} + \frac{1}{\tilde{r}}(\tilde{r}\phi_{\tilde{r}})_{\tilde{r}} + \frac{1}{\tilde{r}^2}\phi_{\theta\theta} = 0 \qquad (2-5a)$$

$$\lim_{\tilde{r} \to 0} \tilde{r}\phi_{\tilde{r}} = \frac{S'(x)}{2\pi} \quad , \quad 0 < x < 1 \qquad (2-5b)$$

$$\phi_{\tilde{r}}(x,0) = 0 \quad , \quad x > 1 \qquad (2-5c)$$

$$\phi_x(x,H,\theta) = f_x(x,\theta;H) = -C_p/2\delta^2 \qquad (2-5d)$$

$$\phi(x,H,\theta) = f(x,\theta;H) \qquad (2-5d')$$

Here, $S(x)$ = streamwise area progression of the test article, $\overline{S}(\overline{x})$ = dimensional cross sectional area, $\overline{x}$ = dimensional coordinate in freestream direction, and $S(x) = \overline{S}(\overline{x})/\delta^2 L^2$, where L is the body length. Problem Q above represents a generalization of those discussed in Ref. 29 because of the fully three-dimensional nature of the equation of motion $(2-5a)$ and in accord with the previous remarks, the more general nature of the external conditions. The latter are given by either $(2-5d)$ or $(2-5d')$.

2.1.3 Large H Theory

The secondary expansions associated with $H \to \infty$ will now be considered. It is anticipated that the structure of the various layers, i.e., Axis, Central, and Wall layers shown in Fig. 2, will resemble those for solid walls. Accordingly, these representations are:

2.1.4 Central Layer

$$\phi = \phi_0(x,\tilde{r}) + \mu_{1/2}(H)\phi_{1/2}(x,\tilde{r},\theta) + \mu_1(H)\phi_1(x,\tilde{r},\theta) + \cdots \qquad (2-6a)$$

$$K = K_0^* + \nu_1(H)K_1^* + \cdots \qquad (2-6b)$$

$$A = A_0 + \kappa_1(H)A_1 + \cdots \qquad (2-6c)$$

which hold in the central limit

$$x,\tilde{r} \text{ fixed as } H \to \infty \quad .$$

These lead to the following generalized hierarchy of approximate equations:

2.1.5 Free Field Approximation

$$\left(K_0^* - (\gamma + 1)\phi_{0_x}\right)\phi_{0_{xx}} + \frac{1}{\tilde{r}}(\tilde{r}\phi_{0_{\tilde{r}}})_{\tilde{r}} = 0 \qquad (2-7a)$$

2.1.6 Variational Equations

$$\left(K_0^* - (\gamma + 1)\phi_{0_x}\right)\phi_{1/2_{xx}} - (\gamma + 1)\phi_{0_x}\phi_{1/2_{xx}} + \frac{1}{\tilde{r}}(\tilde{r}\phi_{1/2_{\tilde{r}}})_{\tilde{r}} + \frac{1}{\tilde{r}^2}\phi_{1/2_{\theta\theta}} = 0 \qquad (2-7b)$$

Fig. 2. Control surface in tunnel.

$$(K_0^* - (\gamma + 1)\phi_{0_x})\phi_{1_{xx}} - (\gamma + 1)\phi_{1_x}\phi_{0_{xx}} + \frac{1}{\tilde{r}}(\tilde{r}\phi_{1_{\tilde{r}}})_{\tilde{r}} + \frac{1}{\tilde{r}^2}\phi_{1_{\theta\theta}} = -K_1^*\phi_{0_{xx}} \qquad (2-7c)$$

where $\nu_1(H) = \mu_1(H)$ to keep the forcing term in $(2-7c)$, and to address the possibility of adjusting K_1^* as a Mach number correction to achieve interference–free flow. The significant complication of Eqs. $(2-7b)$ and $(2-7c)$ over their solid wall counterparts is the presence of the terms involving θ derivatives. On the other hand, a substantial simplification from the Problem Q is the allowability of factorization and superposition due to the linearity of these equations. As will be seen, the angular dependence of the far fields for these problems involve simple factors such as $\cos\theta$, $\cos 2\theta$, etc. It is envisioned that this dependence can be factored out, e.g., by allowing $\phi_1 = \tilde{\phi}_1(x,\tilde{r})\cos\theta$, which gives a two–dimensional equation for $\tilde{\phi}_1$. Also to be confirmed by matching is the assertion that the far field for ϕ_0 has a similar structure to that given in Ref. 29.

2.1.7 Wall Layer

The appropriate representation is assumed to be

$$\phi = \epsilon_0(H)\varphi_0(x^\dagger, r^\dagger, \theta) + \epsilon_{1/2}(H)\varphi_{1/2} + \epsilon_1\varphi_1 + \cdots \quad , \qquad (2-8a)$$

for the wall layer limit,

$$x^\dagger = x/H \quad , \quad r^\dagger = \tilde{r}/H \quad , \quad \text{fixed as } H \to \infty \quad . \qquad (2-8b)$$

Substitution of $(2-8a)$ into the KG formulation gives

$$O(\epsilon_0) : L[\varphi_0] = 0 \qquad (2-9a)$$

$$O(\epsilon_{1/2}) : L[\varphi_{1/2}] \qquad (2-9b)$$

$$O(\epsilon_1, \epsilon_0^2/H) : L[\varphi_1] = ((\gamma + 1)\varphi_{0_{x^\dagger}} - K_1^*)\varphi_{0_{x^\dagger x^\dagger}} \quad , \qquad (2-9c)$$

where

$$L \equiv K_0^* \frac{\partial}{\partial x^\dagger} + \Delta_T^\dagger \quad , \quad \Delta_T \equiv \frac{1}{r^\dagger}\frac{\partial}{\partial r^\dagger}\left(r^\dagger \frac{\partial}{\partial r^\dagger}\right) + \frac{1}{r^{\dagger 2}}\frac{\partial^2}{\partial\theta^2} \quad .$$

2.1.8 Behavior of φ_0 near Origin

As in the solid wall case, if $R^\dagger = \sqrt{\left(\frac{x}{K_0^*}\right)^2 + \tilde{r}^2/H}$, the source–like behavior,

$$\varphi_0 \simeq \frac{S(1)}{\sqrt{K_0^*}}\left\{-\frac{1}{4\pi R^\dagger} + \cdots\right\} \quad , \qquad (2-10)$$

is anticipated.

From $(2-5d')$, the similarity form,

$$f(x,\theta;H) = \frac{1}{H}f(x^\dagger,\theta) \qquad (2-11)$$

9

is appropriate, and leads to the boundary conditions

$$\varphi_0(x^\dagger, 1, \theta) = f(x^\dagger, \theta) = f(x^\dagger, \theta + 2\pi) \qquad (2-12a)$$

$$\varphi_{1/2,1}(x^\dagger, 1, \theta) = 0 \quad . \qquad (2-12b)$$

If

$$\Delta^\dagger = \frac{\partial}{\partial x^\dagger} + \frac{1}{r^\dagger}\frac{\partial}{\partial r^\dagger}\left(r^\dagger \frac{\partial}{\partial r^\dagger}\right) + \frac{1}{r^{\dagger 2}}\frac{\partial^2}{\partial \theta^2}$$

$$X^\dagger = x^\dagger/\sqrt{K_0^*} \quad .$$

Then $(2-10)$ implies

$$\Delta^\dagger \varphi_0 = \frac{S(1)}{\sqrt{K_0^*}}\delta(x^\dagger)\cdot\frac{\delta^+(r^\dagger)}{2\pi r^{\dagger 2}} \quad . \qquad (2-13)$$

With the following exponential Fourier transform pair

$$\overline{\varphi}_0 = \int_{-\infty}^{\infty} e^{-ikX^\dagger}\varphi_0 dX^\dagger$$

$$\varphi_0 = \frac{1}{2\pi}\int_{-\infty}^{\infty} e^{ikX^\dagger}\overline{\varphi}_0 dk \quad ,$$

the boundary value problem for $\overline{\varphi}_0$ corresponding to $(2-10)$, $(2-12a)$ and $(2-13)$ is

$$L\overline{\varphi}_0 = \left(\Delta_T^\dagger - k^2\right)\overline{\varphi}_0 = 0 \qquad (2-14a)$$

$$\lim_{r^\dagger \to 0} r^\dagger \frac{d\overline{\varphi}_0}{dr^\dagger} = \frac{1}{2\pi}\frac{S(1)}{\sqrt{K_0^*}} \qquad (2-14b)$$

$$\overline{\varphi}_0(1, \theta) = \overline{f}(\theta, k) = \overline{f}(\theta + 2\pi, k) \quad . \qquad (2-14c)$$

In contrast to the solid wall case, the decomposition of the solution into the fundamental solution M_0 and a part M_1 that is bounded at $X = \pm\infty$ as indicated in Eqs. (12) of Ref. 29 is not required since with the Dirichlet conditions, there can be mass flow through the interface to eliminate the solid wall source flow division at upstream and downstream infinity. The eigenfunction expansion solving $(2-14)$ is

$$\overline{\varphi}_0 = A_0 K_0(kr^\dagger) + B_0 I_0(kr^\dagger) + \sum_{n=1}^{\infty} I_n(kr^\dagger)\{B_n \cos n\theta + C_n \sin n\theta\} \quad , \qquad (2-15)$$

where K_0 and I_n are Bessel functions, the periodicity condition in $(2-14c)$ has been used to determine the eigenvalues $\lambda_n = n$, $n = 0, 1, 2, \cdots$, and $(2-14b)$ has been utilized to eliminate the K_n for $n > 0$.

10

Application of $(2-14c)$ and inversion gives finally,

$$\varphi_0 = \frac{1}{\pi^2}\int_0^\infty \cos kX^\dagger dk\left\{\frac{S(1)}{\sqrt{K_0^*}}\left[\frac{I_0(kr^\dagger)}{I_0(k)}K_0(k) - K_0(kr^\dagger)\right]\right.$$
$$\left.+\frac{I_0(kr^\dagger)}{I_0(k)}\int_0^{2\pi}\overline{f}(\theta, k)d\theta\right\} \qquad (2-16)$$
$$+\frac{2}{\pi^2}\sum_{n=1}^\infty\int_0^\infty\cos kX^\dagger\frac{I_n(kr^\dagger)}{I_n(k)}dk\int_0^{2\pi}\overline{f}(\theta', k)\cos n(\theta - \theta')d\theta' \quad .$$

The integrals in $(2-16)$ are convergent since the Bessel ratios decay exponentially as $k \to \infty$ and are analytic as $k \to 0$.

As indicated previously, for the analysis in this section, the θ variation will be suppressed. This may be realistic for many practical applications for nearly circular test sections and interfaces in the intermediate region of slender body theory discussed in Ref. 30. For convenience, the f distribution has been assumed symmetric in X, i.e., $f(X) = f(-X)$, to obtain $(2-16)$.* Therein, the exponential transforms have been expressed in terms of cosine integrals. The analysis can be readily generalized to handle unsymmetrical f distributions.

2.1.9 Asymptotic Representation of $(2-16)$ as $R^\dagger \to 0$

To obtain the required representation, the following integrals are considered:

$$\mathcal{I}_1 = \int_0^\infty\cos kX^\dagger\frac{I_0(kr^\dagger)}{I_0(k)}dk\int_0^{2\pi}\overline{f}(\theta, k)d\theta \qquad (2-17a)$$

$$\mathcal{I}_2 = \int_0^\infty\left\{\frac{I_0(kr^\dagger)K_0(k)}{I_0(k)} - K_0(kr^\dagger)\right\}\cos kX^\dagger dk \qquad (2-17b)$$

$$\mathcal{I}_3 = \sum_{n=1}^\infty\int_0^\infty\cos kX^\dagger\frac{I_n(kr^\dagger)}{I_n(k)}dk\int_0^{2\pi}\overline{f}(\theta', k)\cos n(\theta - \theta')d\theta' \quad . \qquad (2-17c)$$

Consistent with the assumption of axisymmetric interface pressures, $\mathcal{I}_3$ will not be considered here. By approximating $I_0(kr^\dagger)$ and $\cos kX^\dagger$ as $R^\dagger \to 0$, and term by term integration of the series obtained, the following approximation for φ_0 results:

$$\varphi_0 = -\frac{S(1)}{4\pi\sqrt{K_0^*}R^\dagger} + (\mathcal{A}_0 + \mathcal{B}_0) + (\mathcal{C}_0 + \mathcal{D}_0)R^{\dagger^2}P_2(\cos\omega)$$
$$+ O\left(R^{\dagger^3}\right) \qquad (2-18a)$$

---

* This restriction will be removed in Section 2.2.

where

$$A_0 = \frac{S(1)}{\sqrt{K_0^*}\pi^2} \int_0^\infty \frac{K_0(k)dk}{I_0(k)} \qquad (2-18b)$$

$$B_0 = \frac{1}{\pi} \int_0^\infty \frac{dk}{I_0(k)} \int_0^\infty f(X^\dagger)\cos kX^\dagger dX \qquad (2-18c)$$

$$C_0 = -\frac{1}{\pi} \int_0^\infty \frac{k^2 dk}{I_0(k)} \int_0^\infty f(X^\dagger)\cos kX^\dagger dX^\dagger \qquad (2-18d)$$

$$\mathcal{D}_0 = \frac{-S(1)}{2\pi^2\sqrt{K_0^*}} \int_0^\infty \frac{k^2 K_0(k)}{I_0(k)} dk \quad . \qquad (2-18e)$$

Here, ω is the scaled analogue of the polar angle defined in Fig. 2 i.e., $\omega = \cos^{-1} X^\dagger/R^\dagger$ and $P_2(\cos\omega)$ is a Legendre polynomial.

The constants given in $(2-18b)$–$(2-18e)$ are all given by convergent integrals. In particular, B_0 converges if $\overline{f}(k)$ is bounded as $|k| \to \infty$, and even under milder conditions on $\overline{f}$. This results from the potent exponential decay of I_0. No problem is encountered as $k \to 0$ since the integrand is analytic at that point.

The terms involving B_0 and C_0 give the effect of the pressure boundary condition.

2.1.10 Matching

For purposes of matching, the following asymptotic approximations for the wall layer and central region are appropriate:

$$\frac{\Phi_{\text{central}}}{U} = x + \delta^2 \left\{ \frac{A_0}{R} + \frac{B_0\cos\omega}{R^2} + \frac{C_0}{R^3}(\cos 3\omega - \cos\omega) + \frac{A}{\sqrt{K_0^*}R^3}P_2(\cos\omega) \right\}$$
$$+ \mu_{1/2}(H)\phi_{1/2} + \mu_1\left(\alpha_0 R^2 P_2(\cos\omega) + \alpha_1 R\cos\omega + \alpha_2\right) + \cdots \qquad (2-19)$$
$$\text{as } R \to \infty$$

$$\frac{\Phi_{\text{wall}}}{U} = x + \delta^2 \left\{ \epsilon_0 \frac{S(1)}{\sqrt{K_0^*}}\left[-\frac{1}{4\pi R^\dagger} + (A_0 + B_0) + (C_0 + \mathcal{D}_0)R^{\dagger^2}P_2(\cos\omega) + \cdots \right] \right\}$$
$$+ \epsilon_{1/2}B_0\cos\omega\left[\frac{1}{R^{\dagger^2}} + (C_0 + \mathcal{D}_0)R^\dagger \right]$$
$$+ \epsilon_1 \left\{ C\left[-\frac{P_2(\cos\omega)}{R^{\dagger^2}} + C_0 + \mathcal{D}_0 \right] + \frac{C_0}{R^{\dagger^3}}(\cos 3\omega - \cos\omega) \right\}$$
$$+ \cdots \quad , \qquad \text{as } R^\dagger \to 0$$
$$(2-20)$$

where A_0, B_0, C_0, and A are constants that have been previously defined in Ref. 29 with a corrected value for C_0 being $\frac{(\gamma+1)S^2(1)}{108\pi^2 K_0^{5/2}}$.

Preliminary matching considerations govern the selection of the various elements comprising $(2-19)$ and $(2-20)$. The ϕ_1 coefficient of μ_1 represents a harmonic solution of $(2-7c)$. The response to the nonlinear forcing terms $(\gamma+1)\phi_{0_x}\phi_{1_{xx}}$ and $(\gamma+1)\phi_{1_x}\phi_{0_{xx}}$ are decaying terms as $R \to \infty$ that are higher order to the order of the matching and can be neglected. Regarding $(2-20)$, $\varphi_{1/2}$ and φ_1, the coefficients of $\epsilon_{1/2}$ and ϵ_1, respectively, consist partially of $X^\dagger$ derivatives of φ_0, such that the multipole expansion has primary singularities which are source, doublet, and quadrupole forms with their appropriate reflections. Thus, the reflection of the doublet is an X derivative of the sources, and the quadrupole has the same relationship to the doublet.

For matching Eqs. $(2-19)$ and $(2-20)$ are written in the intermediate variable

$$R_\eta = \frac{R}{\eta} \qquad (2-21)$$

which is held fixed as $H \to \infty$. The gauge function η is an order class intermediate between 1 and H as $H \to \infty$. This is expressed symbolically as

$$1 << \eta(H) << H \quad . \qquad (2-22)$$

Thus, $\frac{1}{\eta(H)} \to 0$ as $H \to \infty$, and $\frac{\eta}{H} \to 0$ as $H \to \infty$. For axial symmetry of the interface pressures, the matching process is almost identical to that discussed in Ref. 29. The only difference will be the redefinition of certain constants associated with the streamwise integrals of the specified pressure data as well as the switchback terms. For understanding of basic issues related to the extension to non-axisymmetric interface pressures, the matching is diagrammed in Fig. 3.

Referring to the figure, the various labeled terms denoted by the circles give the following matchings:

$\textcircled{1} \leftrightarrow \textcircled{1'} \Rightarrow A_0 = -\frac{S(1)}{4\pi\sqrt{K_0^*}}$, $\epsilon_0 = \frac{1}{H}$

$\textcircled{2} \leftrightarrow \textcircled{4.1'} \Rightarrow \epsilon_{1/2} = \frac{1}{H^3}$

$\textcircled{3} \leftrightarrow \textcircled{5.3'}$ matched

$\textcircled{4} \leftrightarrow \textcircled{5.1'} \Rightarrow \epsilon_1 = \frac{1}{H^3}$, $C = -\frac{A}{\sqrt{K_0^*}}$

$\textcircled{5} \leftrightarrow \textcircled{2'} \Rightarrow \mu_{1/2} = \frac{1}{H}$, $\phi_{1/2} = A_0 + B_0$

$\textcircled{6.1} \leftrightarrow \textcircled{3'} \Rightarrow \mu_1 = \frac{1}{H^3}$, $\alpha_0 = C_0 + D_0$

$\textcircled{6.2} \leftrightarrow \textcircled{4.2'} \Rightarrow \alpha_1 = B_0\alpha_0$

$\textcircled{6.3} \leftrightarrow \textcircled{5.2'} \Rightarrow \alpha_2 = \alpha_0 C \quad .$

As will be seen in the next section, the non-axially symmetric case requires additional terms in the wall, central, and axis layers to deal with the effect of the higher harmonics.

Fig. 3. Matching of central and wall regions for axially symmetric interface pressures.

The matching of the central layer and the axis layer proceeds along similar lines to that given in Ref. 29. All that is required is the essential result for the boundary condition, which is

$$\phi_{1_{\bar{r}}}(x,0) = 0 \quad . \tag{2-23}$$

The expression for the interference pressure remains the same as that given in Ref. 29. However, there is an implicit dependence on the interface pressure data through the far field influence of the terms involving the constants B_0 and C_0 defined in $(2-18c)$ and $(2-18d)$. Also, the flux of streamwise momentum of the interference field through the interface must be considered in the calculation of the interference drag. The implicit dependence on the interface pressure data is shown in the following altered problem P1 denoted P2 for the interference potential in the central region ϕ_1.

P2:

$$[K_0^* - (\gamma+1)\phi_{0_x}]\,\phi_{1_{xx}} - (\gamma+1)\phi_{0_x}\phi_{1_x} + \frac{1}{\bar{r}}(\bar{r}\phi_{1_{\bar{r}}})_{\bar{r}} = -K_1^*\phi_{0_{xx}} \tag{2-24a}$$

$$\phi_{1_{\bar{r}}}(x,0) = 0 \tag{2-24b}$$

$$\phi_1 \simeq \alpha_0 R^2 P_2(\cos\omega) + \alpha_1 R\cos\omega + \alpha_2 \quad \text{as } R \to \infty \tag{2-24c}$$

where

$$\alpha_0 = C_0 + \mathcal{D}_0 \tag{2-24d}$$

$$\alpha_1 = B_0\alpha_0 \tag{2-24e}$$

$$\alpha_2 = -\frac{8\pi b_0 A}{\sqrt{K_0^*}} = \alpha_0 C \quad . \tag{2-24f}$$

For the free jet case, $C_0 = 0$ in $(2-24d)$ and $B_0 = 0$ in Fig. 3. Solid wall conditions are modeled by making $\alpha_0 = b'_0 = b_0 S(1)/\sqrt{K_0^*}$, with $\alpha_1 = 8\pi B_0 b_0$, with $b_0 = .063409^*$.

2.1.11 Discussion

Because of the relationship of P1 to P2, the computational algorithm which has been developed for the solid wall case can be used to solve P2 with corrections of the indicated constants and the post-processing subroutine DRAG1 to account for the flux of streamwise momentum through the interface. Note here that the effect of α_2 in $(2-24c)$ can be neglected.

---

* The determination of this value is discussed in Section 2.12.

2.2 Generalization to Angular and Unsymmetrical Variations

Summary

In this section, the pressure boundary condition asymptotic analysis given in Section 2.1 is extended to handle angular interface and unsymmetrical variations of measured pressure.

Central Layer

With the generalized angular variation at the interface, (2 - 6a) is anticipated to be modified as

$$\phi = \phi_0(x,\tilde{r}) + \mu_{1/2}(H)\phi_{1/2}(x,\tilde{r},\theta) + \mu_{3/4}(H)\phi_{3/4}(x,\tilde{r},\theta) + \mu_1(H)\phi_1(x,\tilde{r},\theta) + \cdots \quad (2-25)$$

As compared to $(2-6a)$, $(2-25)$ contains an extra term (indicated by 3/4 subscripts). This insertion is required by matching considerations associated with the more general class of interface pressure distributions involving angular and asymmetric streamwise variations.

The analysis and results are such that Eqs. $(2-3)$ to $(2-6)$ remain unchanged. Reflecting the more general interface distribution the expression for φ_0 becomes

$$\varphi_0 = \frac{S(1)}{4\pi^2 \sqrt{K_0^*}} \left(\tilde{Q}_1 - \tilde{Q}_2 \right) + \frac{Q_0}{4\pi^2} + \frac{1}{2\pi^2} \sum_{n=1}^{\infty} \left(Q_n \cos n\theta + P_n \sin n\theta \right) \quad (2-26a)$$

where

$$\tilde{Q}_1 = \int_{-\infty}^{\infty} \frac{I_0\left(kr^\dagger\right) K_0(k)}{I_0(k)} e^{ikX^\dagger} dk \quad (2-26b)$$

$$\tilde{Q}_2 = \int_{-\infty}^{\infty} K_0\left(kr^\dagger\right) e^{ikX^\dagger} dk \quad (2-26c)$$

$$Q_n = \int_{-\infty}^{\infty} e^{ikX^\dagger} \frac{I_n\left(kr^\dagger\right)}{I_n(k)} dk \int_0^{2\pi} \overline{f}(\theta,k) \cos n\theta \, d\theta \quad (2-26d)$$

$$P_n = \int_{-\infty}^{\infty} e^{ikX^\dagger} \frac{I_n\left(kr^\dagger\right)}{I_n(k)} dk \int_0^{2\pi} \overline{f}(\theta,k) \sin n\theta \, d\theta \quad . \quad (2-26e)$$

Upon expanding the integrands in $(2-26)$ for small R, and with considerable algebraic manipulation, the asymptotic expansions of the integrals can be obtained. The methodology exemplified in Ref. 29 involves expansion of the Bessel functions for small $r^\dagger$ and the $e^{ikX^\dagger}$ kernel for small $X^\dagger$ and gives a series that can be integrated term by term. These integrals are convergent for the ray limits $(R^\dagger \to 0, \theta$ fixed) of interest.

Collecting results, the desired expansion of φ_0 is

$$\varphi_0 = \frac{\mathcal{A}_{00}}{R^\dagger} + \mathcal{A}_0 + \mathcal{B}_0 + \mathcal{A}_{01} X^\dagger$$

$$+ \underbrace{\mathcal{E}_0 r^\dagger \cos\theta}_{y} + \underbrace{\mathcal{F}_0 r^\dagger \sin\theta}_{z} + X^\dagger \left(\underbrace{\mathcal{E}_{01} r^\dagger \cos\theta}_{X^\dagger y} + \underbrace{\mathcal{F}_{01} r^\dagger \sin\theta}_{X^\dagger z} \right) \cdot \qquad (2-27a)$$

$$\underbrace{\mathcal{G}_0 r^\dagger \cos 2\theta}_{y^2 - z^2} + \underbrace{\mathcal{H}_0 r^{\dagger^2} \sin 2\theta}_{yz}$$

$$(\mathcal{C}_0 + \mathcal{D}_0) R^{\dagger^2} P_2(\cos\omega) + \cdots$$

where the terms shown under those in $(2-27a)$ are listed to indicate their correspondence with spherical harmonics and the spherical coordinates are as shown in Fig. 4.

SC50443

Fig. 4. Spherical coordinates.

From the asymptotic expansions, the constants in $(2-27a)$ are:

$$\mathcal{A}_{00} = -\frac{S(1)}{4\pi\sqrt{K_0^*}} \qquad (2-27b)$$

$$\mathcal{A}_0 = \frac{S(1)}{2\pi^2\sqrt{K_0^*}} \int_0^\infty \frac{K_0(k)}{I_0(k)} dk \quad , \quad \mathcal{B}_0 = \frac{1}{4\pi^2} \int_{-\infty}^\infty \frac{dk}{I_0(k)} \int_0^{2\pi} \overline{f_R}(\theta, k) d\theta \qquad (2-27c)$$

$$\mathcal{A}_{01} = \frac{1}{4\pi^2} \int_{-\infty}^\infty \frac{k\,dk}{I_0(k)} \int_0^{2\pi} \overline{f_I}(\theta, k) dk \qquad (2-27d)$$

$$\mathcal{E}_0 = \frac{1}{4\pi^2} Re\ i \int_{-\infty}^{\infty} \frac{k^2 dk}{I_1(k)} \int_0^{2\pi} \overline{f} \cos\theta d\theta \quad , \quad \overline{\mathcal{F}}_0 = \frac{1}{4\pi^2} Re \int_{-\infty}^{\infty} \frac{k dk}{I_1(k)} \int_0^{2\pi} \overline{f} \sin\theta d\theta$$

$$(2-27e)$$

$$\mathcal{E}_{01} = \frac{1}{4\pi^2} Re\ i \int_{-\infty}^{\infty} \frac{k^2 dk}{I_1(k)} \int_0^{2\pi} \overline{f} \cos\theta d\theta \quad , \quad \overline{\mathcal{F}}_{01} = \frac{1}{4\pi^2} Re\ i \int_{-\infty}^{\infty} \frac{k^2 dk}{I_1(k)} \int_0^{2\pi} \overline{f} \sin\theta d\theta$$

$$(2-27f)$$

$$\mathcal{C}_0 = -\frac{S(1)}{4\pi^2 \sqrt{K_0^*}} \int_0^{\infty} \frac{k^2 K_0(k)}{I_0(k)} dk \quad , \quad \mathcal{D}_0 = -\frac{1}{8\pi^2} \int_{-\infty}^{\infty} \frac{k^2 dk}{I_0(k)} \int_0^{2\pi} \overline{f_R} d\theta \qquad (2-27g)$$

$$\mathcal{G}_0 = \frac{1}{4\pi^2} Re \int_{-\infty}^{\infty} \frac{k^2 dk}{I_2(k)} \int_0^{2\pi} \overline{f} \cos 2\theta d\theta \quad , \quad \mathcal{H}_0 = -\frac{1}{4\pi^2} Re \int_{-\infty}^{\infty} \frac{k^2 dk}{I_2(k)} \int_0^{2\pi} \overline{f} \sin 2\theta d\theta$$

$$(2-27h)$$

Matching

Using the intermediate limit described in Section 2.1.10, matching of the central and wall regions is schematically indicated in Fig. 5 in which both representations are written in terms of the intermediate variable R_η defined in Section 2.1.10. It should be noted that nonlinear effects are associated with Poisson equation forcing terms such as $\phi_{1_x}\phi_{0_{xx}}$ in $(2-7c)$. The Poisson form is associated with $R \to \infty$ ray limit of the central region flow. In Fig. 4, $\Omega^{(1)}$ is a particular solution of the equation

$$\frac{1}{\sin\omega}\left(\frac{d}{d\omega}\sin\omega\frac{d\Omega^{(1)}}{d\omega}\right) + \frac{\Omega^{(1)}}{\sin^2\omega} = \cos\omega \qquad (2-28a)$$

and $\Omega^{(2)}$ is the solution of

$$\frac{1}{\sin\omega}\left(\frac{d}{d\omega}\sin\omega\frac{d\Omega^{(2)}}{d\omega}\right) + \frac{\Omega^{(2)}}{\sin^2\omega} = \frac{3P_3(\cos\omega) + 2P_1(\cos\omega)}{5} \quad . \qquad (2-28b)$$

As indicated in Section 2.1.10, the matching of the central and axis layers proceeds along similar lines to that discussed in Ref. 29.

All that is required is the essential result for the boundary condition, which is

$$\phi_{1_r}(x,0) = 0 \quad .$$

The expression for the interference pressure remains the same as that given in Ref. 29. However, there is an implicit dependence on the interface pressure data through the far field influence of the terms involving the constants defined in $(2-27c)$ to $(2-27h)$. Also, the flux of streamwise momentum of the interference field through the interface must be considered in the calculation of the interference drag. The implicit dependence on the interface pressure data is shown in the following altered problem P1 denoted P2 for the interference potential in the central region ϕ_1.

18

PRESSURES SPECIFIED ON INTERFACE

$$\frac{\Phi_{central}}{U} = x + \delta^2 \left\{ \left[\left(\frac{A_0}{\eta R_\eta} + \frac{B_0 \cos\omega}{\eta^2 R_\eta^2} + \frac{C_0}{\eta^3 R_\eta^3}(\cos 3\omega - \cos\omega) + \frac{A_0}{\sqrt{R_0^2}\,\eta^3 R^3} P_2(\cos\omega) \right] \right. \right.$$

$$+ \frac{1}{H}a_{1/2} + \frac{1}{H^2}\left[A_1 \eta R_\eta \cos\omega + \mathcal{E}_0 \eta R_\eta \sin\omega\cos\theta + \mathcal{F}_0 \eta R_\eta \sin\omega\sin\theta + a_{3/4} + \frac{P_2(\cos\omega)}{3\eta R_\eta} \right]$$

$$+ \frac{1}{H^3}\left[\overline{A_0}\eta^2 R_\eta^2 P_2(\cos\omega) + \overline{A_1}\eta R_\eta \cos\omega + \overline{A_2} + \eta^2 R_\eta^2 \cos\omega\sin\omega(\mathcal{E}_{01}\cos\theta + \mathcal{F}_{01}\sin\theta) \right.$$

$$+ \overline{A_5}\eta R_\eta \sin\omega\sin\theta + \eta^2 R_\eta^2 \sin^2\omega(\overline{A_3}\cos 2\theta + \overline{A_4}\sin 2\theta) + \overline{A_6}\eta R_\eta \sin\omega\cos\theta$$

$$\left. + \alpha\Omega^{[1]}(\omega) + \Omega^{[2]}(\omega)(\beta\cos\theta + \gamma\sin\theta) \right] = x + \delta^2 \phi_{central}$$

$$\frac{\Phi_{wall}}{U} = x + \delta^2 \left\{ \frac{1}{H}\left[\frac{S(1)}{4\pi\frac{\eta R_1}{H}} + \overline{A_0} + \overline{B_0} + A_0 \frac{\eta R_1}{H}\cos\omega + (C_0 + D_0)\frac{\eta^2 R_1^2}{H^2}P_2(\cos\omega) \right.\right.$$

$$+ \frac{\eta R_1}{H}\sin\omega(\mathcal{E}_0\cos\theta + \mathcal{F}_0\sin\theta) + \frac{\eta^2 R_1^2}{H^2}\sin^2\omega(\mathcal{G}_0\cos 2\theta + 2\mathcal{H}_0\sin 2\theta)$$

$$\left. + \frac{\eta^2 R_1^2}{H^2}\cos\omega\sin\omega(\mathcal{E}_{01}\cos\theta + \mathcal{F}_{01}\sin\theta) \right]$$

$$+ \frac{1}{H^2}B\left[\frac{\cos\omega}{\eta^2 R_1^2} + 2(C_0 + D_0)\frac{\eta R_1}{H}\cos\omega + \frac{\eta R_1}{H}\sin\omega(\mathcal{E}_{01}\cos\theta + \mathcal{F}_{01}\sin\theta) + A_{01} \right]$$

$$+ \frac{1}{H^3}\left[C\left(-\frac{1}{2\pi}\frac{P_2(\cos\omega)}{\frac{\eta^3 R_1^3}{H^3}} + 2C_1\right) + \frac{C_0}{\eta^3 R_1^3}(\cos 3\omega - \cos\omega) + \frac{CP_2(\cos\omega)}{\eta R_1} \right.$$

$$\left.\left. + \frac{a_{01}a_{00}P_2(\cos\omega)}{\frac{\eta R_1}{H}} - 2a_{00}(C_0 + D_0)\Omega^{[1]}(\omega) + \Omega^{[2]}(\mathcal{E}_{01}\cos\theta + 2\mathcal{F}_{01}\sin\theta) \right] \right\} = x + \delta^2\phi_{wall}$$

Fig. 5. General case of matching of central region and wall layers.

<u>P2:</u>

$$\left[K_0^* - (\gamma + 1)\phi_{0_x}\right]\phi_{1_{xx}} - (\gamma + 1)\phi_{0_x}\phi_{1_x} + \frac{1}{\tilde{r}}(\tilde{r}\phi_{1_{\tilde{r}}})_{\tilde{r}} = -K_1^*\phi_{0_{xx}} \qquad (2-29a)$$

$$\phi_{1_{\tilde{r}}}(x,0) = 0 \qquad (2-29b)$$

$$\phi_1 \simeq R^2 \left\{ \overline{\mathcal{A}_0} P_2(\cos\omega) + \cos\omega \sin\omega \left(\overbrace{\mathcal{E}_{01}\cos\theta + \overline{\mathcal{F}_{01}}\sin\theta}^{\textcircled{1}} \right) \right.$$

$$\left. + \sin^2\omega \left(\overbrace{\overline{\mathcal{A}_3}\cos 2\theta + \overline{\mathcal{A}_4}\sin 2\theta}^{\textcircled{2}} \right) \right\}$$

$$+ R \left\{ \overline{\mathcal{A}_1}\cos\omega + \sin\omega \left(\overbrace{\overline{\mathcal{A}_5}\sin\theta + \overline{\mathcal{A}_6}\cos\theta}^{\textcircled{3}} \right) \right\} \qquad (2-29c)$$

$$+ \mathcal{A}_2 + \cdots \quad \text{as } R \to \infty$$

where by Fig. 5, with B and C defined in Ref. 29

$$\overline{\mathcal{A}_0} = \mathcal{C}_0 + \mathcal{D}_0 \qquad (2-29d)$$

$$\overline{\mathcal{A}_1} = 2B\overline{\mathcal{A}_0} \qquad (2-29e)$$

$$\overline{\mathcal{A}_2} = 2CC_1 = 2B(\mathcal{C}_0 + \mathcal{D}_0) \qquad (2-29f)$$

$$\overline{\mathcal{A}_3} = \mathcal{G}_0 \qquad (2-29g)$$

$$\overline{\mathcal{A}_4} = \mathcal{H}_0 \qquad (2-29h)$$

$$\overline{\mathcal{A}_5} = \overline{\mathcal{F}_{01}} \qquad (2-29i)$$

$$\overline{\mathcal{A}_6} = \mathcal{E}_{01} \quad . \qquad (2-29j)$$

2.2.1 Discussion

The problem $(2-29a)$–$(2-29c)$ is the generalization of the Problem P2 given in Section 2.1.10 *accounting for asymmetries in the streamwise distribution of the interface pressures as well as angular θ variations.* These effects are given by the terms marked as ① – ③ in $(2-29c)$. They represent averages of the early harmonics *which to this order is all that the far field is sensitive to.* The specialization to the free jet case is obtained by setting $\mathcal{D}_0 = g_0 = \mathcal{H}_0 = \mathcal{E}_{01} = \overline{\mathcal{F}}_{01} = 0$ in Eqs. $(2-29)$.

2.3 Shock Jump Conditions

An important element to be considered in the numerical solution of the Problem P1 referred to in the previous sections is the satisfaction of the shock jump conditions. For

20

the free field case, these relations are satisfied by the divergence or conservation form of the Karman Guderley small disturbance equation. These give the Rankine Hugoniot jump conditions. They are satisfied using type sensitive shock capturing schemes such as those originally developed by Murman and Cole in Ref. 31. On the other hand, the wall interference corrections related to the Problem P1 have to be satisfied by use of explicit relations. These have been derived for the high aspect ratio transonic lifting line theory formulated in Ref. 32. These relations will be derived for axisymmetric flow in this section.

Referring to Fig. 6, conditions across the shock front denoted as S will be discussed. This surface is given by

$$S = x - g(\tilde{r}) = 0 \quad , \tag{2-30}$$

where $\tilde{r} = \delta r$, and consistent with the Problem P1 delineated in Ref. 29, axial symmetry is assumed. The Problem P1 describes the wall interference flow away from the walls on the axis of symmetry of a cylindrical test section. The velocity potential in this zone, denoted by Φ, is given by the asymptotic expansion

SC84-29502

Fig. 6. Orientation of shock surfaces.

$$\frac{\Phi}{U} = x + \delta^2 \left\{ \phi_0(x,\tilde{r}) + \frac{a_0'}{H} + \frac{1}{H^3}\phi_1(x,\tilde{r}) + \cdots \right\} \quad , \tag{2-31}$$

where U is the freestream speed, the ϕ_i are perturbation potentials, a_0' is a constant, H is the wall height in units of the body length, and δ is the confined body's thickness ratio. The secondary expansion in the braces in $(2-31)$ is an approximation for the perturbation potential ϕ which is governed by the Karman Guderley transonic small disturbance equation $(2-5a)$, with $\frac{\partial}{\partial \theta}$ assumed zero.

Equation $(2-5a)$ can be written in the divergence form,

$$L\{\phi\} \equiv \left\{ K\phi_x - \frac{\gamma+1}{2}\phi_x^2 \right\}_x + \frac{1}{\tilde{r}}(\tilde{r}\phi_{\tilde{r}})_{\tilde{r}} = 0 \quad , \tag{2-32}$$

21

where subscripts denote partial differentiation. Denoting the transverse velocity vector as $\vec{v} = v\vec{1}_{\bar{r}}$, $(v = \phi_{\bar{r}})$, the $\bar{r}$ derivative term in $(2-32)$ can be written as $\tilde{\nabla} \cdot \vec{v}$, where $\tilde{\nabla}\cdot$ is the cross flow divergence.

The integral form of $(2-32)$, applied to the infinitesimal thickness $(= \epsilon)$ volume V shown in Fig. 6 is

$$\int\int_V L\{\phi\} 2\pi\bar{r}\, d\bar{r}\, dx = 0 \quad ,$$

and the divergence theorem gives rise to the flux form

$$\int_S \left\{\left[Ku - \frac{\gamma+1}{2}u^2\right] + [\vec{v}]\cdot\frac{\vec{n}}{\delta}\right\} 2\pi\bar{r}\, d\bar{r} = 0 \quad , \tag{2-33}$$

where $[f] \equiv \lim_{\epsilon\to 0}\{f(x, g+\epsilon) - f(x, g-\epsilon)\}$, $u = \phi_x$, and $\vec{n}$ is a unit vector normal to S. Since $(2-33)$ holds for an arbitrary area, the integrand must be zero,

$$\left[Ku - \frac{\gamma+1}{2}u^2\right] + [\vec{v}]\cdot\frac{\vec{n}}{\delta} = 0 \quad . \tag{2-34}$$

Now

$$\vec{n} = \frac{\nabla S}{|\nabla S|} = \frac{\vec{i} - \delta g'(\bar{r})\vec{1}_{\bar{r}}}{\sqrt{1 + \mathcal{O}(\delta^2)}} \quad , \tag{2-35}$$

where $\vec{i}$ is the unit vector in the x direction and $\vec{1}_{\bar{r}}$ that in the $\bar{r}$ direction. Substituting into $(2-34)$, this gives

$$\left[Ku - \frac{\gamma+1}{2}u^2\right] - g'[v] = 0 \quad . \tag{2-34'}$$

By virtue of conservation of tangential momentum across the shock, the perturbation of the velocity vector $\vec{q}$ is normal to the shock surface. This perturbation velocity is given by

$$\frac{\vec{q} - U\vec{i}}{U} = \delta^2 u\vec{i} + \delta^3 v\vec{1}_{\bar{r}} \quad .$$

On the basis of tangential momentum conservation,

$$(\vec{q} - U\vec{i}) \times \nabla S = 0 \quad ,$$

which gives

$$[v] = -[u]g'(\bar{r}) \quad . \tag{2-35}$$

Eliminating g' from $(2-34')$ using $(2-35)$ gives

$$\left[Ku - \frac{(\gamma+1)}{2}u^2\right][u] + [v]^2 = 0 \quad . \tag{2-36}$$

Since tangential momentum is conserved, the tangential velocity component to the shock is continuous across it. Upon tangential integration, and disposing of an unessential constant, the following relation is obtained

$$[\phi] = 0 \quad . \tag{2-37}$$

Equations $(2-36)$ and $(2-37)$ lead upon substitution of the asymptotics into the jump relations for the approximate quantities appearing in $(2-31)$. To obtain a determinate set of quantities, the shock's representation is assumed to be in the same form as that for ϕ, i.e.,

$$g = g_0(\tilde{r}) + \frac{1}{H}g_{1/2}(\tilde{r}) + \frac{1}{H^3}g_1 + \cdots \quad . \tag{2-38}$$

Denoting f as a quantity of interest which has the same asymptotic form as ϕ, on the basis of $(2-38)$ and Taylor's expansion,

$$\begin{aligned}
f(x,g) =& f_0(x,g_0) + \frac{1}{H}\left(f_{1/2}(x,g_0) + g_{1/2}f_{0_x}(x,g_0)\right) \\
&+ \frac{g_{1/2}^2}{H^2}f_{0_{xx}}(x,g_0) + \frac{1}{H^3}\left(f_1(x,g_0) + g_1 f_{0_x}(x,g_0)\right) \\
&+ \cdots \quad .
\end{aligned} \tag{2-39}$$

By virtue of $(2-39)$, substitution of the expansion $(2-31)$ into $(2-36)$ gives the approximate shock relations which are:

$$O(1) \; : \; \left[\left(K - \frac{\gamma+1}{2}u_0\right)u_0\right] + [v_0]^2 = 0 \tag{2-40a}$$

$$\begin{aligned}
[u_1]\left[Ku_0 - \frac{\gamma+1}{2}u_0^2\right] &+ [u_0]\left[(K - (\gamma+1)u_0)u_1\right] \\
&+ 2[v_0][v_1] = -g_1\bigg\{[u_0]\left[(k - (\gamma+1)u_0)u_{0_x}\right] \\
&+ \left[Ku_0 - \frac{\gamma+1}{2}u_0^2\right][u_{0_x}] \\
&+ 2[v_0][v_{0_x}]\bigg\}
\end{aligned} \tag{2-40b}$$

where $u_i \equiv \phi_{i_x}$ and $v_i \equiv \phi_{i_r}$ where i is equal to $0,1$. The quantity $g_{1/2}$ can be shown to vanish on the basis of $(2-37)$ which with $(2-39)$ leads to the additional set of relations:

$$O(1) \; : \; [\phi_0] = 0 \tag{2-41a}$$

$$O(H^{-3}) \; : \; [\phi_1] = -g_1[\phi_{0_x}] \quad . \tag{2-41b}$$

It should be noted that the $O(H^{-1})$, $O(H^{-2})$ equations obtained in the process leading to Eqs. $(2-40)$ are vacuous.

Equations $(2-40)$ and a vorticity relationship to be derived in the next section complete the formulation necessary for the computational solution.

2.4   Shock Conservation Laws for Wall Correction Flow

In addition to the jump relations derived in Section 2.3, a useful conservation law can be derived for use in the numerical solutions. In analogy to the free field large aspect ratio case discussed in Ref. 32, this law will be obtained using the divergence theorem. Considering the region shown in Fig. 7, the divergence form of $(2-7c)$ (with $\frac{\partial}{\partial\theta} = 0$ and dropping the stars on the K's) is

$$\left\{ K_1\phi_{0_x} + K_0\phi_{1_x} - (\gamma+1)\phi_{0_x}\phi_{1_x} \right\}_x + \frac{1}{\tilde{r}}(\tilde{r}\phi_{1_{\tilde{r}}})_{\tilde{r}} = 0 \quad ,$$

or

$$\hat{\nabla} \cdot \left(K_1\phi_{0_x} + K_0\phi_{1_x} - (\gamma+1)\phi_{0_x}\phi_{1_x}, K_0\phi_{1_{\tilde{r}}} \right) = 0 \quad , \qquad (2-42)$$

where $\hat{\nabla}\cdot$ refers to the divergence operator in the $x, \hat{r}$ coordinate system in which $\hat{r} = \sqrt{K_0}\tilde{r}$. From $(2-42)$,

$$\int\int_S (K_1\phi_{0_x} - w\phi_{1_x}, K_0\phi_{1_{\tilde{r}}}) \cdot \vec{n}\, dS \quad ,$$

where $w \equiv (\gamma+1)\phi_{0_x} - K_0$, S represents the surface of revolution consisting of the sphere S_R, $R = R_0$, the cut S_B around $\hat{r} = 0$, S_0 around the shock or shocks, and $\vec{n}$ is the unit normal to the shock surface.

Now, since $\phi_{1_{\tilde{r}}}(x, 0) = 0$,

$$\int\int_{S_B} = \int\int \phi_{1_{\tilde{r}}} \cdot \vec{1}_{\tilde{r}}\, dx = 0 \quad ,$$

where $\vec{1}_{\tilde{r}}$ is the unit vector in the $\hat{r}$ direction. Also, $\int\int_{S_R}$ can be shown to vanish to the order of approximation considered by virtue of Eq. (20b) in Ref. 29. From the previous section, with the first approximation of the shock shape given by

$$X = G_0(\tilde{r})$$

$$\frac{[\phi_{0_{\tilde{r}}}]}{[\phi_{0_x}]} = -G_0'(\tilde{r}) \quad , \quad$$

where $[\ \ ]$ denotes the jump of the indicated quantity across the shocks and

$$\vec{n} = \frac{\vec{i} - G_0'(\tilde{r})\vec{1}_{\tilde{r}}}{\sqrt{1 + G_0'^2(\tilde{r})}} \quad ,$$

the desired conservation law is

$$\int_{S_0} \left\{ K_1[\phi_{0_x}] - [w\phi_{1_x}] - \frac{[\phi_{0_{\tilde{r}}}][\phi_{1_{\tilde{r}}}]}{[\phi_{0_x}]} \right\} d\tilde{r} = 0 \quad , \qquad (2-43)$$

SC85-30608

Fig. 7. Regions appropriate to shock conservation laws.

where S_0 is the shock surface.

2.5 Regularization of the Problem for the Correction Potential ϕ_1

To avoid the singularity at ∞, the problem P1 in Ref. 29 is transformed by subtracting off the far field for ϕ_1. Accordingly, the variable $\hat{\phi}_1$ is introduced in P1, where

$$\hat{\phi}_1 = \phi_1 - \phi_{FF} \quad . \tag{2-44}$$

Here,

$$M\left[\phi_1\right] \equiv \left(K_0 - (\gamma+1)\phi_{0_x}\right)\phi_{1_{xx}} - (\gamma+1)\phi_{0_{xx}}\phi_{1_x} + \frac{1}{\tilde{r}}(\tilde{r}\phi_{1_r})_{\tilde{r}} = -K_1\phi_{0_{xx}} \tag{2-45a}$$

and

$$\lim_{\tilde{r}\to 0} \phi_{1_r} = 0 \quad . \tag{2-45b}$$

Noting that (for solid walls)

$$\phi_1 \simeq \phi_{FF} = b_0'\tilde{R}^2 P_2(\cos\omega) + 8\pi b_0 B_0 \tilde{R}\cos\omega \tag{2-45c}$$

as

$$\tilde{R} = \sqrt{\frac{x^2}{K_0^2} + \tilde{r}^2} \to \infty$$

and

$$\phi_{FF} = b_0'\left(X^2 - \frac{\tilde{r}^2}{2}\right) + 8\pi b_0 B_0 X \quad , \tag{2-46}$$

where

$$b_0' = \frac{S(1)}{\sqrt{K_0}}b_0$$

$$4\pi B_0 = -S(1) + \int_0^1 S(x)dx + \pi(\gamma+1)\int_{-\infty}^{\infty} dx \int_0^{\infty} \tilde{r}^2\phi_{0_x}^2 d\tilde{r}$$

$$\omega = \text{polar angle defined in Fig. 1}$$

$$S(x) = \text{model cross sectional area}$$

$$R = \text{polar radius defined in Fig. 1} \quad .$$

From $(2-44)$ and $(2-46)$, $(2-45a)$ and $(2-45b)$ become

$$M\left[\hat{\phi}_1\right] = \frac{2(\gamma+1)\phi_{0_x}b_0'}{K_0} + \phi_{0_{xx}}\left\{(\gamma+1)\left(\frac{2b_0'x}{K_0} + \frac{8\pi b_0 B_0}{\sqrt{K_0}}\right) - K_1\right\} \tag{2-47a}$$

$$\lim_{\tilde{r}\to 0} \hat{\phi}_{1_r} = 0 \tag{2-47b}$$

$$\hat{\phi}_1 \to 0 \text{ as } \tilde{R} \to \infty \tag{2-47c}$$

where $\tilde{R} = \delta R$.

The slender body interference code will use the regularized form represented by Equations $(2 - 47)$.

2.6 Basic Code Modules

Figures 8 show flow charts which give an overview of the interaction of the functional modules to be used in the design of the wall interference code under Task 1.0. The preprocessor ATF sets up the grid and inputs other parameters through the subroutines INITIA, INPUT. The input geometry data is read in from the disk file. The solver STINT25 has primary subprograms denoted as RELAX1, OUTFNL, SONIC, DRAG1 used to solve the zeroth order flow problem and RELAXV1, OUTFNL1, and DRAG1 for the variational problem for $\hat{\phi}_1$. RELAX1 and RELAXV1 are modules which respectively are the principal successive line overrelaxation routines which serve the purpose of solving the tridiagonal system for the free field and the interference problems. The tridiagonal solver is denoted as TRID. RELAX1 and RELAXV1 include special treatment of far field, internal, boundary, and shock points with appropriate type sensitive switches. SONIC determines subsonic and supersonic zones, and OUTFNL and OUTFNL1 provide the basic flow and interference pressure fields as well as the quantities g_i defined in Ref. 29 necessary to compute free field and interference drags. These are computed in DRAG and DRAG1, respectively. The relationship of the flow solving modules is shown in Figs. 8.

2.7 Upstream and Downstream Far Fields

For slender test articles that are sting mounted inside solid walls, the flow at great distances from the model behaves as a confined source in accord with the analyses given in the previous sections. Referring to the cylindrical coordinate system indicated in Fig. 9, far field behaviors were worked out in certain "ray limits" in which if $R = \sqrt{x^2 + \tilde{r}^2}$ and $\cos \omega = x/R$, $R \to 0$ for θ fixed. The case $\omega = 0$, or π, i.e., $x \to \pm\infty$ however is degenerate and requires special treatment and had not been analyzed.

For a properly posed numerical simulation of the finite height case, the structure of this flow must be properly modeled. This can be achieved using the Divergence Theorem.

If x is the usual dimensionless coordinate in the freestream direction depicted in Fig. 9, then the transonic small disturbance formulation gives the following equation of motion

$$\Delta\phi \equiv \phi_{XX} + \frac{1}{\tilde{r}} (\tilde{r}\phi_{\tilde{r}})_{\tilde{r}} = \frac{(\gamma + 1)}{\sqrt{K}} \phi_X \phi_{XX} \qquad (2 - 48)$$

where $K = (1 - M_\infty^2)/\delta^2$, M_∞ = freestream Mach number, ϕ is the perturbation potential, and $X = x/\sqrt{K}$. The slender body boundary condition is

$$\lim_{\tilde{r} \to 0} \tilde{r} \frac{\partial \phi}{\partial \tilde{r}} = \frac{S'(x)}{2\pi} \qquad , \qquad (2 - 49)$$

where $S(x)$ is the cross sectional area distribution for $0 \leq x \leq 1$, and $S'(x)$ is without great loss of generality assumed zero for $1 \leq x \leq \infty$, (constant diameter sting).

Fig. 8. Flow chart for preprocessor and solver.

SC-0360-CS

Fig. 8. Flow chart for preprocessor and solver (continued). N in the notation STINTN denotes the Nth version of the main driver.

6C 0361 CS

Fig. 8. Flow chart for preprocessor and solver (concluded).

A control cylinder is considered consisting of the walls (S_H), an internal surface bounding the model near the axis, (S_ϵ), and the inflow and outflow faces $(S_{-\infty})$ and S_∞, respectively. Accounting for the impermeability of the walls expressed as

$$\frac{\partial \phi}{\partial \tilde{r}}\bigg|_{\tilde{r}=H} = 0 \quad , \tag{2-50}$$

the divergence theorem when applied to $(2-48)$ gives

$$\int\int_V\int \Delta\phi \tilde{r} V = \int\int_{S_\epsilon+S_H+S_\infty+S_{-\infty}} \frac{\partial\phi}{\partial n} dS = 2\pi \int_0^H \tilde{r} d\tilde{r} \int_{-\infty}^\infty \left\{ \frac{(\gamma+1)}{2\sqrt{K}} \frac{\partial}{\partial X}(\phi_X^2) \right\} dX, \tag{2-51}$$

where V denotes the volume of the control cylinder. Evaluating the terms in $(2-51)$,

$$\int_{S_\epsilon} \frac{\partial\phi}{\partial n} dS = \lim_{\tilde{r}\to 0} \int_0^{2\pi} d\theta \int_0^\infty \frac{\partial\phi}{\partial\tilde{r}} \tilde{r} dX = 2\pi \int_0^\infty \frac{S'(x)}{2\pi} dX = S(1) \quad . \tag{2-52}$$

From $(2-50)$,

$$\int_{S_H} \frac{\partial\phi}{\partial n}\bigg|_{\tilde{r}=H} dS = 0 \quad . \tag{2-53}$$

For a slender configuration, we assert that as in the subsonic case, the lift effect produces a Trefftz plane $(x = \infty)$ flow component that can be represented as an infinitesimal span vortex pair reflected in the walls. This pair is the Trefftz plane projection of the trailing vortex system from the body. Superposed on this flow is an outflow due to the source effect. A similar outflow occurs at $x = -\infty$. Accordingly, we are led to the asymptotic inflow and outflow conditions

$$\phi \simeq C_{FF}x + f(\tilde{y},\tilde{z}) \qquad \text{as } x \to \infty \tag{2-54a}$$

$$\begin{pmatrix} \tilde{y} = \tilde{r}\sin\theta \\ \tilde{z} = \tilde{r}\cos\theta \end{pmatrix}$$

$$\phi \simeq -C_{FF}x \qquad \text{as } x \to -\infty \quad , \tag{2-54b}$$

where $f(\tilde{y},\tilde{z})$ is related to the lift, and the constant factor C_{FF} appears in the manner indicated in order to preserve the anticipated symmetry of the apparent source flow from the sting–mounted, finite base area model. In this connection, it is important to note that Eqs. $(2-54)$ are exact solutions to the nonlinear small disturbance equation $(2-48)$. This is true even for $f(\tilde{y},\tilde{z})$, since it satisfies cross flow Laplace's equation. It should be noted that the inflow and outflow conditions to be specified at $x = \pm\infty$ are independent of the form of f.

From $(2-54)$, it is clear then that

$$\int\int_{S_\infty+S_{-\infty}} \frac{\partial\phi}{\partial n} dS = 2\pi C_{FF}H^2 \quad . \tag{2-55}$$

31

Fig. 9. Model confined by solid cylindrical walls and control volume.

The last term to be evaluated in $(2-51)$ is the right hand side, which is

$$2\pi \int_0^H \tilde{r}\,d\tilde{r} \int_{-\infty}^{\infty} \frac{(\gamma+1)}{2\sqrt{K}} \frac{\partial}{\partial X} \left(\phi_X^2\right) dX = \frac{(\gamma+1)}{2\sqrt{K}} \int_0^H \tilde{r}\left\{\phi_X^2(\infty,\tilde{r}) - \phi_X^2(-\infty,\tilde{r})\right\} d\tilde{r}$$

which vanishes by virtue of $(2-54)$, as a milder condition of symmetry of the axial component of the far upstream and downstream flow. From this, as well as $(2-51)$ to $(2-55)$, it follows that the inflow and outflow conditions are,

$$\phi_x \simeq \pm \frac{S(1)}{2\pi H^2} \qquad \text{as } x \to \pm\infty \quad , \tag{2-56}$$

i.e., the apparent source strength is proportional to the body base area. Equation $(2-56)$ is used in the numerical simulation of the flow field.

A complete asymptotic expansion based on the eigenfunction expansion for a confined point source given in Ref. 29 can be used to obtain refinement of $(2-56)$ and treat the transonic case. From Green's theorem and the properties of the Green's function G, the perturbation potential ϕ in the confined incompressible solid wall circular cross section case is

$$\phi = \frac{1}{2\pi H^2} \int_0^1 |x-\xi| S'(\xi)d\xi + \frac{1}{2\pi H^2} \int_0^1 S'(\xi) \sum_n \frac{e^{-\lambda_n |x-\xi|}}{\lambda_n} \frac{J_0(\lambda_n r)}{\left[J_0(\lambda_n H)\right]^2} d\xi,$$

where the summation is over the eigenvalues λ_n which solve the following secular equation

$$J_1(\lambda_n H) = 0 \quad .$$

Thus,

$$\lambda_1 H = 3.8317$$
$$\lambda_2 H = 10.1734$$
$$\lambda_3 H = 13.3237$$
$$\vdots$$

From these eigenvalues, it is clear that for moderate H, the confined flow decays much more rapidly upstream and downstream than the free field, with the former demonstrating exponential relaxation to the freestream and the latter, algebraic behavior.

Based on these considerations, and extension to compressible flow which introduces a nonlinear volume source the expression for the asymptotic upstream and downstream behavior is

$$\phi \doteq \frac{1}{2\pi H^2} \left\{ \frac{(\pm x \mp 1)S(1)}{K} + V \pm \frac{(\gamma+1)\pi}{K} \int_0^H \tilde{r} d\tilde{r} \int_{-\infty}^{\infty} \phi_{0_x}^2 dx \right\} \qquad (2-56')$$
$$+ \text{TST} \quad \text{as} \quad x \to \pm\infty$$

where TST = exponentially small terms which are

$$O\left(e^{-\frac{3.83}{H}|x|}\right) \quad \text{as} \quad |x| \to \infty$$

$$V = \int_0^1 S(x)dx \quad .$$

The last term in $(2-56')$ represents the average kinetic energy of the horizontal perturbation of the flow.

2.8 Difference Equations for the Wall Interference Correction Potential

A successive line overrelaxation (SLOR) algorithm for the large height correction potential has been coded. The initial approach is to use modifications of type sensitive switches developed by Murman and Cole[31], and pseudo–time operators devised by Jameson[33] as well as generalizations of the procedures developed in Ref. 34. Results to be discussed for the full nonlinear finite height theory algorithm show good convergence for transonic Mach numbers.

The basic code modules to treat this problem have been flow charted in Fig. 8. Principal modules are RELAX1 and RELAXV1 which are used to solve the discretized form of Eqs. $(2-47)$ by nonlinear iteration and SLOR. Some highlights of our approach will now be outlined.

Applying the SLOR approach to Eqs. (2 – 47), the discretized form is

$$2\left\{(1-\mu_{ij})(\text{COEF}_0)_{ij}\left(\frac{\hat{\phi}_{i+1}^+ - \omega^{-1}\phi_i^+ - (1-\omega^{-1})\hat{\phi}_i}{x_{i+1}-x_i} - \frac{\omega^{-1}\hat{\phi}_i + (1-\omega^{-1})\hat{\phi}_i - \hat{\phi}_{i-1}^+}{x_i - x_{i-1}}\right)\right.$$

$$\left.+\mu_{i-1,j}\left(\frac{\hat{\phi}_i^+ - \hat{\phi}_i - \hat{\phi}_{i-1}^+}{x_i - x_{i-1}} - \frac{\hat{\phi}_{i-1} - \hat{\phi}_{i-2} - \hat{\phi}_i^+}{x_{i-1}-x_{i-2}}\right)\right\}/(x_{i+1}-x_{i-1})$$

$$-(\gamma+1)(\phi_{0_{xx}})_{ij}\left\{\frac{\hat{\phi}_i^+ - \hat{\phi}_{i-1}^+}{x_i - x_{i-1}}\right\}$$

$$+\left(\frac{1}{(\tilde{r})_j(\tilde{r}_{j+1}-\tilde{r}_{j-1})}\right)\left\{\left(\frac{\tilde{r}_{j+1}+\tilde{r}_j}{\tilde{r}_{j+1}-\tilde{r}_j}\right)\left(\hat{\phi}_{j+1}^+ - \hat{\phi}_j^+\right)\right.$$

$$\left.-\left(\frac{\tilde{r}_j - \tilde{r}_{j-1}}{\tilde{r}_{j+1}-\tilde{r}_{j-1}}\right)\left(\hat{\phi}_j^+ - \hat{\phi}_{j-1}^+\right)\right\} = \text{RHS}_{ij}$$

$$(2-57a)$$

$$(\text{RHS})_{ij} = \left\{\frac{2(\gamma+1)\phi_{0_x}b_0'}{K_0} + \phi_{0_{xx}}\left((\gamma+1)\left(\frac{2b_0'x}{K_0} + \frac{8\pi b_0 B_0}{\sqrt{K_0}}\right) - K_1\right)\right\}_{ij} \quad , \quad (2-57b)$$

$$(\text{COEF}_0)_{ij} = (K_0 - (\gamma+1)\phi_{0_x})_{ij} \qquad (2-57c)$$

and

$$\mu_{ij} = \begin{cases} 0, & \text{for COEF}_{0_{ij}} > 0 \text{ (subsonic flow)} \\ 1, & \text{for COEF}_{0_{ij}} \leq 0 \text{ (supersonic flow)} \end{cases} \quad . \qquad (2-57d)$$

Here, $(\text{RHS})_{ij}$ is the discretization of the forcing terms in $(2-47a)$, ω is a relaxation parameter chosen such that $1 \leq \omega \leq 2$, the plus superscripts signify current values, the quantities without plus subscripts denote values from the previous sweep through the flow field, quantities with i subscript only, have j suppressed, and j subscripted entities have i suppressed. The structure of $(2-57)$ is similar to that for the free field dominant and finite height (fully nonlinear) problems with the following exceptions:

1) For the nonlinear problems, a factor analagous to COEF_0, COEF appears, involving the actual dependent variables rather than a known quantity, giving a nonlinear difference equation rather than the linear form $(2-11)$.

2) Eq. $(2-57a)$ contains a first order linear contribution and a right hand side $(\text{RHS})_{ij}$ absent in the nonlinear free field and finite H problem.

3) Artificial damping has been used for the nonlinear problem but may not be required for the linear one.

4) $(\text{COEF})_0$ by its nature is frozen in pseudo-time, whereas COEF is constantly being updated using time linearization with ϕ_x given by its value at the previous sweep (time level).

5) Additional boundaries associated with the zero[th] order shocks are required in the $\hat{\phi}$ problem across which the perturbation shock conditions need to be satisfied.

Note, for bodies with pointed tails, Eq. $(2-57b)$ specializes to

$$(\text{RHS})_{ij} = 8\pi b_0 B_0 (\gamma + 1)(\phi_{0_{xx}})_{ij} \quad . \qquad (2-57b')$$

The tridiagonal system for $\hat{\phi}_j$ is then

$$B_j \hat{\phi}_{j-1} + D_j \hat{\phi}_j + A_j \hat{\phi}_{j+1} = C_j \quad , \quad j = 2,3,\cdots, \text{JMAX} - 1 \qquad (2-58a)$$

$$D_j = -2\Bigg\{ (1 - \mu_{ij}) \left(\frac{\text{COEF}_0}{\omega}\right)_{ij} \left(\frac{1}{x_{i+1} - x_i} + \frac{1}{x_i - x_{i-1}}\right)$$

$$-\mu_{i-1,j} (\text{COEF}_0)_{i-1,j} \left(\frac{1}{x_i - x_{i-1}} + \frac{1}{x_{i-1} - x_{i-2}}\right) \Bigg\} / (x_{i+1} - x_{i-1}) \qquad (2-58b)$$

$$-\frac{(\gamma + 1)(\phi_{0_{xx}})_{ij}}{x_i - x_{i-1}} - \frac{1}{\tilde{r}_j (\tilde{r}_{j+1} - \tilde{r}_{j-1})} \left\{ \frac{\tilde{r}_{j+1} + \tilde{r}_j}{\tilde{r}_{j+1} + \tilde{r}_j} + \frac{\tilde{r}_j + \tilde{r}_{j-1}}{\tilde{r}_j - \tilde{r}_{j-1}} \right\}$$

$$B_j = \frac{1}{\tilde{r}_j (\tilde{r}_{j+1} - \tilde{r}_{j-1})} \left(\frac{\tilde{r}_j + \tilde{r}_{j-1}}{\tilde{r}_j - \tilde{r}_{j-1}}\right) \qquad (2-58c)$$

$$A_j = \frac{1}{\tilde{r}_j (\tilde{r}_{j+1} - \tilde{r}_{j-1})} \left(\frac{\tilde{r}_{j+1} + \tilde{r}_j}{\tilde{r}_j - \tilde{r}_{j-1}}\right) \qquad (2-58d)$$

$$C_j = -2\Bigg\{ (1 - \mu_{ij})(\text{COEF}_0)_{ij} \left(\frac{\hat{\phi}_{i+1} - (1 - \omega^{-1})\hat{\phi}_i}{x_{i+1} - x_i} - \frac{(1 - \omega^{-1})\phi_i - \hat{\phi}_{i-1}^+}{x_i - x_{i-1}}\right)$$

$$-\mu_{i-1,j} \left(\frac{\hat{\phi}_i + \hat{\phi}_{i-1}^+}{x_i - x_{i-1}} + \frac{\hat{\phi}_{i-1}^+ - \hat{\phi}_{i-2}}{x_{i-1} - x_{i-2}}\right) \Bigg\} - (\gamma + 1)(\phi_{0_{xx}})_{ij} \left\{ \frac{\hat{\phi}_{i-1}^+}{x_i - x_{i-1}} \right\} + (\text{RHS})_{ij}$$

$$(2-58e)$$

At the body, $j = 2$, and the previously indicated boundary condition, $\phi_1 = 0$ implies

$$D_2 = D_2^{j>2} + \frac{1}{r_2 r_3} \qquad (2-59a)$$

$$B_2 = 0 \quad . \qquad (2-59b)$$

Also, A_2 and C_2 take their specialized values at $\tilde{r} = \tilde{r}_2$ (with $\tilde{r}_1 = 0$).

In $(2-58)$ and $(2-59)$, the μ_{ij} are designed to provide the necessary type sensitive switching and implementation of Murman's shock point operator defined in Ref. 35. This behavior is essential not only for the zeroth order solution but the variational one as well.

Subsequent sections will describe the scheme of shock fitting that interacts with the difference equations $(2-58)$ and $(2-59)$.

2.9 Finite Height Application of Zeroth Order Code

As indication of an application of the zeroth order part of STINT25 calculated by RELAX1, an equivalent body of revolution representative of a transonic/supersonic

blended wing fighter configuration was computed in a solid wall wind tunnel. The cross sectional area progression of the model is indicated in Fig. 10 which shows curvature changes associated with such geometrical features as wing–body intersections, canopies, and inlets. One purpose of this study was to explore aspects of the application of the code to realistic airplane geometries.

Fig. 10. Area distribution of blended wing fighter configuration.

As an indication of the flow environment for subsequent wall interference studies, Fig. 11 shows the pattern of isoMachs over the configuration associated with Fig. 10 in a free field at $M_\infty = .95$. These results could be practically obtained using the nonlinear analogue of the difference method associated with Eqs. $(2-57)$–$(2-59)$ on a VAX computer in a CPU limited Fast Batch or interactive environment. The grid utilized 194 points in the x direction with uniform spacing over the body and logarithmic stretching ahead and behind. In the $\bar{r}$ direction, a similar geometric progression spacing was used with

50 points. Nominal convergence* typically was achieved between 500 to 1500 sweeps, with more sweeps required at the higher transonic Mach numbers.

Fig. 11. IsoMachs over blended wing configuration in free field, $M_\infty = .95$.

The complexity of the flow structure evident in Fig. 11 is to be associated with the multiple inflection points of the area progression and the possibility for envelopes to form in the steeply inclined wave system. In Fig. 11, a shock is formed near about $\frac{2}{3}$ of the body length from such an envelope process.

Figures 12 and 13 illustrate the Mach number and surface pressure distributions at the same freestream Mach number for the free field environment and a solid wall confined case. To obtain a nominal simulation of the free field, the upper computational boundary $j = \text{JMAX}$ was placed at $H \simeq 1.3$ and homogeneous Dirichlet conditions were imposed there. Homogeneous Neumann inflow and outflow conditions at $x = \pm\infty$ were also prescribed. For the solid wall simulation, $H \simeq 0.66$ was utilized. Homogeneous Neumann conditions were used at $j = \text{JMAX}$ and Eq. (2 − 9) applied at $x = \pm\infty$.

---

* Defined as $\max_{\substack{1 \leq i \leq IMAX \\ 1 \leq j \leq JMAX}} \mid \phi_{ij}^+ - \phi_{ij} \mid = 10^{-5}$.

Fig. 12. Finite height solid wall interference effect at $M_\infty = .95$ on blended fighter configuration equivalent body — Mach number distribution over body.

Fig. 13. Finite height solid wall interference effect at $M_\infty = .95$ on blended fighter configuration equivalent body — surface pressures.

From the figures and in accord with simple one–dimensional gasdynamic reasoning, the constrictive effect of the solid walls is to exaggerate the effect of stream tube area changes associated with body area changes.

An experimental validation was performed of the 0th order solver RELAX1 based on one of the variable blockage ratio tests of a blunt nosed model (B-3) in the Langley 8 and 16 foot tunnels, reported in Ref. 36. The test section was slotted and slatted as well as octagonal in shape. For such a blunt body which locally violates small disturbance theory, the agreement with the data is surprisingly excellent as shown in Fig. 14. For this comparison, the special improved accuracy boundary discretization procedure described in the next section was used. The quality of the comparison is believed to be partially attributable to this improvement.

2.10 Improved Accuracy Procedures for Numerical Treatment of Body Boundary Conditions

In the finite wall height application of the code, the interference pressures are computed as the difference between the confined and free field pressures. The numerical truncation error is a larger percentage of this difference than of either of the former quantities. This fact puts a greater demand on numerical accuracy than has been stressed in state of the art codes. Accordingly, all error sources were evaluated. Some items considered within an incompressible and subsonic framework were:

1. Accurate treatment of boundary conditions on axis of equivalent body.

2. Proper application of upstream and downstream far fields.

3. Need for double precision on shorter word length computers such as the VAX to handle high frequency errors propagating on fine grids for large iteration counts.

4. Treatment of nose and tail singularities.

The techniques apply directly to the transonic case. Moreover, study of subsonic flows is particularly useful because of the availability of closed form analytical solutions to check the numerics.

The second of Figs. 8 shows the subroutine RELAX1, which solves the tridiagonal system representing a discretized approximation of the transonic small disturbance partial differential equation of motion (TSDE) $(2 - 5a)$. It contains a special procedure which deals with the boundary conditions. These are satisfied by incorporating the condition of flow tangency at the body into the discretization of the vertical perturbation velocity flux gradient. In the nonlinear difference equation for the free field flow $(2 - 57a)$, this corresponds to an approximation fulfilling the role of the terms in the braces on the left hand side near the equivalent body of revolution (EBR) line of symmetry, $(x$ axis). One scheme employed is associated with Eqs. $(2 - 59a)$ and $(2 - 59b)$.

Figure 15 is a schematic representation of the nodes relevant to the boundary points. In the finite height case, this treatment is made more difficult because the perturbation potential is logarithmically singular as the scaled radial coordinate tends to zero. Existing

Fig. 14. Validation of RELAX1 code against Couch experiment, B-3 body, $M = .99$.

free field codes familiar to us do not properly deal with this singularity. Whereas this limitation may be of moderate consequence to the prediction of free and confined pressures, in accord with the previous remarks, it is absolutely crucial to the treatment of interference pressures and testing of the variational equation solver. Accordingly, attention was given to the development of a scheme that accounts for the singularity in the boundary treatment.

Fig. 15. Nodes in vicinity of axis.

Referring to Fig. 15, the discretization of the third term,

$$T \equiv \frac{1}{\tilde{r}}(\tilde{r}\phi_{0_r})_{\tilde{r}} , \qquad (2-60)$$

in the TSDE will now be discussed. This is the vertical flux gradient previously indicated. Shown in the figure are the first 3 (j) vertical node points as well as $\frac{1}{2}$ node points. If $\tilde{r}_j, j = 1, 2, \cdots, JMAX$ represent the j mesh points,

$$r_{j+1/2} = (r_{j+1} + r_j)/2, \qquad (2-61)$$

we consider (dropping the subscript zero on ϕ and the tildes on r), the discretized version of $T \equiv T_j$, given by

$$T_j = \left\{ \frac{1}{r}(r\phi_r)_r \right\}_j . \qquad (2-62)$$

Using the half node points in the vicinity of the x axis

$$T_2 = \frac{1}{r_2} \frac{(r\phi_r)_{5/2} - (r\phi_r)_{3/2}}{r_{5/2} - r_{3/2}} . \qquad (2-63)$$

42

The essential new idea is that a "regularized" version $\hat{\phi}$ of the perturbation velocity potential ϕ is introduced, where

$$\hat{\phi} = \phi - \frac{S'(x)}{2\pi} \ln r \qquad (2-64)$$

$S'(x) =$ streamwise (x) derivative of the EBR area progression.

The logarithmic singularity is represented by the second term in $(2-64)$. Numerical differentiation of ϕ in the r direction is then accomplished by differentiating ϕ as the sum of a numerical approximation of its regular part and an analytical evaluation of the logarithmically singular component. The truncation error which would have normally become large due to the infinity on the axis will be substantially reduced using the differentiation of the linear polynomial representing the bounded quantity $\hat{\phi}$.

In accord with these ideas, the terms in $(2-63)$ can be evaluated as follows:

$$(r\phi_r)_{5/2} = \frac{(r_3+r_2)}{2} \left\{ \frac{\hat{\phi}_3 - \hat{\phi}_2}{r_3 - r_2} + \frac{S'(x)}{2\pi(r_3+r_2)/2} \right\} = \frac{(r_3+r_2)}{2} \left(\frac{\hat{\phi}_3 - \hat{\phi}_2}{r_3 - r_2} \right) + \frac{S'(x)}{2\pi}$$

$$= \frac{(r_3+r_2)}{2} \left\{ \frac{\phi_3 - \phi_2 - \frac{S'(x)}{2\pi} \ln r_3/r_2}{r_3 - r_2} \right\} + \frac{S'(x)}{2\pi}$$

$$(2-65a)$$

$$(r\phi_r)_{3/2} = r_{3/2} \left\{ \hat{\phi}_r \Big|_{3/2} + \frac{S'(x)}{2\pi r_{3/2}} \right\} = r_{3/2} \hat{\phi}_r \Big|_{3/2} + \frac{S'(x)}{2\pi}$$

$$= \frac{(r_2+r_1)}{2} \left\{ \frac{\phi_2 - \frac{S'(x)}{2\pi} \ln r_2 - g(x)}{r_2 - r_1} \right\} + \frac{S'(x)}{2\pi}$$

$$(2-65b)$$

where the fact that

$$\phi \simeq \frac{S'(x)}{2\pi} \ln r + g(x) + \cdots \qquad (2-66)$$

has been used in $(2-65b)$. Noting that $r_1 = 0$, and collecting results,

$$T_2 = \frac{(r_3+r_2)}{r_2} \left[\frac{\hat{\phi}_3 - \hat{\phi}_2 - \frac{S'(x)}{2\pi} \ln r_3/r_2}{r_3 - r_2} \right]$$

$$- \frac{1}{r_3} \left[\hat{\phi}_2 - \frac{S'(x)}{2\pi} \ln r_2 - g(x) \right]$$

$$(2-67)$$

Accordingly, the tridiagonal system discretizing TSDE

$$B_j \hat{\phi}_{j-1} + D_j \hat{\phi}_j + A_j \hat{\phi}_{j+1} = C_j \quad , \quad j = 1, 2, \cdots, JMAX$$

at $j = 2$, has in accord with $(2-67)$,

$$B_2 = 0 \qquad (2-68a)$$

$$A_2 = A_j^{j>2} \Big|_{j=2} \qquad (2-68b)$$

$$D_2 = D_j^{j>2} \Big|_{j=2} \qquad (2-68c)$$

$$C_2 = C_j^{j>2} \Big|_{j=2} + \frac{1}{2\pi r_2 r_3} \left\{ \frac{S'(x)}{2\pi} \left[\frac{r_3+r_2}{r_3-r_2} \ln \frac{r_3}{r_2} - \ln r_2 \right] - g(x) \right\}. \qquad (2-68d)$$

In the computational implementation, $g(x)$ is initialized as zero and then updated each iteration using $(2-66)$. For $(2-68d)$, $g(x)$ is "time linearized" from the previous iteration without relaxation. As an additional refinement, it is useful to note that the three dots in $(2-66)$

$$= \frac{S'''(x)}{2\pi} \left(\frac{r^2 \ln r}{4} - \frac{r^2}{4} \right)$$

in incompressible and subsonic Prandtl Glauert flow, and is an $O(S'''(x)r^2 \ln^2 r)$ expression at transonic Mach numbers. The updated g is computed using linear extrapolation as

$$g(x) = \dot{\phi}_3 - \frac{r_3}{r_3 r_2} \left(\hat{\phi}_3 - \hat{\phi}_2 \right). \tag{2-69}$$

Numerical experiments show that this produces results equally acceptable to those from an asymptotic approximation based on previously mentioned higher order terms proportional to $S'''(x)$ when $S'''(x)$ is known analytically. For tabular $S(x)$ input, the linear form $(2-69)$ is preferred due to significant errors possible in obtaining $S'''(x)$.

This scheme was applied to treat incompressible flow over a parabolic arc of revolution body, in the free field and confined by solid walls. The normalized radius F which is given by

$$F(x) = 2x(1-x) \qquad (0 \le x \le 1) \tag{2-70a}$$

gives the cross sectional area,

$$S(x) = \pi F^2 = 4\pi x^2 (1 - 2x + x^2) \quad . \tag{2-70b}$$

Thus

$$S'(x) = 8\pi (x - 3x^2 + 2x^3) \quad . \tag{2-70c}$$

Now, in the free field,

$$g(x) = \frac{S'(x)}{4\pi} \ln \frac{1}{4x(1-x)} - \frac{1}{4\pi} \int_0^1 \frac{S'(\xi) - S'(x)}{|x - \xi|} d\xi \quad , \tag{2-71}$$

which for $(2-70a)$ specializes to

$$g(x) = 2x(1 - 3x + 2x^2) \ln \frac{1}{4x(1-x)} + \frac{44}{3} x^3 - 22x^2 + 8x - \frac{1}{3} \tag{2-72a}$$

$$g'(x) = 2 \left(1 - 6x + 6x^2 \right) \{ 3 - \ln 4x(1-x) \} + 6 \left(1 - 6x + 6x^2 \right) \quad . \tag{2-72b}$$

The corresponding confined solution is given in Ref. 37.

2.10.1 Results

Figure 16 gives a comparison of VAX 11/780 application of the finite height code run in the free field to the exact solution represented by $(2-70a)$. The vertical $(\tilde{r})$ grid was developed with logarithmic clustering. The clustering parameter SA provides a uniform

grid when $SA = 1$ and progressively greater clustering near the x axis with increasing SA. For Fig. 16, $SA = 1.0001$ (almost a uniform grid) was used to compute g. (The function $g'(x)$ is an important term in the expression for surface pressures.) Reasonable agreement with the exact solution of Eq. $(2 - 72a)$ is indicated with this grid selection as well as iterative convergence.

Figure 17 demonstrates the effects of changing the clustering parameter SA to 1.1 and mesh convergence. Improved agreement with $(2 - 72a)$ is demonstrated as well as good convergence with respect to the mesh size. In fact, it is clear that acceptable accuracy is obtained with an intermediate 100×50 (100 points in the x direction and 50 in the r direction) grid, as compared to the fine 200×100 grid.

Turning to $g'(x)$, Fig. 18 shows an iterative convergence study on the almost uniform vertical grid configuration considered in Fig. 16. Although excellent convergence (in the mean) to the exact solution $(2 - 72b)$ is indicated, oscillations are present. Two items were investigated in connection with this phenomenon. One involves the relatively short word length available on the VAX and its interaction with roundoff propagation present in the successive line overrelaxation (SLOR) method. If ρ indicates the "chopping" error associated with this word length restriction, there is an adverse effect of mesh refinement. Letting δx and δr represent characteristic step sizes in the x and r direction, respectively, the roundoff error is $O(\rho/\delta x \delta r)$ as $\delta x, \delta r \rightarrow 0$. Therefore, ρ was reduced by a double precision modification of the finite height code. Returning to $SA = 1.1$, Figs. 19 and 20 indicate the benefits of this change, where the single precision oscillations of Fig. 19 are all but eliminated by the double precision algorithm as shown in Fig. 20. There is, however, a latent inaccuracy in the vicinity of the nose and tail stagnation points. From an asymptotic approximation of $(2 - 71)$ in the vicinity of the nose,

$$g(x) \simeq \frac{S'(x)}{2\pi} \ln \frac{r}{2 \left[x + \sqrt{x^2 + r^2} \right]^{1/2}} \qquad \text{as } x, r \rightarrow 0 . \qquad (2 - 73)$$

A similar formula with x replaced by $1 - x$ applies near the tail. The procedure associated with Eqs. $(2 - 67)$ and $(2 - 68)$ must be modified to handle the special x "boundary layers" near $x = 0$ and 1. This not only involves subtracting off the associated logarithmic singularities, but incorporating refinements in the interpolation procedure as well. As mentioned previously, these improvements are important in obtaining an adequate prediction of the interference pressures. Computations of the latter without such measures are shown in Fig. 21 for a 100×50 grid. There, the streamwise distribution of the normalized interference pressure ΔC_p with

$$\frac{\Delta C_p}{\delta^2} = -2\Delta g' \quad , \quad \Delta(\ ) = (\ )_{\text{tunnel}} - (\ )_{\text{free field}} \qquad (2 - 74)$$

is plotted, where Δ signifies the difference between confined and free field distributions at a value of the reduced height parameter H (wall height in units of the body length) $\simeq 1.1$, and δ is the body thickness ratio. Although qualitative agreement with results of Ref. 37
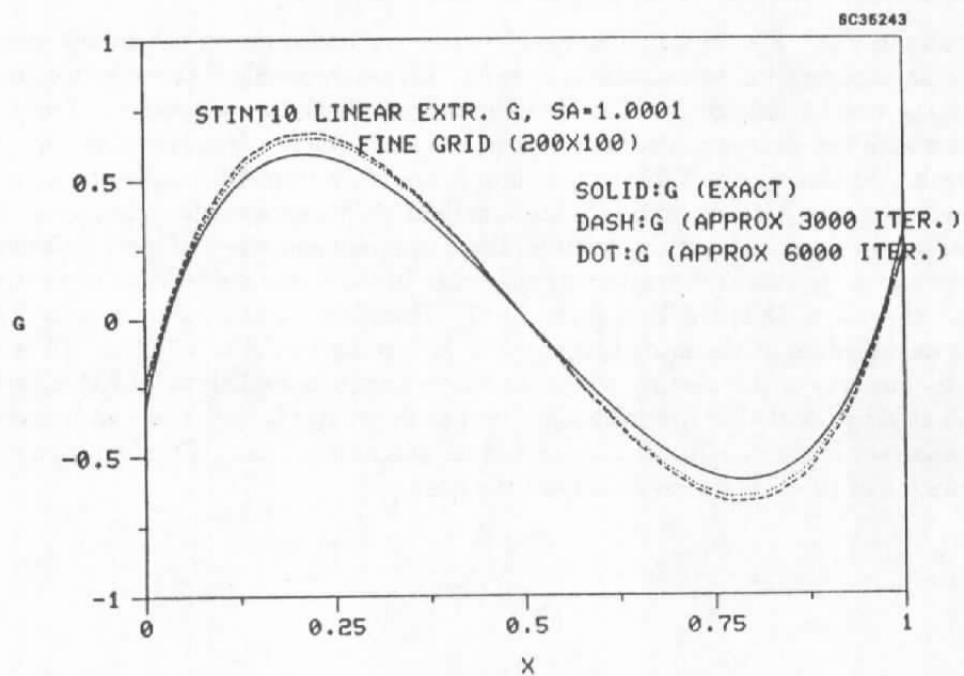
Fig. 16. Iterative convergence study of g.
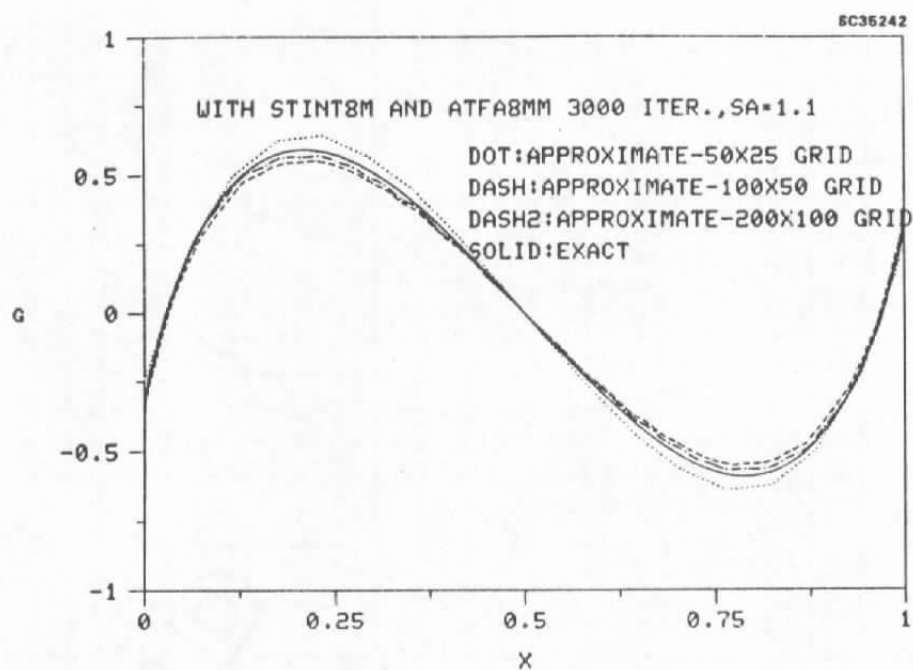
Fig. 17. Mesh convergence study of g (DASH2 legend is the dash–dot curve).

SC36241

STINT10 LINEAR EXTR. G, SA=1.0001
FINE GRID (200X100)

SOLID:G' (EXACT)
DASH:G' (APPROX 3000 ITER.)
DOT:G' (APPROX 6000 ITER.)

GPRIME

20

10

0

-10

-20

0   0.25   0.5   0.75   1

X
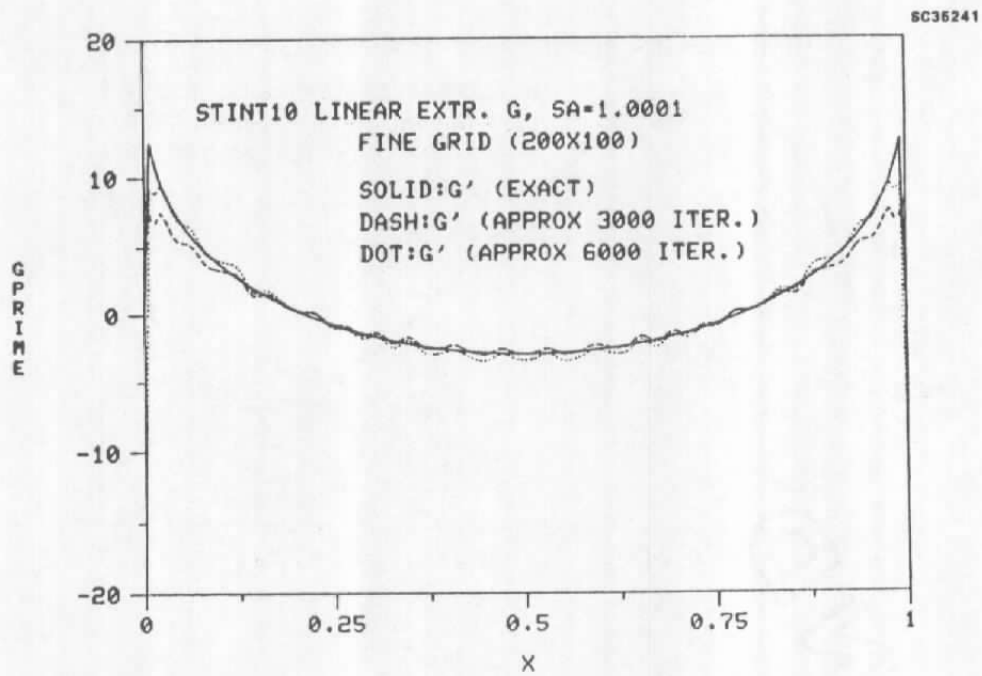
Fig. 18. Iterative convergence study of $g'(x)$.

Fig. 19. Roundoff study of $g'(x)$.

SC35240

20

15 —

10

GPRIME

5

0

-5

-10

0   0.25   0.5   0.75   1

X

3001 ITERATIONS, DOUBLE PRECISION
STINT10:ASYMP. G EXTRAP
RUN N128A WITH ATFA8AMM
SA=1.1, 200X100 GRID

SOLID:GPRIME (EXACT)
DOT:GPRIME (APPROXIMATE)
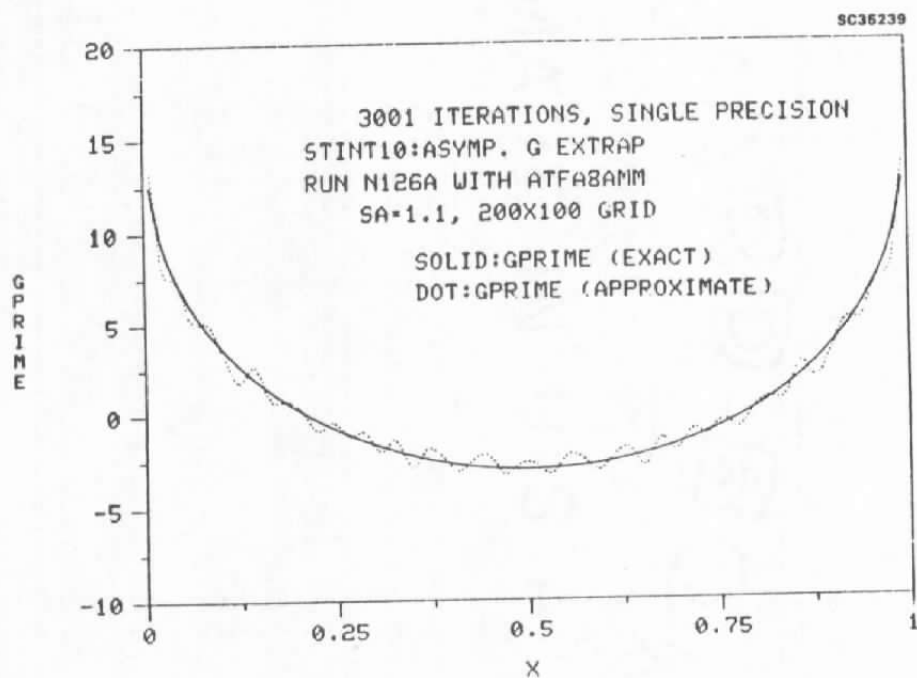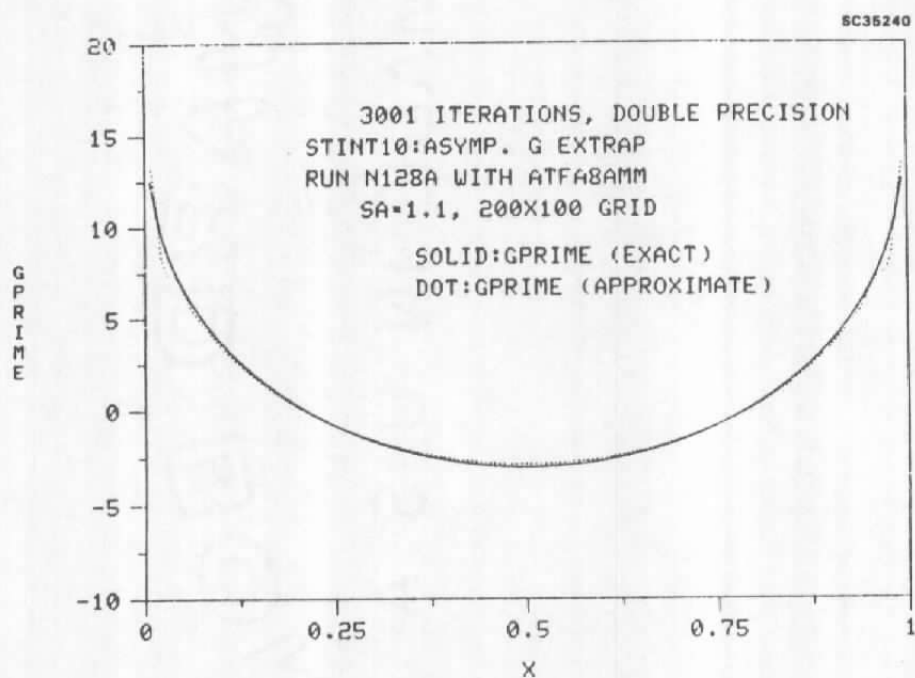
Fig. 20. Roundoff study of $g'(x)$.

are indicated, it is speculated that the mild oscillations shown in Fig. 20 near $x = 0$ and 1 are aggravated by the interaction of the close solid walls and the logarithmic singularities at these points given by Eq. (2 − 73).

2.11 Shock Fitting Scheme for Wall Interference Correction Potential

In Section 2.9, runs were discussed of the finite wall height code option associated with a realistic compact blended wing fighter configuration. This code has been designed to incorporate the proper source-like inflow and outflow boundary conditions associated with solid walls. In addition, difference schemes were developed for the large height theory formulated as the problem P1 in Ref. 29. The variational equation solver uses a special procedure to treat shock jumps in the solution for the wall interference correction potential $\hat{\phi}$. The shock polar relating these jumps to the streamwise and transverse derivatives of $\hat{\phi}$ are given as Eqs. (2 − 40) and (2 − 41).

Figure 22 shows the relationship of the geometry of a typical shock structure arising in the $\hat{\phi}$ problem and the grid. As one choice among various options, also considered in connection with the high aspect ratio code discussed in Section 3, the finite difference implementation will satisfy the shock relations across PO by surrounding it by the internal boundary condition carrying "notch" $ABCD$. The contour of this notch is composed of lines parallel to the $\bar{r}$ and x axes. It is presently felt that this selection provides substantial coding simplifications as compared to another option involving a curved internal boundary not parallel to the axes. A disadvantage of the notch scheme is that it can diffuse the shock somewhat beyond the few mesh points necessary to capture it in the zeroth order approximation for the perturbation potential. However, this additional spreading is provisionally assumed to be small, since the cases of primary concern will involve almost normal shocks.

Referring to Fig. 22, the strategy to be applied is to determine shock jumps in $\hat{\phi}$ at the various j levels $[\hat{\phi}]_j \equiv \hat{\phi}(NSPMAX, j) - \hat{\phi}(NSPMIN, j)$ as a vector sequence

$$\lim_{n \to \infty} J_n = J \quad , \tag{2 − 75}$$

where J_n denotes the vector $\left([\hat{\phi}]_1, [\hat{\phi}]_2, [\hat{\phi}]_3, \cdots, [\hat{\phi}]_{JSMAX} \right)$ at the nth successive line over-relaxation (SLOR) sweep. The iterative sequence (2 − 75) is required since J is coupled to the solution field $\hat{\phi}$.

In the implementation, J is the solution of a bidiagonal or tridiagonal system which is solved by recursion. The coupling of $\hat{\phi}$ is nonlinear through the coefficients appearing in the system. Accordingly, a linearization in pseudo-time involving the values of $\hat{\phi}$ at the $n − 1$ level has been coded. The new values of J are then used for the tridiagonal system along $x = x_i$ lines to update the j row vectors along $\hat{\phi}_i$ along $x = x_i$ on the next sweep. The process is iterated until convergence is obtained.

Differencing the jump conditions (2 − 40) and (2 − 41) gives

$$a_j [u_1]_j + b_j \langle u_1 \rangle + c_j [v_1] + d_j [\phi_1] = 0 \quad , \tag{2 − 76a}$$
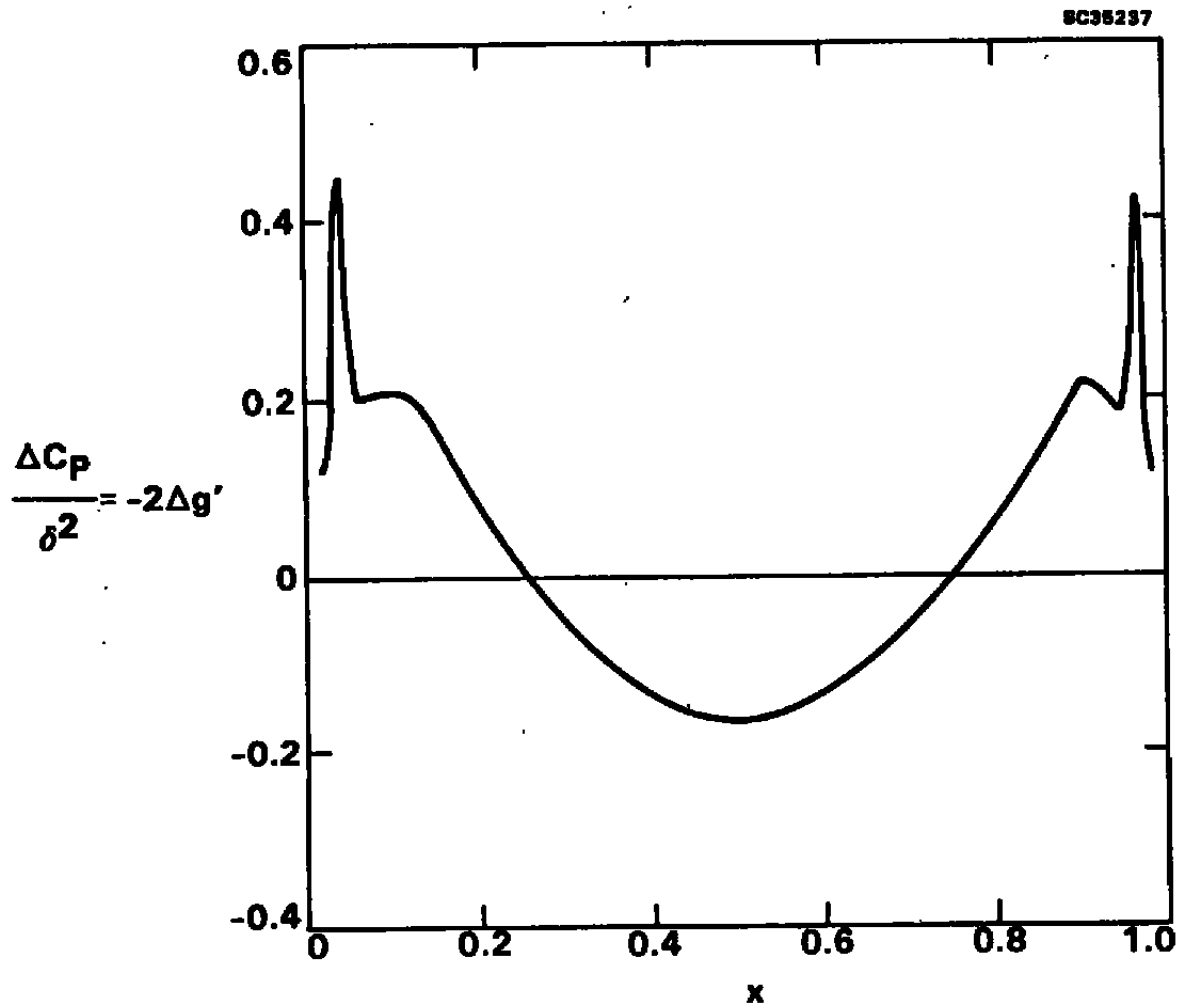
Fig. 21. Interference pressures on a confined parabolic arc body. $H \sim 1.1$, 100×50 grid, 1200 iterations.

SC52215
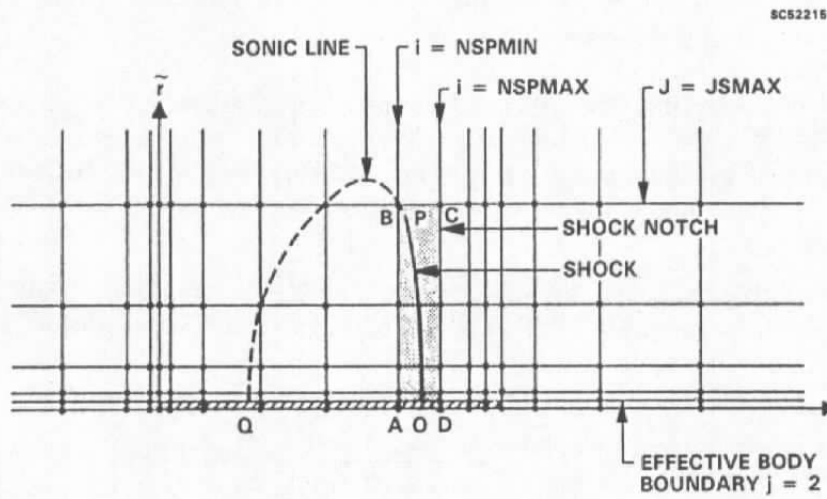
Fig. 22. Schematic of shock fitting geometry for wall interference correction potential.

where ( ) signifies an average across the unperturbed shock, and

$$a_j = \langle K - (\gamma + 1)u_0 \rangle \left[u_0 \right]^2 - \left[v_0 \right]^2 \qquad (2-76b)$$

$$b_j = [K - (\gamma + 1)u_0] \left[u_0 \right]^2 \qquad (2-76c)$$

$$c_j = 2 \left[v_0 \right] \left[u_0 \right] \qquad (2-76d)$$

$$d_j = \frac{\left[v_0 \right]^2 \left[u_{0_x} \right]}{\left[u_0 \right]} - 2 \left[v_0 \right] \left[v_{0_x} \right] - \left[(K - (\gamma+1)u_0)u_{0_x} \right] \left[u_0 \right] \quad . \qquad (2-76e)$$

Using the shock notch idea and assuming without loss of generality, a single shock is in the flow (fishtails for Mach numbers near unity and choking may require special treatments), denote the points in the shock notch as:

$$x_{\text{NSPMIN}}, \ x_{\text{NSPMIN}+1}, \ x_{\text{NSPMIN}+2}, \ \cdots, \ x_{\text{NSPMAX}} \quad , \qquad (2-77)$$

where $x_{\text{NSPMIN}} \leq x_{Hj}$ and $x_{\text{NSPMAX}} \geq x_{Ej}$, and x_{Hj}, x_{Ej} denote the upstream and downstream locations about the shock at each j, or the last hyperbolic and first elliptic points, respectively.

In more compact notation, let superscripts $-$ and $+$ denote the pre- and post-shock sides of the notch, respectively (NSPMIN and NSPMAX) and let s indicate the shock as well as $[\phi_1]_j$ signify the jump of ϕ_1 at j. Then

$$\langle u_1 \rangle = \frac{u_{1_s}^+ + u_{1_s}^-}{2} = \frac{1}{2} \left\{ \frac{\phi_{1_{s+1}} - \phi_{1_s}^- - [\phi_1]}{x_{s+1} - x_s^+} + \frac{\phi_{1_s}^- - \phi_{s-1}}{x_s^- - x_{s-1}} \right\} \qquad (2-78)$$

where the i and j subscripts have been selectively suppressed.

Substitution of Eq. $(2-78)$ into Eq. $(2-76)$ gives the following bidiagonal system of equations for $\left[\hat{\phi}_1 \right]_j$, noting that $\langle \hat{u}_1 \rangle = \langle u_1 \rangle - C$, where $C = \frac{8\pi b_0 B_0}{\sqrt{K}}$

$$\left[\hat{\phi} \right]_j = \frac{C_j - B_j [\hat{\phi}]_{j-1}}{D_j} \quad , \quad 3 \leq j \leq \text{JSMAX} \qquad (2-79a)$$

$$D_j = d_j + \frac{c_j}{\Delta \tilde{r}} - \frac{a_j + b_j/2}{\Delta x_D} \qquad (2-79b)$$

$$B_j = -\frac{C_j}{\Delta \tilde{r}} \qquad (2-79c)$$

$$-C_j = a_j \left\{ \frac{\hat{\phi}_{D+1}^{(n-1)} - \hat{\phi}_U^{(n)}}{\Delta x_D} - \frac{\hat{\phi}_U^{(n)} - \hat{\phi}_{U-1}^{(n)}}{\Delta x_U} \right\}$$

$$+ \frac{b_j}{2} \left\{ \frac{\hat{\phi}_{D+1}^{(n-1)} - \hat{\phi}_U^{(n)}}{\Delta x_D} + \frac{\hat{\phi}_U^{(n)} - \hat{\phi}_{U-1}^{(n)}}{\Delta x_u} + C \right\} \qquad (2-79d)$$

54

where $\Delta \tilde{r} = \tilde{r}_j - \tilde{r}_{j-1}$, U signifies x_{NSPMIN}, D signifies x_{NSPMAX}, $\Delta x_D = x_{D+1} - x_D$, $\Delta x_U = x_U - x_{U-1}$, n is the current time level and $n - 1$ the previous level.

In one version of the variational solver, central difference approximations are applied to the discretization of the v components in $(2 - 76)$, leading to the use of a tridiagonal Thomas algorithm. The bidiagonal formulation results from one-sided differences. If the recursion proceeds downward from the top of the shock notch, it is unstable. At the top, $\left[\hat{\phi}_1\right]$ is determined from the fact that it is a body point. Section 2.16.1 provides more information on the upward bidiagonal recursion scheme represented by $(2 - 79a)$.

For a tridiagonal formulation, there has been an issue regarding the appropriate boundary conditions at the foot of the shock, assumed located at $j = 2$. Since ϕ (the finite wall height perturbation potential) and ϕ_0 are logarithmically singular there, there is a question regarding the behavior of $[\phi_1]$. This appears to be resolved by the fact that $\phi_{1_r}(x, 0) = 0$. Hence, $[\phi_{1_r}] \sim 0$ at $j = 2$. Moreover, in the finite wall (H) case, since

$$\phi \simeq \frac{S'(x)}{2\pi} \ln \tilde{r} \text{ as } \tilde{r} \to 0 \quad , \tag{2-80}$$

then the limit $\tilde{r} \downarrow 0$, x fixed $= x^-, x^+$, where $-$ and $+$ denote the upstream and downstream sides of the shock, respectively, with $S'(x)$ continuous at the shock gives

$$[\phi_{\tilde{r}}] = \infty - \infty = 0 \quad . \tag{2-81}$$

Another approach is to multiply the jump equations by $\tilde{r}$ and note that $[\phi_{\tilde{r}}] = [r\phi_{\tilde{r}}]$. This avoids the infinities in Eq. $(2 - 81)$. The relation $[\phi_{1_r}] = 0$ implies that

$$[\phi_1]_2 = [\phi_1]_3 \quad . \tag{2-82}$$

Equation $(2 - 82)$ is used to find the interference potential on the body.

A related problem was studied in Ref. 38 in regard to the invariance of the shock position on a body of revolution in transonic flow. Some aspects of this question and conditions near the foot of the shock are discussed in the Appendix.

2.12 Determination of Second Term of Central Layer Large Height Expansion

For the numerical work, the asymptotic expansion of the velocity potential Φ in the near field of the test article is given by $(2 - 31)$. The constant a_0 related to a_0' in that expression given by

$$a_0 = \frac{a_0' \sqrt{K_0}}{S(1)} = \frac{1}{\pi^2} \int_0^\infty \left\{ \frac{1}{k^2} - \frac{K_1(k)}{I_1(k)} \right\} dk \tag{2-83}$$

has been numerically determined. This result gives an indication of the small H elasticity of large H theory, a small value being suggestive of extended validity, as in the incompressible case treated in Ref. 37.

Although the integral in $(2-83)$ converges, the convergence is numerically poor on a uniform grid due to an integrable logarithmic singularity associated with the ratio of the modified Bessel functions at the lower limit.

To improve convergence, the asymptotic behavior of the integrand

$$\frac{1}{k^2} - \frac{K_1(k)}{2I_1(k)} \simeq -\frac{1}{2}\ln\frac{k}{2} \quad \text{as} \quad k \to 0 \qquad (2-84)$$

was subtracted and added to regularize the integral to provide the modified expression

$$\pi^2 a_0 = 1 + \int_0^2 \left(\frac{1}{k^2} - \frac{K_1(k)}{2I_1(k)} + \frac{1}{2}\ln\frac{k}{2}\right)dk + \int_2^{k_1}\left(\frac{1}{k^2} - \frac{K_1(k)}{2I_1(k)}\right)dk \quad , \qquad (2-85)$$

where k_1 is assumed to be sufficiently large.

The adequacy of $(2-84)$ on the interval $0 \leq k \leq 2$ is shown in Fig. 23. A good comparison between the left and right hand sides of $(2-84)$ is indicated. In Fig. 24, the second two integrands are plotted. The decay of the Bessel function is rapid, indicating that a k_1 of 10 is quite sufficient for a practical evaluation. Figure 25 indicates the rapid convergence of the trapezoidal rule over a uniform grid giving the desired value of a_0 and b_0 as

$$a_0 = 0.129558$$
$$b_0 = \frac{1}{4\pi^2}\int k^2 K_1(k)/I(k)dk = 0.063409 \quad .$$

The small magnitude of a_0 is consistent with the extended validity of the theory for moderate wall height hypothesized earlier.

2.13 Structural Aspects of Slender Body Code

A great degree of flexibility has been built into the finite and large wall height codes, hereinafter referred to as STINT25. Logical variables have been introduced so that the user can treat incompressible, linear, and transonic flows within the same code by merely changing a NAMELIST file. For ensuing checking, parametric studies, and running economies, provision has been made to start either the free field, wall perturbation parts of the code independently or run the latter serially after the former. Furthermore, both codes can be restarted from a previous solution. Finally, considerable diagnostic I/O has also been built into the codes.

In addition to this logic, a procedure has been conceptualized which can be useful in obtaining a sharper resolution of the shocks than possible in the previously described ("upright") shock notch method. Referring to Fig. 26, the shock is considered to consist of subarcs of the type shown as 1 and 2 in the figure. In the blow-ups of these regions, these negative and positively sloped portions can be considered in terms of the proper difference formulas for the determination of the jump of the vertical component of the
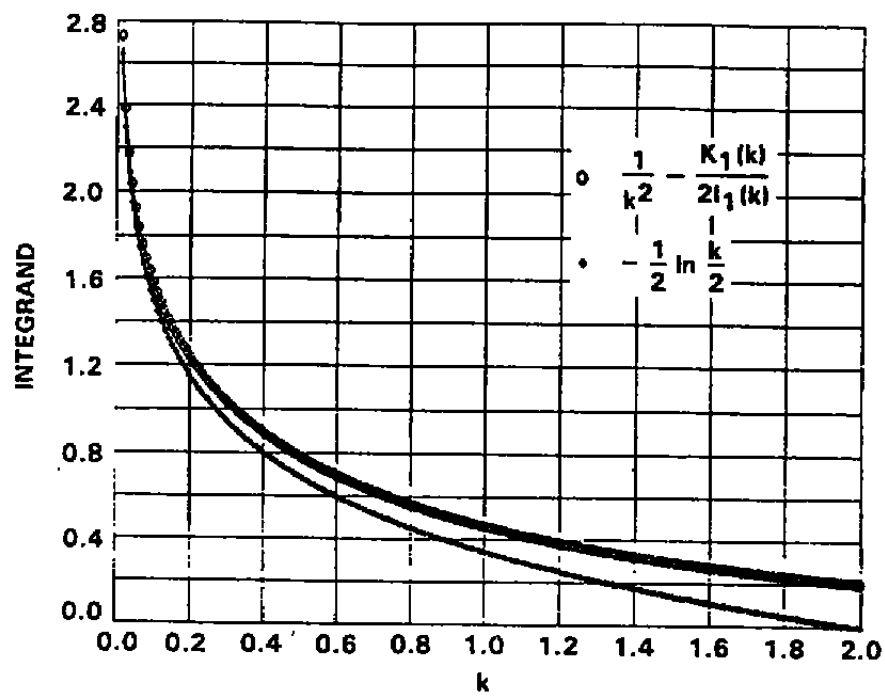
Fig. 23. Comparison of exact and approximate integrands.
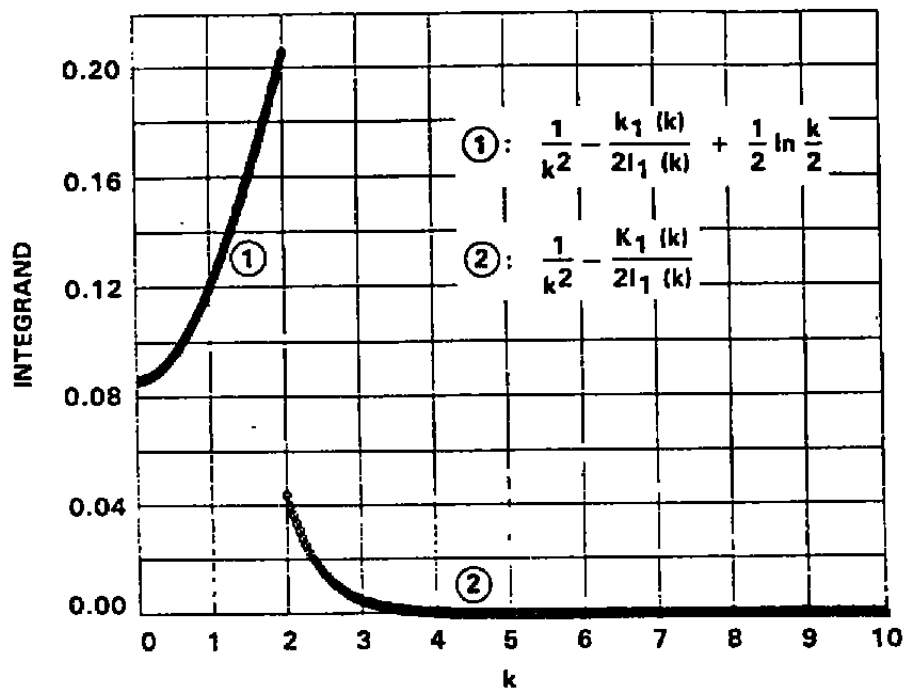
Fig. 24. Integrands used in evaluation of a_0.
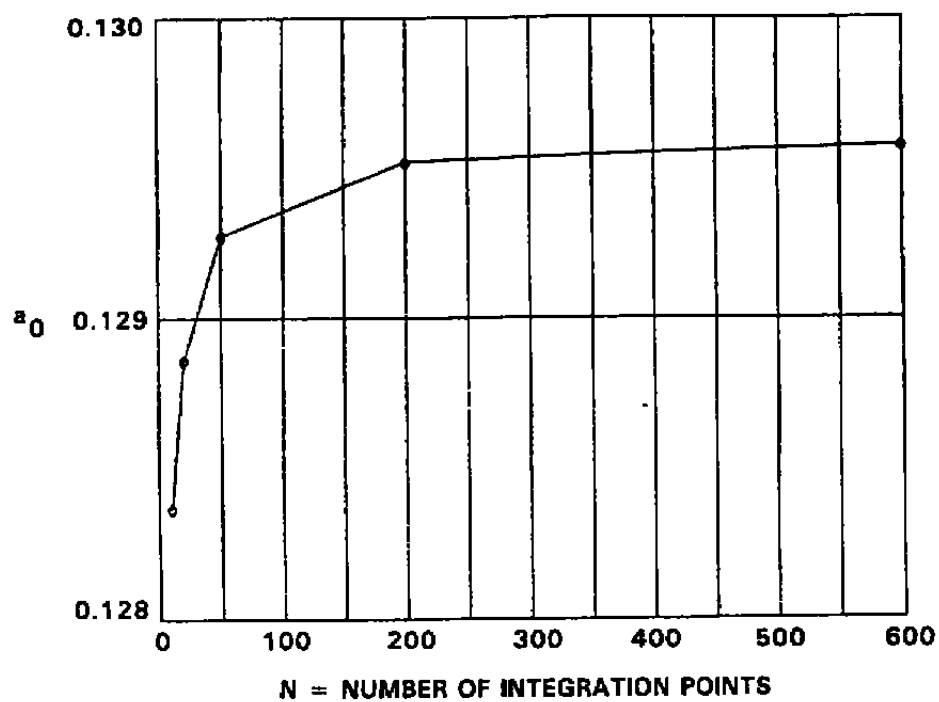
Fig. 25. Convergence study of a_0 integration.

perturbation velocity $[v_1]$. The actual relationship of the points is shown in Figs. 27a–27c which indicate a bubble over a parabolic arc body at Mach .99. The main idea is that depending on whether range 1 and 2 is encountered, an upward/downward one sided difference combination or the reverse is used for obtaining $[v_1]$. A tridiagonal system for the jump in the wall interference potential will be obtained in this scheme rather than the bidiagonal system associated with the shock notch method. However, this slight disadvantage could be outweighed by the potential for improved accuracy.

2.14 Incompressible Validation of Interference Module RELAXV1

The large height interference (variational equation solver (RELAXV1)) code was tested to establish whether it could provide answers in agreement with the analytical ones given in Ref. 37 for incompressible interference pressures. As an illustration, the flow over a confined parabola of revolution was considered. Here, the confining walls are solid and cylindrical. Figure 28 indicates the free field surface pressure distributions computed by an incompressible specialization of the finite height code. It is shown to indicate the stagnation (logarithmic singularities) resolved by the SLOR method in 300 iterations. Further study is needed regarding how the numerics treat the interactions of these singularities with the walls.

For this case, the RELAXV1 portion of the code comparison with analytical results from Ref. 37 is shown in Fig. 29 indicating perfect agreement.

Of great interest is the convergence of both the free field (RELAX1) and RELAXV1 parts of the code. During checkout, considerable study of factors influencing this performance aspect was made. Figure 30 illustrates one such investigation which shows the convergence of the algorithm with number of iterations for free field pressures at different points along the parabolic body of revolution in incompressible flow. It is evident that at this speed condition, adequate convergence is achieved in about 500 iterations. A lesser number of iterations may be needed if a "smarter" than zero initialization is used.

2.15 Transonic Application of Free Field (0th Order) Code

The numerical formulation indicated in previous sections has been applied to obtain an understanding of wall effects on slender bodies. Results will be discussed for a flow over a parabolic arc body of revolution as an illustration of the behavior of the wall interference $\hat{\phi}$ field.

For the calculations to be discussed, a uniform x–grid over the body (in the interval $0 \leq x \leq 1$) and an exponentially stretched version off of it was employed. Exponential stretching was also used in the $\bar{r}$ direction. These variable grids are shown in Fig. 31.

Before discussion of the interference field, the structure of the free field base solution will be indicated. Figure 32 shows that the numerical solution tracks the analytic behavior ϕ_0, reasonably well. Considering that the mesh for this case had a large aspect ratio near $j = 2$, improvements could be obtained by configuring the grid to make the aspect ratio approach unity.
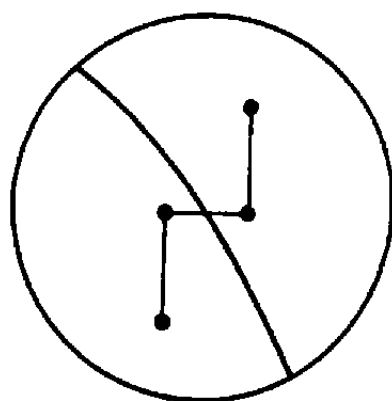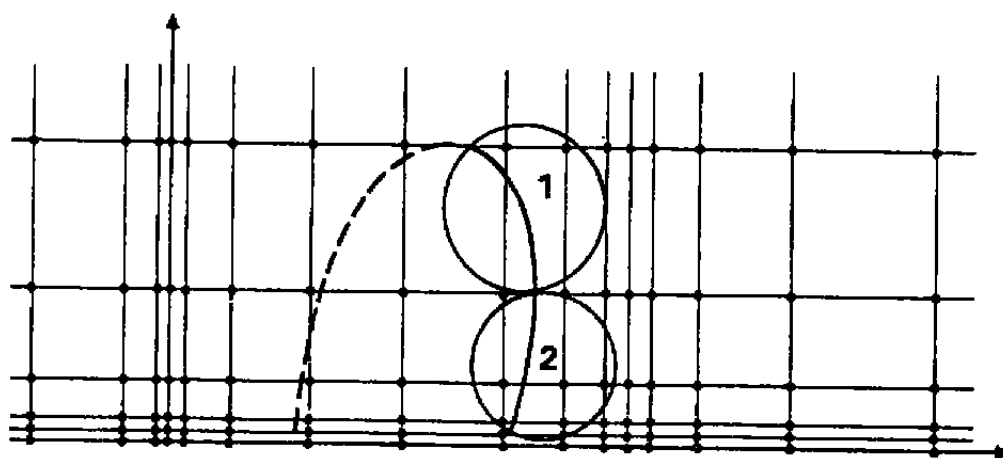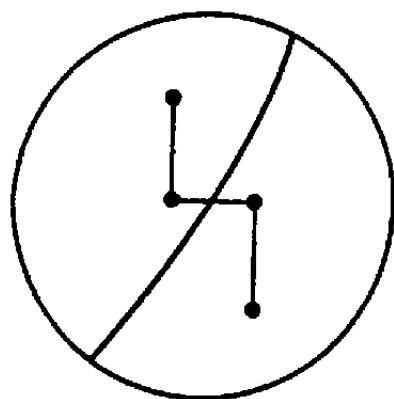
Fig. 26. Scheme for handling jumps in vertical velocities across shocks.
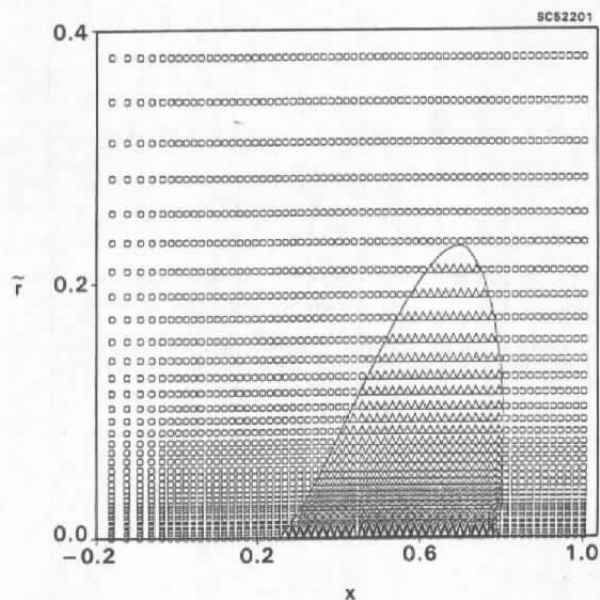
Fig. 27a. Sonic bubble over a parabolic arc body at $M_\infty = .99$, (Δ supersonic points, $\odot$ subsonic points).
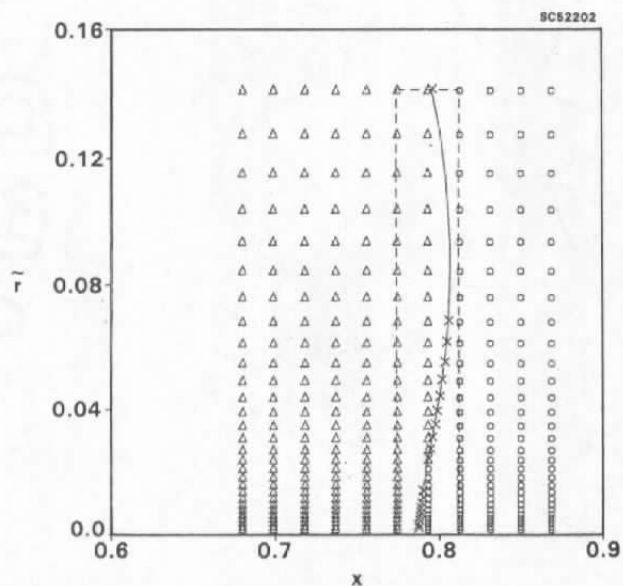
Fig. 27b. Closeup of shock notch for configuration of Fig. 27a, (x signifies points for which $|M_\odot - M_\Delta| \geq .01$).
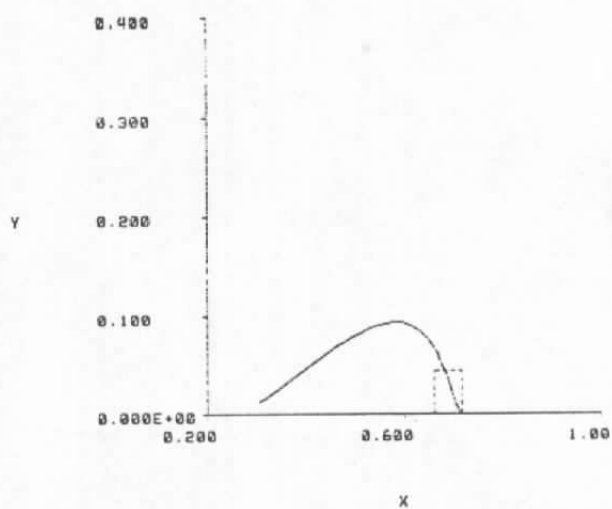
Fig. 27c. Typical overview of notch in relation to sonic line, $M_\infty = .99$, NU = 0, ND = 2, JDEL = 0, NSPMAX = 66, NSPMIN = 59, JSMAX = 19.
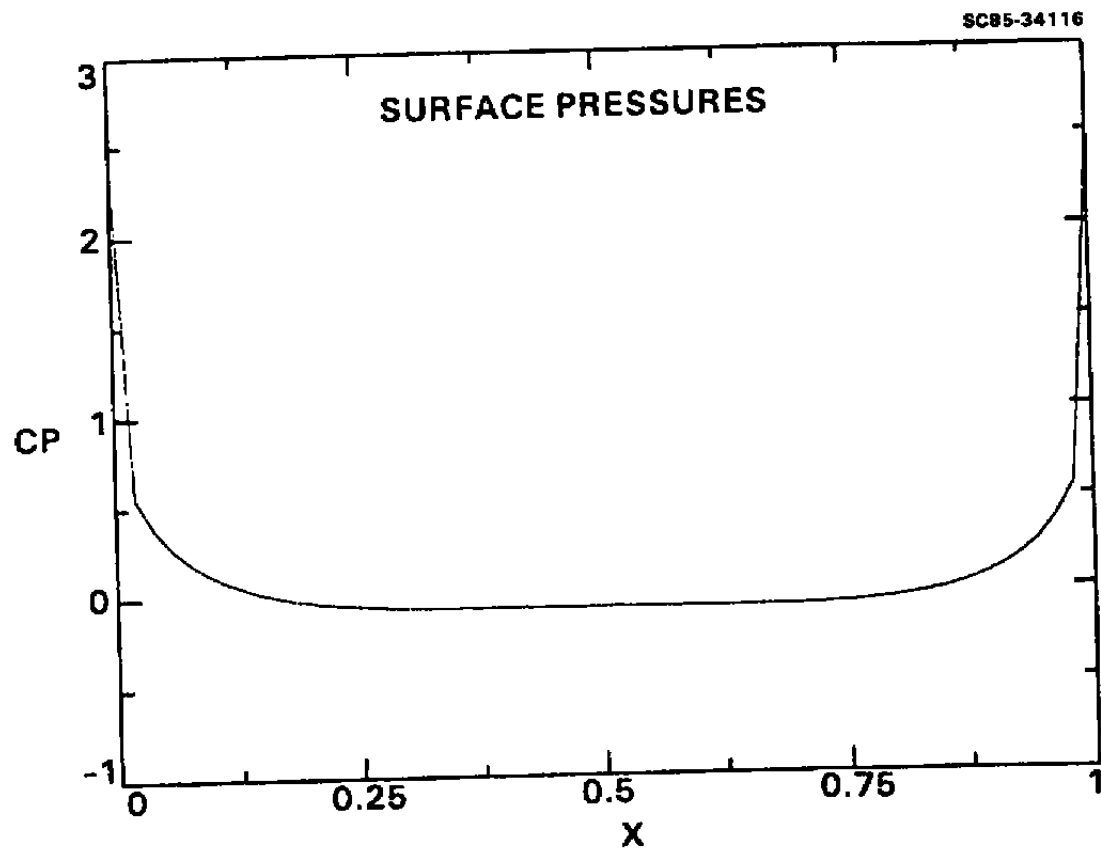
Fig. 28. Logarithmic singularities associated with parabola of revolution.

SC85-34119
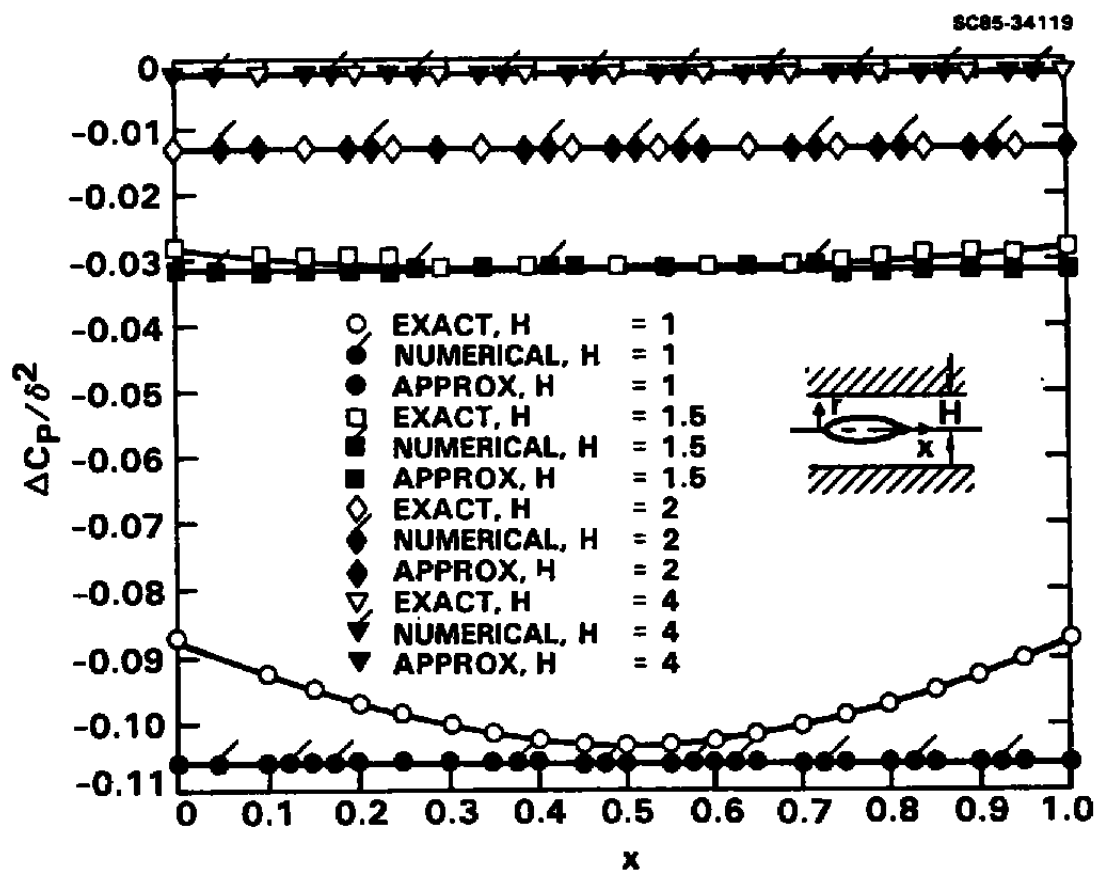
Fig. 29. Comparison of analytical (approximate) and transonic variational code compu-
tation of interference pressures in subsonic flow.
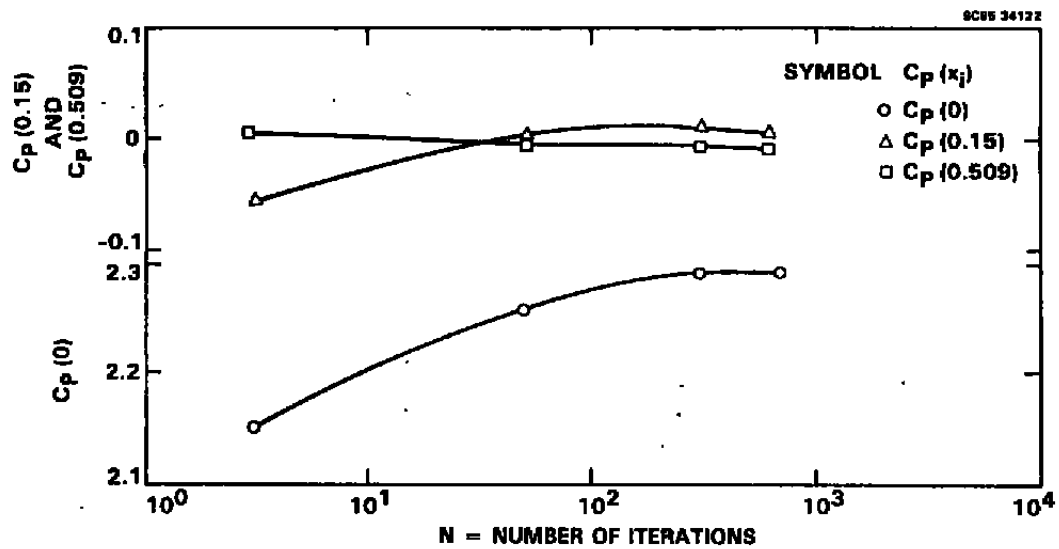
Fig. 30. Convergence study of incompressible free field solution, $\delta = .178$.
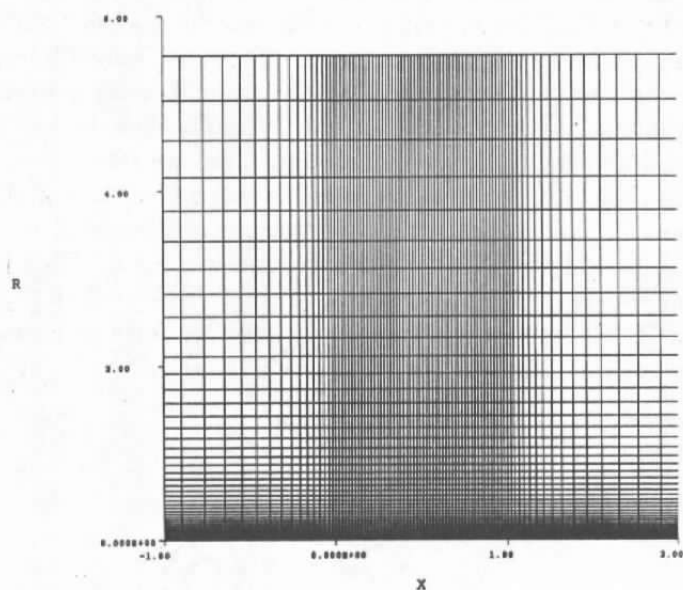
Fig. 31. Grid used in solution.

SC38845

SOLID: STINT 17
DASH: INNER SOLN

STINT 17, XGRID (35), PARABOLIC ARC BODY
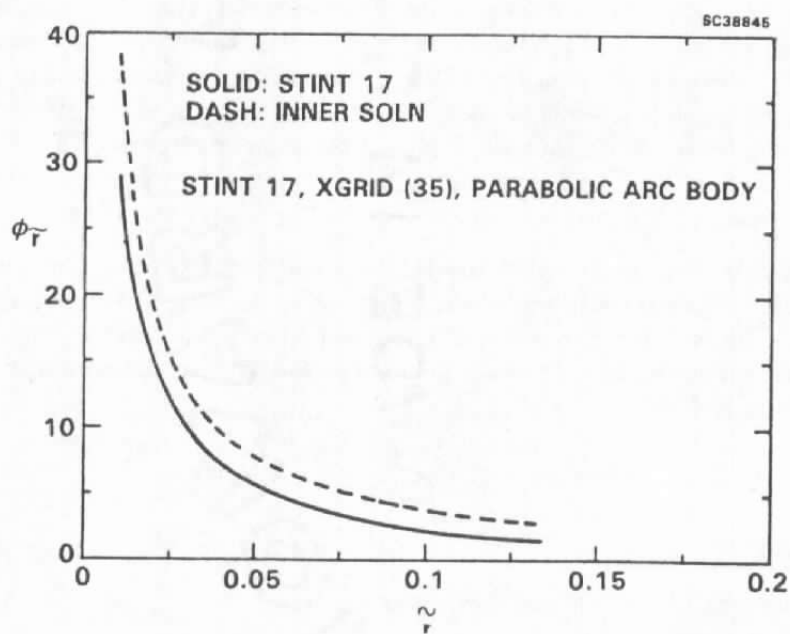
Fig. 32. $\phi_{0_{\tilde{r}}}$ behavior near the body.

67

As an illustration of the use of the code for high subsonic Mach numbers, Fig. 33 shows the streamwise distribution of local Mach number at a freestream Mach number $M_\infty = .99$ over a fore and aft symmetric parabolic arc of revolution of thickness ratio $\delta \sim 0.1$. In the interval $0 \leq x \leq 1$, the highest curve corresponds to $j = 2$ and subsequent lower curves are associated with upward j increments of 4. The dashed line denotes the position of the sonic line and shock. The far field computational boundary for the free field was at $\bar{r} \sim 5.5$ in these calculations. It is clear from these results that the sonic line height is approximately $\bar{r} \sim 0.2$. Further results consistent with these are shown as the isoMachs in Fig. 34. A good, sharp shock formation is indicated in this figure. In Fig. 35, the shock layer structure is indicated. This is of relevance to the use of the shock notch method. From these level lines, it is evident that the shock is almost normal. This is confirmed from the v_0 distributions shown in Figs. 36 and 37, where it is clear that $[v_0] \sim 0$. This leads to simplification of Eq. (2−40b) which is the perturbation form of Prandtl's normal shock relations, i.e.,

$$\langle u_0 \rangle = \frac{K}{\gamma + 1} \equiv u_0^* \qquad (2-86a)$$

$$[\phi_1] = \frac{[u_0]\langle u_1 \rangle}{\langle u_{0_x} \rangle} \qquad (2-86b)$$

where u_0^* is the critical value of the perturbation velocity u_0. As a check, Eqs. (2 − 86) were computationally implemented and the results were close to those obtained from Eqs. (2 − 79). Figures 38 and 39 indicate the u_0 distributions. Figure 39 shows indeed that Eq. (2 − 86a) is closely satisfied by the computational solutions. In related work, a hypothesis suggested by C.C. Wu concerning the invariance of the shock wave intersection with the body was analyzed in Ref. 38. Because of the structure of the near field, this hypothesis asserts that the intersection occurs at a zero of $S''(x)$. Numerical studies such as those discussed give partial but inconclusive evidence to support this assertion*. More detailed fine grid studies are required to resolve the issue.

To appreciate the rate of decay of the solution and the subsonic nature of the far field, Figs. 40 and 41 give three−dimensional reliefs of ϕ_0 and $\phi_{0_{xx}}$. For pointed bodies, the forcing term of the wall interference (variational equation) is proportional to the latter quantity. The subsonic structure of the far field is consistent with the assumptions of the formulation given in Ref. 29.

2.16 Further Remarks on Difference Schemes near Shock Notch

2.16.1 Bidiagonal Approach

In connection with (2 − 40a), and flow tangency, if

$$[v_0] = 0 \qquad (2-87)$$

---

* Some aspects that relate to this are discussed in the Appendix.
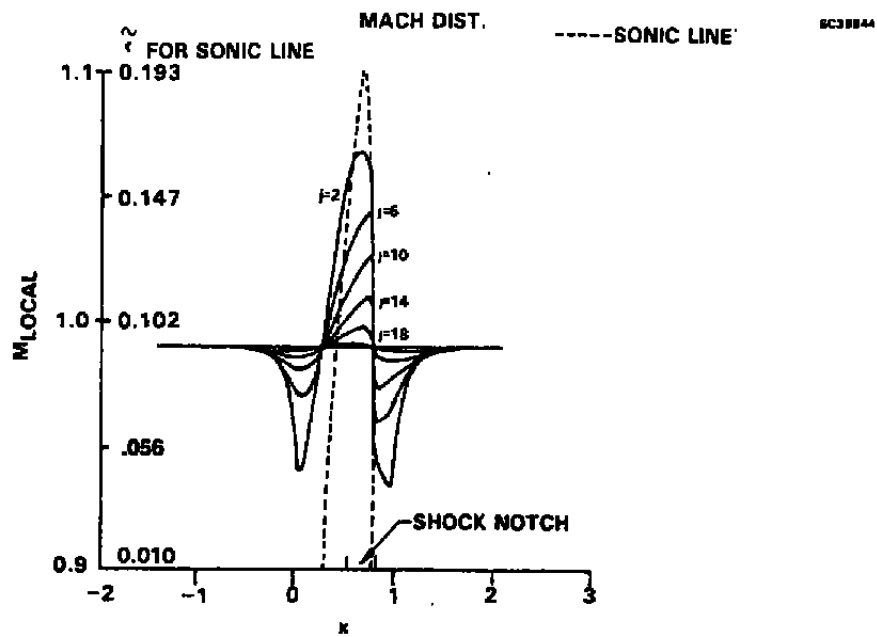
Fig. 33. Streamwise distribution, parabolic arc body, $M_\infty = 0.99$.
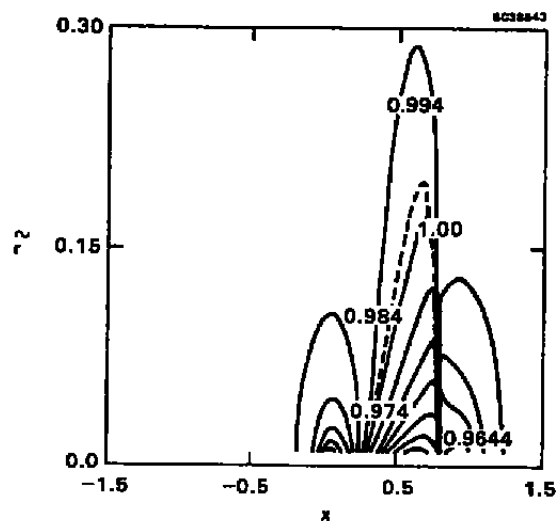
Fig. 34. Formation of shock.

69
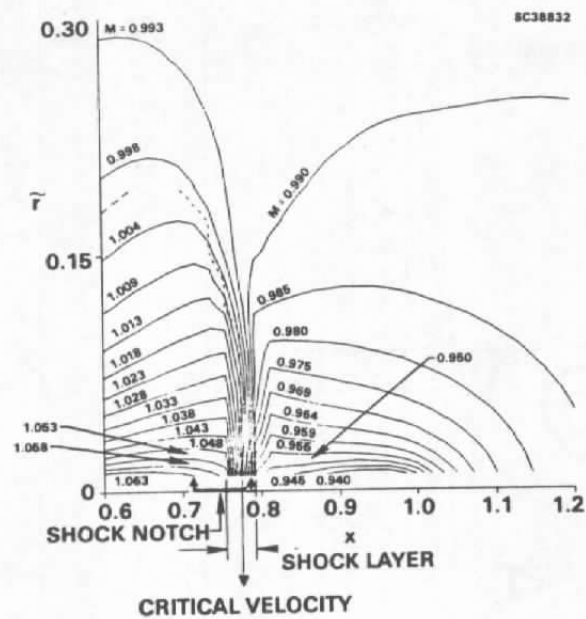
Fig. 35. IsoMachs showing closeup of shock.
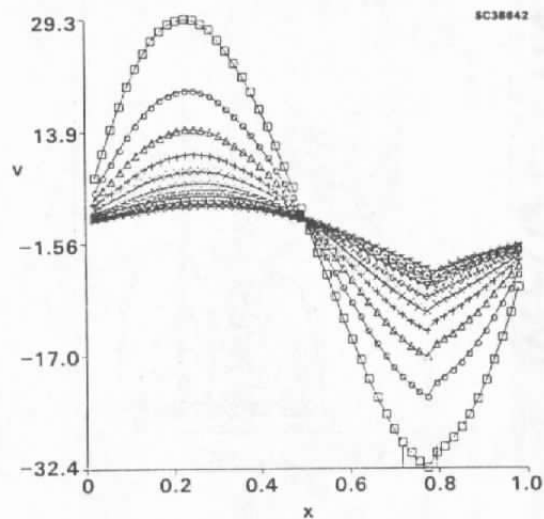
Fig. 36. Perturbation velocity v_0 over the parabolic body at $M_\infty = 0.99$.
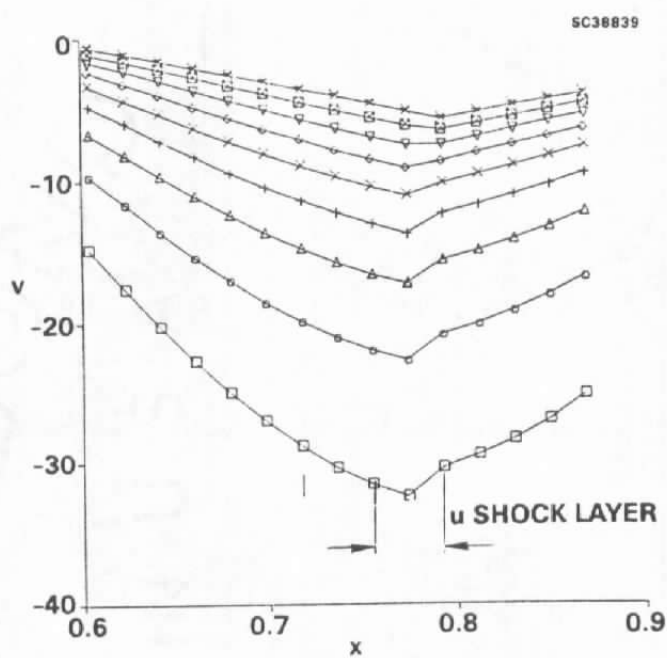
Fig. 37. Closeup of Fig. 36 v_0 distribution near shock.
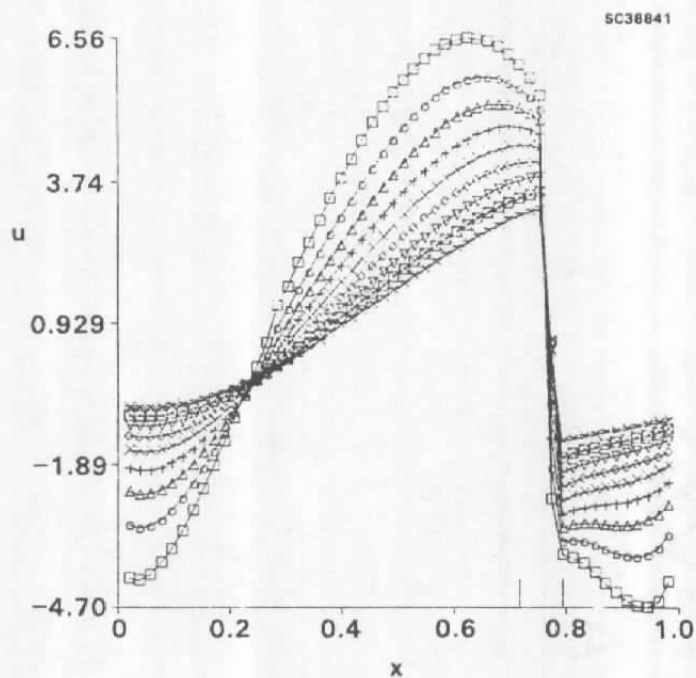
Fig. 38. u_0 distribution for $M_\infty = 0.99$ parabolic arc body.
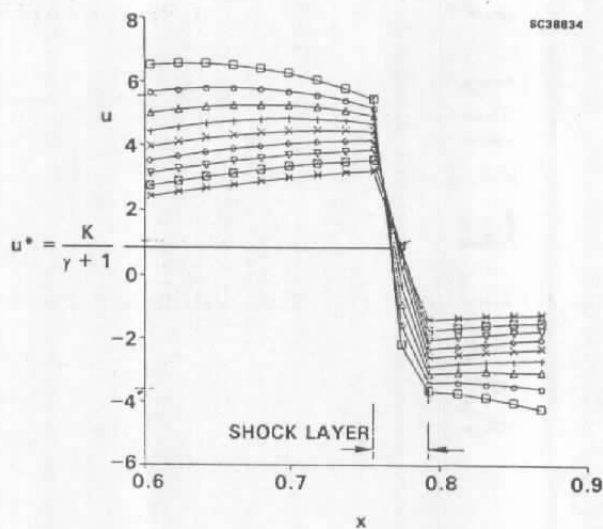
Fig. 39. Closeup of Fig. 34 u_0 distribution.

SC38835
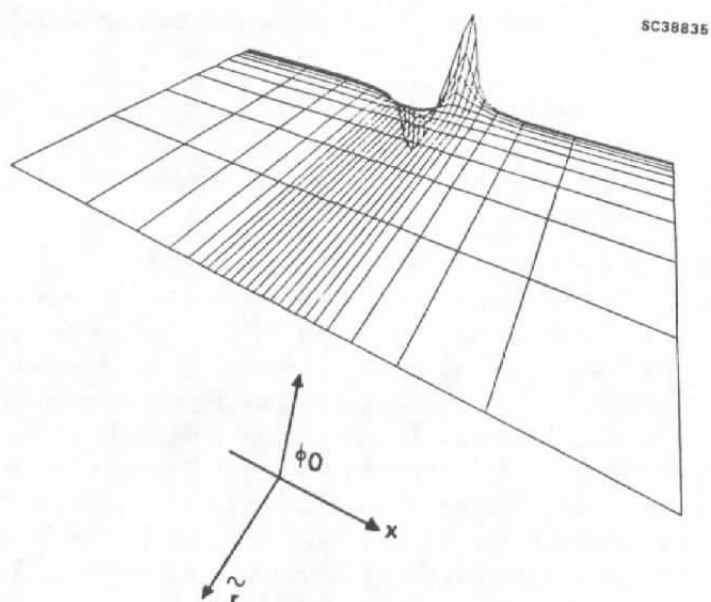
Fig. 40. Three–dimensional relief of ϕ_0 field for $M_\infty = 0.99$ parabolic arc body.

SC38836
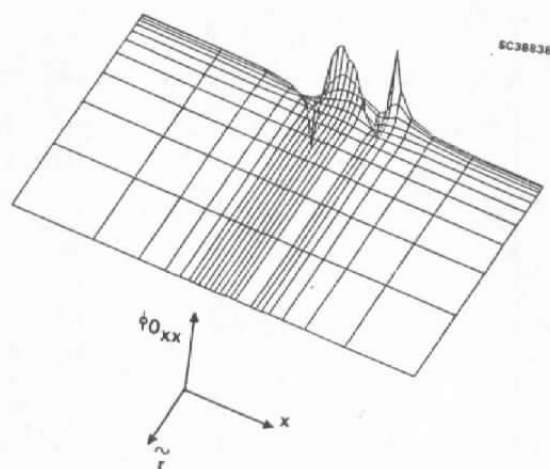
Fig. 41. Three–dimensional relief of $\phi_{0_{xx}}$ field for $M_\infty = 0.99$ parabolic arc body.

is assumed to hold beyond the weaker condition, then Prandtl's relation for normal shocks is obtained in which

$$\langle u_1 \rangle = \frac{[\phi_1] \langle u_{0_x} \rangle}{[u_0]} \quad , \tag{2-88}$$

where $\langle \quad \rangle$ signifies an average across the unperturbed shock. Equation $(2-88)$ can be used as a check on the numerical work.

In the bidiagonal scheme of treating $(2-76a)$ embodied in Eqs. $(2-79)$, one-sided differences were used to approximate the vertical perturbation velocities. This leads to the recursion relation in $(2-79a)$. It is clear that the solution of $(2-76a)$ proceeds forward from some initial condition associated with a specified j. Two options are available for this purpose. Employing the tangency boundary conditions at the body constitutes Method 1, and utilizing the top of the shock represents Method 2. Method 2 was first selected due to the seeming inability of originally assumed Neumann data at $j = 2$ to provide the needed Dirichlet data for the starting point. One problem with Method 2 is the possibility of inaccuracy in prescribing the location of the tip of the shock. Method 1 can be modified to employ $(2-88)$ instead of Neumann data at the node closest to $\tilde{r} = 0$, $j = 2$. This gives

$$[\hat{\phi}]_2 = \frac{\frac{[u_0]}{2} \left\{ \frac{\hat{\phi}_{D+1}^{(n-1)} - \hat{\phi}_u^{(n)}}{\Delta x_D} + \frac{\hat{\phi}_u^{(n)} - \hat{\phi}_{u-1}^{(n)}}{\Delta x_U} \right\}}{\frac{[u_0]}{2\Delta x_D} + \langle u_{0_x} \rangle} \quad . \tag{2-89}$$

A useful device in the implementation of the bidiagonal scheme $(2-79)$ and $(2-89)$ is the relaxation

$$[\hat{\phi}] = \omega [\hat{\phi}]^{(n)} + (1-\omega)[\hat{\phi}]^{(n-1)} \quad . \tag{2-90}$$

The quantity $[v_{0_x}]_2$ in $(2-89)$ is obtained from the zeroth order solution.

The stability of the recursion scheme based on $(2-79a)$, $(2-88)$, and $(2-89)$ has been investigated. A tool employed is an analytic solution which has been obtained by variation of parameters. Letting $X_j \equiv [\hat{\phi}_1]_j$, this is

$$X_j = \prod_{k=1}^{j-1} \left(\frac{-B_k}{D_k} \right) \left\{ X_1 + \sum_{k=1}^{j-1} \frac{-C_k}{B_k \prod_{\ell=1}^{k-1} \left(\frac{-B_\ell}{D_\ell} \right)} \right\} \quad , \tag{2-91}$$

where the products are unity when the upper limit index is unity. A necessary condition for stability therefore is

$$\left| \frac{B_k}{D_k} \right| < 1 \quad . \tag{2-92}$$

We have achieved global convergence with the bidiagonal scheme with marching away from the body using Method 1, providing that we use a stabilized converged free field solution and a fresh start for the interference flow.

2.16.2 Tridiagonal Methodology

The thrust of this approach is to use second order accurate central difference approximations for the vertical differences rather than the first order one–sided differences of the previously described bidiagonal method. Employing half node points, the vertical velocity v_1 is given by

$$
v_{1_j} = \phi_{1_{r_j}} = \frac{v_{1_{j+1/2}} + v_{1_{j-1/2}}}{2}
$$

$$
= \frac{\frac{\phi_{1_{j+1}} - \phi_{1_j}}{\tilde{r}_{j+1} - \tilde{r}_j} + \frac{\phi_{1_j} - \phi_{1_{j-1}}}{\tilde{r}_j - \tilde{r}_{j-1}}}{2} \quad . \tag{2 - 93}
$$

An additional benefit of this approach is consistency with the treatment of the interior nodes of the computational domain. Equation $(2 - 93)$ leads to

$$
2\left[v_1\right] = \frac{\left[\phi_1\right]_{j+1} - \left[\phi_1\right]_j}{\tilde{r}_{j+1} - \tilde{r}_j} + \frac{\left[\phi_1\right]_j - \left[\phi_1\right]_{j-1}}{\tilde{r}_j - \tilde{r}_{j-1}} \quad . \tag{2 - 94}
$$

On the basis of $(2 - 94)$ and $(2 - 76a)$, it follows that

$$
A_j\left[\hat{\phi}_1\right]_{j+1} + D_j\left[\hat{\phi}_1\right]_j + B_j\left[\hat{\phi}_1\right]_{j-1} = C_j \quad , \tag{2 - 95}
$$

where

$$
A_j = \frac{c_j}{2\Delta\tilde{r}_{j+1}} \tag{2 - 96a}
$$

$$
D_j = d_j - \frac{c_j}{2}\left(\frac{1}{\Delta\tilde{r}_{j+1}} + \frac{1}{\Delta\tilde{r}_j}\right) - \frac{1}{\Delta x_D}\left(a_j + \frac{b_j}{2}\right) \tag{2 - 96b}
$$

$$
B_j = -\frac{c_j}{2\Delta\tilde{R}_j} \tag{2 - 96c}
$$

$$
-C_j = a_j\left(\frac{\hat{\phi}_{D+1}^{(n-1)} - \hat{\phi}_U^n}{\Delta x_D} - \frac{\hat{\phi}_U^{(n)} - \hat{\phi}_U^n}{\Delta x_U}\right)
$$

$$
+ \frac{b_j}{2}\left(\frac{\hat{\phi}_{D+1}^{(n-1)} - \hat{\phi}_U^{(n)}}{\Delta x_D} + \frac{\hat{\phi}_U^{(n)} - \hat{\phi}_{U-1}^{(n)}}{\Delta x_U}\right) + C \quad . \tag{2 - 96d}
$$

By $(2 - 89)$

$$
A_2 = B_2 = 0 \tag{2 - 97a}
$$

$$
D_2 = 1 \tag{2 - 97b}
$$

$$
C_2 = \frac{\frac{\left[u_0\right]}{2}\left\{\frac{\phi_{D+1}^{(n-1)} - \phi_U^{(n)}}{\Delta x_D} + \frac{\phi_U^{(n)} - \phi_{U-1}^{(n)}}{\Delta x_U}\right\}}{\frac{\left[u_0\right]}{2\Delta x_D} + \langle u_{0_s}\rangle} \quad . \tag{2 - 97c}
$$

At the top of the shock notch j = JSMAX, $[\hat{\phi}_1] = [\hat{\phi}_1]_I$, where $[\hat{\phi}_1]_I$ is $\hat{\phi}_{\text{NSPMAX}} - \hat{\phi}_{\text{NSPMIN}}$ computing this difference as an interior point calculation. Then

$$D_{\text{JSMAX}} = 1 \qquad (2-98a)$$

$$C_{\text{JSMAX}} = [\hat{\phi}]_I \qquad (2-98b)$$

Equations $(2-95)$–$(2-98)$ constitute a tridiagonal system which can be solved by the same Thomas method employed for the interior nodes. The scheme has been computationally implemented and its performance relative to the bidiagonal approach is an open question.

2.17 Definitions of Interference–Free Conditions in Wind Tunnels from Asymptotic Slender Body Code

Rewriting $(2-24a)$ slightly, the variational equation for the interference perturbation potential ϕ_1 is

$$M[\phi_1] = (K_0 - (\gamma+1)\phi_{0_x})\phi_{1_{xx}} - (\gamma+1)\phi_{1_x}\phi_{0_{xx}} + \frac{1}{\tilde{r}}(r\phi_{1_{\tilde{r}}})_{\tilde{r}} = -K_1 F(x,\tilde{r}) \qquad (2-99)$$

with the boundary conditions

$$\phi_{1_{\tilde{r}}}(x,0) = 0 \qquad (2-100a)$$

$$\phi_1 \simeq b_0' R^2 P_2(\cos\omega) + 8\pi b_0 B_0 R \cos\omega + \cdots \qquad (2-100b)$$

as $R \to \infty$, and the shock relations, where $F = \phi_{0_{xx}}$, R and ω are spherical coordinates, the constants b_0', b_0 have been defined previously and $P_2(\cos\omega)$ denotes a Legendre Polynomial. In shorthand notation, Eqs. $(2-99)$ and $(2-100)$ can be represented as the problem P, in which

$\underline{P}$:

$$M[\phi_1] = -K_1 F \qquad (2-99')$$

$$B[\phi_1] = G(x) \quad , \qquad (2-100')$$

where B is the boundary condition on the union of all boundaries including the free field shock traces. With the decomposition

$$\phi_1 = \phi_h + \phi_p \quad ,$$

the problems for ϕ_h and ϕ_p can be represented as

$\underline{P_h}$:

$$M[\phi_h] = 0$$

$$B[\phi_h] = G(x)$$

$\underline{P_p}$:

$$M[\phi_p] = K_1 F$$
$$B[\phi_p] = 0 \quad .$$

Since M is a linear operator, $\phi_p = K_1 \Psi$, where Ψ is the solution of P_p with $K_1 = 1$. Thus,

$$\phi_1 = \phi_h + K_1 \Psi \quad .$$

If

$$g_1(x; K) = \phi_1(x, 0) \quad ,$$

then

$$g_1 = g_{1_h} + K_1 \Psi_1(x, 0) \quad ,$$

so that for a specific shape, since the normalized interference drag $\Delta \widetilde{C_D} = \frac{\Delta D H^2}{2q\delta^4} = \int_0^1 g_1' S' dx$,

$$\frac{\Delta \widetilde{C_D} - \Delta \widetilde{C_D}^{(K_1=0)}(K_0, A)}{K_1} = \overline{f}(K_0, A) \equiv \int_0^1 S'(x) \Psi_{1_x}(x, 0) dx \quad ,$$

where $A = \alpha/\delta$ in the notation of Ref. 29 is the angle of attack parameter, and S is the normalized cross sectional area.

With the universal relation above, the curves of $\Delta \widetilde{C_D}$ versus K_1 are linear, as schematically depicted in Fig. 42a, and can be determined once and for all for arbitrary K_1 from the solution of the Problem P_p for $K_1 = 1$ for a given K_0 and A.

Because of the linearity with K_1 as indicated in the previous relations, the value of $K_1 = K_1^*$ leading to an interference-free drag measurement can be determined explicitly from the universal relation as

$$K_1^* = -\frac{\widetilde{\Delta C_D}^{(K_1=0)}(K_0, A)}{\overline{f}(K_0, A)} \quad . \tag{2-101}$$

Plots of K_1^* are shown schematically in Fig. 42b. Here, K_1^* represents the necessary perturbation of the tunnel similarity parameter to simulate conditions leading to zero interference drag.

2.18 Determination of Interference-Free Flows

In the preceding sections a formulation of the slender body wall interference problem in which the tunnel similarity parameter is allowed to vary to achieve minimum to interference-free flow is formulated. During the contractual effort, a computational solution has been obtained representing a proof of the feasibility of this concept and also validating the mathematical demonstrations of linearity of the interference drag ΔC_D and
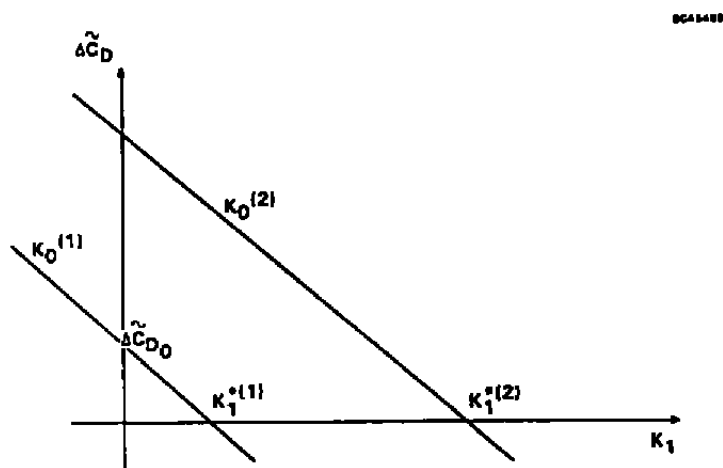
Fig. 42a. Schematic of $\Delta \widetilde{C}_D$ versus K_1.
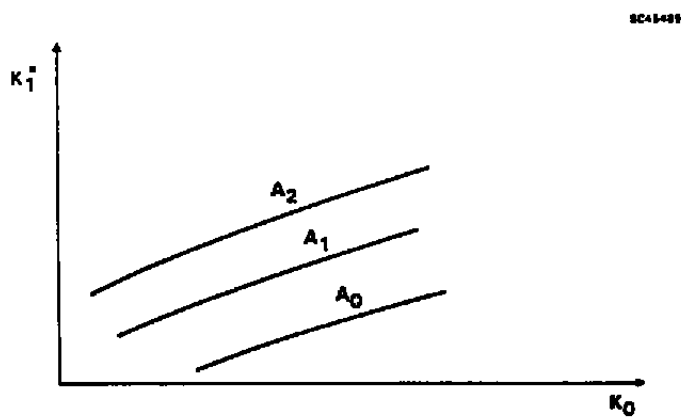
Fig. 42b. Schematic of variation of interference-free K_1^* with K_0.

the tunnel similarity parameter K_1 given in Section 2.17. Figure 43 represents the result of actual calculations corroborating the analysis of the previous section for the $M_\infty = .99$ flow over a parabolic arc of revolution body of thickness ratio $= .1$. The calculations and figure demonstrate that interference–free drag conditions can be achieved in this case at a tunnel similarity parameter value $K_1 = 0.14166$. Additional studies concerning surface pressure distributions can be performed in which K_1 can be optimized to achieve a minimum, for example, in at least a mean square sense, of the interference pressure. To our knowledge, these are the first results of this type to be obtained.

As an approximation of the numerical approach based on the bidiagonal and tridiagonal shock jump conditions, a simplified scheme has been investigated. It is based on the approximation that for slightly subsonic free stream Mach numbers the shock is normal to the flow along its length. This leads to the zeroth order Prandtl relations

$$\langle u_0 \rangle \equiv \frac{1}{2}\left(u_0\left(g_{0-},\hat{r}\right) + u_0\left(g_{0+},\hat{r}\right)\right) = \frac{K}{\gamma+1} \qquad (2-102)$$

and Eq. $(2-87)$.

For a transition occurring over zero mesh points, the geometric interpretation of $(2-87)$ is shown in Fig. 44.

2.19 Numerical Implementation

In accord with the previous formulation, a reduced interference perturbation potential $\hat{\phi}_1$ is defined in which the far field is subtracted off. With the notation given herein and assuming a closed body, this gives

$$\phi_1 = \hat{\phi} + Cx \qquad (2-103a)$$

$$C \equiv \frac{8\pi b_0 B_0}{\sqrt{K}} = \frac{1.594 B_0}{\sqrt{K}} \qquad (2-103b)$$

$$u_1 = \hat{u} + C \quad ,$$

where $b_0 = .063409$ from numerical evaluation of the Bessel function integral (Sect. 2.1.2).

Denoting x grid points on the pre–shock side of the shock notch with s subscripts and those on the post–shock side by p, $(2-103)$ can be used to obtain a discretized form of $(2-87)$ which is

$$\frac{1}{2}\left\{ \frac{\hat{\phi}_{p+1} - \hat{\phi}_p}{x_{p+1} - x_p} + \frac{\hat{\phi}_s - \hat{\phi}_{s-1}}{x_s - x_{s-1}} \right\} + C = \frac{\left[\hat{\phi}\right]}{[u_0]}\langle u_{0_s}\rangle = -g_1(u_{0_s}) \quad , \qquad (2-104)$$

using $(2-41b)$. The sum in the braces in $(2-104)$ can be simplified using the definition of $\left[\hat{\phi}\right]$ which leads to

$$\left[\hat{\phi}\right] = \frac{\frac{\hat{\phi}_{p+1} - \hat{\phi}_s}{x_{p+1} - x_p} + \frac{\hat{\phi}_s - \hat{\phi}_{s-1}}{x_s - x_{s-1}} + 2C}{\frac{1}{x_{p+1} - x_p} + 2\frac{\langle u_{0_s}\rangle}{[u_0]}} \quad . \qquad (2-105)$$
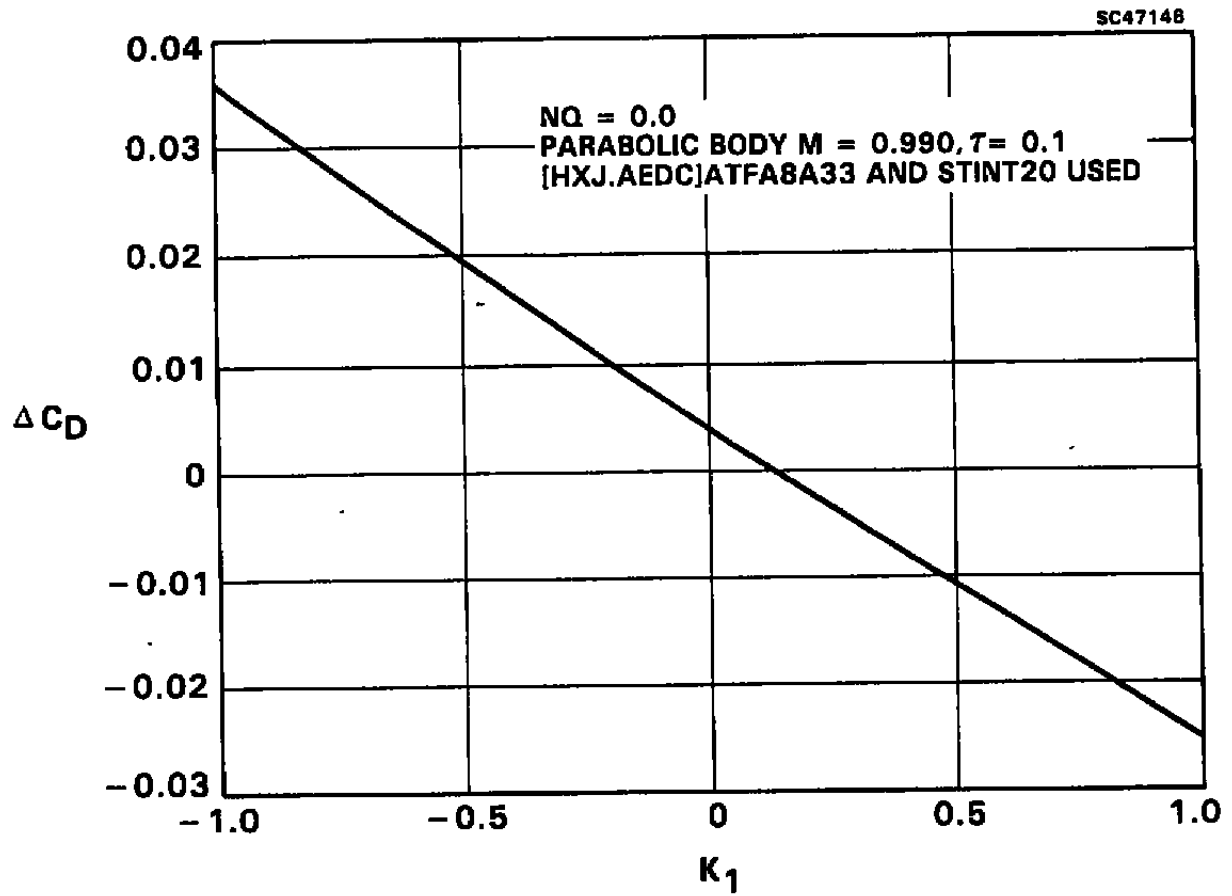
Fig. 43. Interference drag versus interference similarity parameter.

SC46717

$$S_0^-$$

$$\alpha_-$$

$$\epsilon g_1 u_{0_x}\big|_{g_{0-}}$$

$$S^-$$

$$u_- = u_{S_0-} + \epsilon g_1 u_{0_x}\big|_{g_0-}$$

$$u_0(x, g_0-) + \epsilon u_1(x, g_0-)$$

—— SHOCK TO 0th ORDER

– – – SHOCK TO 1st ORDER

—·—·— UPSTREAM NOTCH
          BOUNDARY

—··—··— CRITICAL LINE

$$\epsilon g_1$$

$$u_0(x, g_0-)$$

$$\alpha_- = \tan^{-1} u_{0_x}\big|_{g_0-}$$

$$u_{cr} = \frac{K}{\gamma + 1}$$

$$u$$

$$x$$

$$\alpha_+ = \tan^{-1} u_{0_x}\big|_{g_0-}$$

$$u_0(x, g_0+)$$

$$S_0^+$$

$$\alpha_+$$

$$u_0(x, g_0+) + \epsilon u_1(x, g_0+)$$

$$\epsilon g_1 u_{0_x}\big|_{g_0+}$$

$$S^+$$

$$u_+ = u_{S_0+} + \epsilon g_1 u_{0_x}\big|_{g_0+}$$
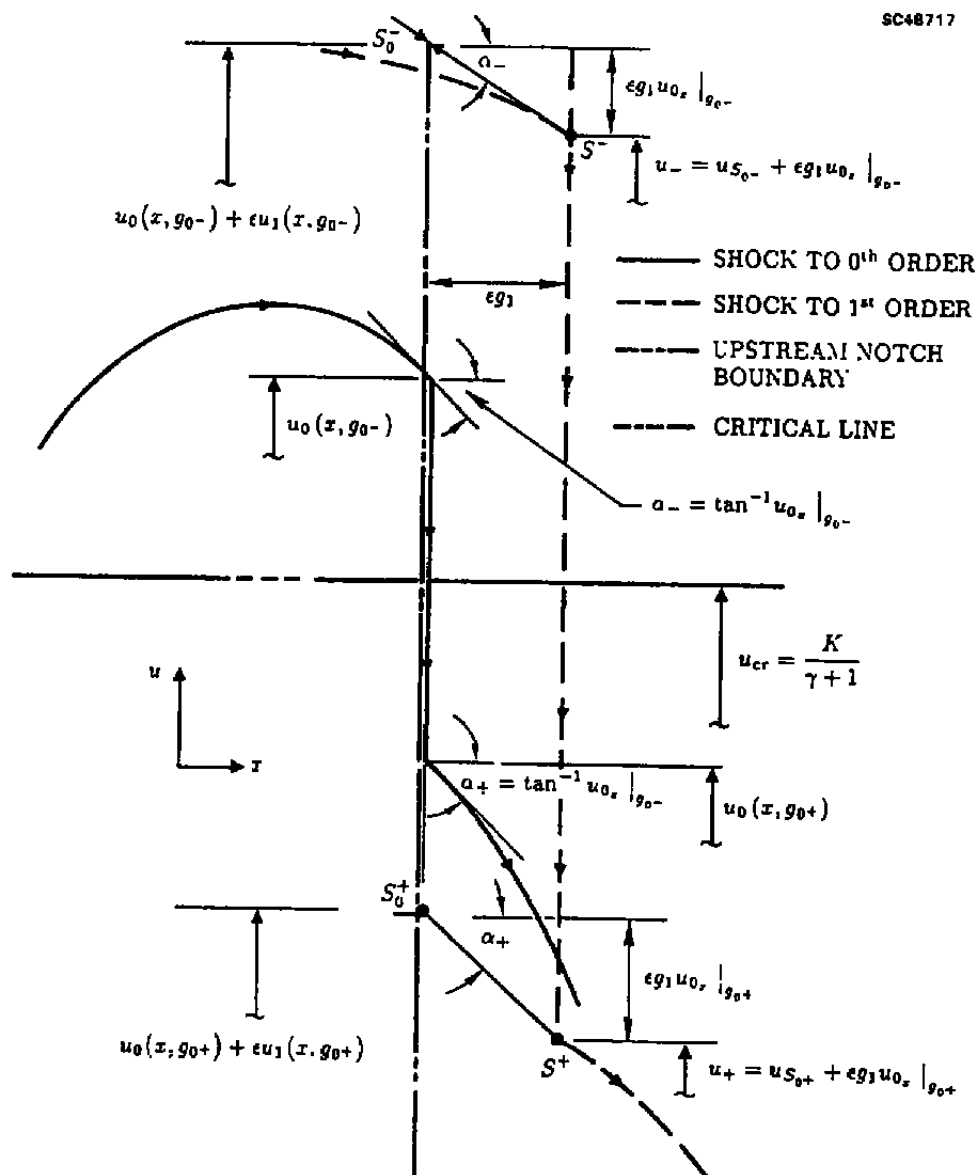
Fig. 44. Shock jump geometry.

Equation $(2-105)$ represents an explicit relationship in which points on the downstream side of the notch can be updated in each relaxation sweep of the code. If the shock slope is non–vanishing, $\left[\hat{\phi}\right]$ is known only implicitly in the tridiagonal scheme of Section 2.16.2.

2.20 Results

The results to be described were computed using the bidiagonal scheme formulated in Section 2.16.1. Others were obtained with the homogeneous Prandtl relation using the approach outlined in the last section. These will not be shown here and give similar relative trends but discrepancies in the actual levels. Because the bidiagonal method contains the effect of the shock shift as well as the variation of the interference vertical velocity v_1 along the shock, it is more accurate than the homogeneous Prandtl method.

In the actual running of the solvers for the 0th order free field basic flow and the 1st order interference component, convergence of both elements were monitored by studies of the maximum error ERRMAX over the computational domain. This error is defined as the difference between the value of the perturbation potential at the current and previous relaxation sweep. Figure 45a shows the behavior of this error as a function of iteration number for the 0th order solution. The iteration number is a counter for the relaxation sweeps across the flow. Although the error decrease is rapid, a more reliable method of establishing the convergence of the solution is the drag level. This is shown in Fig. 45b. A pseudo–time asymptotic for the latter signifies stabilization of the shock location and other flow features. Convergence to the drag for the 0th order solution usually followed the monotonic pattern indicated with a zero initial iterate. The values of the relaxation and other parameters for such behavior will be discussed in the user's manuals. Convergence of the 0th order solver RELAX1 takes about 3000 iterations for the higher subsonic Mach numbers such as the .99 value of Fig. 45b. Approximately 1000 or less iterations are required for supersonic or lower subsonic Mach numbers. Figures 46a and 46b demonstrate the convergence of the interference (variational) solver RELAXV1. In marked contrast to RELAX1, RELAXV1 is at least ten times faster. Both solvers have restart capability and this can accelerate convergence from the performance indicated. One run strategy is to march in Mach number space using solutions for a lower Mach number to initialize the solution at a higher Mach number.

Both RELAX1 and RELAXV1 are scalar and unoptimized in keeping with their research status. Further increases of performance can be achieved by vectorization and other optimizing techniques, which we anticipate will lead to seconds of run–time on CRAY machines. The order of magnitude speed increase of the 1st order interference flow code from the 0th order solver is associated with the frozen coefficients in the difference operators during the sweeps. This is related to the linearization upon the basic flow embodied in the description of the perturbation interference field.

As a baseline, Fig. 47 gives pressure distributions along a parabolic arc body of thickness ratio $\delta = .1$ for different Mach numbers related to the transonic similarity parameter $K = \left(1 - M_\infty^2\right)/\delta^2$. Although there appears to be some upstream movement of the shock as the Mach number is reduced from .99, this may be illusory due to the need
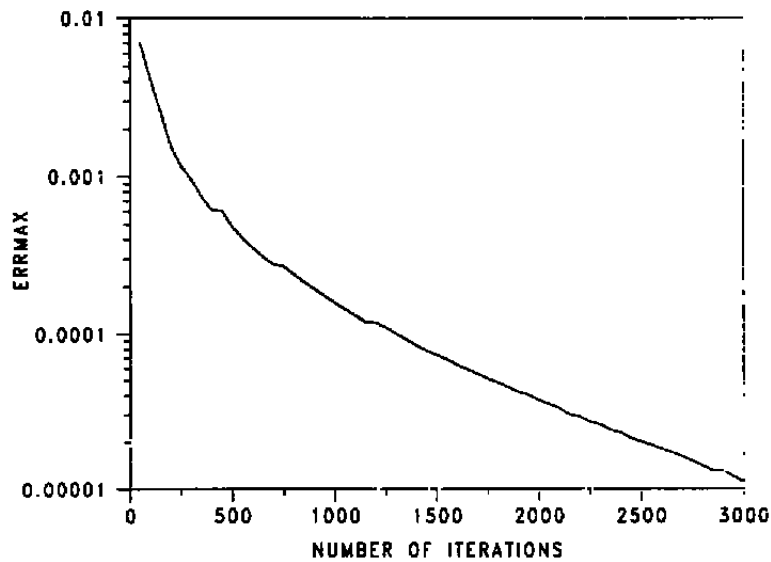
Fig. 45a. ERRMAX convergence history for 0th order flow parabolic arc body $\delta = .1$, $M_\infty = .99$.

PARABOLIC ARC BODY, $\delta = 1$, $M=.99$
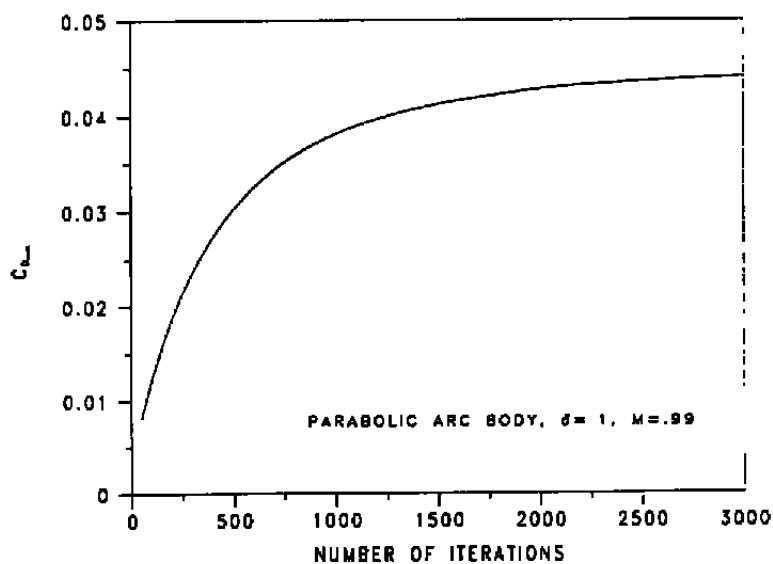
Fig. 45b. C_d convergence history for 0th order flow, parabolic arc body $\delta = .1$, $M_\infty = .99$.
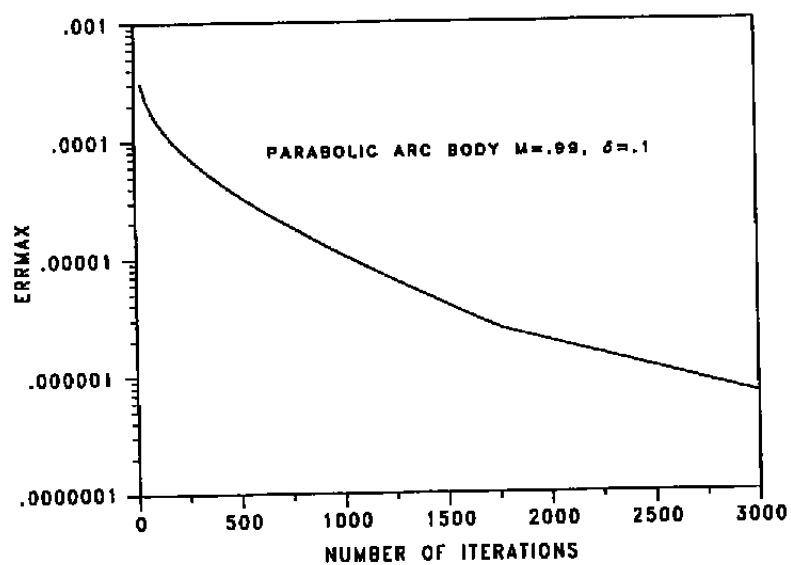
Fig. 46a. Variational solver convergence history, parabolic arc body, $M_\infty = .99$, $\delta = .1$.
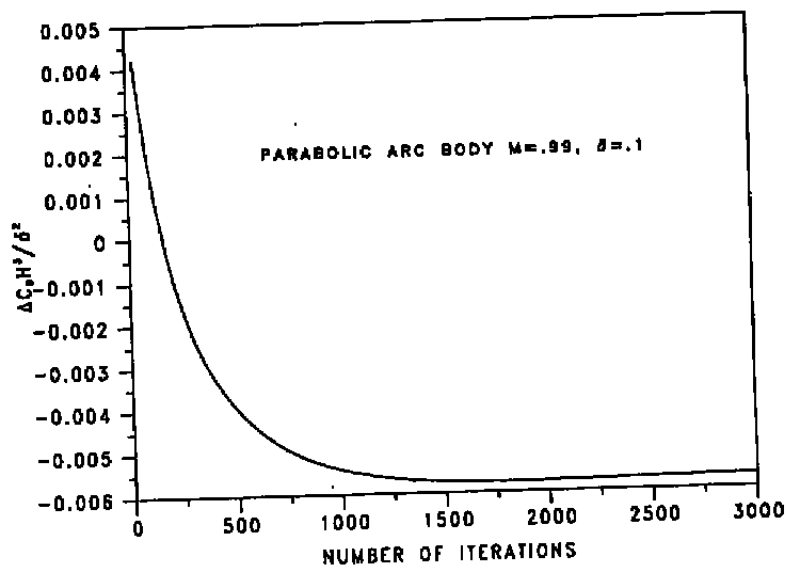
Fig. 46b. Variational solver convergence history, parabolic arc body $M_\infty = .99$, $\delta = .1$.

to numerically resolve the fine structure of the layer near the logarithmically singular line $\tilde{r} = 0$. A recent hypothesis proposed by C.C. Wu and analyzed in detail by J.D. Cole and N. Malmuth in Ref. 38 indicates that the foot of the shock occurs at the zero of $S''(x)$ at the rear of the body. This assertion is based on consistency arguments involving the inner expansion of transonic slender body theory, Prandtl's normal shock relations, and the flow tangency condition at the body. Fine grid solutions are required to investigate this assertion. In addition, there is probably a high x gradient deck near the shock impingement point which asymptotes to the logarithmic layer behavior upstream and downstream of itself*. On the other hand, there is another scenario in which the shock does not strike the body but makes an abrupt turn above it. Evidence to support the first contention is shown in Figs. 33–35 in which the location is very nearly at a downstream $S''(x) = 0$ point $= \frac{1}{2} + \frac{\sqrt{3}}{6} = .7887$ for the fore and aft symmetric parabolic arc body exemplified here. More detailed study is required on the formation of the envelope of the compressive waves reflected downstream from the sonic line, since focussing and the structure of the inner $\tilde{r} \to 0$ layer has a bearing on the use of an internal upright notch which encapsulates the shock transition in the calculation of the interference flow. Surface pressures for the latter are shown in Fig. 48. The anticipated increase in suction over the forebody is indicated and is associated with the constrictive effect of the walls giving an acceleration of the flow over the model. However, there is a sharp compressive spike near the shock. It is interesting to note that the upstream level is qualitatively and phenomenologically similar to that exhibited by the incompressible flow analyzed in Ref. 37, whose transform solution was used to validate the incompressible specialization of the 0th order solver RELAX1 in Fig. 29. This agrees with the qualitative features of the subsonic flow away from the sonic region. Clearly evident in that figure is the nearly constant level of the interference pressures associated with the doublet reflection of the solid walls. This appears as the far field singularity in the formulation of the problem. A rapid localized violent transition spike at the shock interrupts this serene behavior. It is anticipated that the intensity of this spike will be reduced by shock–boundary layer interactions in real flows.

For the case shown, the pressures have the proper antisymmetry about the dotted line in the figure which represents the appropriate average levels from the perturbation form of the Prandtl normal shock relations specialized at the foot of the shock. If the latter strikes the body, the boundary condition of tangent flow implies $[v_1] = 0$ implying that the line of intersection is along the normal to the body. This trend is similarly exhibited as shown in Figure 49 which gives an indication of the lumped normalized interference pressure dependence on Mach number through the similarity parameter K. In accord with expectations, the interference increases with increase in Mach number.

Returning to the $M_\infty = .99$ case, Fig. 50 shows in exaggerated form the tunnel pressure when the interference pressure is superimposed on the free field basic flow. Again, the antisymmetry about the critical pressure level shown as the dotted line is evident as a check on the computational implementation.

One issue that arose in the computations was the sensitivity of the convergence of

---

* See Appendix A regarding this issue.
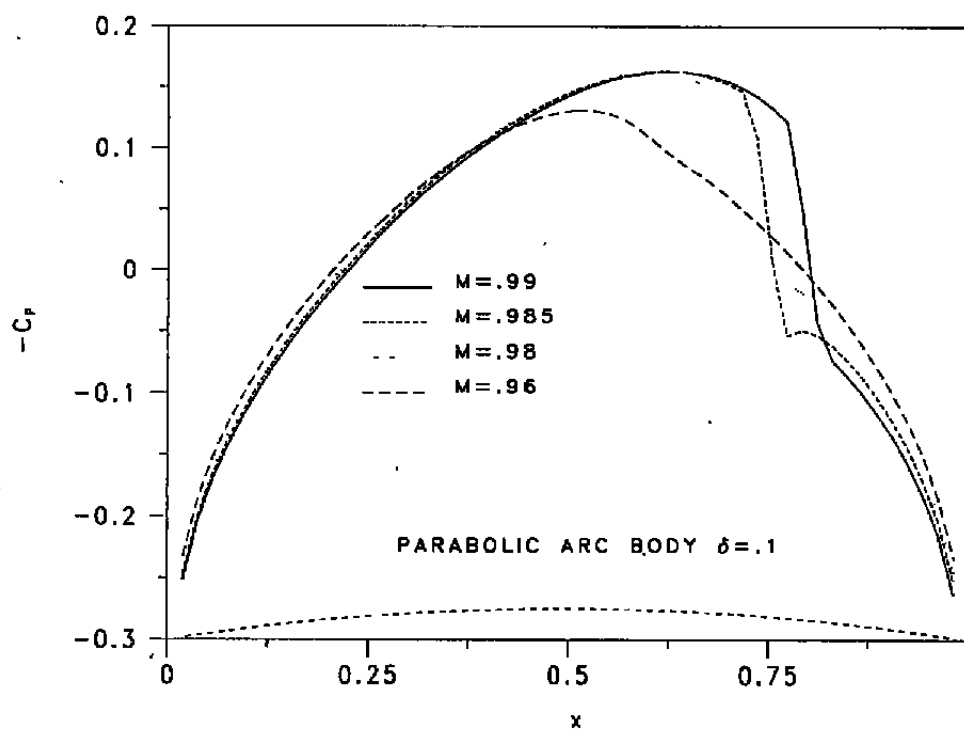
Fig. 47. Free field 0th order C_p for various Mach numbers, $\delta = .1$ parabolic arc body.
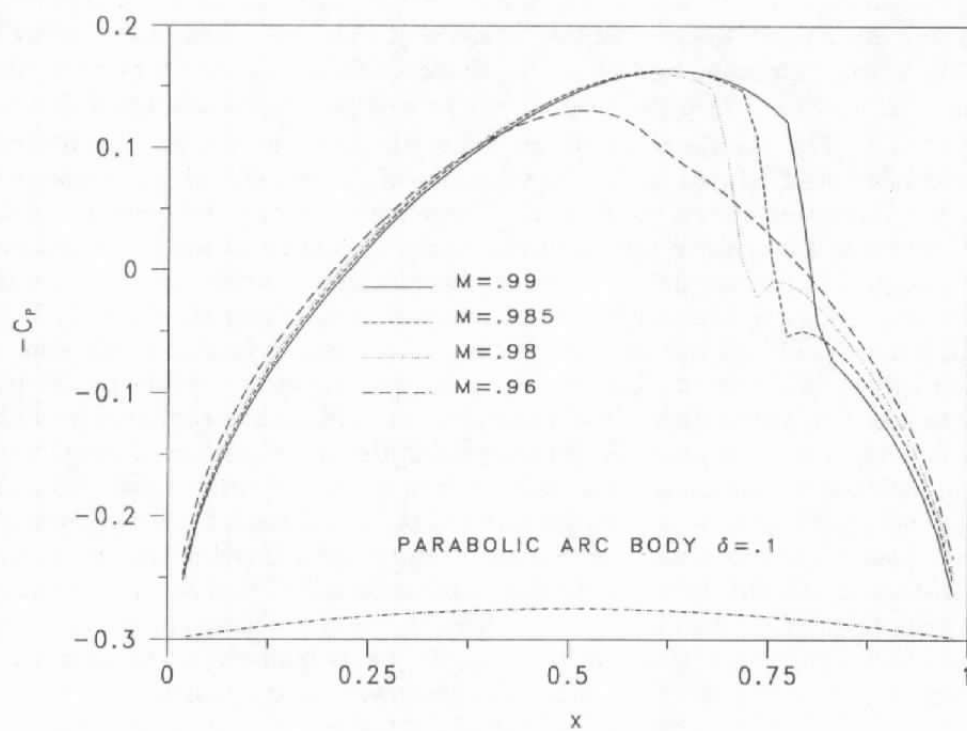
Fig. 47. Free field 0th order C_p for various Mach numbers, $\delta = .1$ parabolic arc body.
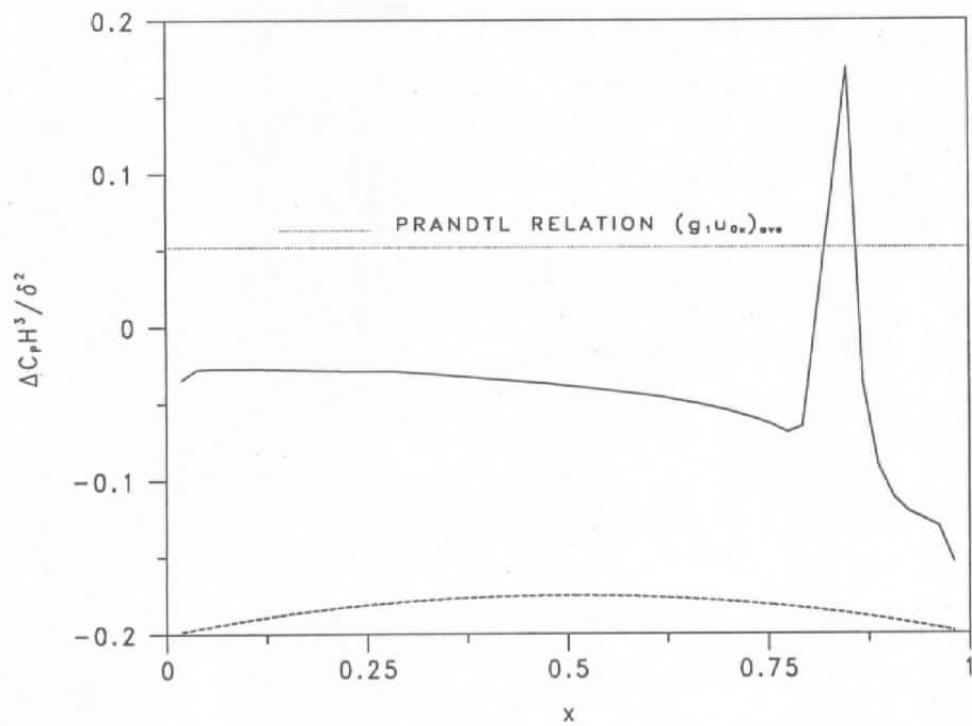
Fig. 48. Normalized interference C_p, $\Delta C_p \dot{H}^3/\delta^2$, parabolic arc body for $M_\infty = .99$, $\delta = .1$, ($K = 1.99$).
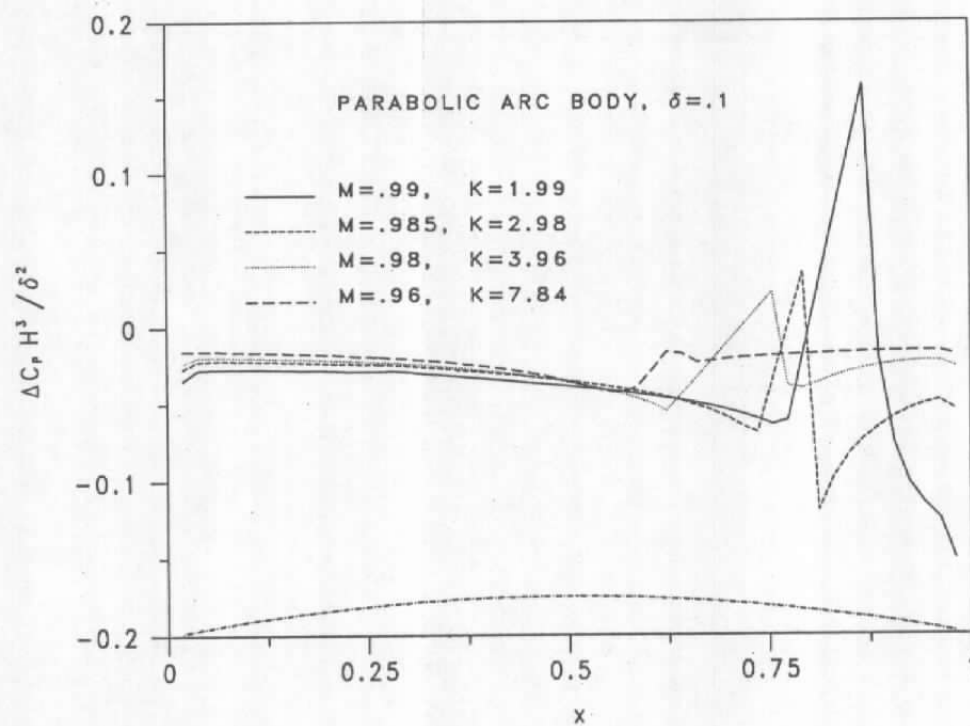
Fig. 49. K dependence of reduced interference pressures — bidiagonal scheme for shock jumps.
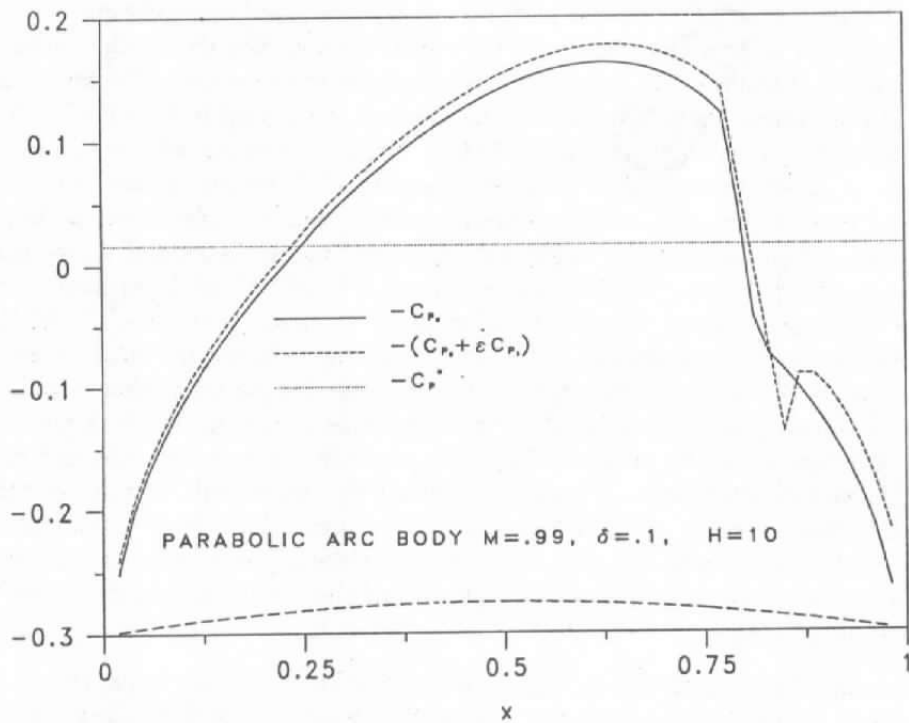
Fig. 50. Comparison of 0th order and total C_p unscaled $H = 10+$, parabolic body, STINT25, $M_\infty = .99$, $\delta = .1$, bidiagonal scheme, $K = 1.99$.

interference flow to notch dimensions. This was pronounced for the bidiagonal recursion scheme for computing $\left[\hat{\phi}\right]$ at the shock but much less evident in the tridiagonal approach described previously. For the calculations, the proper shock tip location and notch width had to be used. An approximation for the upstream and downstream legs of the notch was obtained by a detection scheme implemented in RELAX1 in which the most upstream and downstream location of the downstream part of the sonic line was determined. The shock tip was defined as the subset of this locus for which the pressure gradient exceeded a preassigned tolerance level. Some experimentation is required in adjusting the width of the notch. This was accomplished most efficiently through the use in the control file LOGPARM*.RMS of indices NU, ND, JDEL which represent incremental changes in the upstream and downstream notch vertical boundaries at the x grid indices NSPMIN and NSPMAX respectively and the $\bar{r}$ grid index JSMAX. Some adjustment of these parameters was necessary to prevent divergence. This inconvenience of the bidiagonal scheme over the tridiagonal method was tolerated because it was felt that divergence was a desirable sensitive indicator of an inappropriate encapsulation of the shock. In particular, too narrow a notch allowed artificial numerical fluctuations in the 0th order shock layer to destabilize the 1st order interference flow. Moreover, too large or too small a value of JSMAX was associated with an improper location of the shock tip. In fact, for the $M_\infty = .96$ case, no shock occurs in this supercritical flow and a truly isentropic transition is obtained. Logic in the code was developed to handle this degenerate situation. At the higher Mach numbers, once a base level was obtained for convergence through proper selection of NU, ND and JDEL, rather substantial parametric elasticity was exhibited. The broad band of this tuning is indicated in Fig. 51 which shows that the main features of the interference pressure distribution are retained with perturbations of these parameters. This tuning is more delicate at the lower M_∞ due to the diffusion of the shock and its deviation from normality at its foot.

Corresponding to these pressures, Fig. 52 shows the Mach number dependence of the interference drag. In spite of the generally increased test section Mach number due to the constrictive effect of the walls, there appears to be an interference thrust at the higher tunnel Mach numbers which increases with Mach number as the latter approaches unity from below. This is presumably due to the increasing net suction force on the forebody. A similar trend occurs for all the bodies tested in Ref. 36. The thrust also increases with blockage ratio, again in agreement with Ref. 29. However, before a quantitative comparison with experiment is attempted, sting effects should be incorporated. In addition, the database of Ref. 36 is for slotted rather than solid walls. It also represents values of $H \leq 0.3$ in contrast to the large H results given herein. The sting effect will add the additional term to the far field given in Ref. 29.
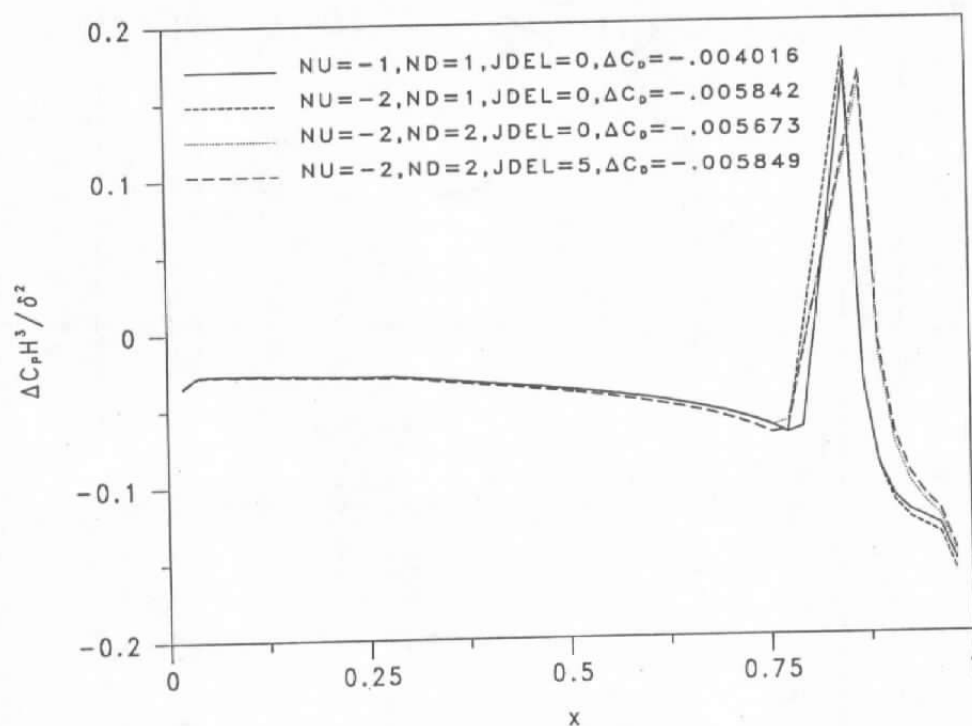
Fig. 51. Sensitivity of interference pressures to notch size parameters, parabolic arc body, $\delta = .1$, $M_\infty = .99$, $(K = 1.99)$.
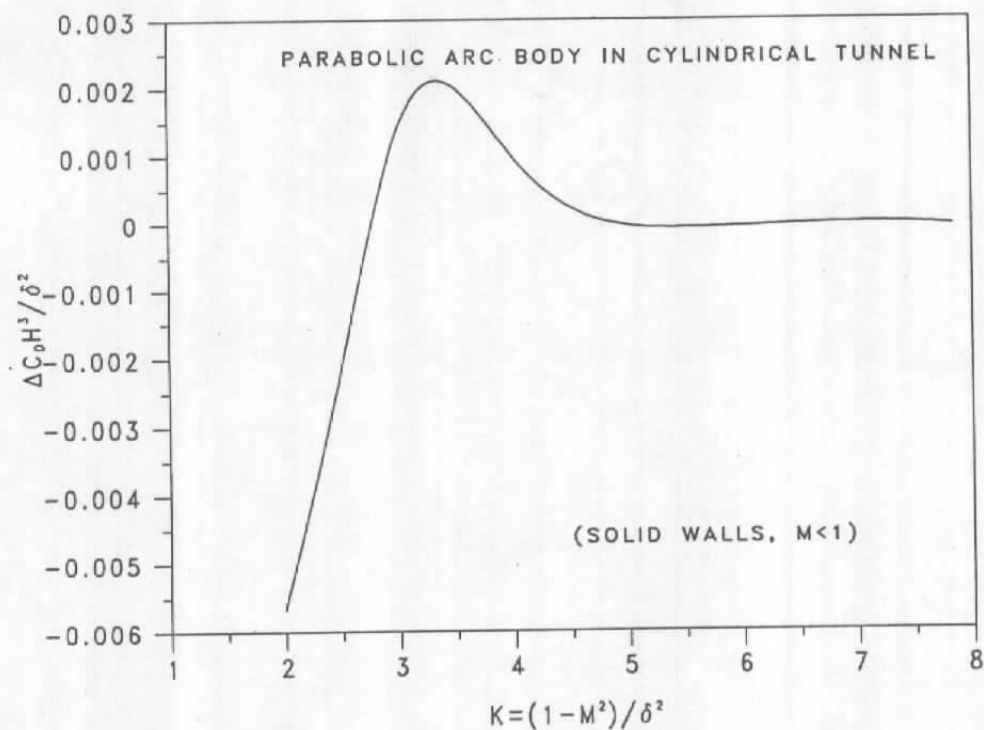
Fig. 52. Normalized interference drag $\Delta C_D H^3/\delta^2$ as a function of transonic similarity parameter $K = \left(1 - M_\infty^2\right)/\delta^2$.

3. LARGE ASPECT RATIO CONFIGURATIONS

In this section, transonic wall interference of configurations having high aspect ratio wings will be treated. The main emphasis of the theoretical and computational effort is the treatment of wing-alone cases. There is evidence to support the belief that the wing interference dominates many high aspect ratio wing-body shapes of practical importance. In spite of this, some discussion will in fact be given to wing-body arrangements. Rather than being concerned with the development of a production code, the exposition that follows will emphasize structural and mathematical features of the flow field and the description of a research code that provides information on these aspects.

3.1 Theory of Far Field Boundary Conditions

A basic feature of the asymptotic theory of wind tunnel wall corrections on high aspect ratio wings to be presented is that it systematically accounts for the influence of the wall modification of the far field induced downwash on the nearly two-dimensional near field flow over the wing. In Section 3.1.1, this correction is obtained for free jet and solid walls. For convenience and without great loss of generality and utility, the analysis is limited to circular test sections, although the initial setup had been made for rectangular test sections in Ref. 29. Section 3.1.2 generalizes the analysis of Section 3.1.1 to account for pressure distributions described on a cylindrical control surface. This part of the effort is motivated by wall interference-assessment-correction (WIAC) methods which use additional pressure measurements on such a control surface to account for factors not present in classical boundary condition simulations such as that of Section 3.1.1 and the usual perforated and slotted wall "radiation" and "oblique derivative" boundary conditions. The additional measurements combined with large-scale computational simulations such as that discussed in Ref. 39 can be used to determine if a wall correction is feasible and evaluate it quantitatively.

3.1.1 Solid Wall and Free Jet Corrections

3.1.1.1 Discussion

An outline of the treatment of closed (solid wall) rectangular cross section test sections is given in Ref. 29. The treatment of pressure specified boundary condition has similarities to the solid wall case and important differences. For a large span wing in a tunnel of comparably large lateral dimensions* both the solid wall and pressure specified case have an asymptotic flow structure similar to an unconfined large aspect ratio case. The near field flow is essentially two dimensional at each span station (strip theory) but with an incidence field modified by downwash associated with the trailing vortex system related to the large but finite aspect ratio. These ideas were the basis of Prandtl's lifting line theory and have been formalized for transonic speeds as a systematic asymptotic approximation by Cook and Cole in Ref. 32. To our knowledge, no one has treated the confined case, even at incompressible speeds using matched asymptotic procedures.

---

* Other limits are possible such as the span tending to ∞ at a slower rate than the tunnel's lateral dimensions.

Both the solid wall and pressure specified situations have nearly two-dimensional near fields which in the asymptotic formulation reduce to the previously outlined strip theory. The finite aspect ratio downwash correction is evaluated from matching with a vortex sheet emanating from a lifting line modeling the far field (outer flow) behavior of the finite span wing. What is different in the three cases is the nature of this downwash correction and the structure of the far field flow. For the free field case, the near field incidence correction is obtained from vortex and divortex representations of the lifting line. These can be also related to a doublet sheet representation as well as Biot Savart's law. For the confined cases, the vortex and divortex elements on the doublet sheet must be properly imaged in order to satisfy the wall conditions. This imaging is obviously different for the solid and pressure specified cases and will thus produce differing incidence corrections in the near (inner flow) field.

In accord with the formulation of Ref. 29, the dominant order equation for the far field flow is the Prandtl–Glauert equation. This is true providing that the far field relaxes to subsonic flow, and is usually associated with high subsonic freestream Mach numbers. Slightly supersonic upstream flows which were not treated in the contract require a different far field treatment, involving the interaction of the characteristics or Mach waves with the control surface or walls.

The Prandtl–Glauert outer flow problem can be rescaled by a stretching in the freestream direction to give a problem mathematically equivalent to the incompressible problem (Prandtl–Glauert/Goethert rules). This problem reduces to the determination of the near field potential of a doublet sheet accounting for interactions with a control surface boundary on which pressures are specified. These features are shown schematically in Fig. 53 for a rectangular cross section control surface $S_V + S_H$ enclosed within a rectangular cross section tunnel. According to the preceding discussion, pressure distributions obtained from measurements are assumed given on the control surface. An integral representation for the perturbation potential ϕ of the doublet sheet S_W can be obtained by using Green's formula. Introducing the Green's function G corresponding to a point source satisfying homogeneous Dirichlet conditions on the wall allows the wall effect to be characterized in terms of the control surface specified pressure distributions and removes a redundant term involving the normal velocity.

Since C_p is proportional to ϕ_x, where x is the streamwise coordinate, an integration with respect to x converts the problem of specifying ϕ_x to one in which inhomogeneous Dirichlet (ϕ) data are given on the control surface.

3.1.1.2 Analysis

As has been indicated in Ref. 29, the appropriate asymptotic expansion for the velocity potential Φ governing transonic small disturbance flow over the high aspect ratio wing shown in Fig. 54 is

$$\frac{\Phi}{U} = x + \delta^{2/3}\phi(x,\tilde{y},\tilde{z};H,B,K) + \cdots \qquad (3-1)$$
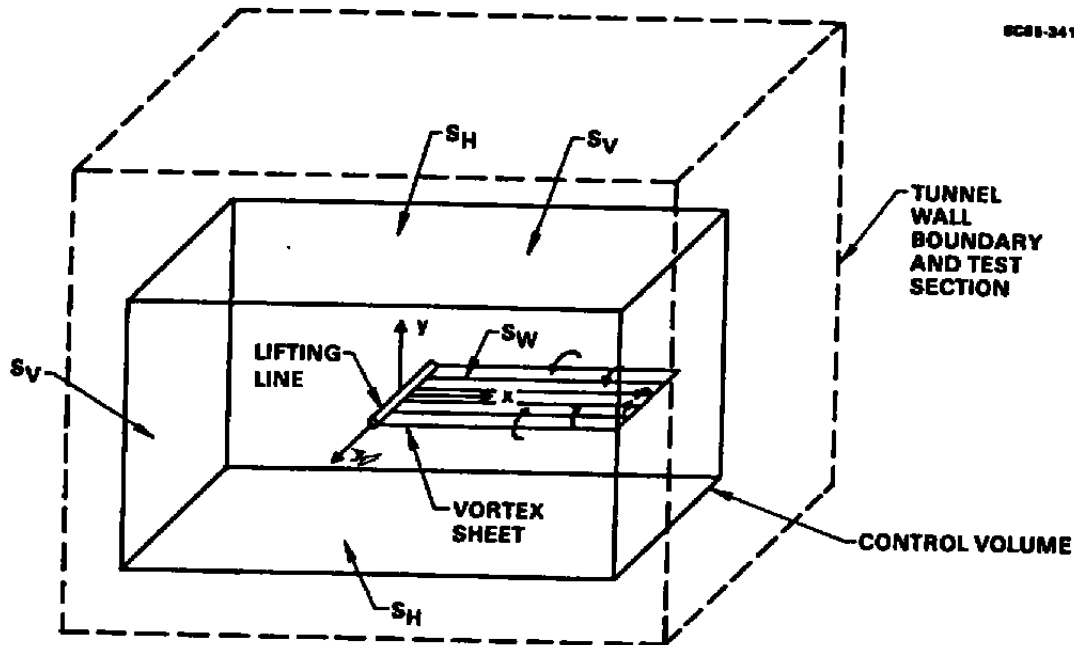
Fig. 53. Lifting line in rectangular cross section wind tunnel.

where U is the freestream velocity, M_∞ is the freestream Mach number, b is the span, h is the tunnel dimensionless radius, δ = wing thickness ratio, (x, y, z) are Cartesian coordinates, r, θ, x cylindrical coordinates shown in Fig. 54, $\tilde{y} = \delta^{1/3}y$, $\tilde{z} = \delta^{1/3}z$, $H = \delta^{1/3}h$, $B = \Lambda H = \delta^{1/3}b$, $K = \left(1 - M_\infty^2\right)/\delta^{2/3}$ are fixed as $\delta \to 0$, where Λ is a fixed span to height parameter making the aspect ratio effect the same size as the wall interference. On substitution of (3 − 1) into the exact equations, the following small disturbance equation for the perturbation potential ϕ results

$$\left(K - (\gamma + 1)\phi_x\right)\phi_{xx} + \phi_{\tilde{y}\tilde{y}} + \phi_{\tilde{z}\tilde{z}} = 0 \quad , \tag{3 − 2}$$

or in cylindrical coordinates:

$$\left(K - (\gamma + 1)\phi_x\right)\phi_{xx} + \frac{1}{\tilde{r}}\left(\tilde{r}\phi_{\tilde{r}}\right)_{\tilde{r}} + \frac{1}{\tilde{r}^2}\phi_{\theta\theta} = 0 \quad . \tag{3 − 2'}$$

In the strained (tilde) coordinate system, the tunnel wall boundary is at $\tilde{r} = H$. Since the pressure coefficient C_p is given by

$$C_p = -2\delta^{2/3}\phi_x \quad , \tag{3 − 3}$$

prescribing the pressure at the wall is equivalent to specifying ϕ there. In fact, measured C_p's on the wall or some control surface can be regarded as a known left hand side of (3 − 3)
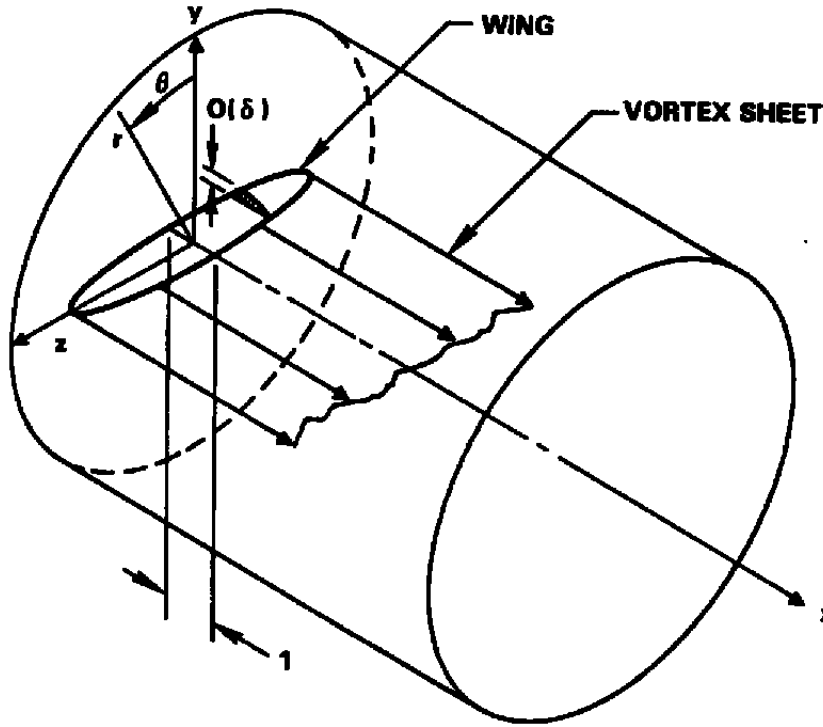
Fig. 54. High aspect ratio wing within cylindrical pressure specified control surface.

from which ϕ can be obtained by an integration with respect to x from some convenient downstream station such as $-\infty$ up to the current x value. Anticipating the x scaling in an outer limit, the resulting Dirichlet boundary condition for ϕ can be written as

$$\phi(x, H, \theta) = W\left(\frac{x}{H}, \theta\right) \quad . \tag{3-4}$$

In accord with previous remarks, an outer expansion which gives a lifting line structure to the high aspect ratio wing as $H \to \infty$ is

$$\varphi(x, \tilde{y}, \tilde{z}; H) = \varphi_0(x^*, y^*, z^*) + \frac{\log H}{H}\varphi_{11} + \frac{1}{H}\varphi_1 + \cdots \tag{3-5}$$

which holds in an outer limit

$$x^* = \frac{x}{H} \quad , \quad y^* = \frac{\tilde{y}}{H} \quad , \quad z^* = \frac{\tilde{z}}{H} \quad \text{fixed as } H \to \infty \quad . \tag{3-6}$$

The transverse straining embodied in the starred variables keeps the walls fixed in the starred coordinate system in the limit $(3-6)$. The outer boundary value problem for the

dominant term φ_0 of the lifting line expansion is

$$K\varphi_{0_{xx}} + \varphi_{0_{r^*r^*}} + \frac{1}{r^*}\varphi_{0_{r^*}} + \frac{1}{r^{*2}}\varphi_{0_{\theta\theta}} = 0 \qquad (3-7a)$$

$$\varphi_0(x^*, 1, \theta) = W(x^*, \theta) \qquad (3-7b)$$

$$[\varphi_0] = \Gamma(z^*) \quad \text{on the wake } x^* > 0, \, y^* = 0, \, -\Lambda \leq z^* \leq \Lambda \qquad (3-7c)$$

where the $[\quad]$ signifies the jump across the vortex sheet shown in Fig. 55 and is proportional to the local circulation at the span station z^*.
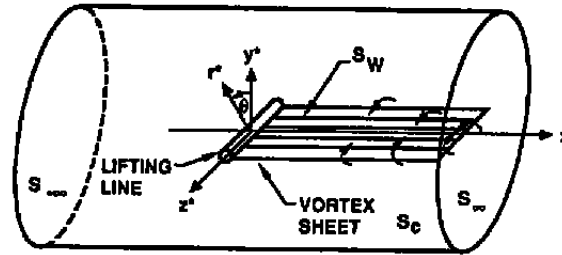
Fig. 55. Far field flow configuration showing lifting line and vortex sheet.

The main result to be obtained in what follows will be the downwash at the loaded line, i.e., the value of $\varphi_{0_{y^*}}(x^*, y^*, z^*)$ as x^*, $y^* \to 0$, z^* fixed.

If $W(x^*, \theta) = 0$ in $(3-7b)$, then the boundary condition on the cylindrical control surface $r^* = 1$ shown in Fig. 55 corresponds to a free jet. The corresponding solid wall condition is

$$\frac{\partial\varphi_0}{\partial r^*}(x^*, 1, \theta) = 0 \quad . \qquad (3-8)$$

An integral representation for φ_0 can be obtained by scaling out the K factor in Eq. $(3-7a)$ as in Refs. 30 and 32 with

$$\hat{y} = y^*/K, \, \hat{z} = z^*/K \qquad (3-9a)$$

and

$$\tan\hat{\theta} = \hat{z}/\hat{y} \qquad (3-9b)$$

$$\hat{r}^2 = \hat{y}^2 + \hat{z}^2 \qquad (3-9c)$$

so that the Prandtl–Glauert equation $(3 - 7a)$ transforms to Laplace's equation in three dimensions. Application of Green's theorem to the boundary value problem for this equation with boundary conditions $(3 - 7b,c)$ in the cylindrical region enclosed by the surfaces S_∞, $S_{-\infty}$, S_W, and S_C leads to the following integral representation

$$\phi = I_v + I_{\text{walls}} \qquad (3 - 10a)$$

where

$$I_v = \iint_{S_w} [\phi] \left(\frac{\partial G}{\partial n} \right) dS \qquad (3 - 10b)$$

$$I_{\text{walls}} = \iint_{\text{walls}} \phi \frac{\partial G}{\partial n} dS \qquad (3 - 10c)$$

where G denotes the Green's function, n is the outward drawn normal, S_w is the vortex sheet surface, and S_{walls} is the wall surface.

In the coordinates shown in Fig. 56, and assuming for convenience that the transonic similarity parameter of the free field, K_0, appearing in Eqs. (54) of Ref. 29* is unity, Eqs. $(3 - 10)$ imply that

$$I_v = - \int_{-B}^{B} \gamma(\zeta) d\zeta \int_0^\infty \left\{ \frac{\partial}{\partial n} G(x^*, y, z^*; \xi, \eta, \zeta) \right\}_{y=r} d\xi \qquad (3 - 11a)$$

$$I_{\text{walls}} = \int_{-\infty}^{\infty} d\xi \int_0^{2\pi} \phi \left\{ \frac{\partial}{\partial \rho} G(x^*, r^*, \theta; \xi, \rho, \theta') \right\}_{\rho=J} \rho d\theta' \quad ,$$
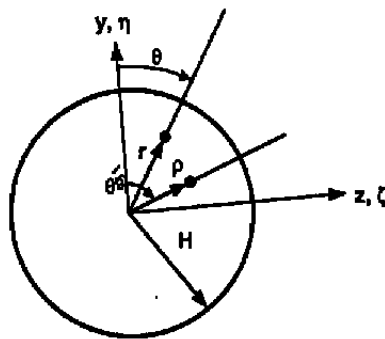
Fig. 56. Angular variables for Green's function associated with cylindrical walls.

---

* The results that follow can be easily generalized to arbitrary K_0 by the scale transformation $X = x^* / \sqrt{K_0}$ used in Ref. 29.

where h = the tunnel radius in units of the root chord, b is the span in the same units, and $B = \delta^{1/3}b$, $H = \delta^{1/3}h$, $\mu = H/B = h/b$. In addition, $\gamma(\zeta)$ = spanwise loading $= [\phi] = \phi(\xi, 0+, \zeta) - \phi(\xi, 0-, \zeta)$, $x^* = x/B$, $y^* = \delta^{1/3}y/B$, $z^* = \delta^{1/3}z/B$, δ = wing maximum thickness, x, y, and z are the Cartesian coordinates normalized to the root chord. In what follows, the star subscripts will be dropped.

As previously discussed, the open jet wind tunnel wall boundary condition

$$\phi(x, \mu, \theta) = 0 \qquad (3-12)$$

corresponding to constant pressure on the jet was assumed. *For this case, $G(x, \mu, \theta) = I_{\text{walls}} = 0$. The Green's function for this problem is applicable to the generalization involving pressure–specified boundary conditions on a control surface surrounding the test article.*

The appropriate Green's function satisfying a homogeneous Dirichlet condition such as Eq. $(3-12)$ on the walls is

$$G = \frac{1}{2\pi\mu^2} \sum_{n=-\infty}^{\infty} \cos n(\theta - \theta') \sum_k \frac{e^{-\lambda_{nk}|x-\xi|} J_n(\lambda_{nk}r) J_n(\lambda_{nk}\rho)}{\lambda_{nk} \left[J'_n(\lambda_{nk}\mu)\right]^2} \qquad (3-13)$$

where

$$\lambda_{nk}\mu = j_{nk} \quad ,$$

j_{nk} are the zeros of the J_n Bessel function given by

$$J_n(j_{nk}) = 0 \qquad (3-14)$$

and $\sum_{n=-\infty}^{\infty}(\cdots) = \sum_{n=0}^{\infty} \epsilon_n(\cdots)$, where $\epsilon_0 = 1$, $\epsilon_n = 2$, $n > 0$.

An alternate representation for G is given by

$$G = -\frac{1}{2\pi^2} \sum_{n=-\infty}^{\infty} \cos n(\theta - \theta') \int_0^{\infty} \cos \xi(x - x') I_n(\xi r') \left\{ K_n(\xi r) - \frac{K_n(\xi H) I_n(\xi r)}{I_n(\xi H)} \right\} d\xi \quad . \qquad (3-15)$$

Equation $(3-15)$ is in a particularly advantageous form in which the free field component can be separated out in the determination of the wall interference effect. In fact, the first term in the braces leads to the singular part of G, which is a point source in the free field. When this is integrated from $x = 0$ to ∞ and across the span, it gives the free field potential of a loaded line, that is, the dominant approximation of lifting line theory, which is

$$\phi_{\text{LL}} = \frac{1}{4\pi} \int_{-1}^{1} \gamma(\zeta) \left\{ 1 + \frac{x}{\sqrt{x^2 + y^2 + (z - \zeta)^2}} \right\} \left\{ \frac{y}{y^2 + (z - \zeta)^2} \right\} d\zeta \quad .$$

This can be shown from the Addition Theorem for the modified Bessel functions

$$\sum_{n=-\infty}^{\infty} \cos n(\theta - \theta') I_n(\xi r) K_n(\xi r') = K_0(\xi R) \qquad (3-16a)$$

$$R^2 = r^2 + r'^2 - 2rr'\cos(\theta - \theta') \qquad (3-16b)$$

and the cosine transform

$$-\frac{1}{2\pi^2}\int_0^\infty K_0(\xi R)\cos\xi(x-x')d\xi = -\frac{1}{4\pi\sqrt{R^2 + (x-x')^2}} \qquad . \qquad (3-17)$$

Thus, the free field potential of a unit intensity isolated source is the right hand side of $(3-17)$ which by Eqs. $(3-16)$ is represented by the first integral in $(3-15)$.

Returning to $(3-11a)$, the inner integral represents the potential ϕ_0 of a line doublet parallel to the x-axis in the $\eta = 0$ plane and at the span location ζ. Performing the indicated operations,

$$\phi_0 = \int_0^\infty \left.\frac{\partial G}{\partial \eta}\right|_{\eta=0} d\xi$$

$$= \frac{1}{2\pi\mu^2\zeta}\sum_{n=-\infty}^\infty n\sin n\left(\theta - \frac{\pi}{2}\right)\sum_k \frac{\left(2 - e^{-\lambda_{nk}x}\right)}{\lambda_{nk}^2\left[J_n'(\lambda_{nk}\mu)\right]^2}J_n(\lambda_{nk}r)J_n(\lambda_{nk}\zeta) \quad ,$$

$$\zeta > 0 \qquad (3-18)$$

$$= \frac{1}{2\pi\mu^2\zeta}\sum_{n=-\infty}^\infty n\sin n\left(\theta + \frac{\pi}{2}\right)\sum_k \frac{\left(2 - e^{-\lambda_{nk}x}\right)}{\lambda_{nk}^2\left[J_n'(\lambda_{nk}\mu)\right]^2}J_n(\lambda_{nk}r)J_n(\lambda_{nk}\zeta) \quad ,$$

$$\zeta < 0 \qquad . \qquad (3-19)$$

Of key interest is the behavior of ϕ_0 and I_v as $x, y \to 0$. This is the essential result sought in determining the downwash on the loaded line and matching with the inner solution. To determine this behavior, ϕ_0 can be further decomposed as follows:

$$\phi_0 = S_1 - S_2 \quad , \quad I_v = \int_{-B}^B \gamma(\zeta)\phi_0 d\zeta \qquad (3-20)$$

where, without loss of generality, only $\zeta > 0$ will be considered*, and

$$S_1 \equiv \frac{1}{2\pi\mu^2\zeta}\sum_{n=-\infty}^\infty n\sin n\underline{\theta}\sum_k \frac{2J_n(\lambda_{nk}r)J_n(\lambda_{nk}\zeta)}{\lambda_{nk}^2\left[J_n'(\lambda_{nk}\mu)\right]^2} \qquad (3-21a)$$

$$S_2 \equiv \frac{1}{2\pi\mu^2\zeta}\sum_{n=-\infty}^\infty n\sin n\underline{\theta}\sum_k \frac{e^{-\lambda_{nk}x}J_n(\lambda_{nk}r)J_n(\lambda_{nk}\zeta)}{\lambda_{nk}^2\left[J_n'(\lambda_{nk}\mu)\right]^2} \quad , \qquad (3-21b)$$

where $\underline{\theta} \equiv \theta - \pi/2$.

Two primary steps are employed to obtain the desired result. These are:

---

* Extension to $\zeta < 0$ is trivial.

1. Recognize that S_1 represents a two–dimensional vortex in the Trefftz plane (and mathematically prove it using the properties of Fourier–Bessel series).

2. Separate out the free field line doublet from S_2 by using a process resembling Kummer's transformation to accelerate the convergence of the series. It consists of subtracting and adding the "tail" of the series which represents the singular part of the Green's function associated with the free field.

<u>Evaluation of S_1</u>

Consider the line source

$$G^* = \int_0^\infty G(x,0,z;\xi,\eta,\zeta)d\xi \quad ,$$

then

$$G^*(0,r,\theta;\rho,\theta') = -\frac{1}{2\pi\mu^2} \sum_{n=-\infty}^{\infty} \cos n(\theta-\theta') \sum_k \frac{J_n(\lambda_{nk}r)\,J_n(\lambda_{nk}\rho)}{\lambda_{nk}^2 \left[J_n'(\lambda_{nk}\mu)\right]^2}$$

$$= \frac{1}{2}G^*(\infty,r,\theta;\rho,\theta') \quad . \tag{3-22}$$

From (3.13.4), p. 134 of Ref. 40, the inner sum can be evaluated as a limit of a Fourier Bessel series. Noting that

$$-\sum_k \frac{J_n\left(j_{nk}\frac{r}{\mu}\right)J_n\left(j_{nk}\frac{\rho}{\mu}\right)}{j_{nk}^2\left[J_n'(j_{nk})\right]^2} = \lim_{\tau\to 0} \frac{\pi}{4}\frac{J_n\left(\frac{r}{\mu}\right)}{J_n(\tau)}\left\{J_n(\tau)Y_n\left(\frac{\rho}{\mu}\right) - J_n\left(\frac{\rho}{\mu}\right)Y_n(\tau)\right\} \tag{3-23}$$

and using the asymptotic properties of the Bessel functions as $\tau \to 0$, from Ref. 41, 9.17 and 9.19, Eq. (3 − 22) becomes

$$G^*(0,r,\theta;\rho,\theta') = \frac{1}{4\pi}\left\{\ln\underline{\rho} - \sum_{n=1}^{\infty}\frac{\underline{r}^n}{n}\{\underline{\rho}^{-n} - \underline{\rho}^{-n}\}\cos n(\theta-\theta')\right\} \quad ,$$

$$0 < \underline{r} < \underline{\rho} < 1 \tag{3-24a}$$

$$= \frac{1}{4\pi}\left\{\ln\underline{r} - \sum_{n=1}^{\infty}\frac{\underline{\rho}^n}{n}\{\underline{r}^{-n} - \underline{r}^n\}\cos n(\theta-\theta')\right\} \quad ,$$

$$0 < \underline{\rho} < \underline{r} < 1 \tag{3-24b}$$

where $\underline{r} \equiv r/\mu$ and $\underline{\rho} \equiv \rho/\mu$. Introducing the complex variables $Z = z + iy$, $Z' = \zeta + i\eta$, Eqs. (3 − 24) can be represented as a geometric series which can be summed. This gives for $\mu = 1$,

$$G^*(0,r,\theta;r',\theta') = -\frac{1}{4\pi}\left\{\log|Z-Z'| - \log\left|Z - \frac{1}{Z'}\right| - \ln|\overline{Z'}|\right\} \quad . \tag{3-25}$$

Equations $(3-22)$ and $(3-25)$ demonstrate that the line source appears as a two-dimensional source reflected in the walls in the Trefftz or $x = 0$ plane. The first term of Eq. $(3-25)$ is a free-field source at the point Z'. The second and third terms are the image of this singularity in the walls using the inversion point $1/\overline{Z'}$. Equation $(3-25)$ represents the classical formula for the Green's function of the first kind for a unit circle.

To evaluate S_1, it can be shown that

$$S_1 = \left. \frac{\partial G^*}{\partial \eta} \right|_{\eta = 0} \quad ,$$

and therefore from Eq. $(3-25)$, with $Z' = \zeta$ on the reals,

$$S_1 = \frac{y}{2\pi} \left\{ \frac{1}{(z - \zeta)^2 + y^2} + \frac{\mu^2}{\zeta^2 \left[\left(z - \frac{\mu^2}{\zeta} \right)^2 + y^2 \right]} \right\} \quad . \tag{3-26}$$

In accord with the previous discussion, the first term in Eq. $(3-26)$ represents a two-dimensional doublet in a free field, and the second its image in the circular projection of the walls. The plus sign in $(3-26)$ corresponds to a free jet, a negative sign is associated with solid walls.

Evaluation of S_2

To implement Step 2, some preliminary processing of S_2 is required. Accordingly, let

$$\underline{S_2} \equiv \frac{\partial S_2}{\partial x} = -\frac{1}{2\pi \mu^2 \zeta} \sum_{n=-\infty}^{\infty} n \sin n\underline{\theta} \sum_k \phi_{kn}(x, r; \zeta) \tag{3-27a}$$

$$\phi_{kn} \equiv \frac{e^{-\lambda_{nk} x} J_n(\lambda_{nk} r) J_n(\lambda_{nk} \zeta)}{\lambda_{nk} \left[J_n'(\lambda_{nk} \mu) \right]^2} \tag{3-27b}$$

and

$$S_2 - S_2(0) = \int_0^x \underline{S_2}\, dx \quad . \tag{3-28}$$

Also, let

$$\underline{S_2} = \frac{\partial u}{\partial \underline{\theta}} \quad . \tag{3-29}$$

Then, using Kummer's transformation

$$u = \underline{U} + \sum_{n=-\infty}^{\infty} \cos n\underline{\theta} \sum_{k=1}^{\infty} (\phi_{kn} - \Psi_{kn}) \tag{3-30}$$

$$\underline{U} = \sum_{k=1}^{\infty} \sum_{n=\infty}^{\infty} \Psi_{kn} \qquad (3-31)$$

$$\Psi_{kn} = \frac{\pi\mu}{2} e^{-k\pi z/\mu} \cos n\underline{\theta} J_n\left(\frac{k\pi r}{\mu}\right) J_n\left(\frac{k\pi\zeta}{\mu}\right) \quad . \qquad (3-32)$$

The Ψ_{kn} defined in Eq. $(3-32)$ represent the asymptotic behavior of ϕ_{kn} in the limit $k/\mu \to \infty$ as $k \to \infty$. Also, the interchange of sums in Eq. $(3-31)$ is assumed to be legitimate.

The quantity $\underline{U}$ is evaluated as follows: Noting from Eq. $(3-31)$

$$\underline{U} = \frac{\pi\mu}{2} \sum_{k=1}^{\infty} e^{-k\pi z/\mu} \sum_{n=\infty}^{\infty} \cos n\underline{\theta} J_n\left(\frac{k\pi r}{\mu}\right) J_n\left(\frac{k\pi\zeta}{\mu}\right) \quad , \qquad (3-33)$$

from the Addition Theorem,

$$\sum_{n=-\infty}^{\infty} \cos n\theta J_n\left(\frac{\pi k r}{\mu}\right) J_n\left(\frac{\pi k \zeta}{\mu}\right) = J_0\left(\frac{k\pi}{\mu}R\right)$$

$$R = \sqrt{x^2 + y^2 + (z-\zeta)^2}$$

and the Schlöemilch series referred to in Refs. 40 and 41,

$$\underline{U} = \frac{1}{2R} + \frac{\pi\mu}{2} \left\{ \frac{1}{2} + \sum_{n=1}^{\infty} [2n!]^{-1} (-1)^{n-1} B_{2n} \overline{R}^{2n-1} P_{2n-1}\left(\frac{\overline{X}}{\overline{R}}\right) \right\} \quad , \qquad (3-34)$$

where

$$\overline{R} = R/\mu$$
$$\overline{X} = x/\mu$$
$$B_{2n} = \text{Bernoulli number}$$
$$P_n = \text{Legendre polynomial} \quad .$$

Noting that

$$S_2(0) = \frac{1}{2} S_1 \quad ,$$

and performing the integrations and differentiations of Eqs. $(3-28)$ and $(3-29)$, it follows that

$$S_2 = \frac{y}{4\pi} \left\{ \frac{1}{(z-\zeta)^2 + y^2} + \frac{\mu^2}{\zeta^2 \left[\left(z - \frac{\mu^2}{\zeta}\right)^2 + y^2 \right]} \right\}$$
$$- \frac{yx}{4\pi \left[(z-\zeta)^2 + y^2\right] R} + O(xy) \qquad (3-35)$$
$$+ x^2 y \sum_{n=2}^{\infty} a_n (z-\zeta)^{2(2n-3)}$$

where the $O(xy)$ terms arise from the second sum in Eq. $(3-30)$ and the term proportional to $x^2 y$ comes from the last sum in Eq. $(3-34)$. Both of these are assumed to be negligible regular functions compared to the singular contributions shown. Because the singular part has been subtracted off, the convergence of the second sum is anticipated to be rapid. The last term in Eq. $(3-35)$ is the dominant term of the sum in Eq. $(3-34)$ evaluated by use of the expansion of $P_n(\nu)$ as a finite series in ν, and summing by rows instead of columns.

Discussion

From Eqs. $(3-11)$, $(3-20)$, $(3-26)$, and $(3-35)^*$, the desired expression for I_v is:

$$I_v = \frac{y}{4\pi} \int_{-B}^{B} \gamma(\zeta) \left\{ \underbrace{\left[\frac{1}{(z-\zeta)^2 + y^2}\right] \left[1 + \frac{x}{\sqrt{x^2+y^2+(z-\zeta)^2}}\right]}_{\textcircled{1}} \right.$$

$$\left. \pm \underbrace{\frac{\mu^2}{\zeta^2 \left[\left(z - \frac{\mu^2}{\zeta}\right)^2 + y^2\right]}}_{\textcircled{2}} \right\} d\zeta + O(xy) \quad . \tag{3-36}$$

Equation $(3-36)$ provides the dominant inner behavior of the outer solution for the open wall (free jet) case. It contains terms $\textcircled{1}$ which correspond to the free field and $\textcircled{2}$ which are associated with the wall effect. For a solid wall, the sign of $\textcircled{2}$ is negative.

The implication of Eq. $(3-36)$ on the matching of the transonic lifting line theory of unconfined high aspect ratio wings given in Ref. 30 is that the horseshoe vortex system because of its imaging in the walls modifies the near field downwash by an amount associated with the term $\textcircled{2}$. Structurally, the matching elements between the outer and inner solution are otherwise unchanged.

3.1.2 Pressure Specified Boundary Conditions

In the previous section, the modification of the downwash on the loaded line to free jet and solid wall boundary conditions for high aspect ratio wings was considered. In this section, the effect of specification of arbitrary boundary conditions on a cylindrical control surface enclosing a high aspect ratio wing will be derived.

Referring to Eq. $(3-7b)$, a decisive step in achieving this result is to split φ_0 as follows:

$$\varphi_0 = \varphi_J + \varphi_c \quad . \tag{3-37}$$

In $(3-37)$, φ_J is the potential associated with free jet boundary conditions, i.e.,

$$\varphi_J(x,1,\theta) = 0 \quad .$$

* An alternate analysis was performed leading to the same results which used asymptotic treatment of Fourier transform representations of the far field flow based on Tauberian theorems.

The quantity φ_J satisfies the jump condition $(3-7c)$. Since the outer problem is linear, we can satisfy the remaining boundary condition by setting

$$\varphi_c(x^*, 1, \theta) = W(x^*, \theta) \qquad (3-38)$$

and $[\varphi_0] = 0$ on the wake. Note also by linearity that φ_J and φ_c both satisfy $(3-7a)$.

The problem for the correction potential can be solved by Fourier transforms and eigenfunction expansions. The appropriate exponential Fourier transform pair is

$$\varphi_c = \int_{-\infty}^{\infty} e^{ikx} \widetilde{\varphi}(k, r^*, \theta) dk \qquad (3-39a)$$

$$\widetilde{\varphi} = \frac{1}{2\pi} \int_{-\infty}^{\infty} e^{-ikx^*} \varphi(x^*, r^*, \theta) dx^* \quad . \qquad (3-39b)$$

Also, W can be represented as

$$W = \int_{-\infty}^{\infty} e^{-ikx} \widetilde{W}(\theta, k) dk \quad . \qquad (3-40)$$

Accordingly, the subsidiary equation for $\widetilde{\varphi}$ is

$$\widetilde{\varphi}_{r^*r^*} + \frac{1}{r^*}\widetilde{\varphi}_{r^*} + \frac{1}{r^{*2}}\widetilde{\varphi}_{\theta\theta} - Kk^2\widetilde{\varphi} = 0 \quad . \qquad (3-41)$$

Equation $(3-41)$ can be solved by eigenfunction expansions. By separation of variables the Sturm Liouville problems for the eigenfunctions $R_n(r^*)$ and $T_n(\theta)$ are

$$T_n'' + \lambda_n^2 T_n = 0 \qquad (3-42a)$$

$$r^* R_n'' + r^* R_n' - (Kk^2 r^{*2} + \lambda_n^2) R_n = 0 \quad . \qquad (3-42b)$$

The T_n and λ_n can be obtained from the conditions

$$\varphi(r^*, \theta) = \varphi(r^*, -\theta)$$
$$\varphi(r^*, \theta + 2\pi) = \varphi(r^*, \theta)$$

and are $T_n = \cos n\theta$, $\lambda_n = n = 0, 1, 2, 3, \cdots$. Equation $(3-42b)$ is the modified Bessel equation, whose solutions are

$$R_n(r^*) = \frac{I_n(k\sqrt{K}r^*)}{K_n(k\sqrt{K}r^*)} \quad .$$

The K_n solutions are discarded since they violate an additional condition that φ_c is bounded as $r^* \to 0$. The resulting eigenfunction expansion for $\widetilde{\varphi}$ can thus be written as

$$\widetilde{\varphi} = A_0 I_0(k\sqrt{K}r^*) + \sum_{n=1}^{\infty} A_n I_n(k\sqrt{K}r^*)\cos n\theta \quad . \qquad (3-43)$$

Writing the transform of (3 – 7b) as

$$\widetilde{\varphi}(1,\theta) = \widetilde{W}(k,\theta) \quad , \tag{3 – 44}$$

$\widetilde{\varphi}$ can be obtained as

$$\widetilde{\varphi} = \langle W(k,\theta) \rangle \frac{I_0(k\sqrt{K}r^*)}{I_0(k\sqrt{K})} + \sum_{n=1}^{\infty} \widetilde{W}_n(k) \frac{I_n(k\sqrt{K}r^*)}{I_n(k\sqrt{K})} \cos n\theta \tag{3 – 45}$$

where

$$\langle W(k,\theta) \rangle = \frac{1}{\pi} \int_0^{\pi} \widetilde{W}(k,\theta) d\theta \tag{3 – 46a}$$

$$\widetilde{W}_n(k) = \frac{2}{\pi} \int_0^{\pi} \widetilde{W}(k,\theta) \cos n\theta d\theta \quad . \tag{3 – 46b}$$

The desired results can be obtained by examining (3 – 45) in the limit $y^* \rightarrow 0$. Since $\cos\theta = \frac{y^*}{\sqrt{y^{*2}+z^{*2}}} \approx \frac{y^*}{z^*}$, this corresponds to $\theta \rightarrow \frac{\pi}{2}$. Some useful asymptotic expansions in this limit are

$$\cos(2n-1)\theta = (-1)^{n-1}(2n-1)\cos\theta + O(y^{*3}) \tag{3 – 47a}$$

$$\cos 2n\theta = (-1)^{n-1} + O(y^{*2}) \tag{3 – 47b}$$

for $n = 1, 2, 3, \cdots$ fixed.

Letting

$$G_n = W_n(k) \frac{I_n(k\sqrt{K}r^*)}{I_n(k\sqrt{K})} \quad ,$$

then splitting the sum into odd and even components as follows,

$$\sum_{n=1}^{\infty} (\cdots) = \sum_{n=1}^{\infty} G_{2n} \cos 2n\theta + \sum_{n=1}^{\infty} G_{2n-1} \cos(2n-1)\theta \quad ,$$

and noting that

$$I_{2n}(k\sqrt{K}r^*) \doteq I_{2n}(k\sqrt{K}z^*) + O(y^{*2})$$

gives

$$\widetilde{\varphi}_{y^*}(k,0,z^*) = \frac{1}{z^*} \sum_{n=1}^{\infty} (-1)^{n-1}(2n-1) \widetilde{W}_{2n-1}(k) \frac{I_{2n-1}(k\sqrt{K}z^*)}{I_{2n-1}(k\sqrt{K})}$$

or

$$\widetilde{\varphi}_{y^*}(x^*,0,z^*) = \frac{1}{2\pi z} \sum_{n=1}^{\infty} (-1)^{n-1}(2n-1) \int_{-\infty}^{\infty} e^{ikz^*} W_{2n-1}(k) \frac{I_{2n-1}(k\sqrt{K}z^*)}{I_{2n-1}(k\sqrt{K})} dk$$

so that

$$\widetilde{\varphi}_{y^*}(0,0,z^*) = \frac{1}{2\pi z} \sum_{n=1}^{\infty} (-1)^{n-1}(2n-1) \int_{-\infty}^{\infty} W_{2n-1}(k)\frac{\cdots}{\cdots}dk \quad .$$

By virtue of $(3-46)$,

$$\widetilde{W}(k,\theta) = \widetilde{W}_0(k) + \sum_{k=1}^{\infty} \widetilde{W}_n(k)\cos n\theta \qquad (3-48a)$$

$$W(x^*,\theta) = W_0(x^*) + \sum_{k=1}^{\infty} W_n(x^*)\cos n\theta \quad . \qquad (3-48b)$$

Also,

$$\widetilde{W}_{2n-1} = \int_{-\infty}^{\infty} W_{2n-1}(x^*)e^{-ikz^*}dx^* \quad .$$

Thus

$$\varphi_{c_{y^*}}(0,0,z^*) = \frac{1}{2\pi z^*} \sum_{n=1}^{\infty} (-1)^{n-1}(2n-1) \int_{-\infty}^{\infty} W_{2n-1}(x^*)dx^*$$

$$\times \int_{-\infty}^{\infty} e^{-ikx^*} \frac{I_{2n-1}(k\sqrt{K}z^*)}{I_{2n-1}(k\sqrt{K})}dk \quad . \qquad (3-49)$$

Here,

$$W_{2n-1}(x^*) = \frac{2}{\pi} \int_0^{\pi} W(x^*,\theta)\cos(2n-1)\theta d\theta \quad .$$

If it is assumed that all higher harmonics such as $n = 2, 3, \cdots$ are zero in $(3-48b)$, then $(3-49)$ simplifies to

$$\varphi_{c_{y^*}}(0,0,z^*) = \frac{1}{2\pi z^*} \int_{-\infty}^{\infty} W_1(x^*)dx^* \int_{-\infty}^{\infty} e^{-ikx^*} \frac{I_1(k\sqrt{K}z^*)}{I_1(k\sqrt{K})}dk \quad . \qquad (3-50)$$

The inner integral in $(3-49)$ can be evaluated by residues. The poles are pure imaginaries given by

$$k = ij_{n,s} \quad , \quad s = 1, 2, 3, \cdots$$

where the j_{ns} are the zeros of J_n, i.e.,

$$J_n(j_{ns}) = 0$$

which are all real and simple.

The higher order pole at $k = 0$ is negligible since the integrand is bounded at the origin. If $k = \xi + i\eta$, then the asymptotic behavior of the integrand is

$$e^{-ikx^*} \frac{I_n(k\sqrt{K}z^*)}{I_n(k\sqrt{K})} = O\left(e^{-(\sqrt{K}|z^*-1|+|\eta||z^*|)}\right) \quad \text{as} \quad |k| \to \infty, \eta < 0, x^* > 0, |z^*| < 1 \qquad (3-51)$$

107

which implies that the inversion integral can be evaluated by summing residues inside a semicircle ($|\kappa_1^i| = R$, $\eta < 0$) in the lower half plane as shown in Fig. 57. Equation $(3-51)$ insures that the integral will converge. Summing the residues gives finally after some interchange of the orders of integration

$$\varphi_{c_{y^*}}(0,0,z^*) = \frac{1}{\sqrt{K}z^*} \sum_{n=1,3,5,\cdots}^{\infty} (-1)^n n \sum_{s=1}^{\infty} \frac{J_n(j_{ns}z^*)}{J_n'(j_{ns})} \int_{-\infty}^{\infty} e^{-j_{ns}|z^*|} W_n(x^*)dx^* \quad (3-52)$$
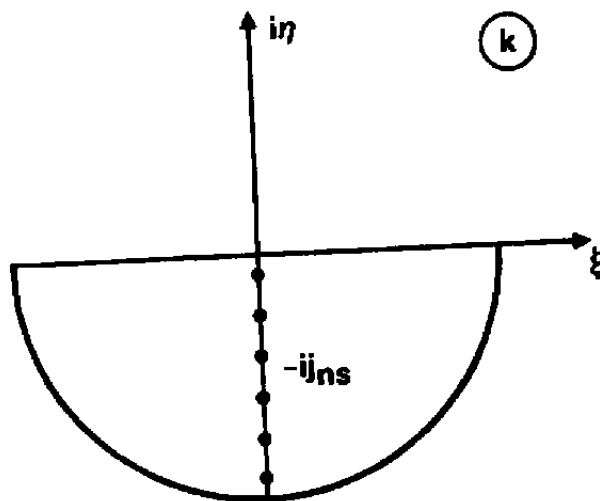
Fig. 57. Contour for inversion of the inner integral in Eq. $(3-51)$

where the continuation of the inversion for $x^* < 0$ has been made. Now the integral in $(3-49)$ can be expressed as

$$\int_{-\infty}^{\infty} e^{-\lambda|x|} f(x)dx \doteq \frac{2}{\lambda} \int_0^{\infty} e^{-u} \left\{ f(0) + O(\lambda^{-1}) \right\} du$$

$$= \frac{2}{\lambda} \left\{ f(0) + O(\lambda^{-1}) \right\}$$

if the integrand is expanded assuming that λ is large. This can be a useful approximation since $j_{ns} \geq 3.83171$. It implies finally that

$$\varphi_{c_{y^*}}(0,0,z^*) = \frac{2}{\sqrt{K}z^*} \sum_{n=1,3,5,\cdots}^{\infty} \frac{(-1)^n(n)}{j_{n1}} W_n(0) \frac{J_1(j_{n1}z^*)}{J_1'(j_{n1})} \quad . \quad (3-53)$$

If the higher harmonics are neglected, due to the rapidity of convergence of the series, (3 − 53) reduces to

$$\varphi_{y^*}(0,0,z^*) = \frac{2}{\sqrt{K}z^*}\frac{W_1(0)}{j_{11}}\frac{J_1(j_{11}z^*)}{J_1'(j_{11})} \qquad (3-53')$$

where

$$W_n(0) = \frac{2}{\pi}\int_0^\pi W(0,\theta)\cos n\theta\, d\theta \quad .$$

Thus, to obtain the wall interference associated with a series of pressure measurements on a control cylinder, only those at the location of the wing are important. Equations (3 − 53) give the effect of non-zero wall pressure on the downwash at the loaded line.

3.2 Numerical Procedures and Outline of Code

A formulation of the high aspect ratio problem is given in Ref. 29. As indicated in Section 3.1.1.2, the asymptotic expansion for the velocity potential Φ is

$$\frac{\Phi}{U} = x + \delta^{2/3}\phi(x,\tilde{y},\tilde{z};K,A,H,B) + \cdots, \qquad (3-1)$$

which is valid in the Karman Guderley (KG) limit

$$x,\tilde{y} = \delta^{1/3}y\,,\ \tilde{z} = \delta^{1/3}z\,,\ K = \frac{1-M_\infty^2}{\delta^{2/3}}\,,\ A = \frac{\alpha}{\delta}\,,\ B = \delta^{1/3}b,\ H = h\delta^{1/3} \quad \text{fixed as } \delta \to 0, \qquad (3-54)$$

where δ = thickness ratio, b = semispan in units of wing root chord, M_∞ = Mach number, h = open jet, closed wall, pressure specified control surface radius in units of wing root chord, and α = wing geometric angle of attack.

Within the KG limit (3 − 54), a secondary (confined lifting line) limit is considered for a high aspect ratio wing in which the wall interference is of the same order as the three-dimensional effect associated with finite aspect ratio. Accordingly, in an "inner limit" near the wing, the flow field is almost two dimensional with

$$\phi(x,\tilde{y},\tilde{z};A,K,\mu) = \phi_0(x,\tilde{y};A_0,K_0,\mu) + \frac{1}{B}\phi_1(x,\tilde{y},z^*;A_0,A_1,\mu,K_0,K_1) + \cdots \quad (3-55a)$$

$$K = K_0 + \frac{1}{B}K_1 + \cdots \qquad (3-55b)$$

$$A = A_0 + \frac{1}{B}A_1 + \cdots \qquad (3-55c)$$

in the inner limit

$$z^* = \frac{\tilde{z}}{B}\,,\ x,\tilde{y},\mu = \frac{H}{B} = \frac{h}{b} \quad \text{fixed as } B \to \infty\,,\ \delta \to 0 \text{ independently.} \qquad (3-56)$$

As indicated in Ref. 29, the far field for the inner problem for the finite aspect ratio, wall interference correction ϕ_1 is governed by a far field associated with an outer problem corresponding to a bound vortex shedding a trailing vortex sheet.

In what follows, the formulation and description of the pilot lifting line code accounting for wind tunnel wall interference will be given. The analyses will assume without excessive loss of generality that $K_1 = A_1 = 0$.

3.2.1 Boundary Value Problem for ϕ_0

3.2.1.1 Analytic Formulation

Input Parameters

The airfoil shape shown in Fig. 58 is given by $y_{u,\ell} = \delta F_{u,\ell}(x), |x| \leq 1$, $\max|F| = 1, u \sim$ upper surface, $\ell \sim$ lower surface

Angle of attack: α

Ratio of specific heats: $\gamma = 1.4$

Transonic similarity parameter: $K = \frac{1-M_\infty^2}{\delta^{2/3}}$;

(or, for Krupp scaling, $K = \frac{1-M_\infty^2}{M_\infty \delta^{2/3}}$).

Boundary Value Problem

$$(K - (\gamma+1)\phi_{0_x})\, \phi_{0_{xx}} + \phi_{0_{\tilde{y}\tilde{y}}} = 0 \qquad (3-57a)$$

$$\phi_{0_{\tilde{y}}}(x, 0\pm) = \frac{\partial}{\partial x} F_{u,\ell}(x) - A \quad , \quad A = \frac{\alpha}{\delta} \quad , \quad |x| \leq 1 \qquad (3-57b)$$

$$[\phi_0]_{\tilde{y}=0} = \Gamma \text{ for } x \geq 1 \quad [\text{Kutta} - \text{Joukowski condition}] \qquad (3-57c)$$

$$\phi_0 \rightarrow -\frac{\Gamma\theta}{2\pi} + \frac{(\gamma+1)\Gamma^2}{16\pi^2 K} \frac{\ln r}{r}\cos\theta + \cdots \quad \text{as } r \rightarrow \infty, 0 \leq \theta < 2\pi$$

$$\left(r = \sqrt{x^2 + K\tilde{y}^2}\right) \qquad (3-57d)$$

$$\left(\theta = \tan^{-1}\frac{K\tilde{y}}{x}\right) \quad .$$

3.2.1.2 Numerical Formulation

A rectangular computational grid schematically indicated in Fig. 59 is employed which is approximately uniform on and near the wing, with geometric stretching in the far field. (There is a capability to adapt the grid spacing on the wing to the airfoil shape, as indicated subsequently.) The grid is displaced from $\tilde{y} = 0$ and from the singularities at $(-1, 0)$ and $(1, 0)$.

Solution values are stored in PHI(1:IMAX,1:JMAX), with an extra row/column for the boundary values.

The airfoil ordinates are input in a table, then interpolated and differentiated (using smoothed cubic splines) to get the Neumann body boundary conditions. A parabolic arc airfoil and the NACA 00nn series are available analytically.

Equation $(3-57a)$ is solved by successive line overrelaxation (SLOR), based on techniques developed in Refs. 31, 33–35, and 42, solving the finite difference equations a line at a time, from i=1 to i=IMAX.

SC37646
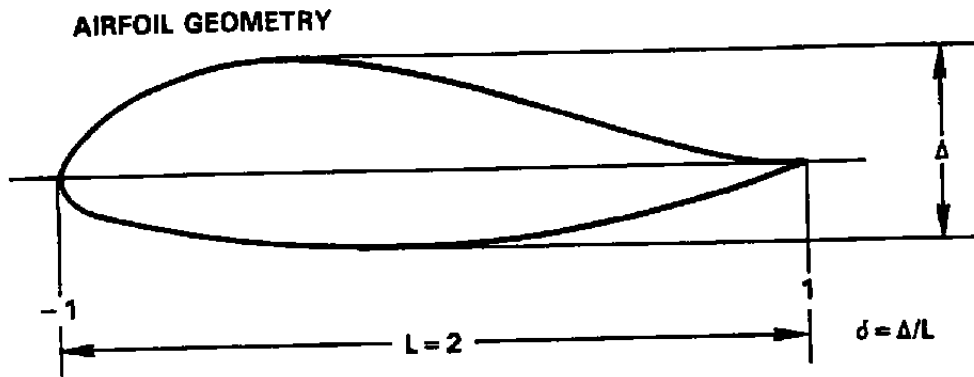
AIRFOIL GEOMETRY

Fig. 58. Airfoil geometry.

SC-0459-CS
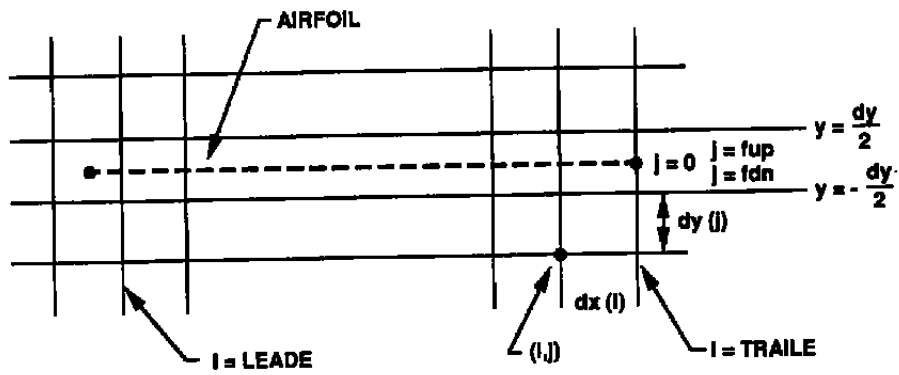
Fig. 59. Computational grid.

Basically, 3–point centered differences are used. The grid can be nonuniform. The differentiation formulas employed are:

$$\overset{\underset{\displaystyle \;\; h_1 \;\;\; h_2}{}}{\underset{i-1 \quad i \quad i+1}{\bullet\!\!-\!\!\bullet\!\!-\!\!\bullet}} \;\; : \;\; \phi_{0_x i} = \frac{-h_2}{h_1(h_1+h_2)}\phi_{0_{i-1}} + \frac{h_2-h_1}{h_1 h_2}\phi_{0_i} + \frac{h_1}{h_2(h_1+h_2)}\phi_{0_{i+1}} + O(h^2)$$

$$\phi_{0_{xx} i} = \frac{2}{h_1(h_1+h_2)}\phi_{i-1} - \frac{2}{h_1 h_2}\phi_{0_i} + \frac{2}{h_2(h_1+h_2)}\phi_{0_{i+1}} + O(h^2) \quad .$$

Set $\mu_{i,j} = K - (\gamma+1)\phi_{0_x i,j}$ using this central difference. Then $\mu_{i,j}$ controls the type of the equation at (i,j). There are four cases which are tabulated in Table 1:

Table 1. Type Sensitive Switches Employed by ϕ_0 Modules

	$\mu_{i-1,j}$	$\mu_{i,j}$	Type of Point	Representation of $(K - (\gamma+1)\phi_{0_x})\phi_{0_{xx}}$
(i)	> 0	> 0	elliptic	$\mu_{i,j}\phi_{0_{xx} i,j}$ [central differencing]
(ii)	< 0	< 0	hyperbolic	$\mu_{i-1,j}\phi_{0_{xx} i,j}$ [backward differencing]
(iii)	> 0	< 0	parabolic	0 [$\mu \sim 0$ any way]
(iv)	< 0	> 0	shock	(i) + (ii)

The representations for Cases (i)–(iii) shown in the table keep the equations stable and the marching direction toward positive x. In (iv), Murman's shock point operator is applied. This is consistent with the Rankine–Hugoniot weak solutions at the shock. For $\phi_{0_{yy}}$, central differences are employed, giving a tridiagonal system.

(i) In $|x| \le 1$, i.e., leade $\le i \le$ traile, the Neumann boundary conditions are satisfied by the following discretization method:

Above the wing, at $j = fup$:

$$\phi_{0_{yy}} = \frac{\phi_{0_y}|_{j+1/2} - \phi_{0_y}|_{j-1/2}}{\tilde{y}_{j+1/2} - \tilde{y}_{j-1/2}} + O\left((dy)^2\right)$$

$$= \frac{\frac{\phi_{0_{j+1}} - \phi_{0_j}}{dy} - \phi_{0_y}|_{y=0}}{dy} \quad \text{specified in B.C.}$$

(Similarly below the wing.)

(ii) In $x > 1$, i.e., $i >$ traile, there is a branch cut with constant jump Γ in ϕ_0. However, ϕ_{0_x} and ϕ_{0_y} are continuous across the cut. Accordingly,

at $j = fup$, use $(\phi_{0_{ij-1}} + \Gamma)$ for $\phi_{0_{ij-1}}$ (above cut)

at $j = fdn$, use $(\phi_{0_{ij+1}} - \Gamma)$ for $\phi_{0_{ij+1}}$ (below cut).

Once the line $i =$ traile$(x = 1)$ has been solved, the circulation Γ is reset to $[\phi]_{TE} = \phi_{\text{traile,fup}} - \phi_{\text{traile,fdn}}$ and the far field is updated with this new value. The whole process

is repeated until ϕ_0 and Γ have converged. In practice, Jameson overrelaxation is used, together with cyclic acceleration.

A flow chart of the main program that computes ϕ_0 is given in Fig. 60. Descriptions of the subroutines indicated therein follow. Additional information is given in Figs. 61–64.

Principal Subroutines

SOLVE: This calls SLOR, and manages the sweeps across the flow field including convergence accelerators and is depicted in Fig. 63.

SLOR: This is the successive line overrelaxation module which solves for the solution column vector on l=constant lines (see Fig. 64).

GRID – This sets up the grid data from the user's description (see the file 2D.DOC).

Output: imax,jmax – size of grid

$x(0{:}\text{imax}{+}1)$, $y(0{:}\text{jmax}{+}1)$ (grid points)

$dx(0{:}\text{imax}{+}1)$, $dy(0{:}\text{jmax}{+}1)$ (grid spacings)

fdn,fup   (lines above and below wing)

leade,traile   (position of leading and trailing edges)   .

There is an option to adapt the grid spacing on the wing to the local slope gradients of the airfoil. This is implemented by letting $dx = \frac{a}{b+|F'_{x,i}(x)|}$. Here, b is a constant which controls the extent of the grid stretching; 2.0 is the default, while $b < 2.0$ will cause greater variations in the spacing and $b > 2.0$ will cause less. The user can control this by modifying the variable "expand" in the control file. The parameter a is adjusted iteratively until the grid just fits nicely onto the wing, i.e., $x(\text{leade}) = -1 + \frac{1}{2} \cdot x(\text{leade})$.

The user gets a summary of the grid and can decide if the computational domain is big enough. (With adaptive gridding, it is difficult to tell beforehand.)

This IMSL routine fits smoothed cubic splines. ICSSCU is used with a user–specified smoothing constant.

ANGLES – Calculates two arrays needed for computing the far field value of ϕ at the boundary.

$$\text{angle} = -\frac{\theta}{2\pi} \qquad \theta = \tan^{-1}\frac{\sqrt{K}\tilde{y}}{x}$$

FARFLD – Updates the far field using the current value of Γ.

$$\phi = \Gamma.\text{angle} + \Gamma^2.\text{ffld2}$$

OUTPUT – Builds two files of results, one formatted (FOR011.DAT) and one unformatted (FOR012.DAT) for graphing.

The data output are C_p and Mach, the local pressure and Mach number distributions, where:

$$C_p = -2\delta^{2/3}M_\infty^n \phi_x$$

SC37666
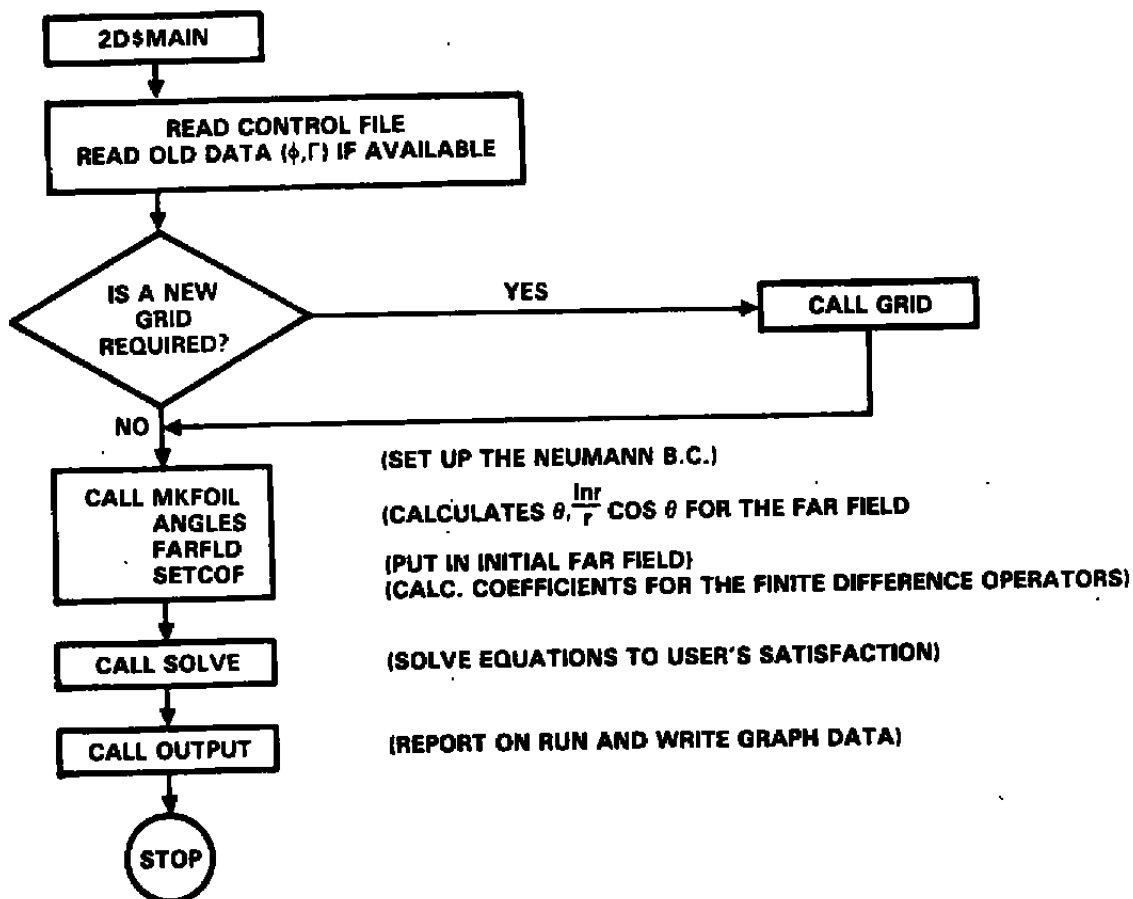
Fig. 60. Flow chart for MAIN program computing ϕ_0.

SC37593

MKFOIL — BUILDS AN ARRAY CONTAINING THE NEUMANN B C VALUES. $F_{u,\ell}(x)-A$

CASE 1 FOR AN NACA 00nn AIRFOIL OR A PARABOLIC ARC AIRFOIL THE F VALUES ARE COMPUTED ANALYTICALLY BY SUBROUTINE FOIL

CASE 2 THE AIRFOIL HEIGHTS ARE GIVEN IN A TABLE
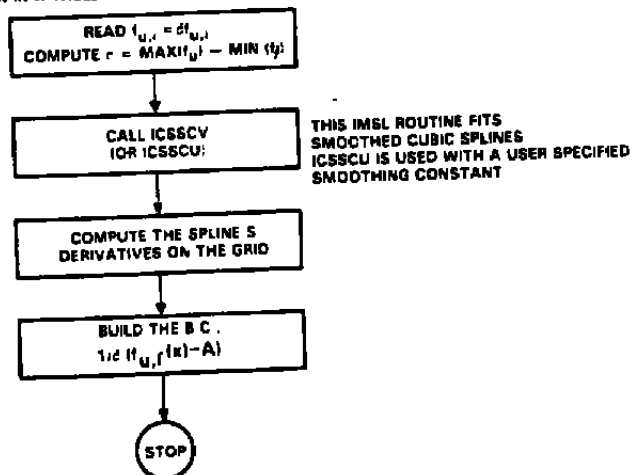
Fig. 61. Flowchart of subroutine MKFOIL.

SC37641
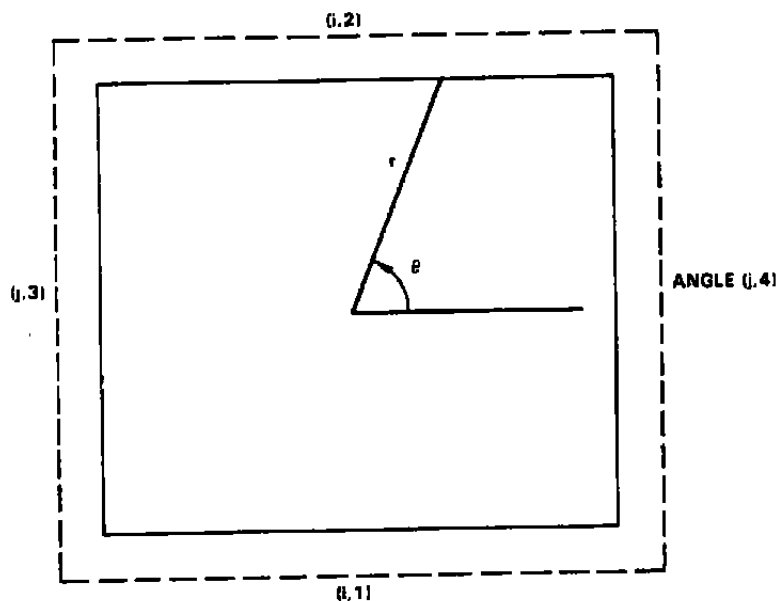
Fig. 62. Angular relations for far field.

6C37674

SOLVES THE TRANSONIC EQUATION BY REPEATEDLY
CALLING SLOR UNTIL ϕ AND Γ HAVE CONVERGED
TO THE USERS SATISFACTION

SOLVE

GET ITERATION COUNT
FROM USER

CALL SLOR.
PRINTOUT MADE $|\Delta\phi|$ AND Γ

IF AT ITERATION n-k
OR n-2k THROUGH A CYCLE
SAVE ϕ

(THIS IS NEEDED FOR THE CYCLIC
ACCELERATION)

IF AT ITERATION n,
ACCELERATE ϕ

IF AT n

ESTIMATE THE LARGEST EIGENVALUE
$\lambda_1 = \delta^T_{n-k}\delta_n/\delta^T_{n-k}\delta_n$
WHERE $\delta_n = \phi_n - \phi_{n-k}$

IF NOT

ACCELERATE ϕ: $\phi_n \leftarrow \phi_{n-k} + \dfrac{1}{1-\lambda_1}(\phi_n - \phi_{n-k})$

RECOMPUTE Γ
CALL FARFLD

COUNT ITERATIONS
LOOP IF MORE TO DO
STOP WHEN COUNT OF 0
0 IS ENTERED

RETURN

Fig. 63. Flowchart for subroutine SOLVE.

8C37663

SUCCESSIVE LINE OVER-RELAXATION
(ONE ITERATION PERFORMED HERE)

SLOR

SAVE 'PHI' IN 'OLD' (NEEDED BY JAMESON OPERATORS)

FOR EACH COLUMN
(i = 1, IMAX)

WHEN DONE

RETURN

FOR EACH ROW
(j = 1, JMAX)

WHEN DONE

REMEMBER $\mu_{i-1,j}$
COMPUTE $\mu_{i,j}$
$(= K - (\gamma + 1)\phi_x)$

BUILD FINITE DIFFERENCE
TERMS FOR
$(K - (\gamma + 1)\phi_x)\phi_{xx}$
BASED ON SIGNS OF
$\mu_{i-1,j}$ AND $\mu_{i,j}$

BUILD F.D. TERMS FOR
ϕ_{yy}

AT
THE WING
?

INCLUDE NEUMANN B.C.   YES

NO

AT
THE CUT
?

INCLUDE JUMP OF Γ   YES

NO

NO

RECOMPUTE Γ
CALL FARFLD

AT
TRAILING
EDGE? (i =
TRAILE?)

YES

SOLVE TRIDIAGONAL SYSTEM
BY GAUSSIAN ELIMINATION

CHECK FOR MAX $|\Delta\phi_{ij}|$

F.D. = FINITE DIFFERENCE

Fig. 64. Flowchart for subroutine SLOR.

117

$$\text{Mach} = 1 - \delta^{2/3} M_\infty^m (K - (\gamma + 1)\phi_x) \qquad \text{(This is actually } M^2.)$$

Here, n and m are the Krupp scaling factors, as used by Krupp, $n = -\frac{3}{4}$; $m = \frac{4}{3}$. For no scaling, $n = m = 0$.

The graph data also contains the critical pressure,

$$C_p^* = -2\delta^{2/3} \frac{K}{\gamma + 1} M^n,$$

above which the flow is supersonic.

Since C_p is only known off the wing, the graphing program extrapolates linearly to find $C_p|_{\tilde{y}=0\pm}$:

$$C_p|_{\tilde{y}=0+} = \frac{3}{2} C_p|_{\tilde{y}=1/2 d y} - \frac{1}{2} C_p|_{\tilde{y}=3/2 d y}.$$

Other subroutines are shown in Figs. 63 and 64.

3.2.2 The Three–Dimensional and Wall Interference Correction ϕ_1

3.2.2.1 Analytic Formulation

Input Parameters

The relevant program modules treat similar and nonsimilar airfoil section wings and obtain interference corrections for these shapes. A similar planform wing is defined as one having the same airfoil section along its span but with its chord varying with span. The numerical methods employed here are a generalization of those used in Ref. 43 for unconfined similar section wings. Remarks on various geometrical aspects are:

(i) The wing is normalized by b so that it lies in $|z| < 1$. The half–chord $c(z)$ is input. For an elliptic wing, shown in Fig. 65, $c(z) = \sqrt{1 - z^2}$.

(ii) As previously indicated, the small parameter for the expansion is $1/B$, where if $AR =$ aspect ratio,

$$B = \delta^{1/3} \cdot b$$
$$= \delta^{1/3} AR \cdot \frac{1}{4} \int_w \quad , \quad \text{where } \int_w = \text{area of planform}$$
$$= \delta^{1/3} AR \cdot \frac{1}{2} \int_{-1}^1 c(z) dz \quad .$$

(iii) The wing may be in a circular wind tunnel as indicated in Fig. 66. The parameter $\mu = \frac{H}{B}$ is input as the reciprocal of the fraction of the tunnel spanned by the wing.
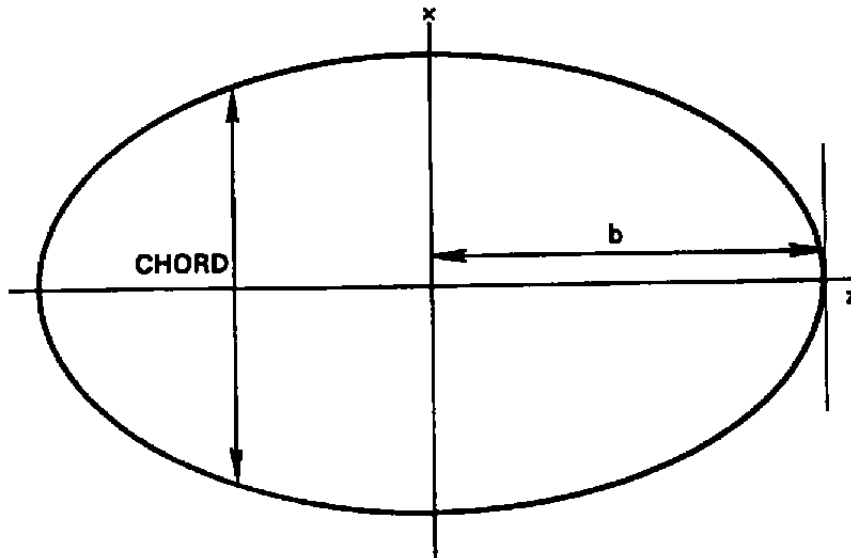
Fig. 65. Elliptic planform.

Boundary Value Problem for ϕ_1

This is:

$$L[\phi_1] \equiv (K - (\gamma+1)\phi_{0_z})\phi_{1_{zz}} - (\gamma+1)\phi_{0_z}\phi_{1_z} + \phi_{1_{\tilde{y}\tilde{y}}} = 0 \qquad (3-58a)$$

$$\phi_{1_{\tilde{y}}}(x,0) = 0 \,;\; \phi_1 \to -\tilde{y}\big(d(z) + w(z)\big) - \frac{\Gamma_1(z)}{2\pi}\theta + \cdots \quad \text{as } r \to \infty \qquad (3-58b)$$

$$[\phi_1]_{\text{wake}} = \Gamma_1(z) \equiv [\phi_1]_{\text{T.E.}} \quad, \quad \text{T.E.} \sim \text{TRAILING EDGE} \;. \qquad (3-58c)$$

Here, $d(z)$ and $w(z)$ are crucial functions controlling the size of the aspect ratio and wind tunnel corrections, respectively. They are given by the integrals

$$d(z) = \frac{1}{4\pi} \fint_{-1}^{1} \frac{\Gamma_0'(\xi)}{z-\xi} d\xi \qquad (3-59a)$$

$\left(\fint = \text{principal value integral}\right)$

$$w(z) = \pm\frac{\mu^2}{4\pi} \fint_{-1}^{1} \frac{\Gamma_0(\xi)}{(z\xi - \mu^2)^2} d\xi \;. \qquad (3-59b)$$

The quantity $w(z)$ in (3−59b) has been obtained from the far field analysis of Sections 3.1.1 and 3.1.2, and the (+) and (−) apply to free jet and closed wall test sections, respectively.

119

SC37848

WING IN OPEN JET TUNNEL
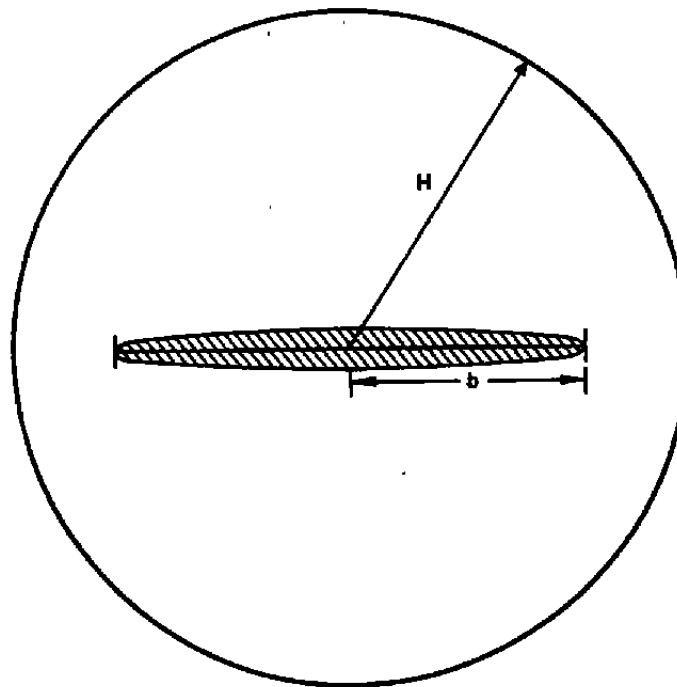
Fig. 66. Front view of wing confined in circular wind tunnel.

Now, taking advantage of the assumption of similar sections*, let

$$\phi_0 = c(z)\psi_0(X,Y) \; ; \; X = \frac{x}{c(z)} \; ; \; Y = \frac{y}{c(z)} \; ; \; F_{u,\ell}(x,z) - Ax = c(z)G_{u,\ell}(X)$$

which gives the reduced problem for ϕ_0

$$(K - (\gamma + 1)\psi_{0_X})\psi_{0_{XX}} + \psi_{0_{YY}} = 0 \quad ; \quad \psi_{0_Y}|_{Y=0} = G_X(X) \quad ; \quad [\psi_{0_X}]_{\text{TE}} = 0 \; . \quad (3-60)$$

The problem $(3-60)$ has no explicit dependence on z. From $\psi_0 = \phi_0(0)$, its solution is obtained as

$$\phi_0(z) = c(z)\phi_0(0) \quad ; \quad \Gamma_0(z) = c(z)\Gamma_0(0) \quad .$$

Use of a similar scaling for ϕ_1 for which $\phi_1 = (d + w)c(z)\psi_1(X,Y)$, gives

$$(K - (\gamma + 1)\psi_{0_X})\psi_{1_{XX}} - (\gamma + 1)\psi_{0_{XX}}\psi_{1_X} + \psi_{1_{YY}} = 0 \qquad (3-61a)$$

$$\psi_{1_Y} = 0 \text{ in } |X| < 1 \quad ; \quad [\psi_{1_X}]_{X=1} = 0 \quad ; \quad \psi_1 \to -Y - \frac{\Gamma_1}{2\pi}\theta + \cdots \quad . \qquad (3-61b)$$

---

* Nonsimilar sections will be treated in Section 3.7.

A modified form of $(3-58)$ is useful to regularize the far field. For this purpose, part of the known far field is subtracted off and $\phi^* = \psi_1 + Y$ is solved for. The resulting boundary value problem for ϕ^* is

$$(K - (\gamma + 1)\phi_{0_X}(0)) \phi_{XX}^* - (\gamma + 1)\phi_{0_{XX}}\phi_X^* + \phi_{\bar{Y}\bar{Y}}^* = 0 \qquad (3-62a)$$

$$\phi_{\bar{Y}}^*|_{\bar{Y}=0} = 1 \quad \text{in} \quad |X| < 1 \qquad (3-62b)$$

$$\phi^* \to -\frac{\Gamma^*}{2\pi}\theta \quad \text{as} \quad r \to \infty \qquad (3-62c)$$

$$[\phi^*]_{\text{wake}} = \Gamma^* \equiv [\phi^*]_{\text{T.E.}} \quad . \qquad (3-62d)$$

The actual solution ϕ_1 is then obtained from

$$\phi_1(z) = (d(z) + w(z))(c(z)\phi^* + y) \qquad (3-63a)$$

$$\Gamma_1(z) = (d(z) + w(z))c(z)\Gamma^* \qquad (3-63b)$$

where now

$$d(z) = \frac{\Gamma_0(0)}{4\pi} \fint_{-1}^{1} \frac{c'(\xi)}{z-\xi}d\xi \quad ; \quad w(z) = \frac{\Gamma_0(0)\mu^2}{4\pi} \fint_{-1}^{1} \frac{c(\xi)}{(z\xi - \mu^2)^2}d\xi \quad . \qquad (3-63c)$$

Within the problem given by $(3-62)$, the position of the shock is known, having been captured by the ϕ_0 solution. It is therefore natural to fit its perturbation into the ϕ_1 problem by using the shock jump relations to provide a set of internal boundary conditions as in Section 2. These are:

$$[\underline{\mu}\phi_x^*] - \beta^2 [\phi_x^*] + 2\beta [\phi_y^*] = -\Delta \frac{[\phi^*]}{[\phi_{0_x}]} \qquad (3-64a)$$

where

$$\underline{\mu} = K - (\gamma + 1)\phi_{0_x} \qquad (3-64b)$$

$$\beta = [\phi_{0_y}] / [\phi_{0_x}] \qquad (3-64c)$$

and

$$\Delta = \beta^2 [\phi_{0_{xx}}] - [\underline{\mu}\phi_{0_{xx}}] - 2\beta [\phi_{0_{xy}}] \qquad (3-64d)$$

are known from the ϕ_0 solution.

3.2.2.2   Numerical Formulation

In the solution for ϕ^*, all of the other scalings are applied only at the output stage. The various elements are calculated as follows:

<u>(i) $d(z)$</u>

$$d(z) = \frac{1}{4\pi} \fint_{-1}^{1} \frac{\Gamma_0'(\xi)}{z-\xi}d\xi = \frac{\Gamma_0(0)}{4\pi} \fint_{-1}^{1} \frac{c'(\xi)}{z-\xi}d\xi \quad . \qquad (3-65)$$

The simplest case is for an elliptical planform, $c(z) = \sqrt{1 - z^2}$. Then,

$$d(z) = \Gamma_c(0)/4 \quad . \qquad\qquad (3 - 66)$$

Otherwise, the trigonometric substitution

$$z = -\cos\theta \qquad\qquad (3 - 67)$$

is used and the planform shape is represented by the sine series

$$c(z) = \sum_{n=1}^{\infty} A_n \sin n\theta \quad .$$

The integral $(3 - 65)$ then becomes

$$d(z) = \frac{\Gamma_0(0)}{4} \frac{1}{\sin\theta} \sum_{n=1}^{\infty} n A_n \sin n\theta \quad . \qquad\qquad (3 - 68)$$

In practice, $c(z)$ is given at a series of span stations. The transformation $(3 - 67)$ is used and a cubic spline is fitted to $c(z)$. It is evaluated at $\theta = 2\pi\frac{m}{n}$, where $m = 0, \cdots n$ (say), and the A_n are then computed with a discrete Fourier transform.

This works well for smooth, near–elliptical planforms, but for others (e.g., sharp cornered wings such as rectangular and delta planforms), $d(z)$ may have singularities which need further treatment.

(ii) $w(z)$

$$w(z) = \pm\frac{\mu^2}{4\pi} \int_{-1}^{1} \frac{\Gamma_0(\xi)}{(z\xi - \mu^2)^2} d\xi \quad . \qquad\qquad (3 - 69)$$

Here, $\mu > 1$. Therefore, the integrand is finite everywhere, and a straightforward quadrature using the trapezoidal rule seems perfectly adequate.

(iii) Solution for ϕ^* (Shock–Free Case)

In the solution of $(3-62)$, the grid and ϕ_0 are input from some previous run which used an identical computational grid. The coefficients $(K-(\gamma+1)\phi_{0_x})$, $(\gamma+1)\phi_{0_{xx}}$ are computed using central differences in elliptic regions, and backward differences in hyperbolic zones. The parabolic value zero is used for $K - (\gamma + 1)\phi_{0_x}$ at a subsonic to supersonic transition. This keeps the system stable. The subsonic and supersonic regions are already known from the ϕ_0. Apart from this, the solution proceeds in the same way as for ϕ_0.

The initial guess for ϕ^* can be $\phi^* = 0$, an old solution, or an analytic solution to the Prandtl–Glauert equation. Since ϕ_{0_x} and $\phi_{0_{xx}} \to 0$ as $r \to \infty$,

$$K\phi^*_{xx} + \phi^*_{\bar{y}\bar{y}} = 0$$

122

will be a reasonable approximation, at least in the subsonic case, with the boundary conditions $(3 - 62b)$–$(3 - 62d)$. This "flat plate" problem can be solved analytically with the following rescaling

$$\tilde{Y} = \sqrt{K}\tilde{y} \Rightarrow \psi_{xx} + \psi_{YY} = 0 \quad , \quad \psi_Y|_{Y=0} = \frac{1}{\sqrt{K}} \quad ; \quad \Rightarrow \phi^*(x,\tilde{y}) = \frac{1}{\sqrt{K}}\psi(x,\sqrt{K}Y)$$

to give

$$\psi(x,\tilde{y}) = \mathrm{Re}\left\{-iZ + \sqrt{1 - Z^2} + 2\tan^{-1}\sqrt{\frac{1+Z}{1-Z}} + \pi\right\}$$

$$\left(Z = x + i\sqrt{K}\tilde{y}\right) \quad . \tag{3-70}$$

To evaluate $(3 - 70)$, the following branch cuts may be used:

$$0 < \theta_{\pm} \leq 2\pi \quad , \quad \arg(Z + 1) = \theta_- \tag{3 - 71a}$$

$$\arg(Z - 1) = \theta_+ \quad , \tag{3 - 71b}$$

where θ_+ and θ_- are shown in Fig. 67. This solution has $\Gamma^* = -\frac{2\pi}{\sqrt{K}}$, which is not too far from the value obtained from a numerical solution of $(3 - 62)$.

8C37638

ARGUMENTS FOR
"FLAT PLATE" SOLUTION
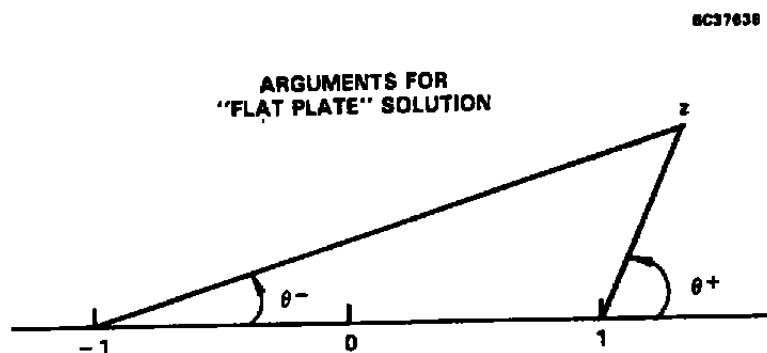
Fig. 67. Arguments used in Eq. $(3 - 70)$.

(iv) Treatment of Shock Conditions

From Refs. 29 and 32, the shock equations are:

$$\text{Zeroth order} \begin{cases} [\phi_0] = 0 & (3\text{-}72a) \\ \left[K\phi_{0_x} - \frac{\gamma+1}{2}\phi_{0_x}^2\right][\phi_{0_x}] + [\phi_{0_j}]^2 = 0 & (3\text{-}72b) \end{cases}$$

$$\text{First order} \begin{cases} [\mu\phi_x^*] - \beta^2[\phi_x^*] + 2\beta[\phi_{\tilde{y}}^*] = g_1\left\{\beta^2[\phi_{0_{xx}}] - [\mu\phi_{0_{xx}}] - 2\beta[\phi_{0_{xj}}]\right\} & (3\text{-}73a) \\ [\phi^*] = -g_1[\phi_{0_x}] & (3\text{-}73b) \end{cases}$$

123

where $\underline{\mu} = K - (\gamma + 1)\phi_{0_x}$, $\beta = \left[\dfrac{\phi_{0_y}}{\phi_{0_x}}\right]$, and $x = g_1(\bar{y})$ is the correction to the shock locus.

Eliminating g_1 and using the zeroth order equations yields

$$\left[\underline{\mu}\phi_x^*\right] - \beta^2\left[\phi_x^*\right] + 2\beta\left[\phi_{\bar{y}}^*\right] = -\Delta\frac{[\phi^*]}{[\phi_{0_x}]} \tag{3-74}$$

where $\Delta = \beta^2\left[\phi_{xx}^*\right] - \left[\underline{\mu}\phi_{0_{xx}}\right] - 2\beta\left[\phi_{0_{x\bar{y}}}\right]$. This is the governing equation for the ϕ^* shocks.

The shock is fitted over three mesh spacings — empirically, the numerical width of the captured shocks. If $\mu_{i-2,j} < 0$ and $\mu_{i-1,j} > 0$, then the two sides of the shock notch are at (i,j) and $(i-3,j)$, respectively, downstream and upstream as shown in Fig. 68. The case when not all shock points lie between the same two grid points will be considered later.

The coefficients μ_I, μ_{I-3}, β, and Δ are all evaluated by taking differences of the quantities evaluated at I and $I - 3$.

The solution proceeds normally up to and including $i = I - 3$. At that line, all the points on the notch will be either hyperbolic or parabolic. Accordingly, the difference equations will be numerically explicit.

Lines $I - 2$ and $I - 1$ are solved normally above the notch; values for $(I - 2, jsmax)$ and $(I - 1, jsmax)$ are extrapolated linearly from either side, under the assumption that the jump falls entirely between $I - 2$ and $I - 1$. This is indicated schematically in Fig. 69. The shock strength is assumed to vanish at $jsmax$.

At line I, $(3-74)$ is used to provide equations for points fup to $jsmax$; $j = jsmax + 1$ to $jmax$ are treated normally as interior points in the usual manner. In $(3-74)$ the jumps are computed from

$$[(\cdot)] = (\cdot)_I - (\cdot)_{I-3} \qquad . \tag{3-75}$$

In the treatment of the jumps of the derivatives,

ϕ_{xI}^* uses a two point forward difference, $\dfrac{\phi_{I+1,j} - \phi_{I,j}}{(dx)_I}$

ϕ_{xI-3}^* uses a three point backward difference,

e.g., $\dfrac{1}{2(dx)_{I-4}}\left(3\phi_{I-3} - 4\phi_{I-4} + \phi_{I-5}\right)$ (for a uniform grid).

$\phi_{\bar{y}}^*$ uses a three point centered difference, $\dfrac{1}{2(dy)}\left(\phi_{I,j+1} - \phi_{I,j-1}\right)$ (for a uniform grid)

At $j = fup$, the known Neumann boundary condition on the 1/2 node of tangent flow on the wing is used with the following average of point values, recognizing that the body is at a 1/2 node point.

$$\phi_{\bar{y}}^* = \frac{1}{2}\left(\phi_{\bar{y}j+1/2}^* + \phi_{\bar{y}}^*|_{\bar{y}=0}\right) \tag{3-76}$$

Because $\phi_{\bar{y}}^* = 1$ everywhere on the wing, it cancels out in $\left[\phi_{\bar{y}}^*\right]$. Thus

$$\left[\phi_{\bar{y}}^*\right]_{j=fup} = 0 \qquad . \tag{3-77}$$
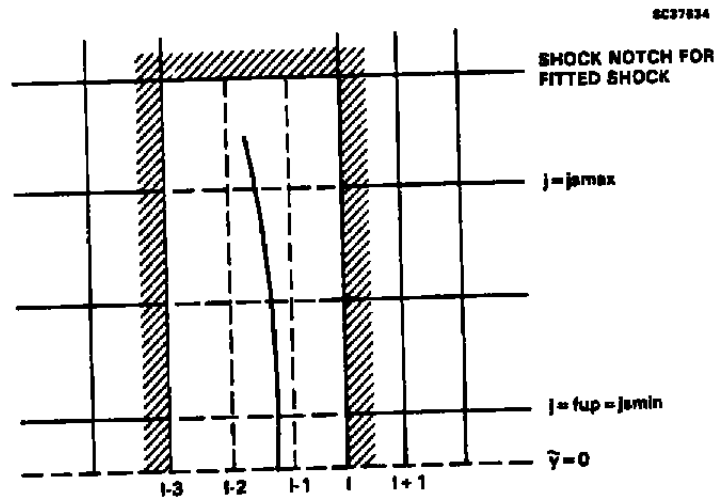
Fig. 68. Orientation of shock notch.
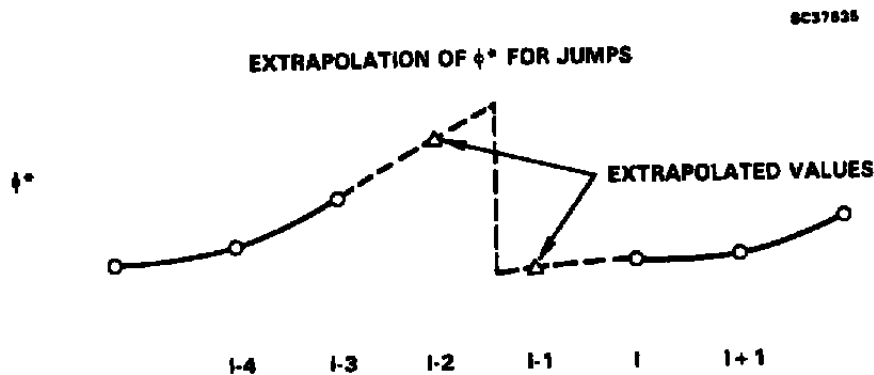
Fig. 69. Linear extrapolation at shock.

This approach gives a full tridiagonal system of equations for line I. Once solved, the solution proceeds normally at line $I + 1$.

The shocks captured in the ϕ_0 solution are not always vertical. It is unlikely that the sonic line will stay between the same two I values for the entire shock. There seem to be three options when this occurs:

(i) Use a wide notch so as to cover the whole shock (see Fig. 70a). For strongly inclined shocks (not typical of the transonic case or coarse grids), some of the information on

the computational grid will be lost. Also, differences (*i.e.*, $[\phi^*]$) would include more than just the shock. This has the advantage of logical simplicity and is incorporated in the slender body code.

(ii) Use a one point notch which follows the shock (see Fig. 70b). Here we would use direction–sensitive differences for $\phi_{\bar{y}}^*$ and stencils that look like ($\not{r}$ or $\natural$). To get the correct coefficients, however, $\left([\phi_{0x}] \text{ etc.} \right)$ they would need to be still calculated across three mesh spacings. This could be somewhat inconsistent for some points (such as Column I) which would be using coefficients from the middle of the numerical shock.

(iii) Use a three point notch which follows the shock (see Fig. 70c). This avoids some of the problems of (ii), but has some of its own, e.g., how to calculate $\phi_{\bar{y}}^*$ at points like ① and ② . Central differences (as currently used) would require ϕ^* values from inside the notch. These could be obtained by linear extrapolation in x, as explained earlier, but this introduces errors of at least $O(h)$, and possible inconsistencies.

This is the method currently implemented. Perhaps a better way to calculate $\phi_{\bar{y}}^*$ would be direction–sensitive one–point difference as in (ii). Here, one point forward on the right (downstream) side and one point backward on the left for backwardly inclined shocks and the reverse for forward inclinations.

(v) Output

The total lift L is given by

$$L = \rho U_\infty^2 b \frac{\delta^{2/3}}{M_\infty^n} \int_{-1}^{1} \Gamma(z) dz \quad , \quad \text{where } b = \text{semispan} \qquad (3-78)$$

and $\Gamma(z) = $ total circulation

$$= \Gamma_0(z) + \frac{1}{B}\big(d(z) + w(z)\big)\Gamma^*(z) \quad . \qquad (3-79)$$

Then,

$$C_L = \frac{L}{\frac{\rho U_\infty^2}{2} S_W} \quad \left(S_W = \text{area of wing} = 2b \int_{-1}^{1} c(z) dz \right)$$

$$= \frac{\delta^{2/3}}{M_\infty^n} \left(\int_{-1}^{1} \Gamma(z) dz \right) \frac{1}{\int_{-1}^{1} c(z) dz} \qquad (3-80)$$

$$= \frac{\delta^{2/3}}{M_\infty^n} \Gamma_0(0) \frac{\int_{-1}^{1} c(z)[1 + \frac{1}{B}(\bar{d} + \overline{w})\Gamma^*] dz}{\int_{-1}^{1} c(z) dz} \quad \text{for the similar sections case} (3-81)$$

where $\bar{d} = \frac{d(z)}{\Gamma_0} = \frac{1}{4}$ for an elliptic planform. For the free field case,

$$C_L = \frac{\delta^{2/3}}{M_\infty^n} \Gamma_0(0) \left(1 + \frac{\Gamma^*}{4B} \right) \quad , \quad B = \delta^{1/3} \cdot AR \cdot \frac{1}{2} \int_{-1}^{1} c(z) dz$$

$$= \delta^{1/3} \cdot AR \cdot \frac{\pi}{4} \text{ for an elliptic planform.} \qquad (3-82)$$

126

WIDE NOTCH
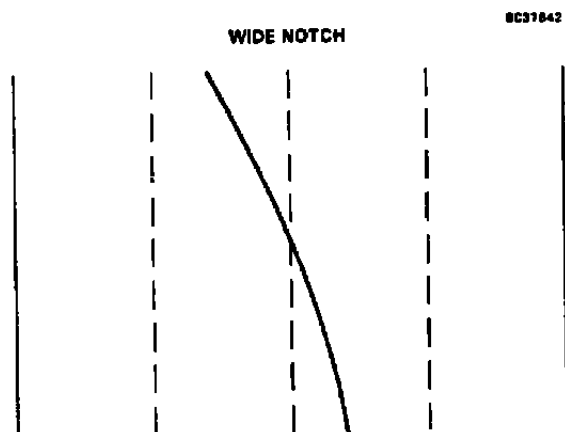
Fig. 70a. Wide shock notch.
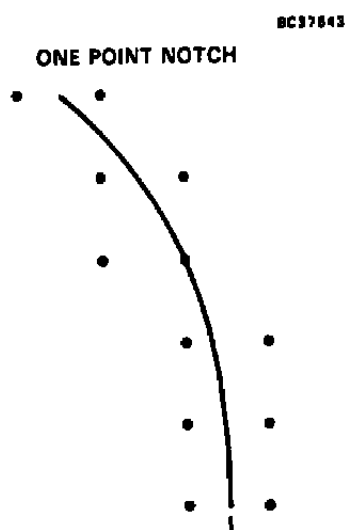
ONE POINT NOTCH

Fig. 70b. One point shock notch.

THREE POINT NOTCH

① ②
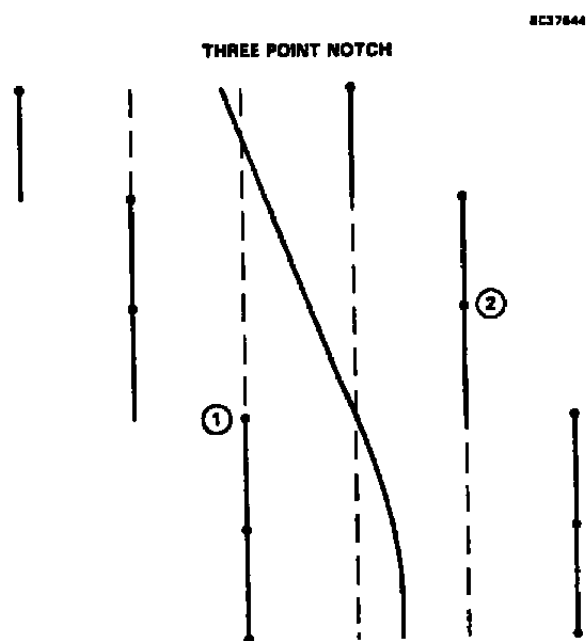
Fig. 70c. Three point shock notch.

Other quantities, such as the corrected pressure on the wing at a particular span station, can be similarly calculated using

$$\phi = \phi_0 + \frac{1}{B}\phi_1 \qquad (3-83a)$$

$$C_p = -2\delta^{2/3}\phi_x \quad . \qquad (3-83b)$$

3.2.2.3   Program Operation and Flow Chart

Many of the modules in PHI1 have the same function and implementation as in 2D. (In fact, SOLVE, ANGLES, and FARFLD are used directly by both programs.) Accordingly, only the substantial changes are discussed here.

Principal Subroutines

PHI1

Functions:

> Read control file.
>
> Read zeroth order results.
>
> Read ϕ^*, Γ^* if available.
>
> Initialize ϕ^* (method controlled by user).
>
> (i) to 0, $\phi^* = \Gamma^* = 0$.
>
> (ii) to the solution of $K\phi^*_{xx} + \phi^*_{yy} = 0$, by calling PHILAPL.
>
> (iii) to an old solution.
>
> Call WINGSC to compute the span scaling function $d(z)$.
>
> If $\mu \neq 0$, call TUNLSC to compute $w(z)$.
>
> Call SETUP to compute partial differential coefficients, and the shock relations.
>
> Call SOLVE to solve the ϕ_1 boundary value problem.
>
> Call OUTPUT to write graphics and informative results.
>
> Write ϕ^* and Γ^* to OUT_FILE, if requested.
>
> Stop.

WINGSC — Computes $d(z)$; see Section 3.2.2.2 (i).

The wing profile is read from WING_FILE, which should consist of $(z, c(z))$ pairs, one per line. This is extended, first to form a symmetrical wing, and then a periodic function, as shown in Fig. 71.

z is mapped into θ via $z = -\cos\theta$; $0 \le \theta \le 2\pi$. A periodic cubic spline is fitted in θ. The idea is that wings may often look like $\sqrt{1-z^2}$ near the tips; the transformation will remove the singularity in $c'(z)$ which will help to provide a more accurate spline fit in this neighborhood.

The spline is evaluated at m equally spaced points in $[0, 2\pi)$ where $m = 2n$, $n =$ number of input and extended points. (Too many would start to fit wiggles in the splines; too few will not give enough Fourier coefficients.)

These values are used to compute a discrete Fourier transform of $c(\theta)$.

The downwash integral $\frac{1}{4\pi} \int_{-1}^{1} \frac{c'(\xi)}{z - \xi} d\xi$ (Eq. $(3 - 65)$) is then evaluated.

These values of $d(z)$ are then used to compute weffect $= \dfrac{\int_{-1}^{1} d(z)c(z)dz}{\int_{-1}^{1} c(z)dz}$ by trapezoidal quadrature.

"weffect" is the relative lift contribution due to aspect ratio (see Section 3.2.2.2 (v)).

TUNLSC — Computes $w(z)$; see Section 3.2.2.2 (ii).

The wind tunnel ratio μ is an argument (variable um); the integral is calculated by the trapezoidal rule on a 51-point grid on $[-1, 1]$.

The integral teffect $= \dfrac{\int_{-1}^{1} w(z)c(z)dz}{\int_{-1}^{1} c(z)dz}$ is calculated similarly to weffect. It is the relative lift contribution due to wall interference (see Section 3.2.2.2 (v)).

SETUP — Calculates various coefficients used in the ϕ_1 boundary value problem and shock relations (see Fig. 72).

Principal Variables

$CX(1 : IMAX, 1 : 3)$ Computational molecule for first x derivative (centered).

$$CX(I, 1 : 3) = \frac{-h_2}{h_1(h_1 + h_2)} \quad , \quad \frac{h_2 - h_1}{h_1 h_2} \quad , \quad \frac{h_1}{h_2(h_1 + h_2)}.$$

$CXX(1 : IMAX, 1 : 3)$ Molecule for second x derivative (centered).

$$CXX(I, 1 : 3) = \frac{2}{h_1(h_1 + h_2)} \quad , \quad \frac{-2}{h_1 h_2} \quad , \quad \frac{2}{h_2(h_1 + h_2)}.$$

$PX(1 : JMAX, 1 : JMAX)$ Values of $K - (\gamma + 1)\phi_{0_x}$, calculated with

— central differences in elliptic regions

— backward differences in hyperbolic regions

— parabolic (i.e., $PX = 0$) at the elliptic to hyperbolic transition

No shock operator is used at the hyperbolic to elliptic transition; since it is handled by the fitted shock).

$PXX(1 : IMAX, 1 : JMAX)$ Values of $(\gamma + 1)\phi_{0_{xx}}$, using central/backward differences.

$SHK(1 : JMAX)$ Relates to the fitted shock.

129

$SHK(J) = I$ Denotes the position of the downwind side of the shock notch at line J as indicated in Fig. 73 and $= 0$ if there is no shock at that line.

$JSMIN, JSMAX$ denote the j-limits of the shock. If the shock is only above the wing say, $JSMIN = FUP$. If there is no shock at all, $JSMAX < JSMIN$.

The second part of SETUP evaluates various jumps and coefficients across the shock, and prepares them for the treatment of the numerical shock jump equation. Suppose $SHK(J) = I$. Then:

$a = \left[\phi_{0_x}\right] = \phi_{xI} - \phi_{xI-3}$ (central differences)

$b = \left[\phi_{0_f}\right] / \left[\phi_{0_s}\right] \leftrightarrow \beta.$

$\quad = \frac{\phi_{yI} - \phi_{yI-3}}{a}$

For this quantity, $\phi_{\bar{y}}$ is calculated using central differences away from the wing. On it, the known boundary condition, i.e., $\phi_{y_1} = \frac{1}{2}\left[\frac{\phi_2 - \phi_1}{\Delta y} + \phi_{y_0}\right]$ with ϕ_{y_0} given is employed.

$c = \beta^2\left[\phi_{0_{xx}}\right] - \left[\mu\phi_{0_{xx}}\right] - 2\beta\left[\phi_{0_{xy}}\right] \leftrightarrow \Delta$, where $\mu = K - (\gamma + 1)\phi_{0_x} = PX.$

From these quantities, eight coefficients are stored in a common block for SLOR to access later. These are:

$CJMP(J, 1:3) = 2\beta \cdot CY(J, 1:3)$ The molecule for $2\beta\phi_{1_y}$

$CJMP(J, 4) = \Delta / \left[\phi_{0_x}\right] = \frac{c}{a}$

$CJMP(J, 5) = \frac{\mu_I}{x_{I+1} - x_I}$

$CJMP(J, 6:8)$ The computational molecule for $\mu_{I-3}\phi_{1_{xI-3}} + \frac{\Delta}{\left[\phi_{0_x}\right]}\phi_{1I-3}$.

The differencing used here for ϕ_{1_x} is backwards and has error $O(h^2)$, not $O(h)$.

$$\begin{array}{ccc} I-5 & I-4 & I-3 \\ \cdot & \cdot & \cdot \\ & h_2 \quad\quad h_1 & \end{array}$$

The coefficients of $\phi_{I-5,4,3}$ are:

$$\frac{h_1}{h_2(h_2 + h_2)} \quad , \quad \frac{-(h_1 + h_2)}{h_1 h_2} \quad , \quad \frac{2h_2 + h_2}{h_1(h_1 + h_2)} \quad .$$

With these eight coefficients, the shock relation

$$\left[\mu\phi_x^*\right] - \beta^2\left[\phi_x^*\right] + 2\beta\left[\phi_y^*\right] = -\Delta\frac{\left[\phi^*\right]}{\left[\phi_{0_x}\right]}$$

is represented as

$$CJMP_1\phi_{I,J-1} + CJMP_{2+4-5}\phi_{I,J} + CJMP_3\phi_{I,J+1} = CJMP_{6,7,8} \cdot \phi_{(I-5,4,3),j}$$
$$- CJMP_5\phi_{I+1,j} + CJMP_{1,2,3} \cdot \phi_{I-3,U}$$
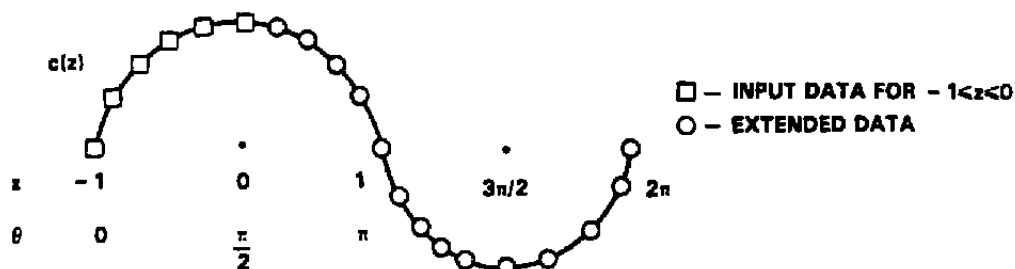
Fig. 71. Periodic extension of planform.

Fig. 72. Computational
molecule used in SETUP.
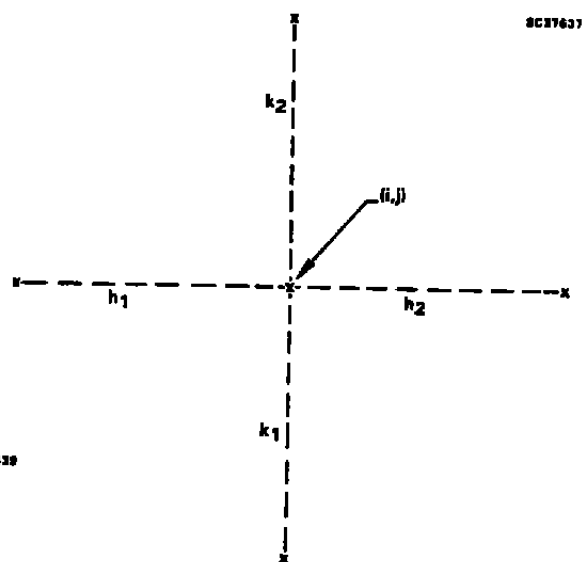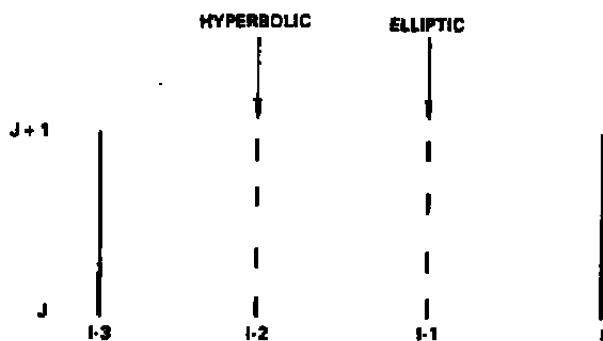
Fig. 73. Pre and post shock
sides of shock notch.

where U can equal $J - 1$, J, or $J + 1$.

As before, $\phi_{\tilde{y}}^*$ at $J = FDN$ or FUP is computed using the Neumann boundary condition $\phi_{\tilde{y}}^*|_{\tilde{y}=0} = 1$ (see Section 3.2.2.2 (iv)).

PHILAPL $(x, \tilde{y}, \sqrt{K})$ calculates the analytic solution to the Prandtl Glauert "flat plate" problem (PG1) $K\phi_{xx} + \phi_{\tilde{y}\tilde{y}} = 0$; $\phi_{\tilde{y}} = 1$ at $\tilde{y} = 0, 0 \le x \le 1$; $\phi \to -\frac{\Gamma\theta}{2\pi}$ as $r \to \infty$ at the point $(x, \tilde{y})$, with $\theta = \tan^{-1}\sqrt{K}\tilde{y}/x$ and $r^2 = x^2 + K\tilde{y}^2$.

If $Z = x + iY$, with $Y = \sqrt{K}\tilde{y}$, then the solution is obtained from the incompressible map (IPG1) of PG1: $\phi_{xx} + \phi_{YY} = 0$ with $\phi \to \frac{-\Gamma}{2\pi}\tan^{-1}\frac{Y}{x}$ as $x^2 + Y^2 \to \infty$ and $\phi_Y(x,0) = \frac{1}{\sqrt{K}}$, $0 \le x \le 1$. This is:

$$\phi = \operatorname{Re} F(Z) = \frac{1}{\sqrt{K}}\operatorname{Re}\left\{-iZ + \sqrt{1 - Z^2} + 2\tan^{-1}\sqrt{\frac{1+Z}{1-Z}} + \pi\right\}, \quad \text{(see 3.2.2.2 (iii))}$$

$$= \frac{1}{\sqrt{K}}\operatorname{Re}\left\{-iZ + \sqrt{1 - Z^2} + 2\tan^{-1}\sqrt{\frac{1-Z}{1+Z}}\right\}$$

$$(3 - 84)$$

Equation $(3 - 84)$ is obtained from integration (Ref. 44 195.04) of the complex velocity for IPG1, $F'(Z)$. Thus,

$$F'(Z) = u - iv = i\left(\sqrt{\frac{Z-1}{Z+1}} - 1\right). \tag{3 - 85}$$

$$u = \phi_x(x, Y) \quad, \quad v = \phi_Y(x, Y)$$

The real and imaginary parts of $(3 - 85)$ give

$$u = -\sqrt{\frac{r_+}{r_-}}\sin\left(\frac{\theta_+ - \theta_-}{2}\right) \tag{3 - 86a}$$

$$v = -\sqrt{\frac{r_+}{r_-}}\cos\left(\frac{\theta_+ - \theta_-}{2}\right), \tag{3 - 86b}$$

where

$$\theta_{\pm} = \arg(Z \mp 1) \quad, \quad 0 < \arg(\cdots) < 2\pi \tag{3 - 87a}$$

$$r_{\pm} = \operatorname{mod}(Z \mp 1). \tag{3 - 87b}$$

Equation $(3 - 84)$ indicates that $\Gamma = -2\pi$ for the Neumann boundary conditions assumed. Equation $(3 - 86a)$ exhibits the square root infinity in the perturbation pressure u near the leading edge $(r_- = 0)$, and the fulfillment of the Kutta condition $[u] = 0$ at the trailing edge $r_+ = 0$. These features as well as the satisfaction of the boundary condition on $Y = 0$, $0 \le x \le 1$, can be ascertained from $(3 - 87a)$.

In the notation of the subroutine,

$$\arg 1 \leftrightarrow \arg(Z+1) = \tan^{-1}\left(\frac{Y}{x+1}\right)$$

$$\arg 2 \leftrightarrow \arg(1-Z) = \tan^{-1}\left(\frac{Y}{x-1}\right)$$

$$THETA \leftrightarrow \frac{1}{2}(\arg 1 - \arg 2) \qquad \left(= \arg\sqrt{\frac{1+Z}{1-Z}}\right) \quad .$$

Quantities used to compute $\operatorname{Re}\tan^{-1}\sqrt{\frac{1+Z}{1-Z}}$, where $\tan^{-1}Z = \frac{1}{2i}\ln\frac{1+iZ}{1-iZ} \Rightarrow \operatorname{Re}(\tan^{-1}) = \frac{1}{2}\arg\left(\frac{1+iZ}{1-iZ}\right)$ are:

$$a \leftrightarrow \sqrt{\left|\frac{Z+1}{Z-1}\right|} \qquad \left(i.e., \sqrt{\frac{1+Z}{1-Z}} = ae^{i \cdot THETA}\right),$$

$$b \leftrightarrow i\sqrt{\frac{1+Z}{1-Z}} = -a\sin(THETA) + id\cos(THETA),$$

$$b^* \leftrightarrow \frac{1+b}{1-b},$$

$$a\tan \leftrightarrow \frac{1}{2}\arg(b^*),$$

$$c \leftarrow \sqrt{|1-z^2|},$$

$$THETAI \leftarrow \frac{1}{2}(\arg 1 + \arg 2) \qquad (\text{So that } \sqrt{1-Z^2} = ce^{i \cdot THETAI}) \quad .$$

These results give,

$$\phi \leftarrow \frac{1}{\sqrt{K}}\{Y + c \cdot \cos(THETAI) + 2 \cdot a\tan + \pi\} \quad .$$

Figure 74 outlines the post processing operations and Fig. 75 indicates the subroutine SLOR.

3.2.3 Convergence Acceleration

Slow convergence can occur for lifting cases. This is marked by the error

$$\epsilon_k = \max|\phi_k - \phi_{k-1}|$$

becoming small although the solution is far from its limit value.

One possible acceleration technique developed in Ref. 45 uses estimates of the largest eigenvalue(s) of the error matrix to guess the limit. If these eigenvalues are $\lambda_1 > \lambda_2 > \cdots$, then

$$\phi = \phi_k + \frac{\phi_{k+1} - \phi_k}{1 - \lambda_1} + \delta_k$$

OUTPUT — WRITES 2 FILES OF RESULTS FOR014.DAT WHICH REPORTS
ON THE RUN AND FOR015.DAT WHICH IS UNFORMATTED
AND CONTAINS GRAPHICS DATA

COMPUTE SCALING FACTORS
$SCALCP = -2\delta^{2/3} M^{-n}$
$SCALM = \delta^{2/3} M^{m}$

FOR KRUPP SCALING, $n = \frac{3}{4}$, $m = \frac{4}{3}$

FOR "NORMAL" SCALING, $m = n = 0$.

EXTRAPOLATE ϕ AND ϕ^* ON TO
$y = 0$, LINEARLY

SECOND ORDER EXTRAPOLATION IS
POSSIBLE USING SOLUTION VALUES OF
$\phi_y|_y = 0$ BUT IS NONUNIFORMLY VALID AT
LEADING AND TRAILING EDGES.

COMPUTE C_{P_0} AND C_{P_1}
$(= SCALCP \, \Phi_x)$
AT $y = 0$

LINEARLY INTERPOLATE
FOR C_{P_1} AT THE NOTCH

ANOTHER POSSIBILITY IS TO PUT THE
JUMP ALL IN ONE PLACE AS IN 2(iv)

FOR $j = jsmin$ TO $jsmax$
GET $g1(j) = -[\phi^*]/[\phi_{ox}]$

COMPUTE LIFT COEFFICIENTS:
0TH ORDER, AND ADJUSTED FOR
AR AND WING TUNNEL EFFECTS

$C_{L_0} \cdot \delta^{2/3} \Gamma_0$
$C_{L_1} \cdot C_{L_0} \{1 + \left(\dfrac{w_{EFFECT} + t_{EFFECT}}{B}\right) \Gamma^*\}$

COMPUTE 0TH ORDER AND
CORRECTION MACH
NUMBERS

$MACH0 \sim -\delta^{2/3} (K - (\gamma+1)\phi_{0_x})$
$\Delta MACH1 \sim \delta^{2/3} (\gamma+1)\phi_x^*$

WRITE DATA TO FILES

RETURN

Fig. 74. Flowchart of postprocessing elements, (repeated as Fig. 89)

SC37570

SLOR — PERFORMS ONE LINE OVERRELAXATION ITERATION ON THE FIRST ORDER CORRECTION
TO THE TRANSONIC SMALL DISTURBANCE EQUATION.

$$(K-(\gamma+1)\phi_{ox})\phi^*_{xx}-(\gamma+1)\phi_{oxx}\phi^*_x+\phi^*_{yy}=0$$
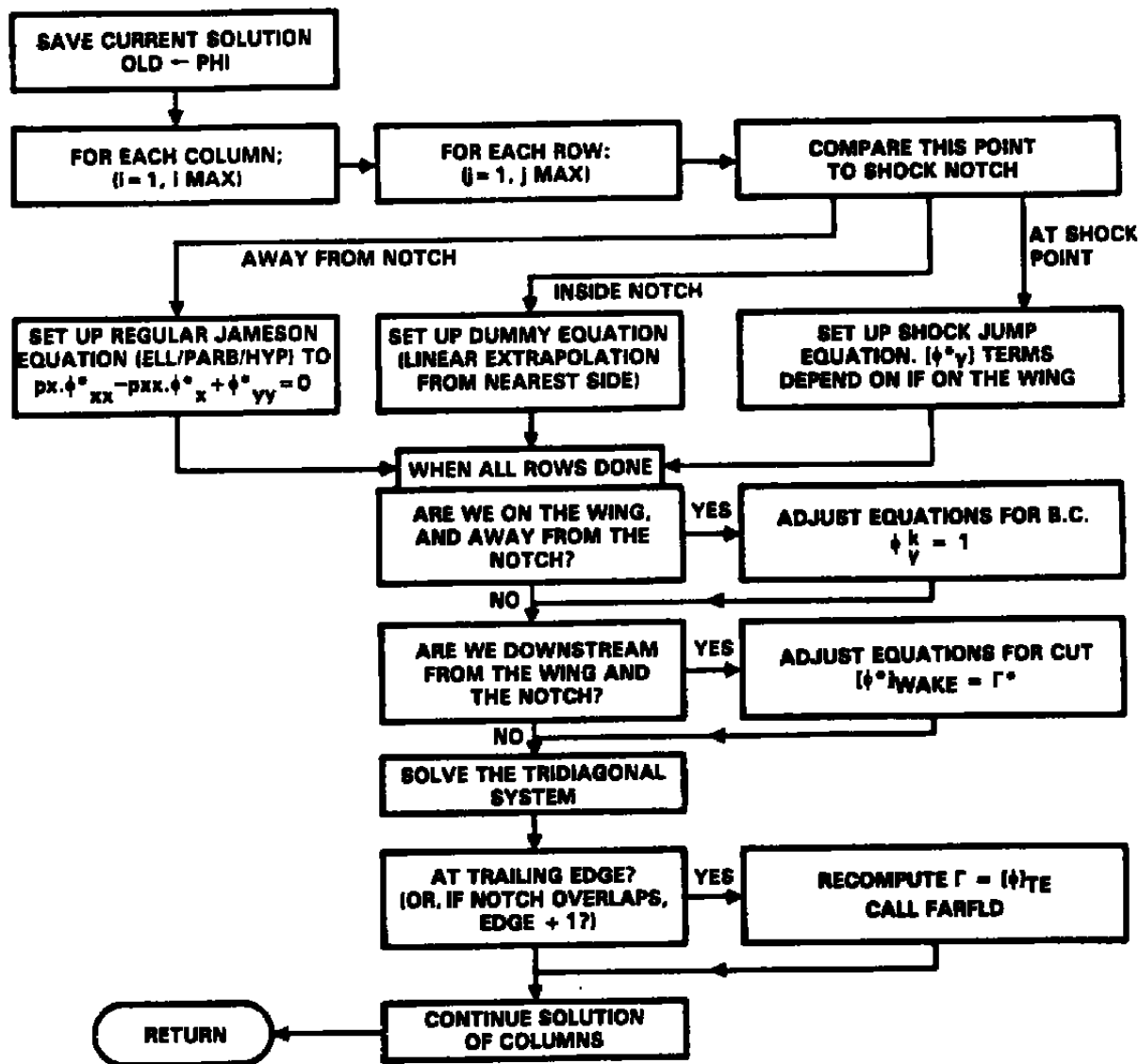
Fig. 75. Flowchart of subroutine SLOR.

is the formal limit, where δ_k is at most of order λ_2^k.

There are several ways of estimating λ. Three of these are given below as λ_1, $\overline{\lambda}_1$, and $\overline{\overline{\lambda}}_1$, where

$$\lambda_1 = \frac{|\phi_{k+1}^* - \phi_k^*|}{|\phi_k^* - \phi_{k-1}^*|} \quad \text{(where } \phi^* \text{ is } \phi \text{ evaluated at some fixed reference point)}$$

$$\overline{\lambda}_1 = \sum |\phi_{k+1} - \phi_k| / \sum |\phi_k - \phi_{k-1}|$$

$$\overline{\overline{\lambda}}_1 = \delta_k^T \delta_{k+1} / \delta_k^T \delta_k \quad , \quad \text{where } \delta_k = \phi_k - \phi_{k-1} \quad .$$

In our experiments, $\overline{\overline{\lambda}}_1$ seemed to be best: λ_1 is sensitive to roundoff and the choice of ϕ^*, while $\overline{\lambda}_1$ seemed to be frequently greater than 1.

Implementation: We use cyclic acceleration with cycle length k (typically 12–16) based on iterates m apart (typically 2 or 4). k iterations are performed normally, then an acceleration performed via:

$$\overline{\overline{\lambda}}_1^m = \delta_{k-m}^T \delta_k / \delta_{k-m}^T \delta_{k-m} \quad ; \quad \delta_k = \phi_k - \phi_{k-m}$$

$$\phi_k \leftarrow \phi_{k-m} + \frac{\phi_k - \phi_{k-m}}{1 - \overline{\overline{\lambda}}_1^m} \quad .$$

Then the cycle is repeated.

Advantages of Method

— As indicated in the Results section, the acceleration method in the long run helps convergence greatly.

— By giving the solution a "kick" every k iterations, it stops it from being trapped in a local near-solution well.

Disadvantages of Method

— As the mesh spacing $\to 0$, $\lambda_1 \to 1$. In practice, $\overline{\overline{\lambda}}_1 > 1$ can occur. In this case, we set $\overline{\lambda}_1 = .985$ (say) which upset the solution in some cases.

— The accelerated ϕ does not satisfy the difference equations. The process may move ϕ and Γ as a whole closer to their limits, but then most of the next cycle is wasted getting back to a near-solution of the difference equations. This can be inefficient and frustrating.

Improvements of the process seem feasible, using a higher order method, i.e., estimating λ_2, λ_3, etc., which could conceivably eliminate both the above disadvantages.

However, since the underlying equation for ϕ_0 is nonlinear, there are some limitations of the method. Convergence could require moving the shock, straining the applicability of the linear method.

3.3   Results for Subcritical Interference Flows

Figure 76 indicates the power of the convergence acceleration method for calculation of a supercritical $M_\infty = .75$, $\alpha = 2°$ flow over a NACA 0012 airfoil on a relatively fine grid. Without acceleration, the circulation has not converged at 500 iterations. By contrast, the acceleration method provides impulsive corrections to achieve almost the asymptotic value of the circulation within the same number of sweeps. The relaxation parameter ω was set equal to 1.7 for these calculations.

Computational studies of the wall interference effect were made on similar section wings. Figure 77 indicates chordwise pressure distributions associated with the dominant two–dimensional term ϕ_0 at $M_\infty = .63$ and $\alpha = 2°$ (solid curve) for a NACA 0012 airfoil wing. This variation has the characteristic leading edge singularity. At higher Mach numbers, clustering the grid near the leading edge was important in achieving convergence. The relative corrections associated with finite aspect ratio and wall interference (ϕ_1) are also shown for the same set of flight conditions for an aspect ratio $(AR) = 8$ elliptic planform. The dotted curves indicate the free field finite aspect ratio chordwise distributions on upper and lower surfaces and the dashed lines denote the additional wall interference effect for a circular open jet test section using the far field correction worked out in Section 3.1, given as Eq. $(3-59b)$ herein. In the figure, C_p^* denotes the critical pressure level. A mean value $C_{p_{mean}}$ is shown for C_p in which

$$C_{p_{mean}} = \frac{\int_{-1}^{1} c(z)C_p dz}{\int_{-1}^{1} c(z)dz} \quad .$$

The parameter μ is the reciprocal of the semispan in units of the tunnel radius. Accordingly, the case indicated in Fig. 77 corresponds to a semispan of 95% of the tunnel test section radius. In agreement with the assumptions of the asymptotic method, the wall interference correction for this case is numerically of the same order as the free field three–dimensional correction associated with finite aspect ratio and the induced angle of attack correction of the trailing vortex system. The correction appears to peak near the leading edge and is greater on the upper surface of the wing than the lower at this positive incidence.

The associated isoMachs for this case are shown in Figs. 78–80. Figure 78 indicates these lines for the zeroth order two–dimensional solution. Figure 79 shows those corresponding to the incremental effect of aspect ratio and wall interference associated with ϕ_1. The resultant field is shown in Fig. 80. In Fig. 79, it is interesting to note the persistence of the leading edge singularity of the ϕ_0 field in the isoMach pattern.

For the elliptic planform of Fig. 77 at $M_\infty = .63$, and $\alpha = 2°$, Fig. 81 shows the variation of the chordwise pressure distribution along the span due to the combined effects of wind tunnel wall interference and finite aspect ratio. Analytical evaluation of $(3-59b)$ specialized to the case of the elliptic planform fully spanning the tunnel ($\mu = 1$) indicates that there is a square root infinity in the span load distribution at the blocked wing tips at their intersection with the open jet or solid wind tunnel walls. This trend persists for

SC37652
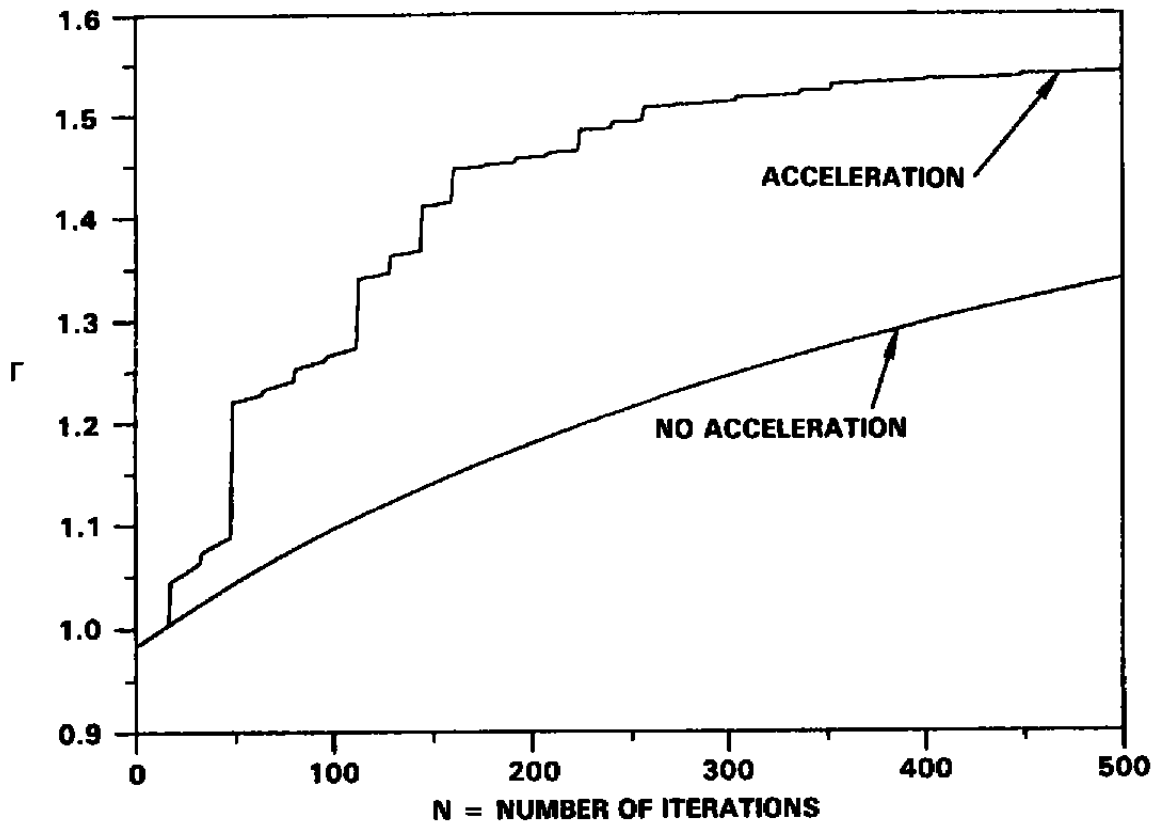
Fig. 76. Effect of convergence acceleration on attainment of asymptotic value of circulation Γ.
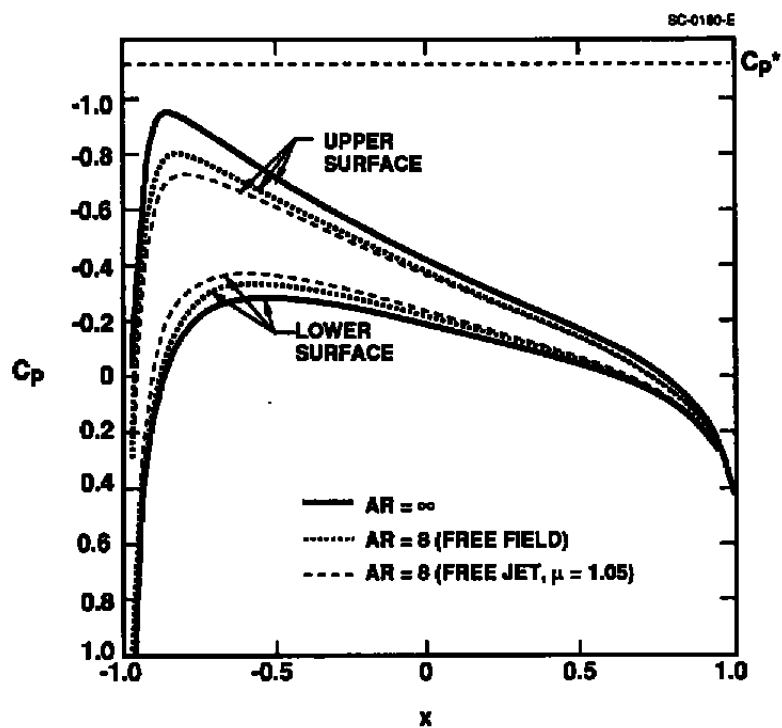
Fig. 77. Mean wing chordwise pressures, circular open jet test section wind tunnel, $M_\infty = .63$, $\alpha = 2°$, NACA 0012 airfoil, 100×60 grid, elliptic planform.

SC37658
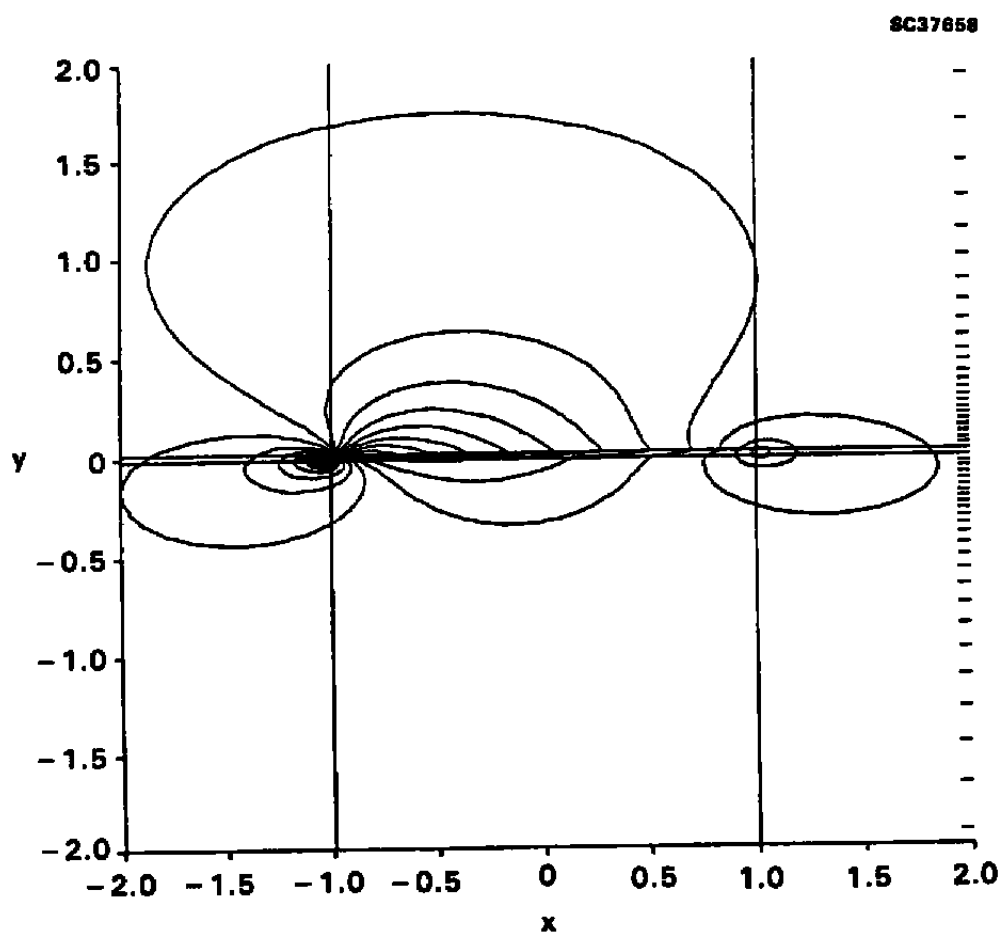
Fig. 78. IsoMachs for zeroth order flow for wing of Fig. 77.
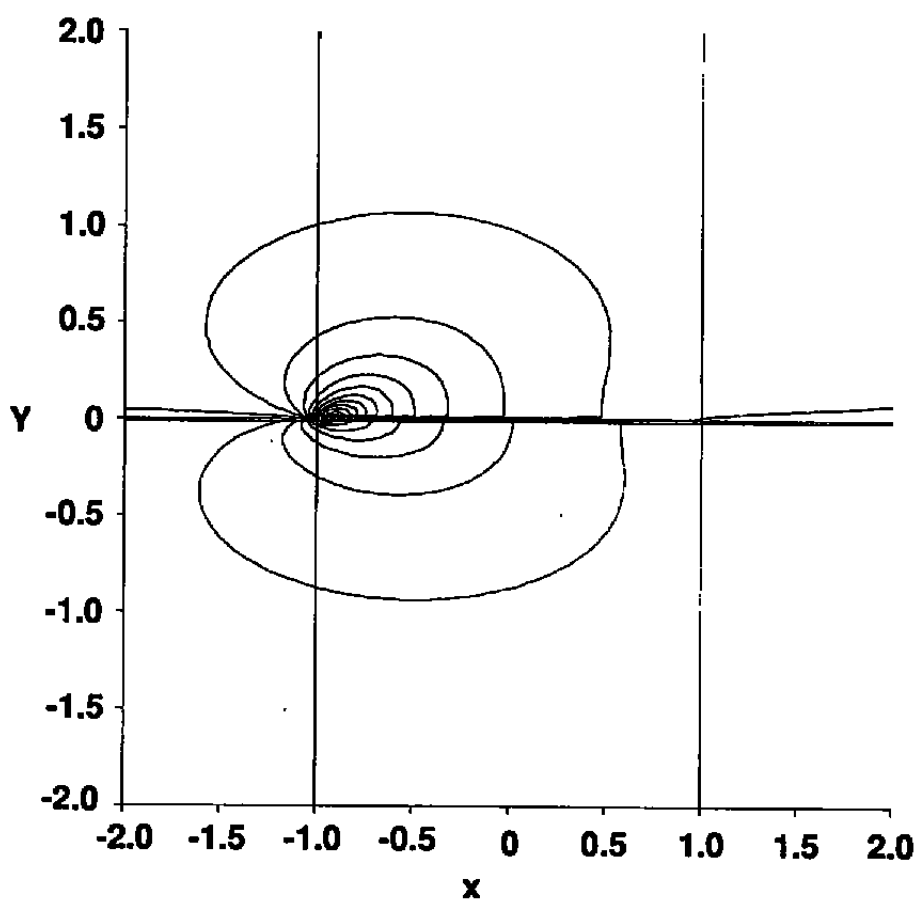
Fig. 79. Perturbation (ϕ_1) isoMachs for wing of Fig. 77.

SC37659
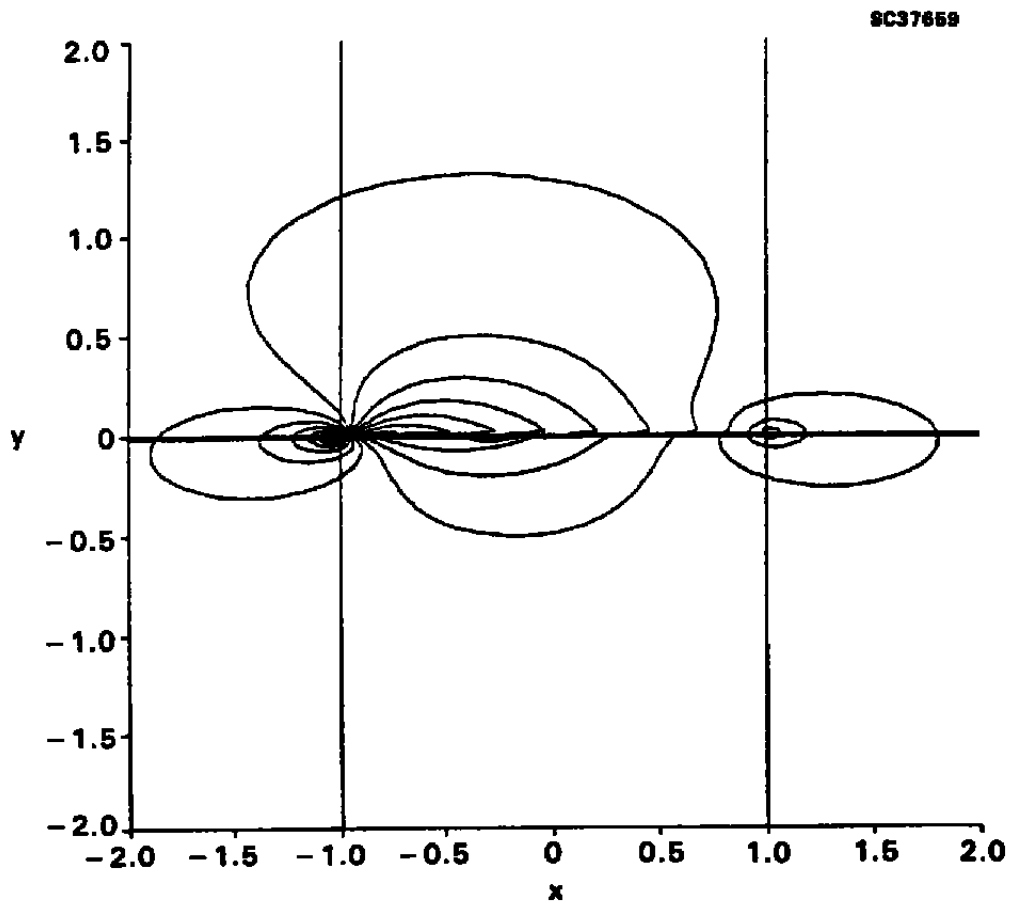
Fig. 80. Total $\left(\phi_0 + \frac{\phi_1}{B}\right)$ isoMachs for wing of Fig. 77.

the $\mu = 1.05$ case, since the wing almost spans the tunnel. Accordingly, the chordwise pressures are almost identical at stations over most of the span, but change drastically at the tips as shown in Fig. 81. *Studies of this type for the supercritical case could guide the twist of the wing to achieve effective free field conditions in the tunnel.*

Associated with these pressures are the spanwise load distributions shown in Fig. 82. The ordinate is the sectional lift coefficient along the span normalized to the two–dimensional value for $M_\infty = .63$ and $\alpha = 2$. Also shown is C_L/C_{L_0}, the total wing lift coefficient corresponding to the separate and combined effects of finite aspect ratio and wall interference normalized to the two–dimensional value. Here, the forementioned exaggerated tip effect is evident and is connected to the wall interference. For this 95% spanning of the test section, both effects combine to give a reduction of the two–dimensional lift by 42%.

The effect of planform shape on these sectional lift distributions is shown in Fig. 83, where the chord variation

$$c(z) = \left(1 - z^2\right)^{3/4}$$

is considered at the same conditions as the elliptic one of Fig. 77. In contrast to the constant downwash effect of the trailing vortex system for the elliptic planform, the free field finite aspect ratio correction now also shows a variable twist effect along the span. For the elliptic wing, this was associated only with the wall interference. It is interesting to note that in spite of this, the magnitude of the total lift reduction due to combined finite aspect ratio and wall interference is still approximately the same as that for the elliptic planform.

Supercritical shock capturing will be described in what follows. Of interest in connection with the shock fitting required for the ϕ_1 solution is the "crispness" of the shocks captured by the ϕ_0 solution. Figures 84 and 85 show pressure distributions along various lines $j = 1, 2, 3, \cdots, jMAX$ for coarse and fine grids, respectively. Figure 85 indicates that our algorithm captures the shock over 2 to 3 mesh points. In Fig. 86, the relationship of the jumps to the Rankine Hugoniot shock polar is shown. If u_1 and v_1 represent preshock reference states, the abscissa and ordinate used for the figure are respectively

$$\overline{u} = \frac{(\gamma + 1)(u - u_1)}{(\gamma + 1)u_1 - K}$$

$$\overline{v} = \frac{(\gamma + 1)(v - v_1)}{4} \left\{ \frac{3}{(\gamma + 1)u_1 - K} \right\}^{3/2},$$

where $u = \phi_{0_x}$, $v = \phi_{0_y}$ and K is the transonic similarity parameter defined previously. The various curves progressing from the $\overline{u}$ axis upwards each represent the variation of $\overline{u}$ with $\overline{v}$ along $\tilde{y} = $ constant lines, starting with a $\tilde{y}$ level closest to the airfoil and moving upwards in unit increments of j. The sharp break in the curves near the non–diffused part of the shock occurs at its downstream side. The proximity of the kink location to the polar is a validation of our algorithm to capture the proper Rankine Hugoniot jumps.

As indication of the effectiveness of the grid clustering employed, Fig. 87 shows iso-Machs for the more supercritical NACA 0012 flow corresponding to $M_\infty = .8$ and $\alpha = 2°$.
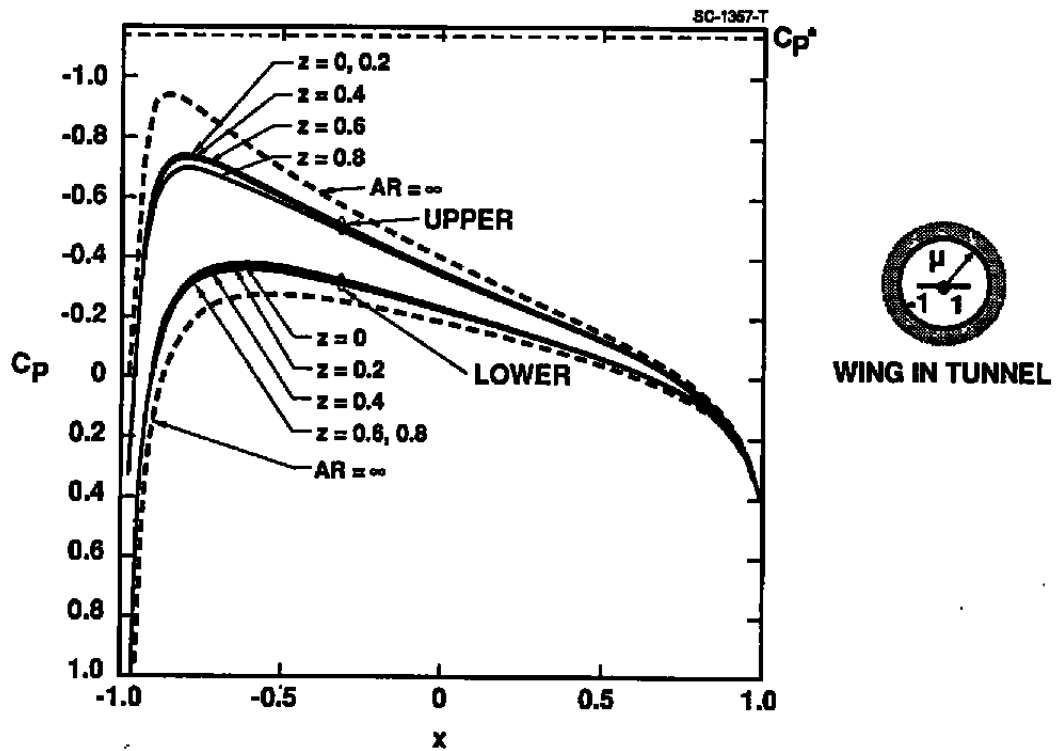
Fig. 81. Variation of the chordwise pressure distribution along the span for wing of Fig. 77, $M_\infty = .63$, $\alpha = 2°$, $\mu = 1.05$.
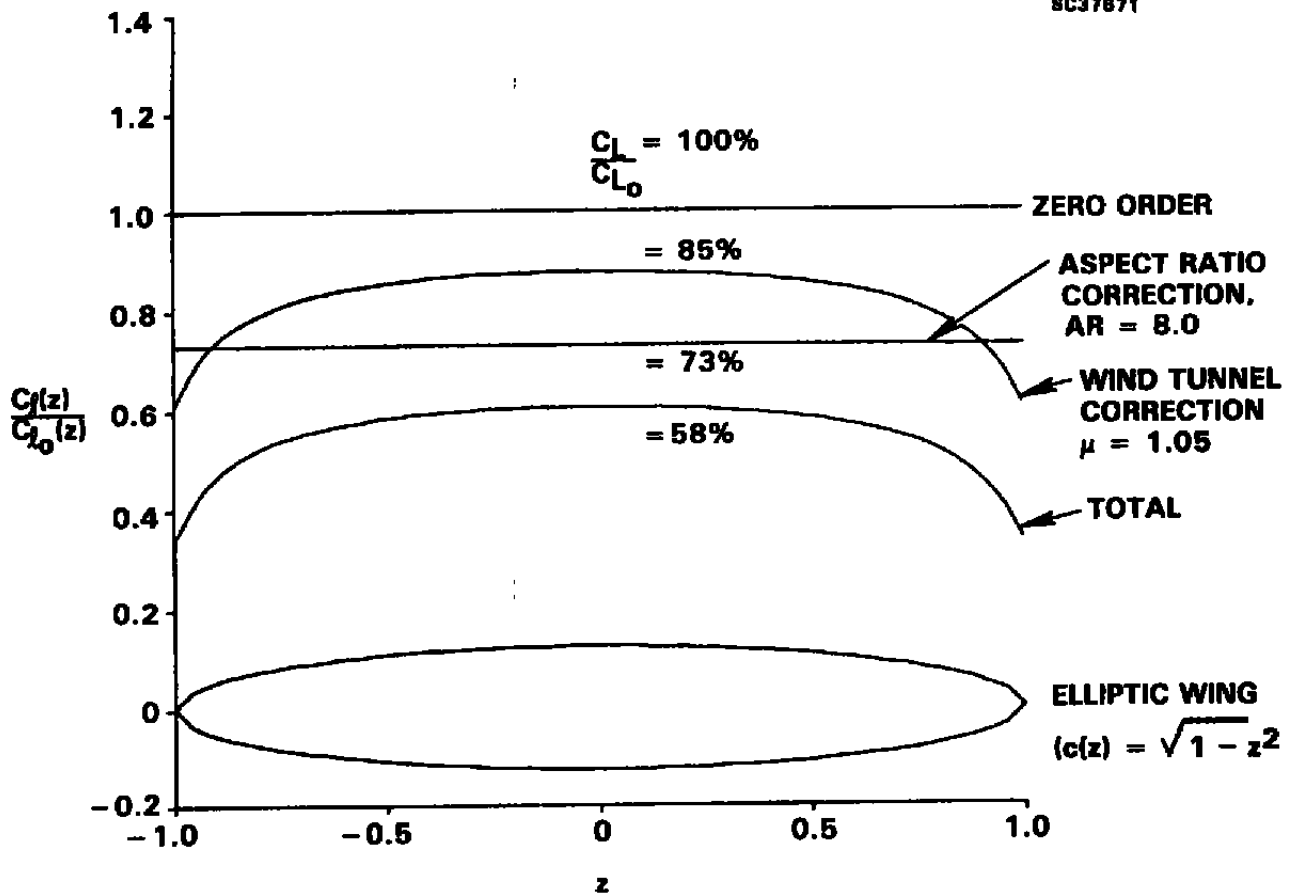
Fig. 82. Spanwise loading for wing of Fig. 77.
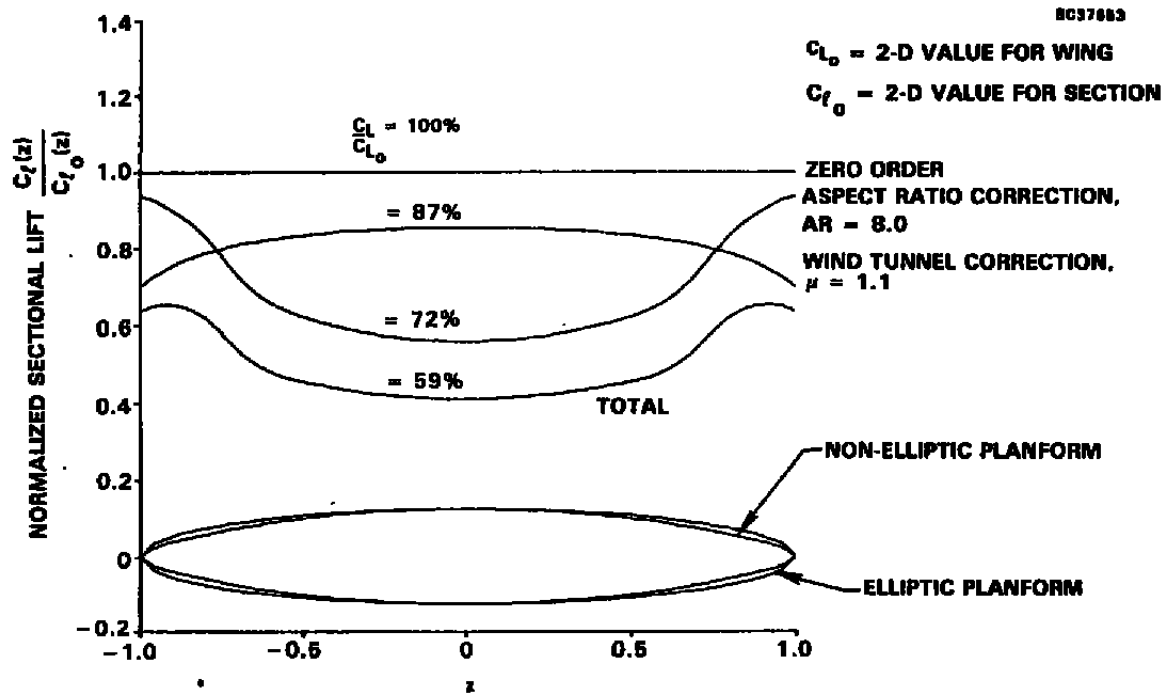
Fig. 83. Spanwise loading for nonelliptic wing. All other parameters identical to those associated with Fig. 77.
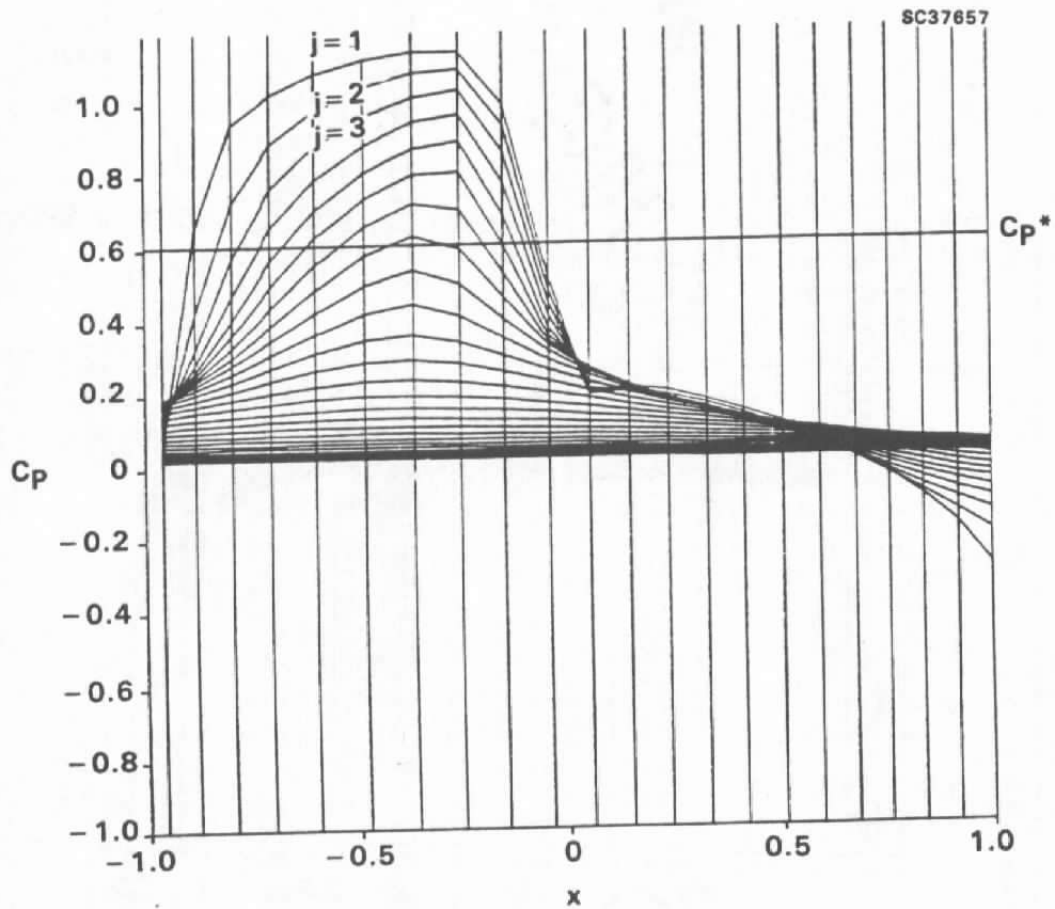
Fig. 84. Pressure distributions over NACA 0012 airfoil, $M_\infty = .75$, $\alpha = 2°$, 50×50 grid, $\Delta y = .05$, $\Delta j = 1$.

SC37654
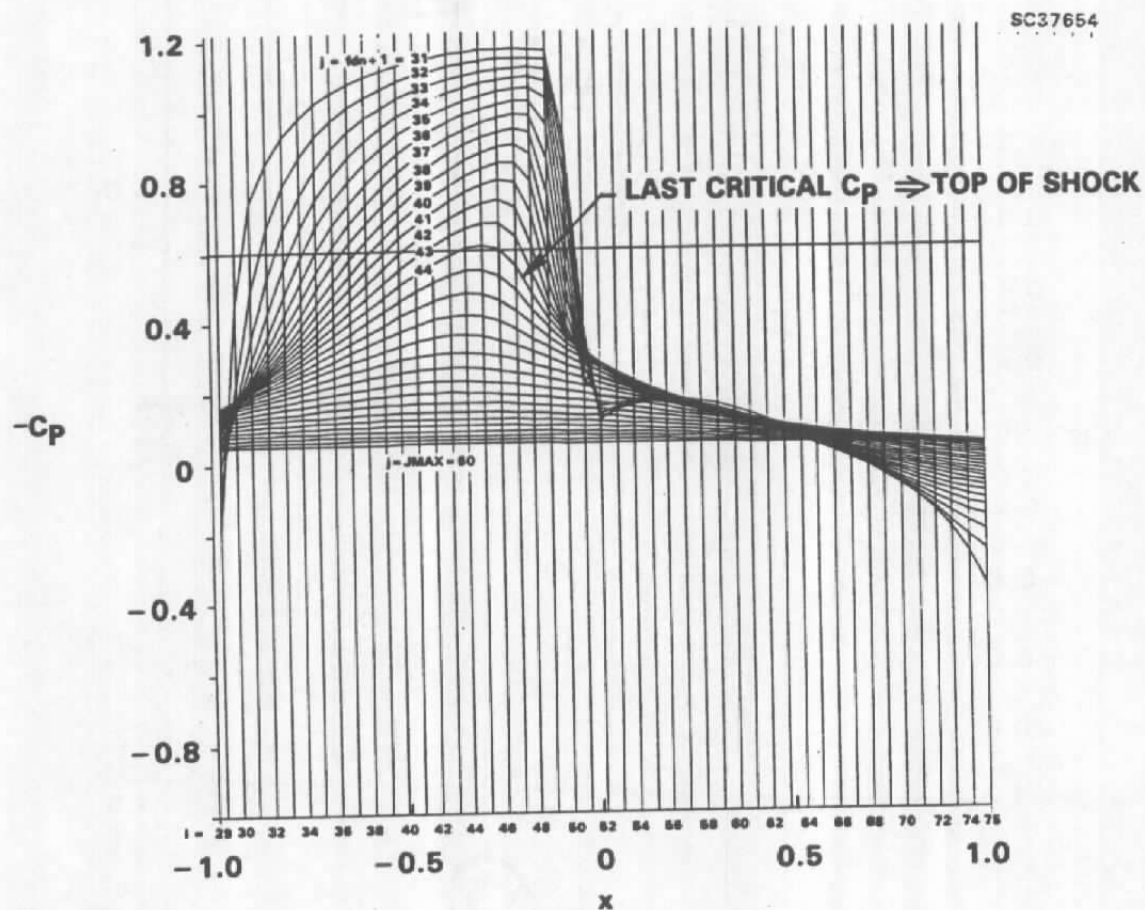
Fig. 85. Pressure distributions over NACA 0012 airfoil, $M_\infty = .75$, $\alpha = 2°$, 98×60 grid.

SC37692
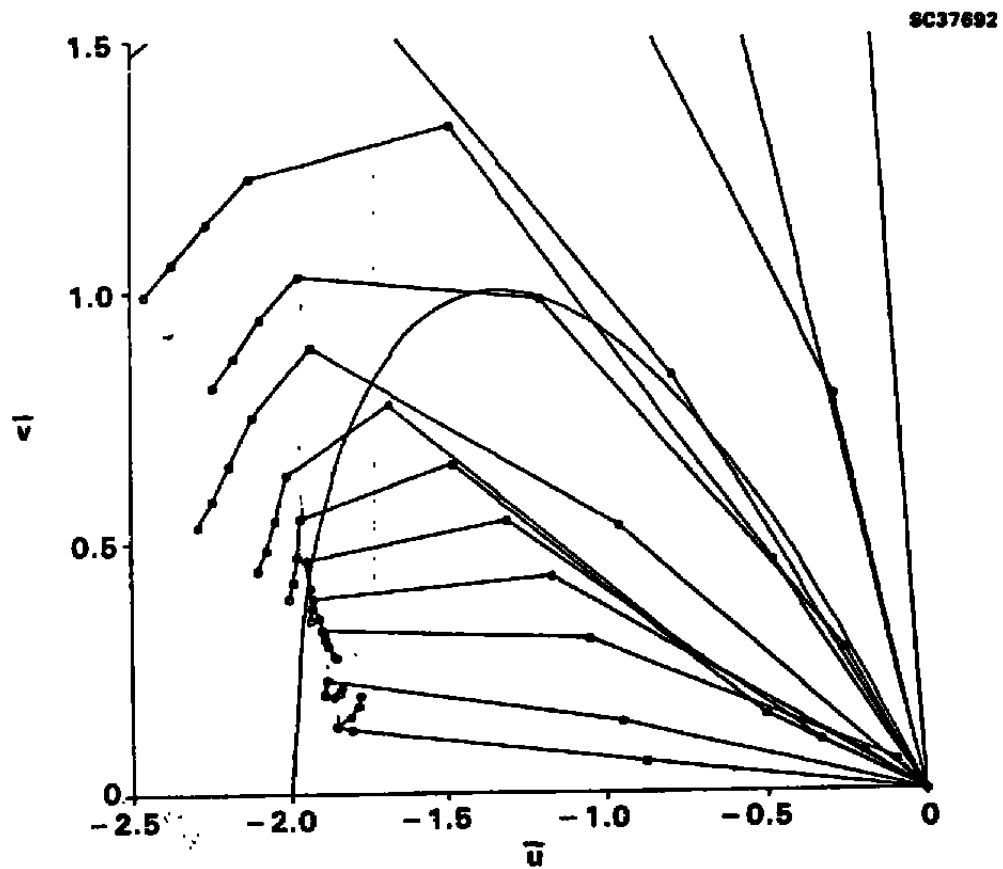
Fig. 86. Variation of perturbation downwash with pressure in relation to shock hodograph, $M_\infty = .75$, $\alpha = 2°$, NACA 0012 airfoil.

Formation of the recompression shock on the rear of the airfoil is evident in these patterns. The horizontal and vertical grid clustering employed are shown near the frame of this plot.

3.4 Supercritical Interference Flows

In Fig. 88, a result is shown for a supercritical interference flow. This calculation represents the chordwise pressures over an aspect ratio 8 elliptic planform which spans 90% of a circular wind tunnel. The wing is at 2° angle of attack, at a tunnel Mach number of 0.7, and has similar NACA 0012 airfoil sections along its span. The effect of the open jet and aspect ratio is to weaken the shock as anticipated.

In the treatment of these supercritical flows, the numerical methods were refined so that the shock fitting methods can adequately handle stronger supercritical cases associated with Fig. 88. Two issues dealt with in this connection are the ϕ^* shock fitting procedures and the treatment of the surface boundary conditions.

In connection with the shock issue, it is useful to note that in practically interesting cases, the shock is almost vertical and the region about it can be contained with a vertically oriented boundary ABCD as shown in Fig. 68. The zone inside the "shock notch" ABCD is a "hole" for which it is not necessary to compute the interference potential ϕ^*. On the other hand, a staggered boundary of a mesh width of three points shown in Fig. 70c can also be used to satisfy the appropriate jump conditions across the shock. The configuration of Fig. 68 is advantageous from the standpoint of programming logic, particularly in the treatment of jumps in $\phi_y^*([\phi_y^*])$ so that differentiation inside the notch is avoided. The disadvantage is that the shock region may be unnecessarily widened. However, for nearly vertical shocks associated with Mach numbers close to unity and fine grids, this disadvantage can be offset. The three point staggered notch has the advantage of following the shock contours.

Subroutines SETUP and SLOR have been optimized so that numerical treatment of the staggered and upright notch can be built into these modules. SETUP is a subroutine that calculates the coefficients needed in the variational (1st order) equation from the zeroth order basic flow solution. It is used in subroutine SLOR and also detects the shock as well as finding the coefficients for the 1st order jumps. SLOR is depicted in Fig. 75.

Other capabilities that are included in the code are adjustment of notch width and batch capability. In regard to the former, the adjustment can be made asymmetrically in the streamwise direction to model the shock layer adequately.

In regard to the boundary conditions, boundary points are handled by averaging the slope information on the boundary with that at the immediately adjacent vertical node point. The resulting discretization is given as Eq. (3 − 76) which is used to numerically evaluate the $\frac{\partial^2}{\partial y^2}$ terms in the equations of motion. Referring to Fig. 59, additional accuracy and consistency with the locally second order accurate discretization for interior points can be achieved based on a Taylor series method. These use the first three vertical nodes points shown in the aforementioned figure. In the upper half plane, noting these by indices 1, 2,

150
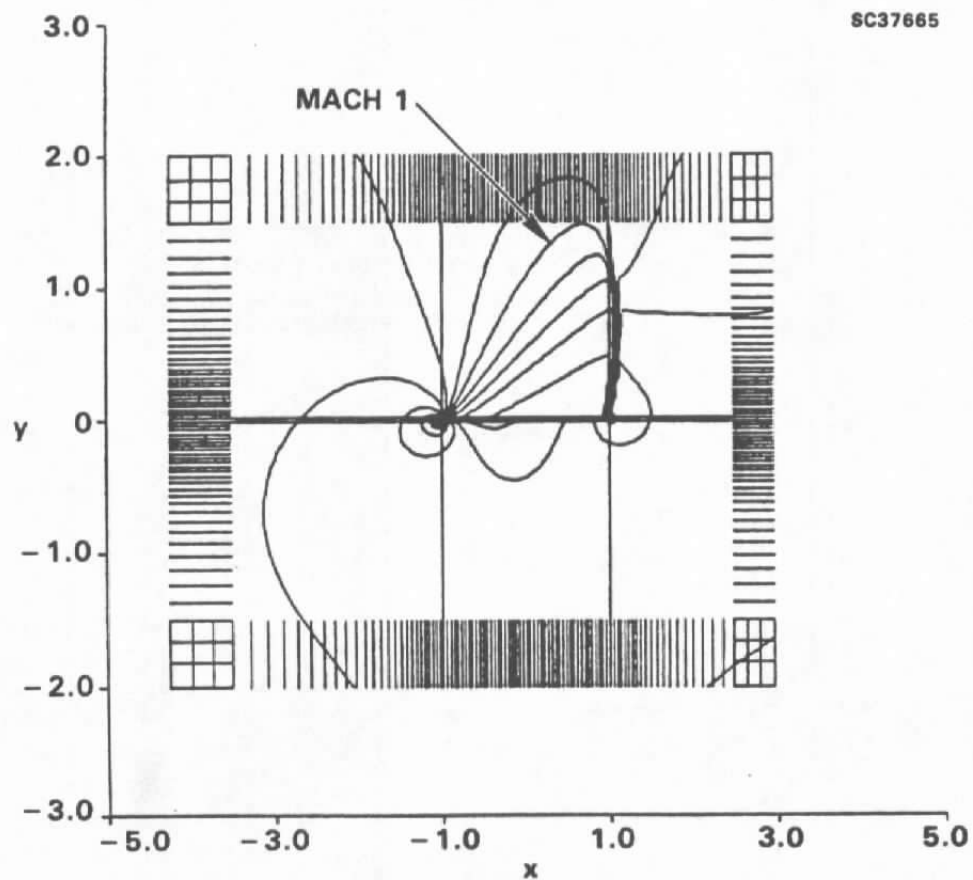
Fig. 87. IsoMachs for NACA 0012 airfoil, $M_\infty = .8$, $\alpha = 2°$, grid adapted to leading edge bluntness.
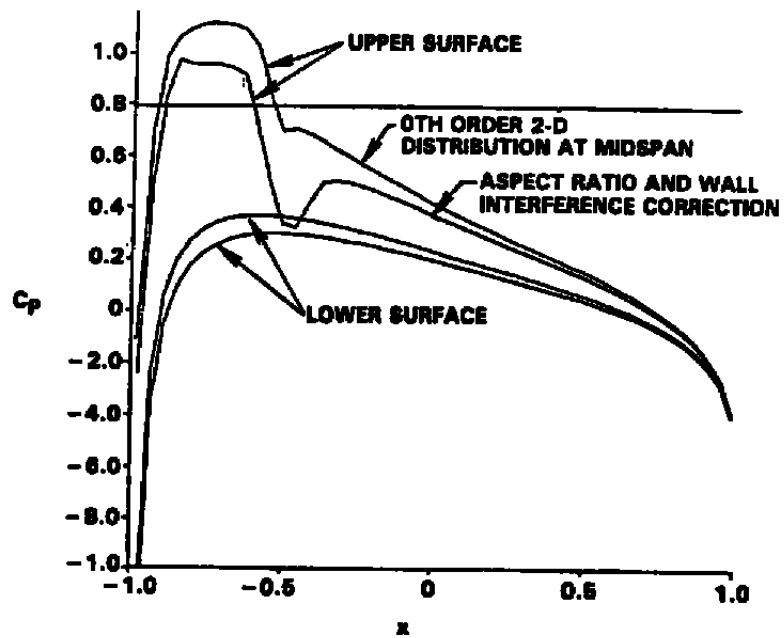
Fig. 88. Chordwise pressures on elliptic planform wing inside open jet wind tunnel, $AR = 8.0$, $M_\infty = 0.7$, $\alpha = 2°$, $\mu = 1.05$, NACA 0012 airfoil, 100×60 grid.

and 3 corresponding to fup, $fup + 1$, and $fup + 2$ and letting

$$h_1 = y_2 - y_1$$
$$h_2 = y_3 - y_2$$

it is possible to obtain a locally second order accurate expression for ϕ_y at y_2 in terms of ϕ_y at $y = 0$, which is not a node point. The Taylor series gives simultaneous equations with information which allows ϕ at $y = 0$ to be eliminated so that the following expression can be obtained:

$$\phi_y \Big|_2 = \frac{2h_1^3 - 2h_1 h_2^2 - h_2^3}{h_1 h_2 (h_1 + h_2)(2h_2 + h_2)} \phi_2 + \frac{h_1 (3h_1 + h_2)}{h_2 (h_1 + h_2)(2h_1 + h_2)} \phi_3 - \frac{h_2}{2h_1 + h_2} \phi_y \Big|_{y=0} \,,$$

$$(3 - 88)$$

where $\phi_y \Big|_{y=0}$ is specified in the boundary conditions.

With the PHI1 code modules charted in Figs. 75 and 89 and other figures, an $M_\infty = 0.75$, $\alpha = 2°$ case was computed for an elliptic planform, aspect ratio 8 wing. The wing was assumed confined by a circular cross section free jet wind tunnel, with the wing spanning 95% of the tunnel diameter.

To accelerate the convergence of the iterative scheme, the special method described in Section 3.2.3 involving the eigenvalues of the error matrices was used. This is particularly important for transonic lifting cases involving supersonic bubbles whose dimensions are a substantial fraction of the airfoil chord such as this one considered here. In Fig. 90, the convergence history of the tunnel wall perturbation of the circulation is shown. Rapid convergence is achieved after only 200 iterations for this grid which had 50 points on the airfoil and 60 vertical nodes. An important factor controlling this behavior was the proper treatment of the shock notch. Referring to Eqs. $(3 - 73)$, particularly, the factors $[\phi_{0_{xx}}]$, $[\phi_{0_{xy}}]$, $[\phi_{0_x}]$, and $[\phi_{0_y}]$, it is imperative in this stronger supercritical case that no differentiation is performed inside the rapidly varying and possibly numerically dispersive shock layer which computationally models its physically discontinuous counterpart. In addition, the width of the notch should be adjusted so that the full Rankine Hugoniot transition is achieved. This is based on the weak solutions associated with the divergence form of the small disturbance equation. As discussed in Section 2.20, the streamwise pressure variations at various heights above the airfoil depicted in Fig. 85 and the isoMachs shown in Figs. 91 and 92 have been considered in establishing the upstream and downstream boundaries for the shock notch.

The basic wind tunnel wall effect of this NACA 0012 similar wing gives rise to corrected isoMach patterns shown in Fig. 93. Clearly evident in this figure is the shock notch.

3.4.1 Refinements of Shock Fitting Procedures

As indicated in Ref. 29 and Section 3.2.2.2 in the numerical implementation of transonic lifting line theory for wind tunnel wall interference, the shock is captured for the 0th order approximation to the flow, while the 1st order perturbation is fitted.

153

OUTPUT — WRITES 2 FILES OF RESULTS FOR014.DAT WHICH REPORTS ON THE RUN AND FOR015.DAT WHICH IS UNFORMATTED AND CONTAINS GRAPHICS DATA

COMPUTE SCALING FACTORS
$SCALCP = -2\delta^{1/2} M^{-n}$
$SCALM = \delta^{1/2} M^m$

FOR KRUPP SCALING, $n = \frac{3}{4}$, $m = \frac{4}{3}$

FOR "NORMAL" SCALING, $m = n = 0$.

EXTRAPOLATE ϕ AND ϕ^* ON TO $y = 0$, LINEARLY

SECOND ORDER EXTRAPOLATION IS POSSIBLE USING SOLUTION VALUES OF $\phi_y|_y = 0$ BUT IS NONUNIFORMLY VALID AT LEADING AND TRAILING EDGES.

COMPUTE C_{P_0} AND C_{P_1}
$(= SCALCP \, \phi_x)$
AT $y = 0$

LINEARLY INTERPOLATE FOR C_{P_1} AT THE NOTCH

ANOTHER POSSIBILITY IS TO PUT THE JUMP ALL IN ONE PLACE AS IN 2(iv)

FOR $j = j_{smin}$ TO j_{smax}
GET $g1(j) = -(\phi^*)/(\phi_{ox})$

COMPUTE LIFT COEFFICIENTS: 0TH ORDER, AND ADJUSTED FOR AR AND WING TUNNEL EFFECTS

$C_{L_0} \cdot \delta^{2/3} \Gamma_0$
$C_{L_1} \cdot C_{L_0} \left(1 + \left(\frac{\text{w}_{EFFECT} + \text{t}_{EFFECT}}{B}\right)\Gamma^*\right)$

COMPUTE 0TH ORDER AND CORRECTION MACH NUMBERS

$MACH0 \sim -\delta^{2/3} (K - (\gamma + 1)\phi_{0_x})$
$\Delta MACH1 \sim \delta^{2/3} (\gamma + 1)\phi_x^*$

WRITE DATA TO FILES

RETURN

Fig. 89. Flow chart of OUTPUT module relevant to variational solver for interference potential, repeated version of Fig. 74 for convenience.
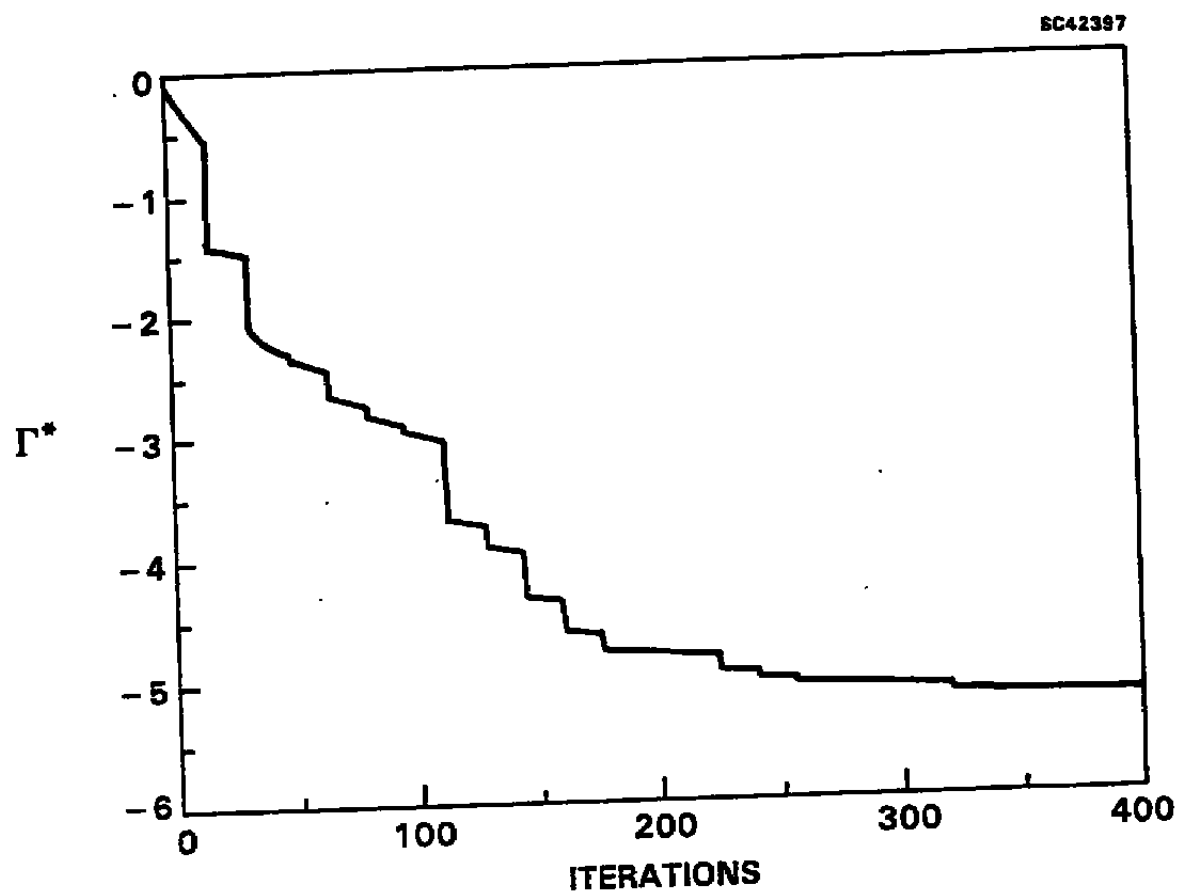
Fig. 90. Circulation perturbation convergence, $M_\infty = 0.75$, $\alpha = 2°$, elliptic planform, NACA 0012 airfoil.
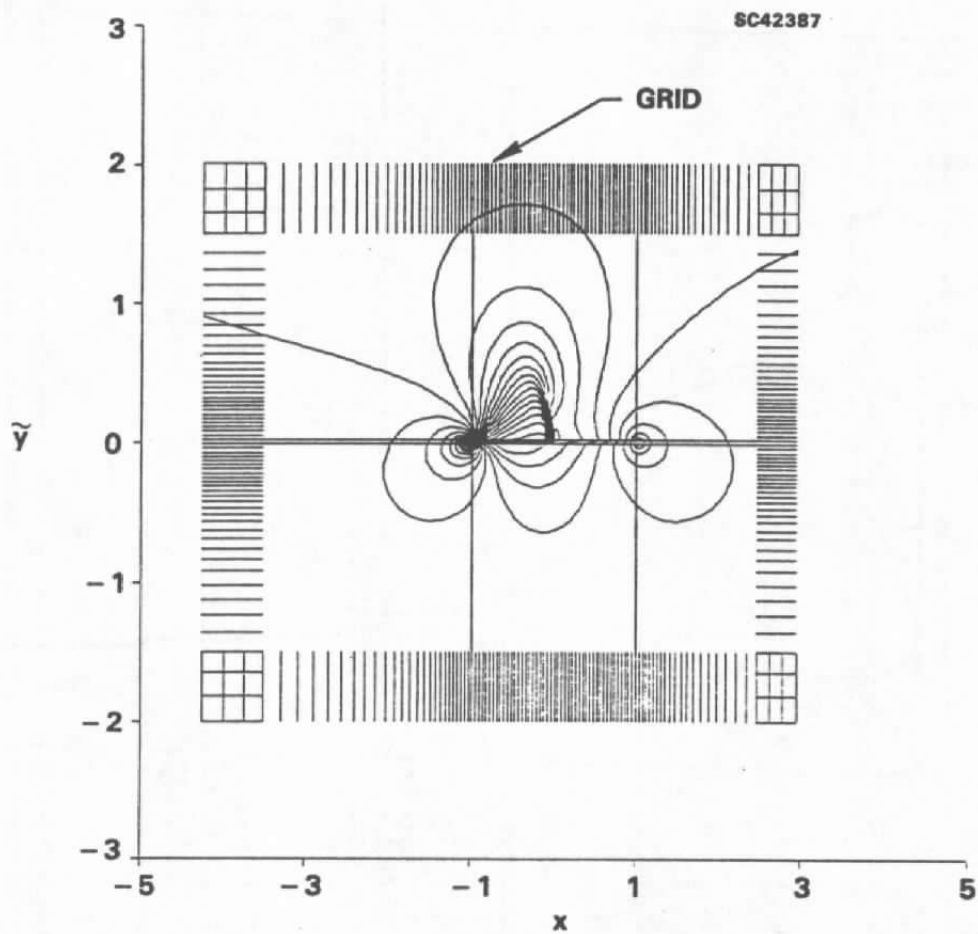
Fig. 91. Free field isoMachs for $M_\infty = 0.75$, $\alpha = 2°$, AR = 8, elliptic planform, NACA 0012 airfoil section.
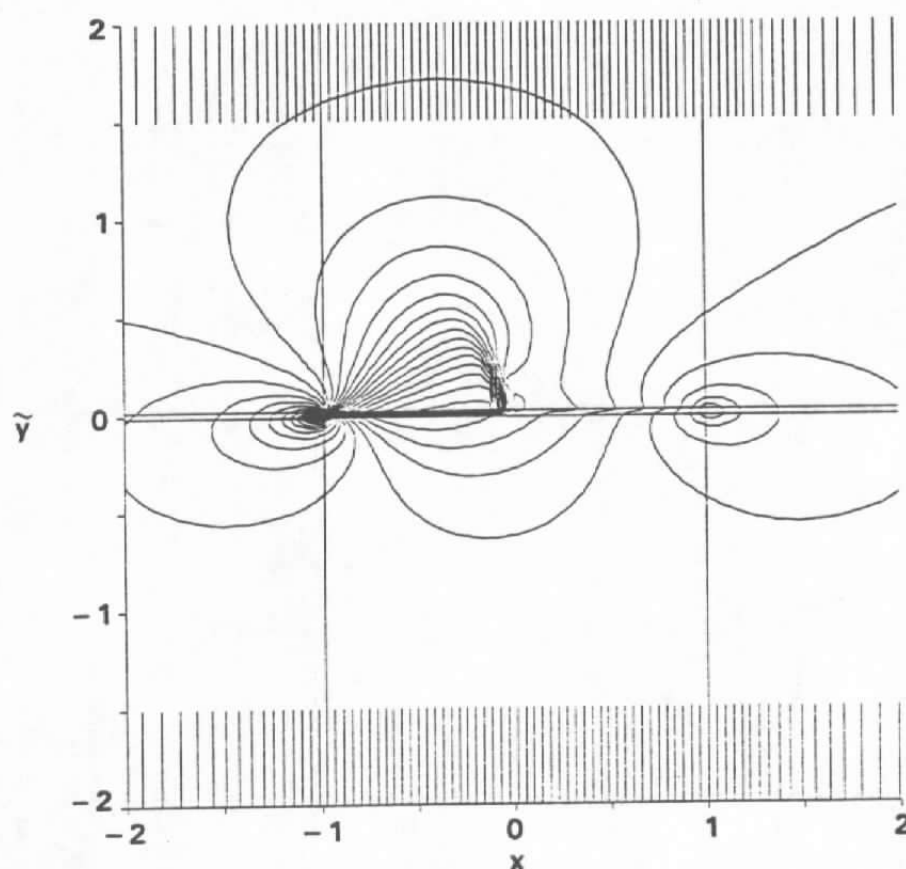
Fig. 92. Free field isoMachs for $M_\infty = 0.75$, $\alpha = 2°$, AR = 8, elliptic planform, NACA 0012 airfoil section — close–up.
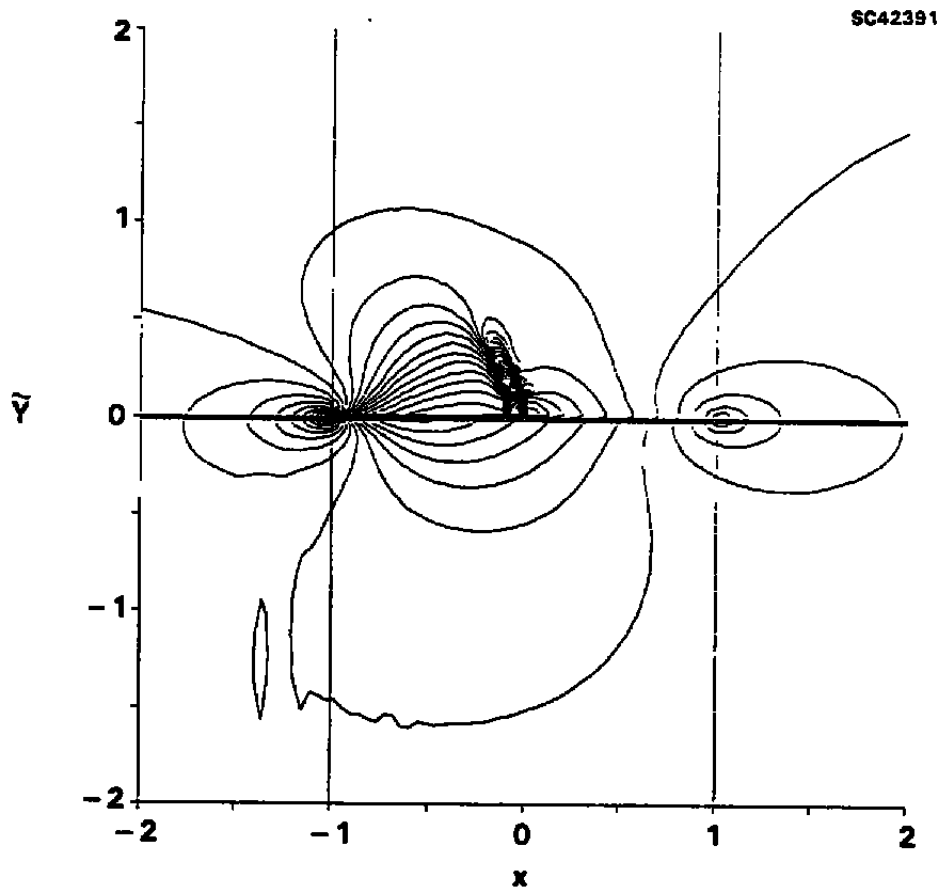
Fig. 93. Free jet wind tunnel corrected isoMachs for $M_\infty = 0.75$, $\alpha = 2°$, AR = 8, $\mu = 1.05$, elliptic planform, NACA 0012 airfoil section.

On the wing, because of the tangent flow condition, $[\phi_{0_y}]_s = [\phi_{1_y}]_s = 0$, the shock conditions $(3-73)$ and $(3-74)$ specialize to

$$\left[K\phi_x - \frac{(\gamma+1)}{2}\phi_x^2 \right]_s = 0 \qquad (3-89)$$

where ϕ is the perturbation potential defined in Eq. $(3-1)$ and ϕ_0 and ϕ_1 are components of the inner expansion given in Eqs. $(3-55)$, and thus $\langle \phi_x \rangle_s = \frac{K}{(\gamma+1)}$ with $\langle \phi_x \rangle_s$ defined as $\dfrac{\left(\phi_x(s^+) + \phi_x(s^-) \right)}{2}$. Similarly, the 0th order shock condition on the wing is

$$\langle \phi_{0_x} \rangle_{s_0} = \frac{K}{(\gamma+1)} \qquad (3-90)$$

and the 1st order shock condition becomes

$$(\phi_{1_x})_{s_0} = -g_1 \langle \phi_{0_{xx}} \rangle_{s_0} \quad . \qquad (3-91)$$

Equation $(3-90)$ is Prandtl's relation for normal shocks and $(3-91)$ corresponds to a perturbation of it. Both $(3-90)$ and $(3-91)$ can be used as checks on the numerical codes. Our experience is that $(3-90)$ can be satisfied to within 10% in the 0th order code with a mesh of 100 points in the streamwise direction and 50 points transverse to the flow. This inaccuracy is important in satisfying $(3-91)$ in the 1st order code. Since in the derivation of $(3-91)$, $(3-90)$ is used, an error in its satisfaction in the 0th order code, corrupts the satisfaction of $(3-91)$.

To alleviate this problem, we have modified the 1st order shock condition $(3-73a)$ by replacing μ with $\mu - \langle\mu\rangle f(y)$, where $f(y)$ is a function that has been defined with special properties for this application. The quantity $\langle\mu\rangle$ is the average of the μ upstream and downstream of the shock s_0 and is 0 when $(3-90)$ is exactly satisfied. The function $f(y)$, whose value is 1 on the wing and decays to 0 away from the wing, is introduced to avoid discontinuous behavior from the shocked region to the unshocked region across the shock notch boundary. With this modification, $(3-91)$ can be satisfied even when $(3-90)$ has numerical errors as has been shown by its recent implementation in the 1st order code.

With ϕ_0 and ϕ_1, ϕ, ϕ_x and the pressures on the wing can be obtained.

The post–processing steps are as follows:

(a) Calculate the shock position on the wing by the relation

$$x = g_0(y) + \frac{1}{B}g_1(y) \quad . \qquad (3-92)$$

Let x_0 denote the shock position from the 0th order result and x_n the shock position for ϕ, then $(3-92)$ gives $x_n = x_0 + \frac{1}{B}g_1(y_{wing}) \equiv x_0 + \delta x$. For the following procedure, we assume x_n is less than x_0. (A similar procedure holds for the case in which x_n is greater than x_0.)

(b) For x in the range $x_{n+} \geq x \geq -1$, $\phi_x = \phi_{0_x} + \frac{1}{B}\phi_{1_x}$. (Subscripts $+$ and $-$ signify upstream and downstream, respectively.)

(c) At $x = x_{n+}$, $\phi_x = \phi_{0_x}(x_{0+}) + \frac{1}{B}\phi_{1_x}(x_{0+}) + \delta x \phi_{0_{xx}}(x_{0+})$.

(d) At $x = x_{n-}$, $\phi_x = \phi_{0_x}(x_{0-}) + \frac{1}{B}\phi_{1_x}(x_{0-}) + \delta x \phi_{0_{xx}}(x_{0-})$.

(e) For x in $1 \geq x \geq x_{0-}$, $\phi_x = \phi_{0_x} + \frac{1}{B}\phi_{1_x}$.

(f) Linear interpolation is used for x between x_{n-} and x_{0-}.

(g) Finally, for graphing purposes, linear interpolation is used for x between x_{n+} and x_{n-}.

The post–processing implies that $\langle\phi_x\rangle_s = \langle\phi_{0_x}\rangle_{s_0}$, so that the shock condition on the wing is satisfied to the accuracy of the 0th order code.

Figure 94 gives pressure distributions for an unconfined finite aspect ratio wing ($AR = 8$) and infinite wing for Mach number $M_\infty = 0.75$ and angle of attack of $2°$ over a NACA 0012 airfoil. Since $C_p = -2\delta^{2/3}\phi_x$, $\langle C_p \rangle = -2\delta^{2/3}K/(\gamma+1) \equiv C_{pcr}$. As shown in the figure, this condition is satisfied for the infinite wing within 13% based on the 0th order result. The condition is also satisfied with the same accuracy for the $AR = 8$ finite wing. The effect associated with free jet wall interference is shown in the span averaged chordwise pressure of Fig. 95. Both the aspect ratio effect and the free jet wall interference agree with qualitative reasoning of the downwash field induced by the trailing vortex system and by the two–dimensional image vortex system in the Trefftz plane. For an elliptic planform, the aspect ratio effect is constant along the wing span due to the uniform downwash induced on the loaded line by the trailing vortex system. By contrast, the wall interference is variable as shown in Fig. 96. The sense of the free jet imaging vortex is the same as the tip and trailing vortices associated with finite span. These reduce the incidence and lift, moving the shock forward.

In summary, Steps (a)–(g) comprising the shock fitting procedure above provide a numerical mechanism to ensure that proper shock conditions are satisfied.

3.5 Computational Implementation of Pressure Specified Boundary Conditions

In addition to development of the strong supercritical capability, the high aspect ratio (HIAR) codes have been generalized to account for pressure boundary conditions on a tunnel interface, which for convenience and without loss of generality have been assumed to be cylindrical.

If the interfacial pressure distribution is $C_{p_I}(x, \theta)$, where x is the flow direction and the subscript I hereinafter refers to the interface, the corresponding transonic small disturbance perturbation backwash on the interface is $\phi_{I_x} = -C_{p_I}/2\delta^{2/3}$, where δ is the wing thickness ratio. Also from analyses given earlier in this report, the outer representation of ϕ in the large height (H) span limit defined before Eq. $(3-2)$, it is clear that $\varphi_{0_I} = \phi_I$. Letting $\varphi_{0_I} = W(x, \theta)$, then
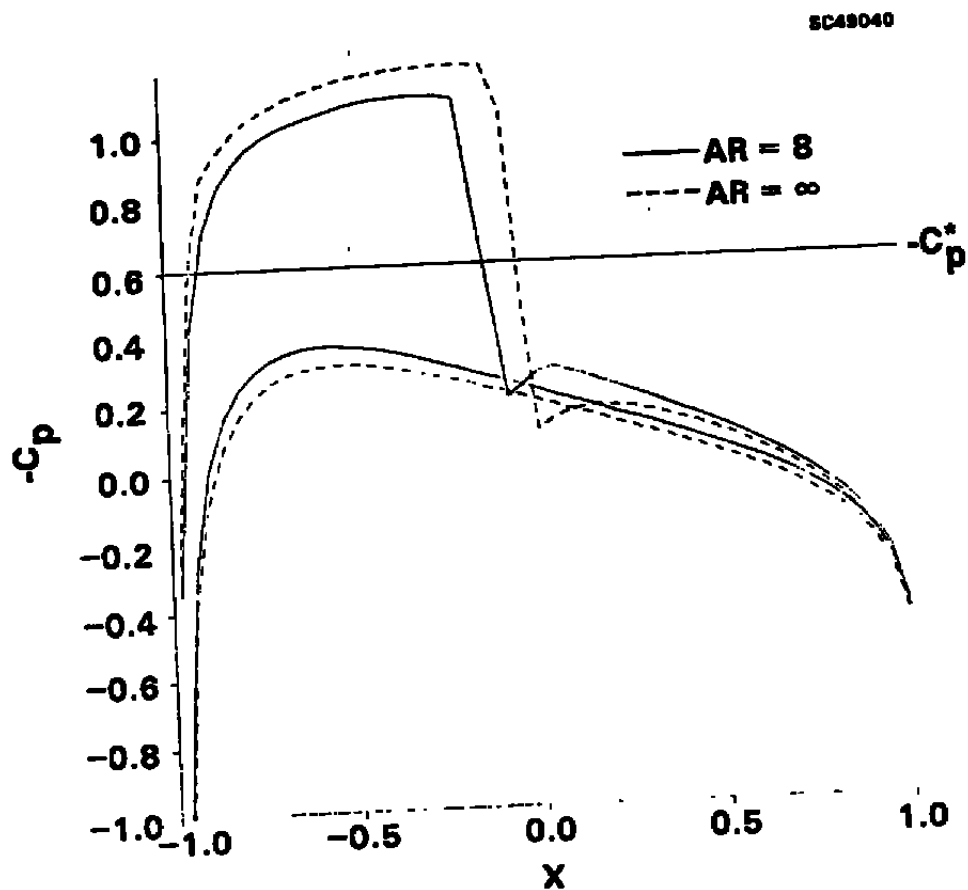
Fig. 94. Chordwise pressures along span in free field, $M_\infty = .75$, $\alpha = 2°$, elliptic planform, NACA 0012 airfoil section.

SC49039
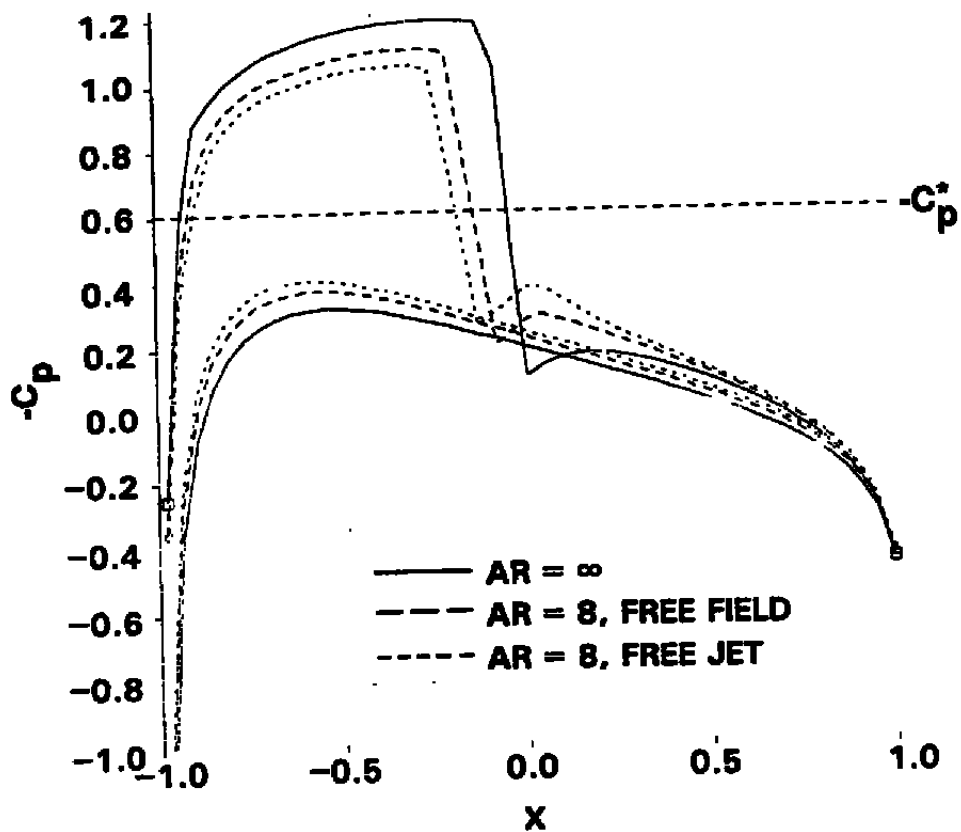
Fig. 95. Mean chordwise pressures in free jet, $M_\infty = .75$, $\alpha = 2°$, elliptic planform, NACA 0012 airfoil section.
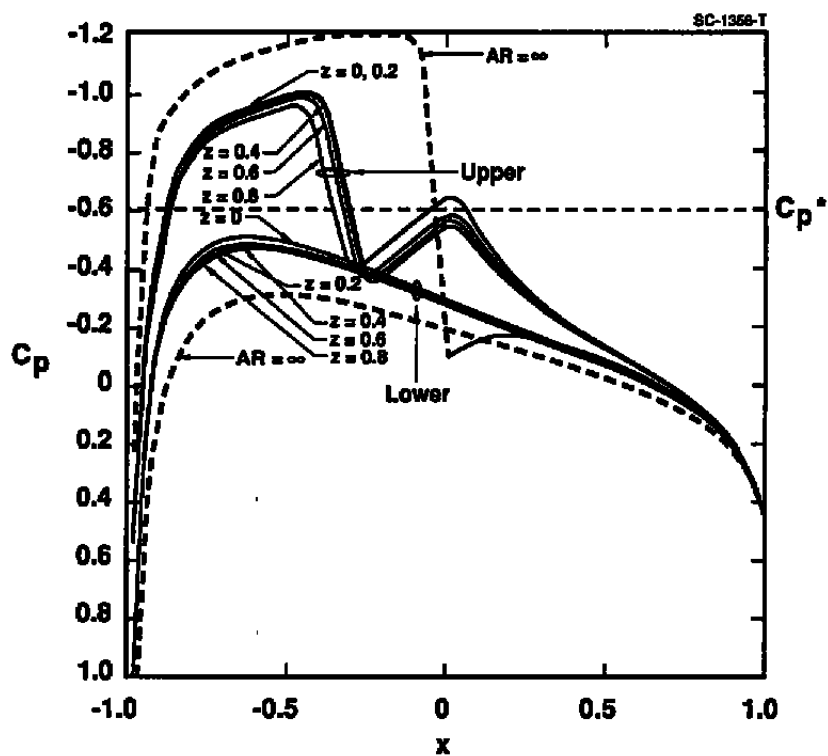
Fig. 96. Chordwise pressures along span within free jet wall boundary, $M_\infty = .75$, $\alpha = 2°$, $\mu = 1.05$, elliptic planform, NACA 0012 airfoil section.

$$W = \int_{-\infty}^{z} -\frac{C_{p_I}}{2\delta^{2/3}} dx \qquad (3-93)$$

where φ_{0_I} at $x = -\infty$ is assumed to vanish. If lateral symmetry $W(x^*, \theta) = W(x^*, -\theta)$ is assumed, where θ is measured from the intersection of the vertical plane of symmetry and the interface, W can be represented as the Fourier series $(3-48b)$ where the W_n are given after Eq. $(3-49)$. On the basis of the analysis given in Section 3.1.2 the additional downwash W on the loaded line due to the interaction of the trailing vortex system with the walls or interface can be represented by a superposition of two effects. If w_0 corresponds to the downwash increment associated with a free jet and w_1 is an increment associated with a pressure specification, then

$$w = w_0 + w_1 = \varphi_y(0, 0, z^*) \,, \quad -B \le z^* \le B \,. \qquad (3-94)$$

In terms of notation used in the code modules related to PHI1, $w \leftrightarrow$ tint. Based on the analysis described in Section 3.1.2

$$w_1 = \frac{1}{\sqrt{K} z^*} \sum_{n=1,3,5,\cdots}^{\infty} n(-1)^n \sum_{s=1}^{\infty} \frac{J_n(j_{ns} z^*)}{J_n'(j_{ns})} \int_{-\infty}^{\infty} e^{-j_{ns}|x^*|} W_n(x^*) dx^* \,, \qquad (3-95)$$

where K is the transonic similarity parameter, and j_{ns} are the zeros of the Bessel functions J_n.

In Section 3.1.2, approximations for the inner integral have been used that suggest that the downstream features of the interface pressure do not contribute strongly to w_1. Because of the substantial exponential factor in the integrand, $(3-95)$ can be approximated by including only the first term in the inner sum to give

$$w_1 = \frac{1}{\sqrt{K} z^*} \sum_{n=1,3,5,\cdots}^{\infty} n(-1)^n \frac{J_1(j_{n1} z^*)}{J_n'(j_{n1})} \int_{-\infty}^{\infty} e^{-j_{n1}|x^*|} W_n(x^*) dx^* \,. \qquad (3-96)$$

Equation $(3-96)$ has been used to evaluate a special interface pressure distribution which has some features of those discussed in summaries of Calspan AEDC WIAC related effort contained in Refs. 46 and 47. The model interface pressure distribution used with the generalized HIAR code is

$$C_{p_I} = \epsilon_2 e^{-|x|} sgn(x^*) \{1 + \epsilon_1 \cos\theta\} \,, \quad -\infty \le x^* \le \infty \qquad (3-97)$$

where ϵ_1 and ϵ_2 are constants, and $sgn(x) = 1$ for $x > 0$, -1 for $x < 0$. Equation $(3-97)$ implies that

$$W(x^*) = \frac{\epsilon_2}{2\delta^{2/3}}(1 + \epsilon_1 \cos\theta)e^{-|x^*|} \,, \qquad (3-98)$$

$$W_1(x^*) = \frac{\epsilon_1 \epsilon_2}{2\delta^{2/3}} e^{-|x^*|} \qquad (3-99a)$$

$$W_n(x^*) = 0 \ , \ n > 1 \ . \tag{3 - 99b}$$

Substitution in $(3 - 96)$ gives

$$w_1(z^*) = \frac{-\epsilon_1\epsilon_2}{\delta^{2/3}\sqrt{K}(1+j_{11})z^*} \frac{J_1(j_{11}z^*)}{J_1'(j_{11})} \tag{3 - 100a}$$

and

$$w_1(0) = \frac{-\epsilon_1\epsilon_2 j_{11}}{2\delta^{2/3}\sqrt{K}(1+j_{11})J_1'(j_{11})} \ . \tag{3 - 100b}$$

A numerical evaluation of Eqs. $(3 - 100)$ reduces them to the following relations:

$$w_1(z^*) = \frac{1.855\epsilon_1\epsilon_2}{\delta^{2/3}\sqrt{K}} \frac{J_1(3.832z^*)}{z^*} \tag{3 - 101a}$$

$$w_1(0) = \frac{.984\epsilon_1\epsilon_2}{\delta^{2/3}\sqrt{K}} \ . \tag{3 - 101b}$$

Equations $(3 - 101)$ were utilized in computing the effect of interfacial pressure boundary conditions in the HIAR code. Figure 97 shows the effect of the interfacial distribution of $(3 - 10)$ on the prediction of the midspan chordwise pressure distribution for the NACA 0012 elliptic wing case mentioned previously for $\epsilon_1 = \epsilon_2 = .2$. With all other parameters the same, the streamwise and angular pressure dependence results in a loss of lift from the free jet and unconfined flow distributions. Associated Zierep singularity behavior is discussed in Appendix B. This example demonstrates a capability which will be useful in testing and exploiting concepts for integrating asymptotic methods with experimental measurements, (AIM) is a new class of WIAC techniques. AIM concepts will be discussed in Section 4. Here, the HIAR code can be a useful means of testing various concepts.

3.6 Viscous Effects

Viscous effects play an important role in wall interference estimates. In connection with this observation, recent complementary Rockwell IR&D effort indicates that viscous effects on a NACA 0012 airfoil for a free field case close to that of Fig. 94 can produce a substantial movement in the shock from its trailing edge position predicted by a purely inviscid full potential solver. This is shown in Figs. 98–100, where an interacted boundary layer solution moves the shock system to the midchord position. On the basis of this experience and other related activity reported in Refs. 48–51, another contemplated future development related to the AIM activity is a viscous version of the HIAR code.

3.7 Nonsimilar Section Wings and Lockheed Database

The primary emphasis of this phase of the contractual effort was focused on relating the high aspect ratio code to an experimental database. Accomplishments were:

- The code was generalized to handle nonsimilar section wings in which the airfoil sections are not the same shape.

- One of the wings tested in Ref. 52 was analyzed with the interference-free code (0th order) as well as the software for assessing wall interference (1st order).

- The 0th order code was used to establish the correctibility of the Ref. 52 data.
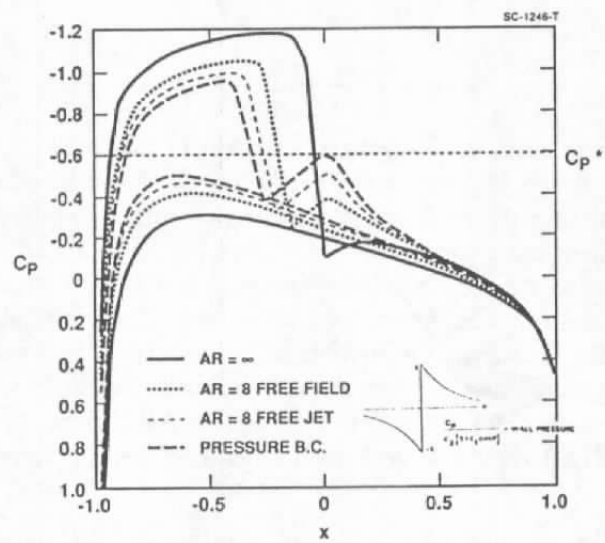
Fig. 97. Chordwise pressures at midspan with pressure boundary condition, elliptic planform wing NACA 0012 airfoil, $M_\infty = 0.75$, $\alpha = 2°$, $\mu = 1.05$, AR = 8, $\epsilon_1 = \epsilon_2 = .2$.
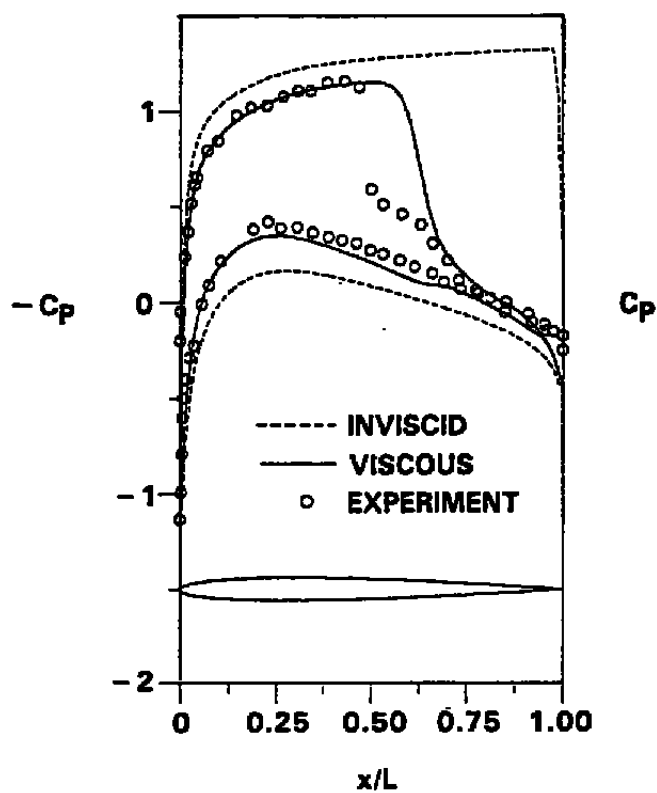
Fig. 98. Comparison of predictions from viscous interacted full potential equation solver and experiment.
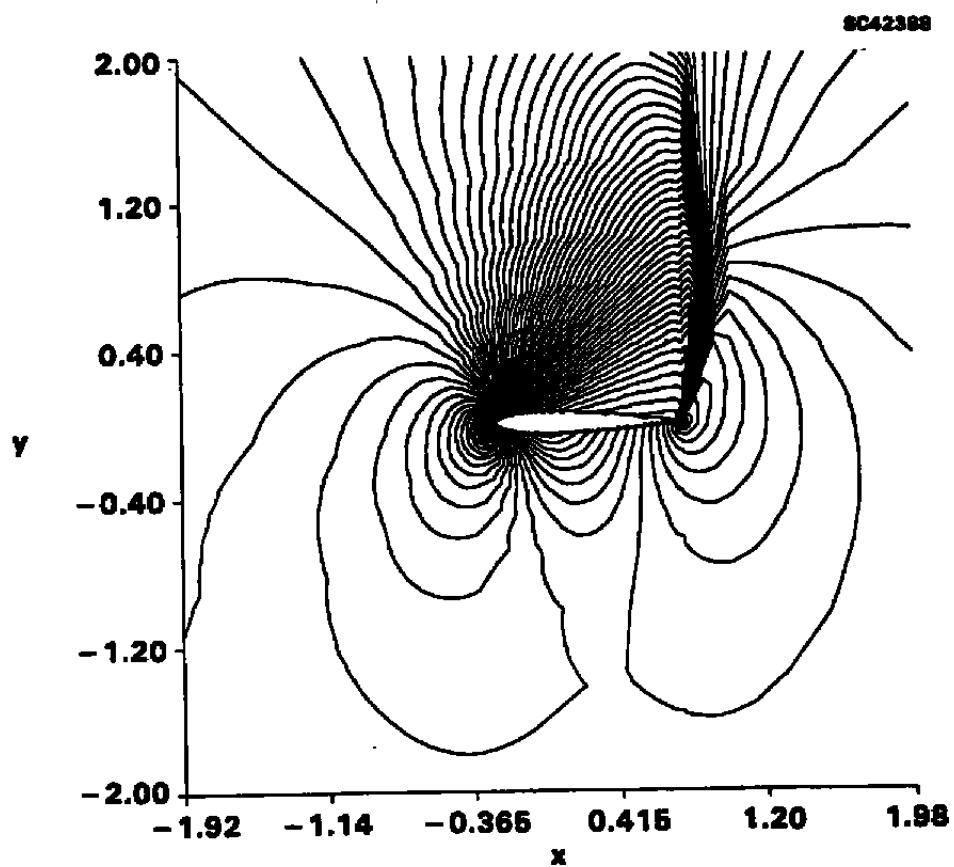
Fig. 99. Density level lines for inviscid flow — shock at trailing edge, NACA 0012 airfoil, $M_\infty = 0.799$, $\alpha = 2.26°$, 1650 iterations.
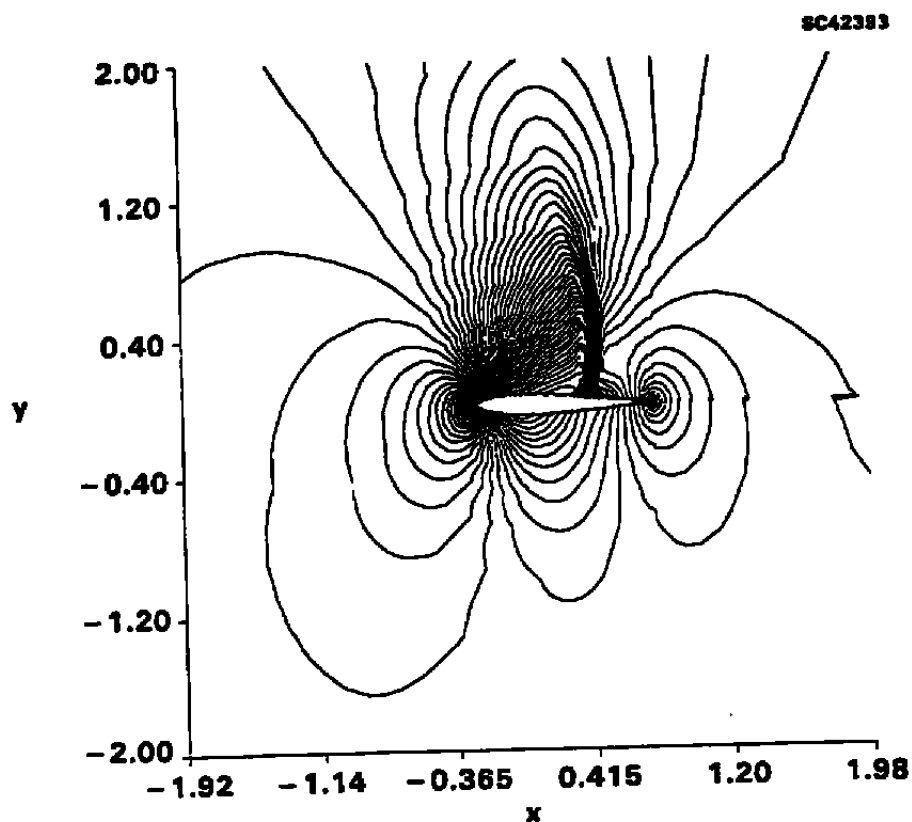
Fig. 100. Density level lines for viscous interacted full potential code. Viscous effect moves inviscid trailing edge shock to midchord, NACA 0012 airfoil, $M_\infty = 0.799$, $\alpha = 2.26°$, 1650 iterations.

3.7.1 Swept Wing Comparison Database

In Ref. 53, databases were reviewed as candidates for interaction with the contractual effort described herein. One of these (Ref. 52), although having sparse pressure data in the far field, was selected to provide an assessment of how the methods of this contract might be applied. In this experiment, three swept wings were tested in the Lockheed tunnel, isolated from, and in combination with, a fuselage at transonic Mach numbers.

3.7.2 Code Generalization to Nonsimilar Section Wings

Table 2 (Table 1 from Ref. 52) gives the geometric parameters of the wings tested and Fig. 101 gives a sketch of their planforms. In Fig. 102, the root, midspan, and tip sections are indicated. This wing has thickness, twist, and camber distributions that vary linearly along the span and is therefore non–similar. Accordingly, the similarity formulation used in Section 3.2.2 must be generalized.

This can be accomplished by simplifying the problem described by Eqs. $(3 - 58)$ and $(3 - 59)$ with the transformation

$$\Phi = \frac{\phi}{\phi_{FF}} - 1 \quad , \tag{3 - 102a}$$

with

$$\phi_{FF} = y(d + w) \quad , \tag{3 - 102b}$$

Equation $(3 - 58a)$ implies

$$L[\Phi] = 0 \quad , \tag{3 - 102c}$$

Equation $(3 - 58b)$ leads to

$$\Phi \simeq -\frac{\Gamma_1}{2\pi\phi_{FF}}\theta \quad \text{as } r \to \infty \quad , \tag{3 - 102d}$$

and

$$\Phi_y(x,0) = 1 \quad (0 \le x \le 1) \quad . \tag{3 - 102e}$$

From Eq. $(3 - 58c)$,

$$[\Phi] = \frac{\Gamma_1}{\phi_{FF}} \quad . \tag{3 - 102f}$$

Thus, the use of $(3 - 102a)$ and $(3 - 102b)$ reduces the calculation to solution of equations identical to the similar–section–wing equations, $(3 - 61)$, with the exception that the nonlinear term has ϕ_{0_z} evaluated not at $z = 0$. In addition, the quantities d and w are used parametrically at each span station from a knowledge of $\Gamma_0(z)$, the spanwise loading of the 0th order problem. This corresponds to a kind of strip theory. In order to obtain Γ_0, the semispan wing is divided into n span stations, and the zeroth order problem $(3-57)$ is solved at each. For the results to be presented, n was selected to be 5. Depending on the planform, some investigation is required to determine if this value provides a good enough approximation of the spanwise loading to obtain the ϕ_1 variational solution accurately.

Table 2. Wing Model Geometry (from Ref. 52)

	WING		
	A	B	C
AR	8.0	3.8	2.6
λ	0.4	0.4	0.3
$\Lambda_{c/4}$, deg.	25.0	30.0	38.4
θ_r, deg.	2.76	2.50	2.38
θ_t, deg.	-2.04	-4.00	-5.79
$(t/c)_r$, %	12.0	6.0	7.0
$(t/c)_t$, %	12.0	6.0	11.0
$S/2$, cm^2 (in^2)	528.0 (81.8)	530.0 (82.1)	523.0 (81.0)
$b/2$, cm (in.)	45.7 (18.0)	31.8 (12.5)	26.1 (10.26)
C_r, cm (in.)	16.51 (6.50)	23.88 (9.40)	30.83 (12.14)
C_t, cm (in.)	6.60 (2.60)	9.55 (3.76)	9.25 (3.64)
MAC, cm (in.)	12.26 (4.825)	17.71 (6.974)	21.95 (8.642)
Y_{MAC}, cm (in.)	19.59 (7.714)	13.60 (5.355)	10.68 (4.206)

SC80720

WING	A	B	C
AR	8.0	3.8	2.6
Λ_{LE}	27°	35°	45°
λ	0.4	0.4	0.3
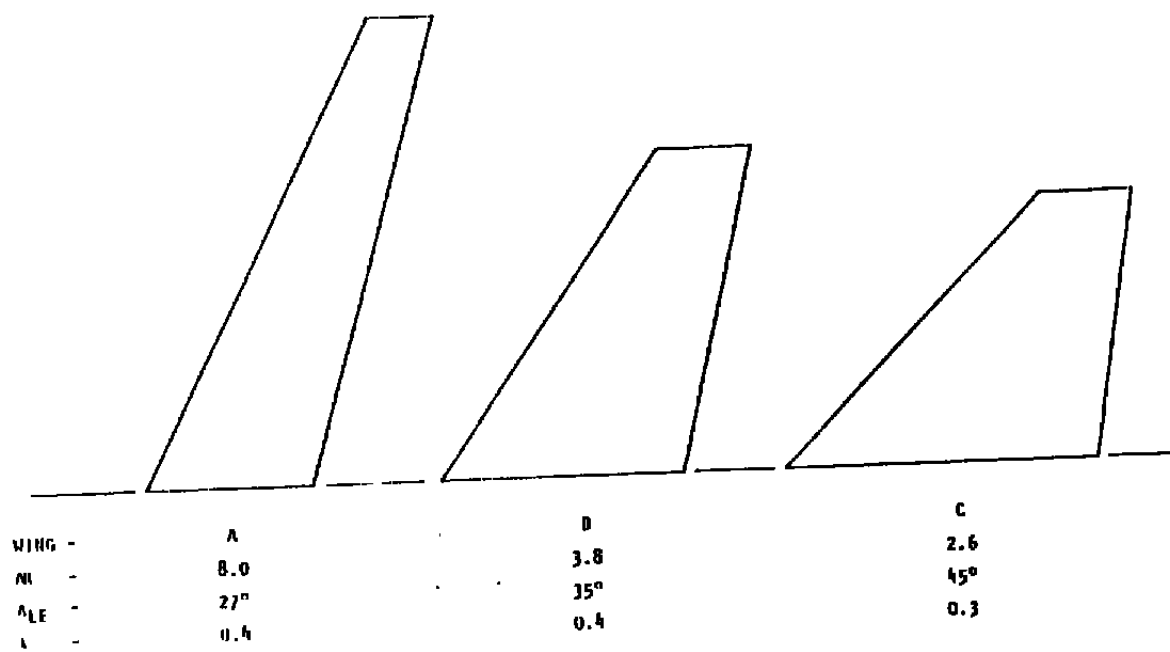
Figure 101. Planforms of tested wings (from Ref. 52).

172

SC50716
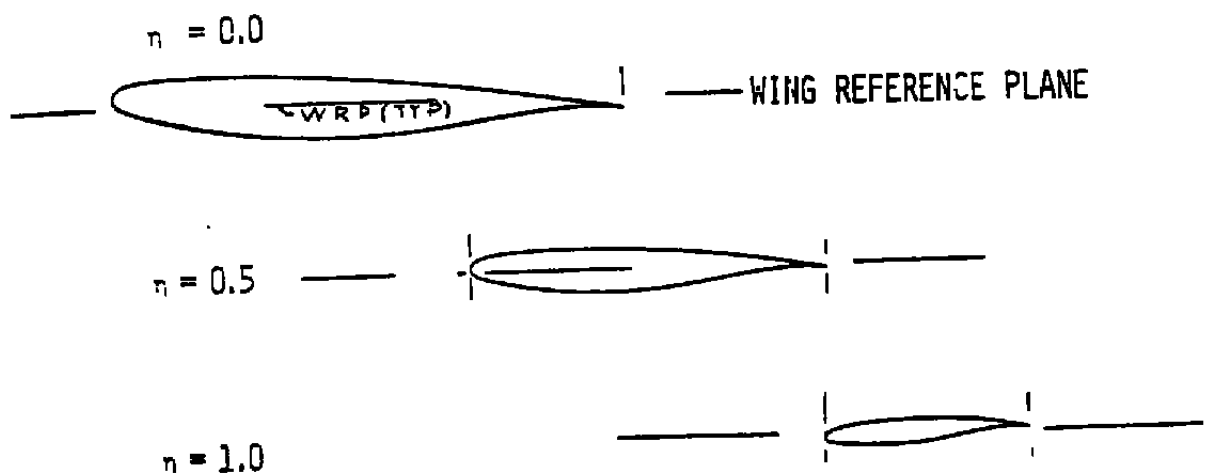
Figure 102. Wing A airfoil sections (from Ref. 52).

3.7.3 Results

Chordwise pressure distributions on the swept wing (Wing A) configuration of Ref. 52 were computed at various angles of attack α, and Mach number M. To achieve rapid convergence, the streamwise grid was clustered near the blunt leading edge. To demonstrate a typical calculation, Figs. 103 and 104 show the effect of wall interference and finite span corrections on the chordwise pressures of Wing A at nearly midspan, and at two angles of attack. The largest corrections appear to be near the shock at $\alpha = 0°$. By contrast, the more supercritical case corresponding to $\alpha = 1°$ shows a greater extent of the corrections. For both incidences, they are most pronounced on the upper wing surface.

In Ref. 30, modifications to the boundary value problem $(3 - 57)$ are discussed for a yawed wing. The analysis shows that these changes occur in the far field for the three-dimensional 1st order perturbation flow and in both the far field and equations of motion for the 2nd order flow.

The HIAR code is based on a theory not designed for swept wings. This is because the dominant approximation of the inner flow assumes that all spanwise stations are approximately two dimensional. If a discontinuity occurs in the slope of the leading edge, a local three-dimensional flow occurs, nullifying this assumption. Such discontinuities occur at the root apex and tips of swept and other kinds of planforms. More general cases are cranked shapes. Asymptotic procedures are under consideration to treat these corner flows and involve "canonical" numerical problems for the nonlinear flow near the corner. These canonical problems remain the same for planform changes away from the corner.

In spite of this limitation, it was of interest to assess the correctability of the Wing A results using the 0th order code. Figures 105 and 106 indicate chordwise pressure comparisons of our 0th order code with data from Ref. 52. In both figures, the effective tunnel Mach number and angle of attack were modified to match the data. The similarity of the pressure distributions suggests the correctability of the test data. In Fig. 105, the influence of shock–boundary layer interaction is not as great as in Fig. 106. For treating viscous effects more effectively, under complementary IR&D funding, the contractor has developed an interactive boundary layer code based on Green's Lag Entrainment model that would presumably reduce the effective increment in K associated with the combined Mach, angle of attack corrections used in Figs. 105 and 106. This was used to obtain the previously discussed results indicated in Figs. 98–100.

3.7.4 Discussion

In comparisons such as Figs. 105 and 106, what needs to be analyzed are the combined effects of sweepback and viscous interactions on the interference. In Ref. 29, the similarity parameter K was allowed to vary from the 0th order flow to the 1st order wall interference flow. This flexibility should be investigated with the aim of systemizing the corrections that can be obtained through studies of the type associated with Figs. 105 and 106. The variation of K is expressed in a perturbation form related to the asymptotic expansion of the perturbation potential ϕ. This perturbation gives the flexibility of varying the tunnel Mach number and geometric angle of attack to correct or simulate free field conditions.

SC50708
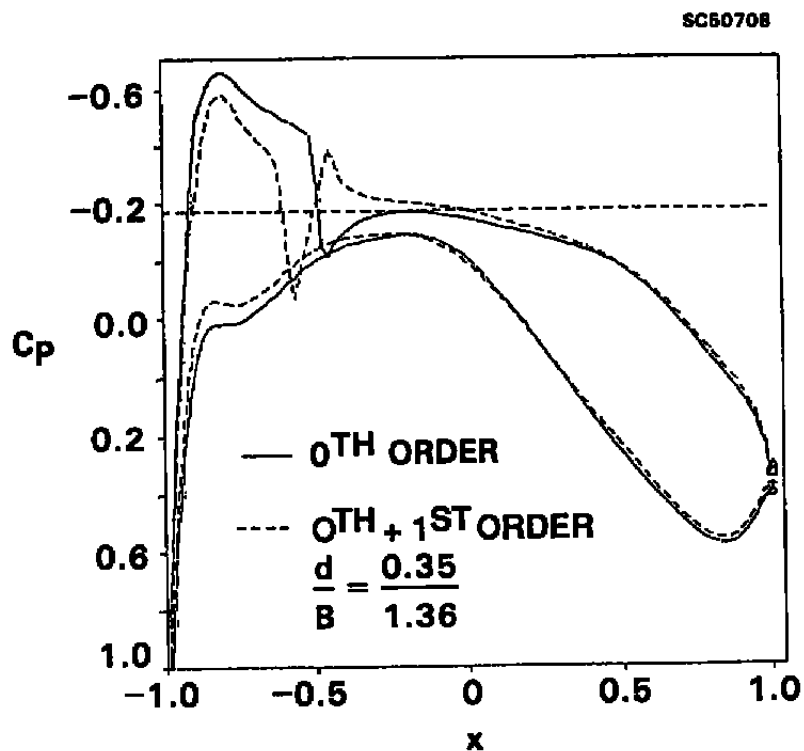
Figure 103. 0th and 1st order chordwise pressure distributions on Wing A, $\eta = 0.45$, $M = .76$, $\alpha = 0°$.

SC50709
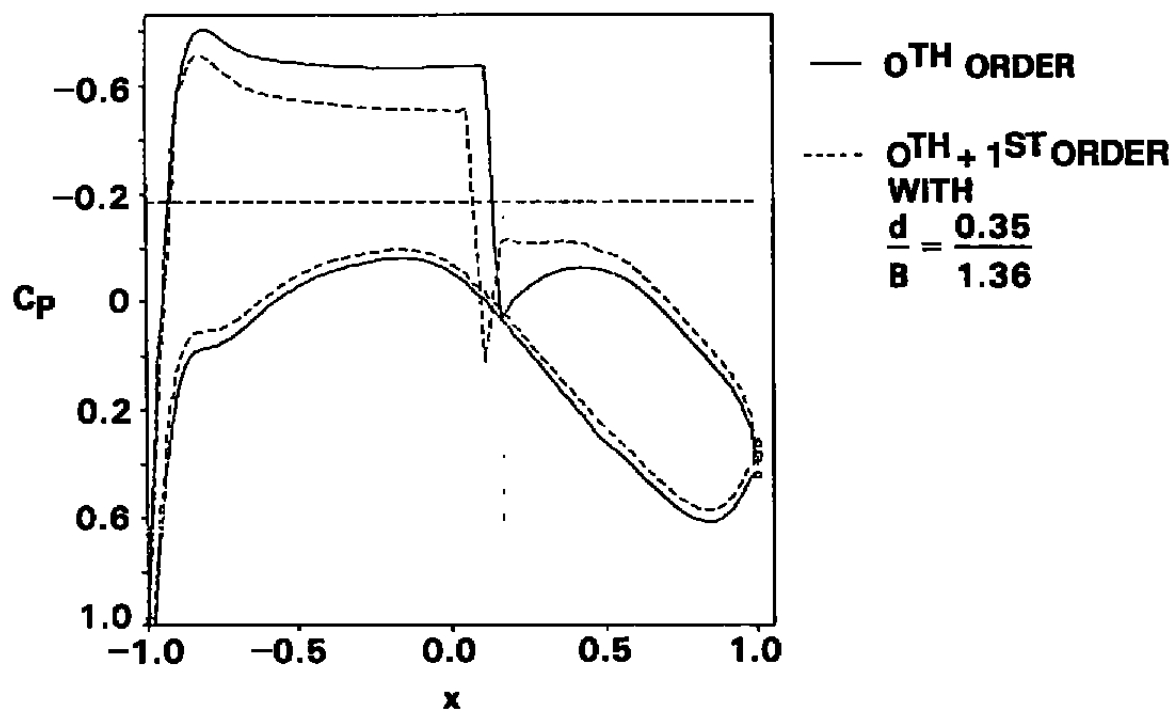
Figure 104. 0th and 1st order pressure distributions on Wing A, $\eta = 0.5$, $M = .76$, $\alpha = 1°$.
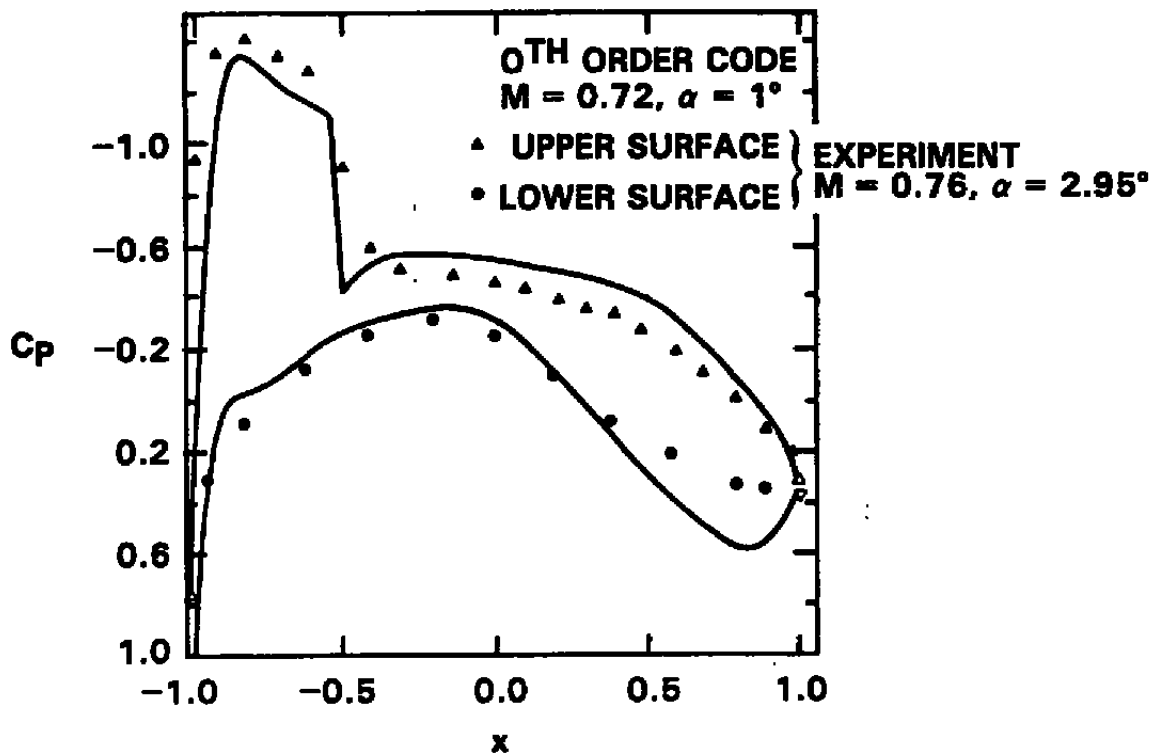
Figure 105. Comparison of theoretical and experimental chordwise pressures for Wing A, $\eta = 0.5$, tested at $M = 0.76$, $\alpha = 2.95°$.
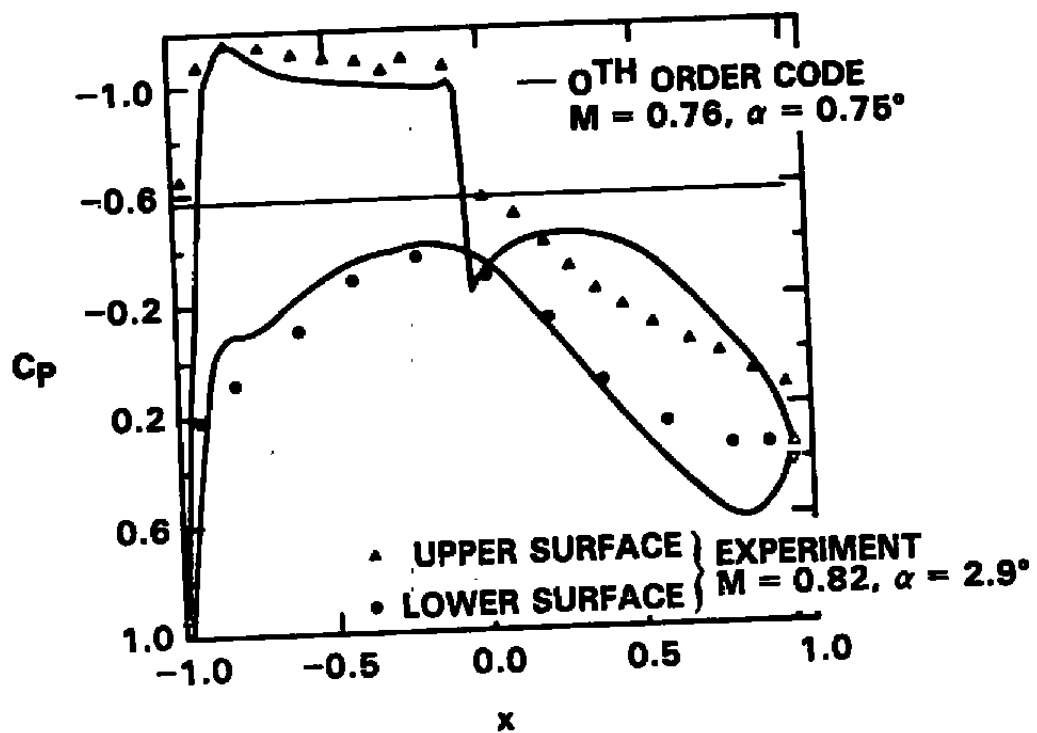
Figure 106. Comparison of theoretical and experimental chordwise pressures for Wing A, $\eta = .5$, tested at $M = 0.82$, $\alpha = 2.9°$.

3.8 Fuselage Effects

A high aspect ratio wing–body configuration is shown inside a wind tunnel in Fig. 107. In what follows, the effect of the fuselage on the theory for wing–alone transonic wall interference will be considered. For this purpose, the fuselage will be considered slender and axisymmetric. Within the coordinate system shown in Fig. 107, the equation of the body is

$$B = r - \delta F(x) = 0 \quad . \tag{3-103}$$

The analyses in the previous sections and Ref. 29 indicate that the transonic high aspect ratio wing flow in a wind tunnel could be treated by an extension of the lifting line theory for the unconfined case discussed in Ref. 30. The principal ideas are that:

1) The near field (inner expansion) in the vicinity of the wing is two dimensional in the sense that the span stations are independent.

2) The finite span effect is felt through the effective downwash of the trailing vortex system on a bound vortex or lifting line simulating the wing. The trailing vortex system corresponds to the outer (far field) expansion.

3) The effective "twist" of Item 2 is computed by a form of Biot Savart's law which was systematically derived from an integral representation based on Green's formula. This twist represents matching of the inner and outer expansions.

4) The wall interference problem can be solved by using an appropriate redefinition of the Green's function used in the Green's formula of Item 3 which satisfies the appropriate wall boundary conditions in contrast to the free field definition.

Based on the findings of Section 3.1.1.2, the Green's function amounts to imaging the streamwise projection in the Trefftz plane of the wing trailing vortex system into the projection of the wind tunnel wall boundary. This theory is an outgrowth of a systematic asymptotic treatment of the transonic case. It gives a Green's function which has the same form as for incompressible flow derived by a different method in Ref. 54. The basic features of the lifting line idealization of the flow are shown in Fig. 55 for a circular wind tunnel.

If the tunnel Mach number is such that the far field is subsonic, then Green's formula can be used to solve the Prandtl Glauert equation of motion which can be recast as Laplace's equation if the transonic similarity parameter K is scaled out in the usual way. Green's formula can then be used to give an integral representation of the flow. Characterizing the field by a perturbation potential ϕ which has been defined in Section 3.1.1.2, the integral representation $(3-10a)$ with addition of the body is now

$$\phi = I_{\text{BODY}} + I_{\text{WALLS}} + I_v \tag{3-104a}$$

where:

$$I_{\text{BODY}} = \int_{\text{BODY}} \int \left(\phi \frac{\partial G}{\partial n} \right) dS \tag{3-104b}$$

179

SC46484A

MODEL

Y

r

θ

**INNER LIMIT
REGION OF OUTER**

WAKE

z

x

TUNNEL BOUNDARY
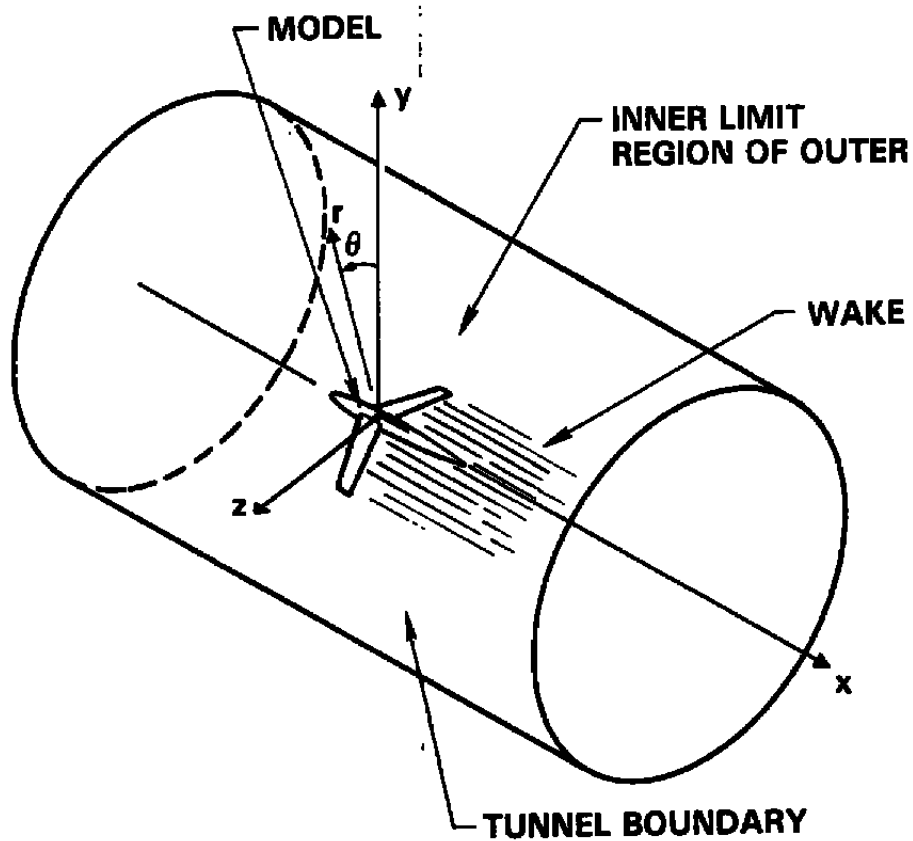
Fig. 107. Confined high aspect ratio wing–body model.

and I_{WALLS} and I_v are defined in $(3-10\text{b})$ and $(3-10\text{c})$ and $G = 0$ on the walls as in Section 3.1.1.2. Therefore, if a free jet wall boundary condition $\phi = 0$ is considered, $I_{\text{WALLS}} = 0$. For convenience, the thickness effect of the wing will be neglected in what follows. The analysis can be easily extended to include it.

It will be seen that the principal effect of the body is to modify the integral I_v in $(3-11\text{a})$. This causes a change in the finite–aspect–ratio downwash all along the loaded line. A more local effect occurs in the near field at the wing–body junction in the case of the flow near the tips or a kink at the center of a planform. In these regions, the assumption of independence of spanwise sections is invalid. The resulting fully three–dimensional flows are assumed to lead to only a secondary influence on wall interference and will therefore not be considered in what follows. The main focus will be the calculation of I_v. Prior to its calculation, we note that I_{BODY} is given by

$$I_{\text{BODY}} = \lim_{\rho \to 0} \int_0^\ell \frac{\partial \phi}{\partial \rho} \cdot 2\pi\rho G_{\text{BODY}} d\xi \quad . \tag{3-105}$$

By linearity of the outer flow field, the body is assumed to be characterized by a line source which is superimposed on the trailing vortex sheet flow shown in Fig. 55. Here,

$$\lim_{\rho \to 0} \rho \frac{\partial \phi}{\partial \rho} = \frac{A'(\xi)}{2\pi} \quad , \tag{3-106}$$

where A is the local cross sectional area. Because of the superposition property, a more general fuselage shape can be considered. For such a configuration, $(3-105)$ and $(3-106)$ would still be valid.

In a free field,

$$G = -\frac{1}{4\pi} \frac{1}{\sqrt{(x-\xi)^2) + (y-\eta)^2 + (z-\zeta)^2}} \tag{3-107}$$

where for y, η, z, ζ will hereinafter signify scaled coordinates.

For free jet boundary conditions on a circular wall, it was shown in Section 3.1.1.2 that

$$G = \frac{1}{2\pi\mu^2} \sum_{n=-\infty}^{\infty} \cos n\theta \sum_k \frac{e^{-\lambda_{nk}|z-\xi|} J_n(\lambda_{nk}r) J_n(\lambda_{nk}\rho)}{\lambda_{nk} \left[J_n'(\lambda_{nk}\mu) \right]^2} \quad , \tag{3-13'}$$

where the J_n are Bessel functions and λ_{nk} their zeros in accord with definitions given earlier, and by symmetry the θ' argument given in $(3-13)$ is omitted. Because of axial symmetry, the effect of I_{BODY} on the finite aspect ratio downwash effect will be zero.

To treat I_v, the result obtained from a systematic approximation procedure for the wing–alone case will be generalized. The generalization will be obtained by modifying the imaging solely in the Trefftz plane. Accordingly, the doublet sheet interaction with the free jet tunnel boundaries will be considered as depicted in Fig. 108. As in Section 3.1.1.2, the effect of the line doublet is obtained by superposition of individual elements. A circular

cross section body is analyzed herein. More general cross sections can be handled by the techniques described in Refs. 49 and 51.

To expedite the solution, only slender bodies in the sense that the maximum body diameter is small compared to the wing span will be treated. In fact, in the outer limit certain stretched coordinates were introduced in Ref. 29. Denoting the span in units of the chord as b, these are

$$x^* = \frac{x}{B} \quad , \quad y^* = \frac{y}{B} \quad , \quad z^* = \frac{z}{b} \quad , \quad B = \delta^{1/3} b \quad \text{fixed as } \delta \to 0 \quad . \quad (3-108)$$

Accordingly, $\epsilon = \frac{\delta^{4/3}}{B}$. Obviously, other choices are possible besides using δ as the body maximum thickness in $(3-1)$. This option gives a region of transonic flow around the body that has lateral dimensions of $O(\delta^{-1})$.

To obtain the image of a doublet in the annular region $\epsilon \leq r^* \leq \mu$ shown in Fig. 108, perturbation methods are used. Here, $r^* = \sqrt{y^{*^2} + z^{*^2}}$. Two cases can be identified:

$$(i) \qquad \zeta = O(1)$$
$$(ii) \qquad \zeta = O(\epsilon)$$

Case (i)

Denoting the complex potential as $F(Z) = \phi(z,y) + i\psi(z,y)$ with $Z = z + iy$, where the stars on y and z will be dropped, the appropriate expression for F is

$$2\pi i F = \underbrace{\frac{1}{Z-\zeta}}_{①} + \underbrace{\frac{\epsilon^2}{\zeta^2}\left(\frac{1}{Z - \frac{\mu^2}{\zeta}}\right)}_{②} - \underbrace{\left(\frac{1}{\epsilon^2} + \frac{1}{\zeta^2}\right)\frac{\epsilon^2}{Z}}_{③}$$
$$\underbrace{+\frac{1}{\zeta}}_{④} \qquad\qquad (3-109)$$

In $(3-109)$, ① represents the doublet, ② its "reflection" in the tunnel boundary $r = \mu$, ③ is a compensation term to make the body a stream surface, and ④ is a constant added to match the Case (ii) expression for ζ in an overlap domain of mutual validity. This feature will be used to obtain a uniformly valid representation in ζ. Term ③ is associated with the behavior

$$① + ② \doteq \left(\frac{1}{\epsilon^2} + \frac{1}{z^2}\right) Z \quad \text{as} \quad Z \to 0$$

and the circle theorem for homogeneous Dirichlet conditions. Thus if $A = \frac{1}{\epsilon^2} + \frac{1}{z^2}$,

$$① + ② + ③ = A\left(Z - \frac{\epsilon^2}{Z}\right)$$

SC48993
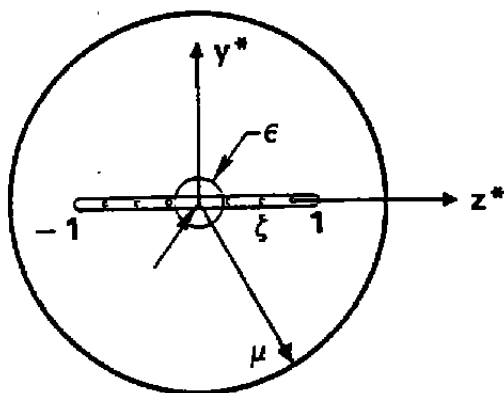
Fig. 108. Projection of doublet sheet in Trefftz plane.

and since $\overline{Z} = \frac{\epsilon^2}{Z}$ on $r = \epsilon$, then

$$① + ② + ③ = A(Z - \overline{Z})$$

so that

$$Re(① + ② + ③) = 0$$

which is the desired property.

It is important to note that the reflection term ③ does not spoil the boundary condition on the tunnel boundary $|Z| = \mu$.

Case (ii)

For this case,

$$2\pi i F = \underbrace{\frac{1}{Z - \zeta}}_{①'} - \underbrace{\frac{\epsilon^2}{\zeta^2}\left(\frac{1}{Z - \frac{\epsilon^2}{\zeta}}\right)}_{②'} - \underbrace{\frac{Z}{\mu^2}\left(1 - \frac{\epsilon^2}{\zeta^2}\right)}_{③'} \ . \qquad (3 - 110)$$

In $(3 - 110)$, Term ③$'$ plays the same role at $|Z| = \mu$ that ③ did in $(3 - 109)$ at $|Z| = \epsilon$.

Equations $(3 - 109)$ and $(3 - 110)$ can be used for separate ranges of a convolution integral representing the perturbation potential of the doublet sheet in the Trefftz plane. To remove arbitrariness associated with the cutoff between Case (i) and Case (ii), a combined uniformly valid expression in ζ is preferred. This is obtained for the function

$$U(Z; \zeta) \equiv 2\pi i F - \frac{1}{Z - \zeta} \ . \qquad (3 - 111)$$

An intermediate limit is considered in which

$$\zeta_\eta = \frac{\zeta}{\eta} \quad \text{fixed as} \quad \epsilon \to 0$$

where $\epsilon \ll \eta(\epsilon) \ll 1$.

Thus, for both Case (i) and Case (ii),

$$U = -\frac{Z}{\mu^2} + O\left(\frac{\epsilon^2}{\eta^2}\right) \ . \qquad (3 - 112)$$

The uniformly valid representation is therefore the sum of the representations for Case (i) and Case (ii) minus the common part given by $(3 - 112)$. The resulting expression is

$$2\pi i F = \frac{1}{Z - \zeta} + \frac{1}{\zeta^2}\left\{\frac{\mu^2}{Z - \frac{\mu^2}{\zeta}} - \frac{\epsilon^2}{Z - \frac{\epsilon^2}{\zeta}}\right\} + \frac{1}{\zeta} - \left(\frac{1}{\mu^2} + \frac{1}{\zeta^2}\right)\frac{\epsilon^2}{Z} + \frac{\epsilon^2}{\zeta}\frac{Z}{\mu^2} \ . \quad (3 - 113)$$

Taking the real part in $(3-113)$, the resulting expression for I_v is:

$$I_v = \frac{y}{4\pi} \int_{-1}^{1} \gamma(\zeta) \left\{ \frac{1}{(z-\zeta)^2 + y^2} \left(1 + \frac{x}{\sqrt{x^2 + y^2 + (z-\zeta)^2}} \right) \right.$$

$$+ \frac{1}{\zeta^2} \left[\frac{\mu^2}{\left(z - \frac{\mu^2}{\zeta} \right)^2 + y^2} - \frac{\epsilon^2}{\left(z - \frac{\epsilon^2}{\zeta} \right)^2 + y^2} \right] + \frac{1}{\zeta} \qquad (3-114)$$

$$\left. - \left(\frac{1}{\mu^2} + \frac{1}{\zeta^2} \right) \frac{\epsilon^2}{y^2 + z^2} + \frac{\epsilon^2}{\zeta^2 + \mu^2} \right\} d\zeta \quad .$$

3.8.1 Discussion

Equation $(3-114)$ represents the downwash expression associated with finite span for a high aspect ratio wing–body combination in which the body maximum thickness is a small fraction of the span. This expression is the generalization of that being used for the inner solution far field for the wing–alone code. It contains interactions between the tunnel boundaries and the body. It is clear that the most important contribution is when $\zeta = O(\epsilon)$.

4. ASYMPTOTICS INTEGRATED WITH MEASUREMENT (AIM) INTERFERENCE ESTIMATION METHODS

Analytical and computational techniques were described in the previous sections to predict transonic wind tunnel interference over slender and high aspect ratio models. These methods are oriented to interference prediction strictly from a knowledge of the tunnel and model geometry as well as the flow parameters such as test section Mach number. They are based on an inviscid approximation of the flow. However, by allowing the boundary conditions on an outer wall or cylindrical interface to correspond to the specification of pressure, viscous and other phenomena may be indirectly incorporated into the analysis in accord with methodology developed by workers at AEDC, NAE Ottawa, NASA, and elsewhere. For purposes of the following discussion, such techniques will be grouped under the category of Wind Tunnel Interference Assessment/Correction (WIAC) methods. By contrast to the methodology in Sections 2 and 3, these approaches combine the analysis and computation with experimental methods to determine the magnitude of the interference as well as the feasibility of accounting for the interference either by simulating an interference-free condition corresponding to the test environment or providing some sort of post-test correction to the data.

In what follows, procedures are described that can augment the effectiveness of WIAC concepts. They exploit the theoretical knowledge developed under this contract described earlier in this report as well as experimental measurements in the determination of wall interference. The scope of the discussion is to outline the basic concepts. A more detailed feasibility study as well as proof of concept is intended as future effort.

4.1 Interference on Moderate and Low Aspect Ratio Configurations

As described in Ref. 29 and elsewhere, the two variable method (TVM) provides a basis for simulating the effective body shapes in the tunnel which may differ from the "hard" physical geometry of the model due to viscous interactions and other effects. If this representation is assumed to be the same in the free field, then its knowledge from measurement and computation can be utilized with further computation to obtain the free field aerodynamics or the interference. Existing transonic TVM's such as those described in Ref. 13 typically employ a second measurement on the interface to establish the effective body shape with an iterative computational inverse procedure. In the inverse method, a first guess is successively refined in a feedback loop to satisfy the second interface condition. A concept has been developed in the contract to avoid this loop or accelerate its convergence. Application to nonaxisymmetric compact configurations that satisfy a class of requirements which may be of considerable practical WIAC utility has been investigated.

The method is motivated by slender body theory. Using previous notation in which α = angle of attack, δ = maximum thickness ratio, b = semispan, h = characteristic wall lateral dimension, the flow over a test article shown in Figs. 109 and 110, and given by

$$r = \delta F(x,\theta) \qquad (4-1)$$

186

o

is considered, where the normalized cylindrical coordinates

$$x = \frac{\bar{x}}{c} \quad , \quad y = \frac{\bar{y}}{c} \quad , \quad z = \frac{\bar{z}}{c} \quad , \quad r = \frac{\bar{r}}{c} \quad , \qquad (4-2)$$

are employed and c is a characteristic body length. In the inner near field, close to the model as described in Refs. 29 and 30, the following asymptotic expansion is assumed to be valid for $H = h\delta$ fixed*

$$\frac{\Phi}{U} = x + 2\delta^2 \log \delta S_1(x) + \delta^2 \varphi_1(x, y^*, z^*; A) + \delta^4 \log \delta \varphi_{21}(x, y^*, z^*; A) + \delta^4 \varphi_2(x, y^*, z^*; A) \qquad (4-3)$$

which is valid in the inner limit

$$x, y^* = \frac{y}{\delta} \quad , \quad K = \frac{1 - M_\infty^2}{\delta^2} \quad , \quad A = \frac{\alpha}{\delta} \quad \text{fixed as} \quad \delta \to 0 \quad . \qquad (4-4)$$

The "far field" of this inner expansion worked out in Ref. 30 is if $r^* = r/\delta \to \infty$

$$\varphi_1 = S_1(x) \log r^* + g_1(x) + \frac{D_1(x)\cos\theta}{r^*} + \frac{E_1(x)\cos 2\theta}{r^{*2}} + \cdots \qquad (4-5a)$$

$$\varphi_{21} = 2S_1 S_1' \log r^* + g_{21}(x) + 2S_2(x) + \cdots \qquad (4-5b)$$

$$\varphi_2 = S_1 S_1' \log^2 r^* + S_2(x) \log r^* + g_2(x) + \cdots \qquad (4-5c)$$

where if $A^*(x) =$ normalized cross sectional area, $S_1 = \frac{A^{*''}(x)}{2\pi}$ and S_2 can be found from integral theorems based on the inner boundary value problems but will not be considered further here. This approximation is nonuniform with respect to r^*. Two other approximate representations are required to overcome this nonuniformity. For $H = $ fixed, and a cylindrical wall, there is an outer region in which the asymmetries relax to nonlinear axial symmetry in a manner that has been discussed in Refs. 29, 30 and elsewhere**. Preliminary studies based on integral equation asymptotics and particular solutions indicate that the wall reflections are regular functions of r^* which do not perturb the singular behavior that controls matching with another representation needed in an intermediate domain to obtain consistent approximations in the higher orders. This fact has implications on the magnitude of the lift interference.

From Ref. 30, the outer expansion of Φ is:

$$\frac{\Phi}{U} = x + \delta^2 \phi_1(x, \tilde{y}, \tilde{z}; K, A, H) + \delta^4 \log \delta \phi_{21} + \delta^4 \phi_2 + \cdots \qquad (4-6a)$$

---

* The $H \to \infty$ approximation made in Ref. 29 will be suppressed.

** This property can be extended to mildly noncircular test sections such as octagonal shapes or measurement interfaces that are sufficiently distant so that the angular perturbations are weak. This can be formalized asymptotically.

SC83-22869
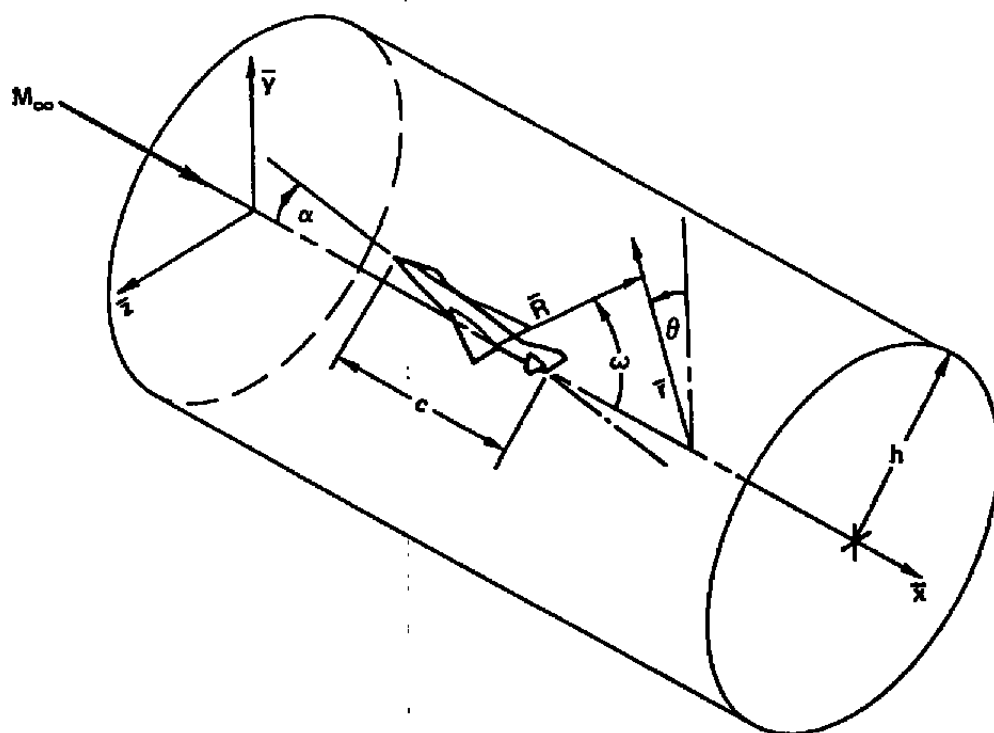
Fig. 109. Slender vehicle confined inside cylindrical wind tunnel walls.
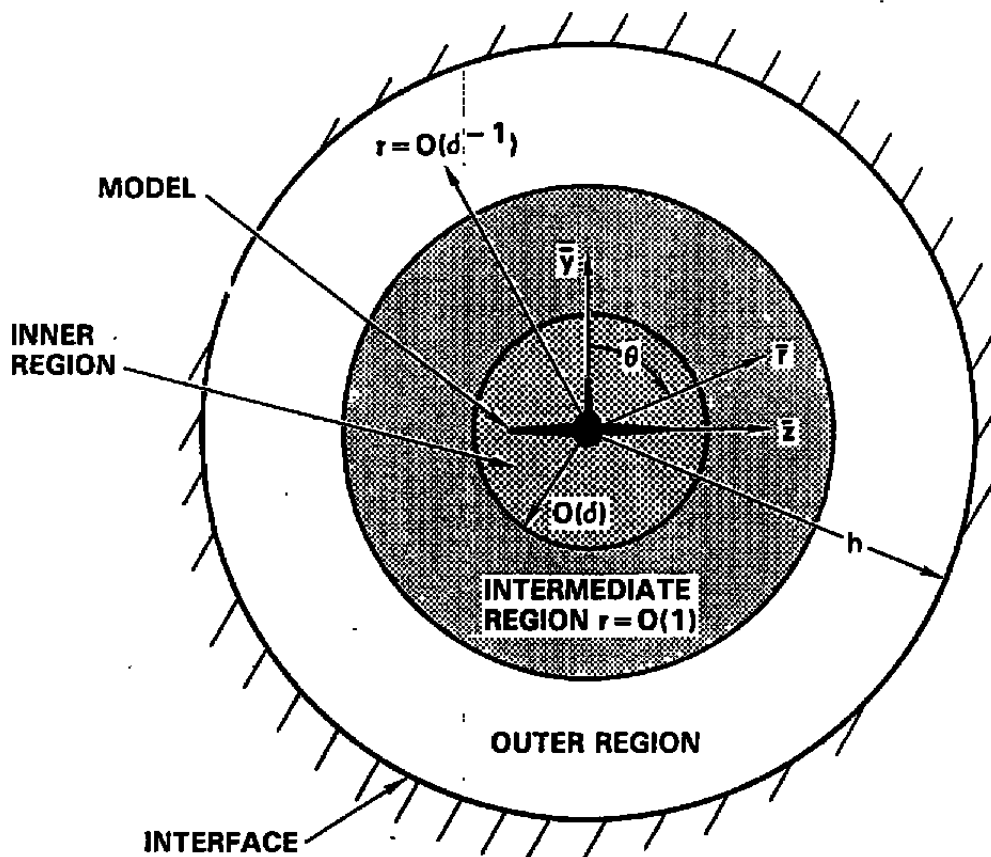
Fig. 110. Front view of wind tunnel model confined by cylindrical walls, showing important regions.

for

$$x, \tilde{y}, \tilde{z}, K, A, H \text{ fixed as } \delta \to 0 \quad . \tag{4-6b}$$

The equation for ϕ_1 is the Karman Guderley (KG) equation,

$$(K - (\gamma + 1)\phi_{1_s})\phi_{1_{ss}} + \frac{1}{\tilde{r}}(\tilde{r}\phi_{1_r})_{\tilde{r}} = 0 \tag{4-7}$$

where no tunnel perturbation in K is assumed.

In contrast to a large H far field or a subsonic line source free field asymptotic, an axisymmetric pressure-specified interface condition for $(4-7)$ is

$$\phi_1(x, H) = F(x) \tag{4-8}$$

which in accord with previous remarks is assumed to leave the free field $\tilde{r} \to 0$ asymptotics of $(4-6s)$ unaffected to dominant order. These are:

$$\phi_1 = S_1(x)\log \tilde{r} + g_1(x) + \left(\frac{\gamma+1}{4}S_1'S_1''\right)\tilde{r}^2 \log^2 \tilde{r} + T(x)\tilde{r}^2 \log \tilde{r} + V(x)\tilde{r}^2 + \cdots \tag{4-9a}$$

$$\phi_{21} = -2S_1 S_1' \log \tilde{r} + g_{21} + \cdots \tag{4-9b}$$

$$\phi_2 = \frac{D_1(x)\cos\theta}{\tilde{r}} + S_1 S_1' \log^2 \tilde{r} + g_2 + \cdots \quad . \tag{4-9c}$$

The intermediate expansions are

$$\frac{\Phi}{U} = x + \delta^2 \log \delta S_1(x) + \delta^2 \overline{\phi_1}(x, y, z) + \delta^3 \phi_2 + \delta^4 \log^2 \delta \overline{\phi_{32}}(x, y, z)$$
$$+ \delta^4 \log \delta \overline{\phi_{31}}(x, y, z) + \delta^4 \overline{\phi_3}(x, y, z) + \cdots \tag{4-10a}$$

for

$$x, y, z, r, K \text{ fixed as } \delta \to 0 \quad , \tag{4-10b}$$

where for matching with the inner expansions the following representations hold:

$$\overline{\phi_1} = S_1(x)\log r + g_1(x) + \cdots \tag{4-11a}$$

$$\overline{\phi_2} = \frac{D_1 \cos\theta}{r} + \cdots \tag{4-11b}$$

$$\overline{\phi_{31}} = g_{21}(x) + S_2(x) + \frac{\gamma+1}{4}(S_1'^2)r^2 \log r$$
$$+ [(\gamma+1)(g_1'S_1')' - KS_1'' - (\gamma+1)(S_1'^2)']\frac{r^2}{4} + \cdots \tag{4-11c}$$

$$\overline{\phi_{32}} = -S_1 S_1' + \frac{\gamma+1}{4}S_1'S_1''r^2 \tag{4-11d}$$

$$\overline{\phi_3} = \frac{E_1 \cos^2 \theta}{r^2} + S_1 S_1' \log^2 r + S_2(x) \log r + g_2(x) \qquad (4-11e)$$

$$+ \frac{\gamma+1}{4} S_1' S_1'' r^2 \log^2 r + T(x) r^2 \log r + V(x) r^2 \quad . \qquad (4-11f)$$

For purposes of assessing drag interference, *the key idea in one possible AIM TVM concept being evaluated is that Eqs. (4 - 11) can be used to determine the "effective body" interaction with nonlinear outer flow field.* For example, it is envisioned that $(4-11a)$ can be used to determine the effective source strength $S_1(x)$ by a simple radial differentiation, i.e.,

$$\frac{\Phi_r}{U} = \delta^2 \overline{\phi_{1_r}} + O(\delta^3) = \frac{\delta^2 S_1(x)}{r} \qquad (4-12)$$

and a measurement of the radial velocity Φ_r on an interface surface $r = O(1)$ at each x station. The function $S_1(x)$ can be used with the boundary condition associated with the dominant term of $(4-9a)$ to obtain the solution of $(4-7)$ subject to $(4-8)$, where F can be obtained from pressure measurements as

$$F = -\frac{2}{\delta^2} \int_{-\infty}^{x} C_p(x, H) dx \quad . \qquad (4-13)$$

The solution of the outer KG problem will give the free field drag and the interference. For example, under mild restrictions on the equivalent body of revolution source strength distribution $S_1(x)$, the free field wave drag D is

$$\frac{D}{\rho_\infty U^2} = 2\pi\delta^4 \int_0^1 S_1'(x) g_1(x; K) dx \qquad (4-14)$$

based on a momentum theorem given in Ref. 30. In $(4-14)$, the function g_1 is computed from the numerical solution of the free field KG problem.

In accord with previous remarks, it is envisioned that this approach may be generalized to weak deviations about axial symmetry on a measurement interface in the outer region $\tilde{r} = O(1)$.

Analyses of the free field structure for the highly and intermediately loaded cases have been given in Refs. 48 and 55, respectively. Reference 48 describes the case where $K = \frac{1-M_\infty^2}{\epsilon_1}$, with $\epsilon_1 = \alpha^2 \ln \frac{1}{\sqrt{\epsilon_1}}$, and Ref. 21 considers the thickness $\delta = O(\epsilon_1)$. For Ref. 48, in contrast to the case described in detail above, the first order term in the near field is approximately a dipole. No intermediate expansion is needed to match with the outer representation which still relaxes to KG axial symmetry to dominant order. However, the effective source strength S_1, rather than being controlled by the rate of change of cross-sectional area $A^*(x)$ as in the weakly loaded case, is given by:

$$S_1 = \frac{\gamma+1}{2} \frac{\ell_1'(x)\ell_1''(x)}{(2\pi)^2} \qquad (4-15)$$

where $\ell_1(x)$ is the cumulative free field lift up to a station x, which can be computed by Jones' theory. For a cambered, zero-thickness wing on $(0 \leq x \leq 1, -z_{LE} \leq z \leq z_{LE})$, for which $y = \alpha f(x)$, $\ell_1(x) = -\pi f'(x) z_{LE}^2(x)$. Studies are in progress of the matching to assess what is the role of the wall reflections on the inner flow field structure and their importance relative to the interference lift. For drag of a zero thickness configuration, the effective source strength distribution may be inferred from the measurement procedure previously described, since the outer solution has the same dominant behavior given by $(4 - 11a)$, in spite of the different interpretation in $(4 - 15)$.

The relaxation to the structure given by $(4 - 9a)$ in about the $r = O\left(\frac{1}{c_1}\right)$ scale of the lift dominated theory has been corroborated with zonal gridding procedures and free field Euler calculations of K. Szema which were funded under another program using codes and algorithms developed by S. Chakravarthy. The F-14 configuration shown in Fig. 111 was analyzed with simulated flow-through inlets at $M_\infty = .8$, and $\alpha = 13.5°$. The isobars are shown in Fig. 112. There is also a suggestion of near field $\frac{\cos\theta}{r}$ behavior in the contours which are however skewed by strong tip vortices.

The relaxation shown in Fig. 112 is a suggestion of the feasibility of the radial velocity unfolding concept previously indicated to obtain the effective source strength S_1. One possible application of the method could be the cruise missile configuration discussed in Ref. 47.

4.2 High Aspect Ratio Configuration WIAC Method

Considering the high aspect ratio arrangement shown schematically in Fig. 113, at a wake station PQ associated with a near field limit of the outer solution, downwash due to the vortex sheet reflected in the tunnel walls has been derived and discussed in connection with the lifting line theory of transonic wall interference in Section 3.1.1.2. Suppressing the additional fuselage upwash effect and its interaction with the walls, which can be handled by conformal mapping procedures, the net downwash in a $y = 0$ downstream plane of the wing alone is

$$w = -\frac{1}{4\pi} \int_{-B}^{B} \gamma'(\zeta) \left\{ \frac{1}{z-\zeta} + \frac{\mu^2}{z(z\zeta - \mu)} \right\} d\zeta + w_1(z) \qquad (4-16)$$

where using previously defined notation $\mu = H/B = \frac{h}{b}$, $H = \delta^{1/3}h$, $B = \delta^{1/3}b$, γ is proportional to the free field infinite aspect ratio sectional lift coefficient and w_1 is the downwash effect associated with deviation of the pressure field on the interface from zero perturbation pressure, where from Section 3.1.2, if the interface pressure is C_{P_I}

$$W(x^*, \theta) = \int_{-\infty}^{x^*} \frac{C_{P_I}(x^*, H, \theta)}{-2\delta^{2/3}} dx^*$$

$$= W_0(x) + \sum_{n=1}^{\infty} W_n(x) \cos n\theta$$

$$x = Hx^* \quad , \quad \bar{y} = \delta^{1/3}y = Hy^* \quad , \quad \bar{z} = \delta^{1/3}z = Hz^*$$

SC45487
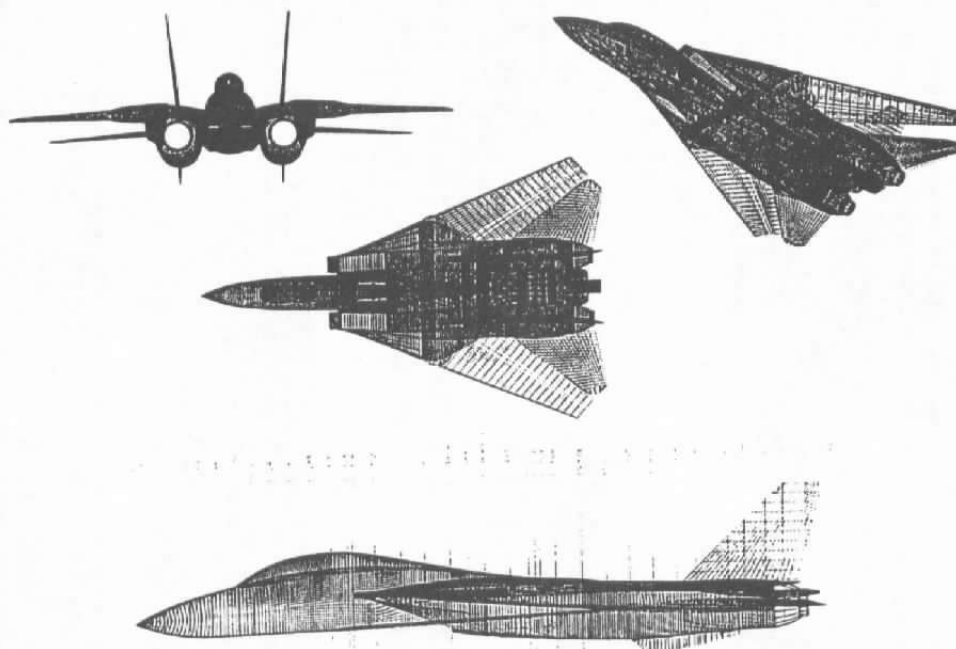
Fig. 111. F–14 configuration.
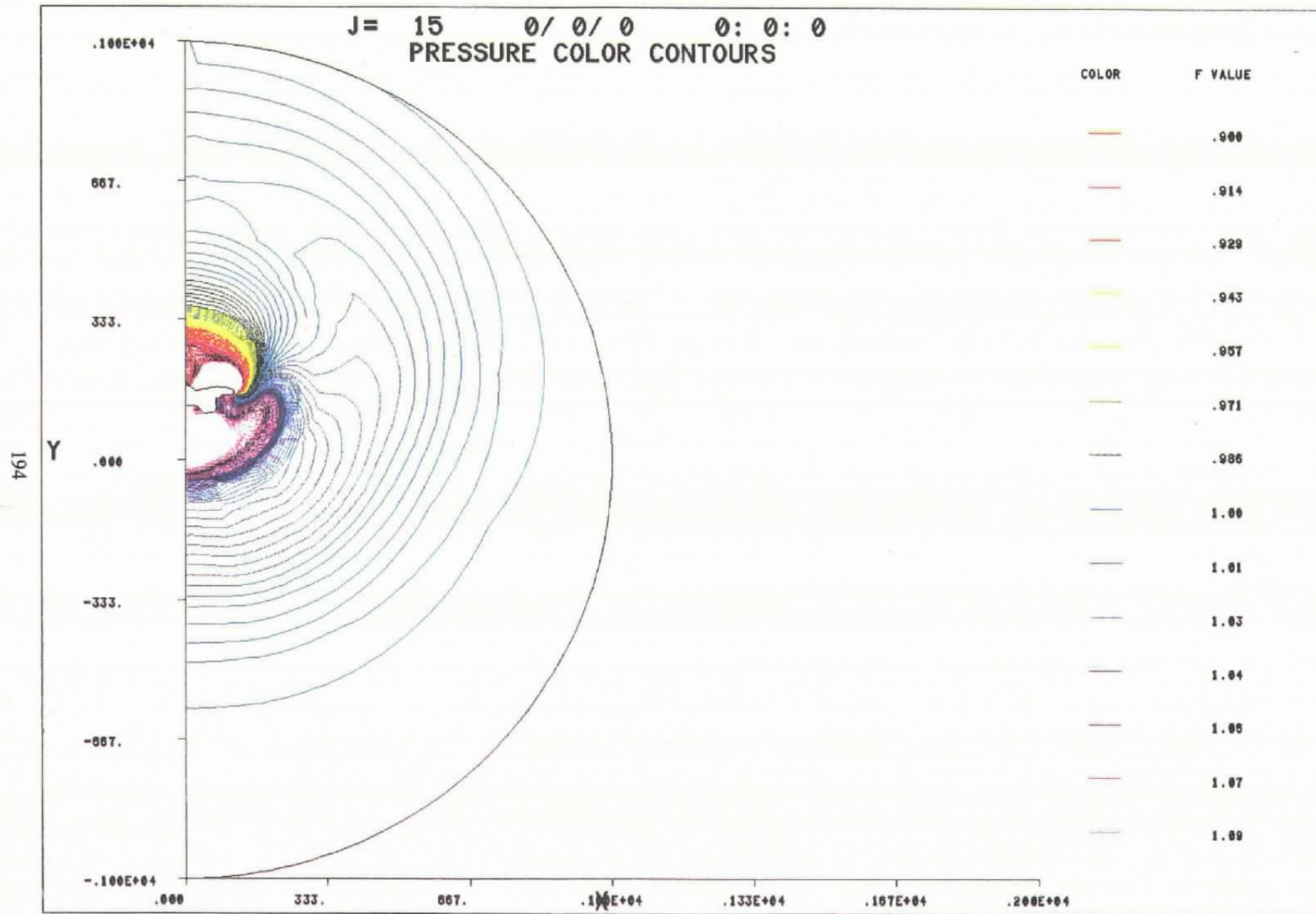
Fig. 112. Isobars in F–14 cross–flow plane.

SC45484

MODEL

y

INNER LIMIT
REGION OF OUTER

θ

Q

WAKE

z

P

x

INTERFACE
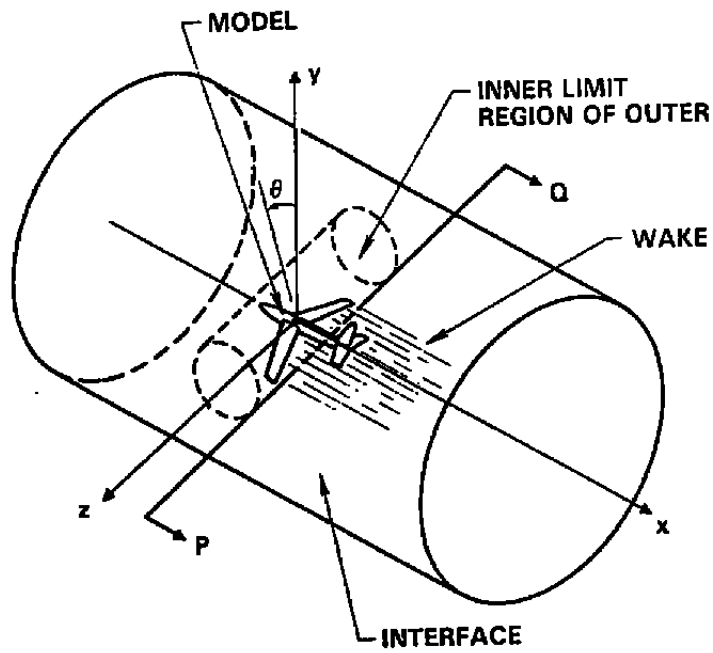
Fig. 113. High aspect ratio wing model.

with

$$W_0 = \frac{1}{\pi} \int_0^\pi W(x^*, \theta) d\theta$$

$$W_n = \frac{2}{\pi} \int_0^\pi W(x^*, \theta) \cos n\theta d\theta$$

and

$$w_1 \sim \frac{1}{\sqrt{K}z} \sum_{n=1,3,5,\cdots}^\infty n(-1)^n \frac{J_1(j_{n1}z^*)}{J_n'(j_{n1})} \int_{-\infty}^\infty e^{-j_{n1}|x^*|} W_n(x^*) dx^*$$

where K is the transonic similarity parameter and the j_{n1} are the zeros of the Bessel functions $J_n(z^*)$.

Equation $(4-16)$ can be used to determine the free field lift and span loading as follows:

1. Measure the left hand side w at PQ. A generalized form of $(4-16)$ applies at $y \neq 0$ and the measurement could be made above or below $y = 0$, if this is more practical.

2. Equation $(4-16)$ can be inverted once and for all numerically and presumably also analytically with a Green's function based on conformal mapping.

3. An analytic inversion of $(4-16)$ can be used to compute $\gamma'(\zeta)$ by a quadrature. This could be interpreted as the "effective" span loading associated with viscous effects.

4. The function $\gamma'(\zeta)$ in Item 3 can be used to compute the free-field finite aspect ratio downwash correction w_{∞} on the loaded line given by

$$w_{\infty} = -\frac{1}{4\pi} \int_{-B}^B \frac{\gamma'(\zeta)}{z - \zeta} d\zeta \qquad (4-17)$$

where the principal value of the integral is to be taken.

5. The HIAR code can be used with w_{∞} to compute the free field span loading and lift.

4.2.1 Discussion

Steps 1–5 in the high aspect ratio AIM method sidestep the need for computationally intensive three-dimensional simulations as well as time-consuming gridding preparation. It however requires a knowledge of the downwash field behind the model. This can be done by a rake or other instrumentation. Once this is obtained, $(4-16)$ can be inverted using Fourier series or collocation methods. *The approach indicated is by no means limited to a downwash measurement.* Other derivatives of the scheme can be conceived such as using pressure measurements. Since the approach depends on the application of lifting line theory, its elasticity with respect to moderate aspect ratio shapes needs to be assessed. This can be achieved by comparisons with three-dimensional numerical simulations and experiment.

5. CONCLUSIONS, HIGHLIGHTS AND SUMMARY OF FINDINGS

Transonic wall interference asymptotic formulations developed under a previous AEDC contract, "Study of Asymptotic Theory of Transonic Wind Tunnel Wall Interference," (Contract F40600-82-C-0005) have been computationally implemented. This activity motivated additional asymptotic studies and the development of AIM (Asymptotics Integrated with Measurement) techniques that are designed to extend the applicability of the computational and analytical methods.

Key findings and highlights of the effort are:

1. The "Area Rule" for transonic wall interference of slender airplane test articles discovered in the previous contract, applies for pressure boundary conditions in the large height limit, $H \rightarrow \infty$. Its validity for pressure interface boundary conditions needs to be assessed for $H = O(1)$.[*]

2. The scalings associated with the gauge functions appearing in the formal asymptotic expansions for the interference potential in the slender body limit agrees with that deduced by Goethert in Ref. 56 using non-asymptotic methods and validated against experiment.

3. Pressure specified interface boundary conditions over confined, slightly subsonic slender bodies give an asymptotic triple deck structure resembling that arising from free jet and and solid-wall, classical conditions, providing that the interface circumferential variations are mild. Such angular distributions are anticipated in the sensible far field with circular or octagonal test sections, even for realistic, compact fighter configurations having appreciably asymmetric cross sections, but at moderate angles of attack. This occurs because of the strong three-dimensional flow relief associated with this small average effective thickness ratio or characteristic flow deflection (δ) regime and the associated rapid relaxation to axial symmetry in the radial direction transverse to the freestream.

4. The inner deck has the usual Oswatitsch Equivalence Rule cross-flow harmonic structure. For large height, the intermediate layer is a weak perturbation about free field conditions, where the strength of the perturbation is $o(H)$ as $H \rightarrow \infty$. In this region, matching with the outer deck shows that the effect of the pressure boundary conditions is felt in an average sense, *i.e.*, only the first few harmonics of the circumferential variation are important. The outer or "wall" deck is an effective tube vortex reflection of the multipole representation of the test article. Higher order approximations of the intermediate or central deck lead to $\frac{\partial^2}{\partial \theta^2}$ terms in the equation of motion. However, the significant computational overhead of the resulting three dimensional formulation can be avoided since the θ variation is simple and can be factored out due to linearity. This leads to a

---

[*] The asymptotic treatment of these pressure conditions was undertaken over and above the Work Statement of the current contract.

two dimensional (axisymmetric) formulation similar to that encountered in the FJSWCI (free-jet or solid wall cylindrical interface) problem, except with forcing terms (in the higher approximations). These can be readily treated with superposition procedures that are allowable due to linearity of the variational interference equations.

5. With pressure interface boundary conditions, the H scaling of the similarity laws for ΔC_P and ΔC_D, respectively, the interference pressures and drag, are unchanged from the FJSWCI case. Again, in contrast to the $H = O(1)$ problem, but as in the FJSWCI case, the H scaling is known, eliminating the need to solve for new H's associated with different test facilities when all other parameters are unchanged.

6. For solid walls, and for the $H = O(1)$ numerics, the structure of the upstream and downstream far fields was determined. For a blunt or stinged base, a uniform source flow at infinity results, in which $\phi \simeq \pm Cx$ as $x \to \pm\infty$, where $C \sim$ body base area. For a closed body, $\phi \simeq \pm D$ as $x \to \pm\infty$, where D=doublet strength which consists of a linear part, proportional to the body volume, and a nonlinear portion proportional to the average kinetic energy of the interference perturbation of the streamwise velocity component. It was expedient to avoid this term in computational implementations for closed bodies. Homogeneous Neumann conditions were used at the inflow and outflow boundaries $x = \pm\infty$ rather than the doublet condition. This step was justified due to the exponentially small higher order terms in the $x \to \pm\infty$ far field expansion. This structure is similar to two-dimensional flow solutions worked out in Ref. 57, in which the wall condition "drives" a faster decay than the algebraic one associated with the free field. The exponential rate of decay for the axisymmetric case of slender body theory differs from the two-dimensional airfoil case since these are eigenvalues arising from the Sturm–Liouville problem for the Green's function and these differ in both situations.

7. Consistent with the contractual Statement of Work (SOW), Task 1.0, a code solving only the FJSWCI case was developed. (Pressure boundary conditions however can be treated by the high aspect ratio code developed under Task 3.0.) Two solver modules (RELAX1 and RELAXV1) were developed to model the 0th order free field basic flow and its 1st order wall interference perturbation, respectively. An excellent experimental validation of RELAX1 was achieved for a blunt nosed axisymmetric body tested by Couch et al. It is believed that an intrinsic element in obtaining this validation was the special procedure developed to discretize the boundary points near the logarithmically singular line $\tilde{r} = 0$ in the inner Axis deck of the flow. In keeping with the thrust of the contractual effort that combines the best features of asymptotics and numerics, these discretizations used the inner expansion instead of a one term Taylor expansion with a remainder to characterize the nodes near $\tilde{r} = 0$.

8. Special techniques extending those originally developed by Small and Cole were utilized to fit the shock in the numerical treatment of the interference perturba-

tion flow. Schemes were worked out to surround the shock by an "upright" notch having vertical and horizontal sides. This scheme which is easier to program and avoids subtle issues associated with an alternative method which actually follows the shock curve with a "staggered notch" was computationally implemented. More effort is required to compare the effectiveness and accuracy of both approaches. An important issue is the accuracy of the discretization of the vertical velocity component v_1 of the variational flow and the avoidance of unnecessary smearing out of the shock region beyond the normal Rankine–Hugoniot transition zone if an upright notch is used. For slender bodies, this concern seems to be relieved by the fact that the shocks are almost normal, since the freestream Mach number needs to be very close to unity to obtain a supersonic bubble of any significant size. A study of the relative criticality of this issue for the high aspect ratio problem is also needed.

9. Other sensitivities of the numerical treatment of the interference field are the proper dimensions of the notch and the definition of the tip of the shock. For the two-dimensional airfoil case, Murman numerically investigated the formation of the shock as the envelope of the characteristics of the second family reflecting from the sonic line. Because of its steepness, this envelope is poorly defined. The calculations showed some sensitivity to this definition as well as the location of the position of the upstream and downstream vertical legs of the notch. More work is needed to improve this part of the method. From experimentation and an examination of the pressure profiles as well as the x discretizations, a four point transition seemed appropriate for the width of the notch for slightly subsonic tunnel Mach numbers.

10. In a separately funded AFOSR effort, the structure of the triple point singularity at the foot of the shock was examined in connection with handling the perturbation Rankine–Hugoniot shock conditions at the notch, particularly at the foot. As a part of this, Cole and Malmuth in Ref. 38 analyzed a shock position invariance with Mach number discovered by the latter in calculations of the flow over a parabolic arc body. More work is needed to understand this phenomenon in free and confined flows in connection with generalized Lavrentef–Bitsadze models.

11. Calculations for flow over a parabolic arc body at a freestream Mach number of .99 indicate that the wall perturbation flow has a very dominant spike localized about the shock region. The preshock influence is very weak compared to the postshock influence. The shock spike phenomenon seems to control the entire structure of the interference flow and there is rapid decay away from this region.

12. Allowing for a perturbation K_1 in the similarity parameter K in the asymptotic expansions for the perturbation potential provides flexibility in defining minimum interference or interference-free conditions. A proof of concept has been obtained in which interference-free conditions for the drag have been been defined for a parabolic arc body through alteration of the tunnel Mach number or its thickness ratio using methodology discussed in Section 2.18.

13. Lift interference is negligible compared to drag interference for the thickness dominant distinguished limit of the free field slender body basic flow.

14. Pressure specified boundary conditions include the same mechanism governing wall interference for high aspect wings as with free jet and solid wall boundary conditions. Namely, the interaction is still primarily associated with the alteration of the downwash field on the loaded line (bound vortex) due to the interference of the walls or interface with the trailing vortex system. The effect of the variable interface pressures can be handled by a superposition of a tube vortex and a free jet solution. The tube vortex corresponds to the interfacial pressure data and is continuous across the wing wake. The sum of both solutions satisfies the boundary conditions of the complete problem. The tube vortex modifies the downwash on the loaded line, i.e., the effective angle of attack along the span of the wing.

15. The interference downwash on the loaded line due to the imaging of the trailing vortex sheet into the walls or interface was analyzed to successfully accomplish Task 2.0 of the contractual effort. A Green's function method was developed to provide an extremely powerful means of obtaining an asymptotically consistent approximating sequence for the imaging. Properties of the Bessel functions appearing in the integral or eigenfunction representation of this Green's function indicate that even for the transonic case, the downwash field is essentially the same as that for incompressible flow. In particular, it is the solution of a two-dimensional problem in the Trefftz plane infinitely far downstream. This problem reduces to the interaction of a two-dimensional vortex sheet distributed along the projection of the wake in the Trefftz plane with the circular projection of the walls or interface in this plane. Another Green's function which can be obtained by the Method of Reflection involving inversion in a circle solves this problem. However, the expansions of the Bessel functions in the expression for the first Green's function give this interpretation directly. Corresponding information is needed for choked and slightly supersonic tunnel flows.

16. Under Task 3.0, a code capable of handling high aspect ratio configurations was developed. As in the slender body code written under Task 1.0, an upright notch was used to treat the shock in the interference flow. The downwash boundary conditions developed in Task 2.0 were used for the solver module which determines the interference field. The code can handle wings with spanwise nonsimilar sections by use of a normalizing "trick" which reduces the computational problem to one resembling that for similar sections. Pressure interface boundary conditions can be treated in many situations through the post–processing rather than the solving step. This feature is another saving in computational overhead. The code is quite inexpensive, with practical results readily accessible on VAX6000-410 type mainframes and clusters. It is ideally suited for use on workstations such as SUNs and VAXstations. For more utility and geometric applicability, the effect of sharp kinks in the planform shape needs to be analyzed. A special issue not present in the slender body code needed attention in the development of this

code. It concerned the improvement of the efficiency of the algorithm by use of convergence acceleration methods. Application produced significant speedup in the attainment in the pseudotime asymptotic for the interference circulation Γ_1. To improve the numerical conditioning as for the slender body code, the far field singularity was regularized by subtracting it out from the dependent variable ϕ_1, converting the homogeneous boundary conditions on the body to inhomogeneous ones. For the slender body case, a forcing term was added to the equation of motion with this method. Another change in the formulation under this transformation is a slight modification of the shock jump conditions. Regarding grids, the main issue relates to adequate clustering at blunt leading edges, shocks and trailing edges. From the previous discussion, those related to embedding the wind tunnel or interface boundaries into the grid are vastly simpler than those encountered in large–scale Navier Stokes simulations.

17. Calculations with the high aspect ratio code indicate that the effect of free jet boundary conditions on slightly subsonic wings is to reduce the lift and make the wing less supercritical. The shock is weakened and moved upstream. For many cases, it is envisioned that the change of the spanwise loading tends to follow the inner solution "strip theory" scaling with the local chord variations as in incompressible flow. More work is required to help define the role of interference on the nonlinear interaction between vortex and wave drag which differentiates transonic flows over these high aspect ratio wings from their low Mach number counterparts.

18. Preliminary analytical work has been done on the effect of a fuselage on high aspect ratio wings. It is envisioned that the most important change in this regard is the interruption of the projection of the trailing vortex system in the Trefftz plane by the body, providing that the body size is small compared to the wing span. For such configurations, the interaction of the body thickness with the far field near the interface and the inner solution does not appear to be significant in determining the lift interference. However, the effect on drag needs to be investigated.

19. Two techniques were developed to extend the applicability of the asymptotic approaches developed to more realistic viscous environments. These AIM methods integrate asymptotic techniques with experimental approaches and have the potential of making WIAC approaches such as the TVM more economical, practical, fast–response and accurate. For missile configurations and typical compact fighter arrangements such as ATF blended wing shapes, the cross–flow gradient dominant inner deck and the Area Rule for wall interference developed in this effort indicate that a measurement of the radial variation across the flow of the pressure or the velocity field can be used to define the effective viscous "soft body", as contrasted to the "hard" geometry of the test article. One of the AIM methods employs this viewpoint to bypass iterative sequences in previous TVM schemes such as that discussed in Ref. 13 for axisymmetric bodies.

20. In addition to the low to moderate aspect ratio approach of the previous item,

another AIM method exploiting the role of the Trefftz plane imaging in high aspect ratio transonic wing wall interference has been developed. Since the 1st order interference effect is the modification of the incidence of the airfoil sections along the span, the "soft" circulation distribution can be determined from a solution of an integral equation, once the downwash or other suitable observable is measured in the wake behind the wing or on some other convenient control surface. The deconvolution of the integral equation can be done on a microcomputer with simple collocation or other methods. From the soft circulation distribution, an extrapolation to free field conditions can be obtained by a quadrature as shown in Section 4.2.

Many of the previous items enhance our knowledge of the physics of transonic wall interference and can be used in its efficient pre–test or post–test estimation. In the next section, specific recommendations are made for sharpening the tools to provide the wind tunnel test community with quick response techniques to complement large–scale CFD approaches.

6. RECOMMENDATIONS

Section 5 summarizes progress toward applying combined asymptotic and numerical methods to transonic wind tunnel interference prediction. Within the contractual effort reported herein, two computer codes were developed to handle small and large aspect ratio configurations in an inviscid flow context. Other theoretical developments have been described that provide new insights into our understanding of the physics and structure of interference at near sonic Mach numbers. To extend the applicablity of the methods to viscous and more realistic environments, AIM techniques were conceptualized that augment the theoretical approaches by interacting them with experimental data.

From the observations in the previous section, it appears that it is beneficial to further develop the tools described. Opportunities exist for further theoretical progress as well as "tuning" the methodology to actual databases. In this connection, other possibilities involve further experimentation that could be performed in parallel with the methods development. In contrast to the preponderance of tests that have been performed thus far, emphasis should be placed on integrating flow field measurements with surface pressure and force evaluations. Such a procedure would provide an excellent opportunity to validate the AIM concepts in this report and provide a means to develop others that can strengthen WIAC methods.

Specific analytical items that should receive further attention are:

1. Treatment of slightly supersonic flow.

2. Choked and nearly choked cases for slender bodies.

3. Incorporate the asymptotic and numerical methodologies developed herein into large–scale computational procedures such as Navier–Stokes, and thin layer Navier–Stokes codes. Various options in this context are:

    3.1 Use combined asymptotic–numerical (CAN) methods to initialize large scale computational solutions to accelerate convergence to pseudo–time asymptotics.

    3.2 Use structure of CAN flow to reduce gridding preprocessing effort for large scale implementation from knowledge of solution curvature it affords.

    3.3 Employ "defect" approximation to develop a corrector to first guess by expressing large scale solution as an increment on CAN result. Solve for the defect dependent variable instead of usual primitive variables.

   In addition to speeding up the large–scale simulations, these items could result in reduction of computational costs.

4. Validate the two AIM methods developed under this contract against other solutions and experiment.

4.1 For both techniques, set up experimental programs in suitable facilities in which the requisite flow measurements can be made at the same time pressures and forces are measured. Specific recommendations for such tests have been made in relation to a survey of existing databases in Ref. 53.

4.2 Compare the assumed CAN variations in both AIM methods with large scale computational simulations as another validation and proof of concept.

4.3 As part of the AIM work for slender bodies, computationally implement the pressure specified interface theory described in this report.

5. Extend the slender and high aspect ratio codes to handle viscous interaction effects. The motivation for this approach is to make the simulations developed under this contract more comparable with the test data. Integral methods such as Green's Lag Entrainment Technique could be used to facilitate the introduction of viscous effects in the CAN simulations. Viscous phenomena can be important in transonic interference as shown by recent Calspan studies at AEDC. The effectiveness and accuracy of the Science Center's viscous interaction code has been demonstrated earlier in this report in comparisons with experiment for two-dimensional flow over a NACA 0012 airfoil. These procedures can be extended to a three-dimensional context accounting for wind tunnel effects by generalizing the theories and codes developed in this contract to account for viscous interactions.

6. Computationally implement and more thoroughly develop the theory generalizing the wing-alone high aspect ratio models to wing-bodies and kinked planforms.

7. Develop adaptive wall concepts based on AIM technology. In this item, the AIM advantage of reducing computer overhead would be exploited in developing on-line closed-loop feedback systems for streamlining the walls. As discussed in previous sections of this report, the application of the inner expansion avoids the need for iterative determination of the "soft body" in the application of the TVM for axisymmetric bodies. This savings could also occur for more realistically shaped compact fighter and missile test articles.

8. Determine range of applicability of models by comparison with experiment. Particular items of interest under this heading are:

8.1 Validity of wall height scaling law from asymptotic slender body theory for interference wave drag and pressures.

8.2 Range of applicability of Area Rule for wall interference — It would be of interest to determine what constraints exist on section and test article geometry for validity of the interference Area Rule.

9. The asymptotic models developed in this contract should be integrated with local asymptotic multideck descriptions of slot and porous wall flows.

In addition to the foregoing, more theoretical work is required concerning the effect on interference of bluntness as well as lift–dominated flows for the slender body case. For the high aspect ratio limit, effort is required to study the influence of displacement of the vortex sheet on results obtained with the planar assumptions of the theory.

7. REFERENCES

1. Garner, H.C., Rogers, E.W.E., Acum, W.E.A. and Maskell, E.E., "Subsonic Wind Tunnel Wall Corrections," *AGARDograph 109*, October 1966.

2. Pindzola, M. and Lo, C.F., "Boundary Interference at Subsonic Speeds in Tunnels with Ventilated Walls," AEDC-TR-69-47 (AD 687441), May 1979.

3. Mokry, M., Chan, Y.Y. and Jones, D.V., "Two-Dimensional Wind Tunnel Wall Interference," *AGARDograph 281*, edited by L.H. Ohman, Nat. Aeronautical Establishment, Nat. Res. Council, Canada, November 1983.

4. Kemp, W.B., Jr., "Toward the Correctable-Interference Transonic Wind Tunnel," AIAA 9th Aerodynamic Testing Conference, 1976, pp. 31-38, AIAA-76-1794CP.

5. Barnwell, R.W. and Sewall, W.G., "Similarity Rules for Effects of Sidewall Boundary Layer in Boundary Layer in Two-Dimensional Wind Tunnels, presented at the AGARD Fluid Dynamics Panel Specialists Meeting, Wall Interference in Wind Tunnels, AGARD, CP-335, London, England, May 19-20, 1982, pp. 3-1-3-10.

6. Jacocks, J.L., "Aerodynamic Characteristics of Perforated Walls for Transonic Wind Tunnels," AEDC TR-77-61, June 1977.

7. Erickson, J.C., and Homicz, G.F., "Numerical Simulation of a Segmented-Plenum Perforated Adaptive Wall Wind Tunnel," *AIAA J.* 20, 5, May 1982, pp. 612-623.

8. Mokry, M., *et al.*, "Wall Interference on Two-Dimensional Supercritical Airfoils using Wall Pressure Measurements to Determine the Porosity Factors for Tunnel and Ceiling," NRC (Canada) LR-575, February 1974.

9. Lo, C.F., "Tunnel Interference Assessment by Boundary Measurements," *AIAA J.* 16, 4, April 1978.

10. Kraft, E.M. and Dahm, W.J.A., "Direct Assessment of Wall Interference in a Two-Dimensional Subsonic Wind Tunnel," presented at the AIAA 20th Aerospace Sciences Meeting, Orlando, Florida, January 11-13, 1982.

11. Sickles, W.L. and Erickson, J.C., "Evaluation of Wall Interference and Correction Techniques," AEDC-TR-87-45 AD-A195873, June 1988.

12. Rizk, M.H., and Murman, E.M., "Wind Tunnel Wall Interference Corrections for Aircraft in the Transonic Regime," *J. of Aircraft* 21, 1, January 1984, pp. 54-61.

13. Lo, C.F., and Sickles, W.L., "Two-Measured Variable Method for Wall Interference Assessment/Correction," Transonic Symposium: Theory, Application and Experiment, NASA CP-3020, 1988, pp. 853-866.

14. Newman, P.A., Kemp, W.B., and Garriz, J.A., "Wall Interference Assessment and Corrections," Transonic Symposium: Theory, Application and Experiment, NASA CP-3020, 1988, pp. 817-852.

15. Tuttle, M. and Cole, K., "Wind Tunnel Wall Interference," (January 1980–May 1988), A Selected Annotated Bibliography, NASA TM 4061, 1988.

16. Anon., "Aerodynamic Data Accuracy and Quality: Requirements and Capabilities in Wind Tunnel Testing," AGARD–CP–429, 1988.

17. Lifshits, Y.B. and Fonarev, A.S., "Effect of Flow Boundaries on Parameters of Transonic Flows Around Bodies of Revolution," *Fluid Dynamics* 13, 1978, pp. 393–399.

18. Chan, Y.Y., "A Singular Perturbation Analysis of Two–Dimensional Wind Tunnel Interferences," *ZAMP* 31, 1980, pp. 605–619.

19. Elynskaya, A.A. and Lifshits, Y.B., "Transonic Flows Around an Airfoil in Wind Tunnels," *Fluid Dynamics* 16, 1981, pp. 711–718.

20. Cole, J.D., Malmuth, N.D. and Zeigler, F., "An Asymptotic Theory of Solid Tunnel Wall Interference on Transonic Airfoils," AIAA Paper No. 82–093, presented at the AIAA/ASME Joint Thermophysics, Fluids, Plasma and Heat Transfer Conference, St. Louis, Missouri, June 7–11, 1982, also presented at the NASA Langley Workshop on Wind Tunnel Wall Interference Assessment/Correction–1983, in proceedings, NASA CP–2319, 1984, pp. 193–203.

21. Malmuth, N., Wu, C.C., and Cole, J.D., "Transonic Wave Drag Estimation and Optimization Using the Nonlinear Area Rule," *J. of Aircraft* 24, 3, March 1987, pp. 203–210.

22. Lock, C.N.H. and Beavan, J.A., "Tunnel Interference at Compressibility Speeds using Flexible Walls of the Rectangular High Speed Tunnel," British ARC R&M 2005, 1944.

23. Ferri, A. and Baronti, P., "A Method for Transonic Wind Tunnel Corrections," *AIAA J.* 11, 1973.

24. Sears, W.R., "Self Correcting Wind Tunnels," (The Sixteenth Lanchester Memorial Lecture), *Aeronautical J.* 78, 1974, pp. 80–89.

25. Parker, R.L., Jr. and Erickson, J.C., Jr., "Development of a Three–Dimensional Adaptive–Wall Test Section with Perforated Walls," paper presented at the AGARD Meeting on Wall Interference in Wind Tunnels, London, May 19–20, 1982.

26. Sears, W.R., and Erickson, J.C., "Adaptive Wind Tunnels," in *Annual Review of Fluid Mechanics* Annual Reviews Inc., 20, 1988, pp. 17–34.

27. Goodyer, M.J., and Cook, I.D., "Two and Three–Dimensional Model and Wall Data from a Flexible–Walled Test Section," presented at the NASA Langley Workshop on Wind Tunnel Wall Interference Assessment/Correction–1983, NASA CP–2319, 1984, pp. 79–88.

28. Kilgore, R.A., Dress, D.A., Wolf, S.W.D., Britcher, C.P., "Test Techniques–A Survey Paper in Cryogenic Tunnels, Adaptive Wall Test Sections, and Magnetic Suspension and Balance Systems, Transonic Symposium: Theory, Application and Experiment, NASA CP–3020, 1988, pp. 705–740.

29. Malmuth, N.D. and Cole, J.D., "Study of Asymptotic Theory of Transonic Wind Tunnel Interference," Final Report for Period May 30, 1982 through August 30, 1983, Contract No. F40600-82-C-0005, Arnold Engineering Development Center/DOS Report AEDC-TR-84-8, Tullahoma, Tennessee, May, 1984.

30. Cole, J.D., and Cook, L.P., *Transonic Aerodynamics*, North-Holland, New York, 1986.

31. Murman, E.M. and Cole, J.D., "Calculation of Plane Transonic Flows," *AIAA J.* 6, January, 1971, pp. 114-121.

32. Cook, L.P. and Cole, J.D., "Lifting Line Theory for Transonic Flow," *SIAM J. Appl. Math.* 35, 2, September, 1978, pp. 209-228.

33. Jameson, A., "Iterative Solution of Transonic Airfoils and Wings, Including Flows at Mach 1," *Comm. Pure Appl. Math.* 27, 1974, pp. 283-309.

34. Bailey, F.R., and Ballhaus, W.F., "Comparisons of Computed and Experimental Pressures for Transonic Flow Computations About Isolated Wings and Wing Fuselage Configurations," NASA Langley Conference on Aerodynamics Requiring Advanced Computers, NASA SP 347, 1975.

35. Murman, E.M., "Analysis of Embedded Shock Waves Calculated by Relaxation Methods," *AIAA J.* 12, 5, May, 1974, pp. 626-633.

36. Couch, L.M., and Brooks, C.W. Jr., "Effect of Blockage Ratio on Drag and Pressure Distributions for Bodies of Revolution at Transonic Speeds," NASA TN D-7331, 1973.

37. Malmuth, N.D.,"An Asymptotic Theory of Wind Tunnel Wall Interference on Subsonic Slender Bodies," *J. Fluid Mechanics* 177, 1987, pp. 19-35.

38. Cole, J.D., and Malmuth, N.D., "Shock Wave Location on a Slender Transonic Body of Revolution," *Mechanics Research Communications* 16, 6, June 1989, pp. 353-357.

39. Newman, P.A. and Barnwell, R.W., eds., "Wind Tunnel Wall Interference Assessment/Correction 1983," Proceedings of Workshop held at NASA Langley Research Center, Hampton, Virginia, January 25-26, 1983, NASA CP-2319, 1984.

40. Magnus, W., Oberhettinger, F., and Soni, R.P., *Formulas and Theorems for the Special Functions of Mathematical Physics*, Springer-Verlag, N.Y., 1966.

41. Gradshteyn, I.S. and Ryzhik, M., *Tables of Integrals Series and Products, Corrected and Enlarged Addition*, Academic Press, 1980.

42. Krupp, J.A., and Murman, E.M., "Computational Transonic Flows Past Lifting Airfoils and Slender Bodies," *AIAA J.* 10, 7, July, 1972, pp. 881-886.

43. Small, R.D., "Studies in Transonic Flow VI, Calculation of a Transonic Lifting Line Theory," UCLA Report UCLA-ENG-7836, April, 1978.

44. Dwight, H.B., *Tables of Integrals and Other Mathematical Data*, Macmillan, 1947.

45. Hafez, M.M., and Cheng, H.K., "Convergence Acceleration of Relaxation Solutions for Transonic Computations," AIAA Paper 75-71, 1975.

46. Kraft, E.M., Ritter, A. and Laster, M., "Advances at AEDC in Treating Transonic Wind Tunnel Wall Interference," presented at the 15th Congress of the International Council of Aeronautical Sciences, London, U.K., ICAS Paper 86-1.6.1, September 9-12, 1986.

47. Donegan, T.L, Benek, J.A., and Erickson, J.C., "Calculation of Transonic Wall Interference," AIAA Paper 87-1432 presented at the AIAA 19th Fluid Dynamics, Plasma Dynamics and Lasers Conference, June 8-10, 1987, Honolulu, Hawaii.

48. Cole, J.D., and Malmuth, N.D., "Wave Drag Due to Lift of Transonic Airplanes," Transonic Symposium: Theory, Application and Experiment, NASA CP-3020, 1988, pp. 293-308.

49. Malmuth, N.D., Wu, C.C., and Cole, J.D. "Slender Body Theory and Space Shuttle Transonic Aerodynamics." AIAA Paper 85-0478, presented at the AIAA 23rd Aerospace Sciences Meeting, January 14-17, 1985, Reno, Nevada.

50. Malmuth, N.D., "Unsteady Euler and Asymptotic Methods for Lagrange's Problem of Internal Ballistics," AIAA Paper 88-0623, presented at the AIAA 26th Aerospace Sciences Meeting, Reno, January 11-14, 1988.

51. Rajagopal, K., Malmuth, N.D., and Lick, W., "Application of Transonic Slender Body Theory to Bodies of Varying Complexity," *AIAA J.* 27, 8, September 1989, pp. 1220-1229.

52. Hinson, B.L., and Burdges, K.P., "Acquisition and Application of of Transonic Wing and Far Field Test Data for Three-Dimensional Computational Method Evaluation," AFOSR Report 80-0421, March 1980.

53. Malmuth, N., Letter to Dr. K.L. Kushman, February 15, 1989.

54. Durand, W., ed., *Aerodynamic Theory*, II, (1934), reprinted at the California Institute of Technology, 1943.

55. Cole, J.D. and Cook, L.P., "Some Asymptotic Problems of Transonic Flow Theory," presented at the Symposium Transsonicum III, Göttingen, West Germany, May 1988.

56. Goethert, B.H., *Transonic Wind Tunnel Testing*, Pergamon, N.Y., 1961.

57. Shankar, V., Malmuth, N.D., and Cole, J.D., "A Consistent Design Procedure for Supercritical Airfoils," *Proceedings of NASA Advanced Technology Airfoil Research Conference 1*, NASA CP 2045, held at NASA Langley Research Center, Hampton, Virginia, March 7-9, 1978, pp. 101-117.

NOMENCLATURE

a'_0	constant in Central Layer expression Eq. (2-31)
A	reduced angle of attack $= \alpha/\delta$
A_j, B_j, C_j, D_j	coefficients appearing in discretized partial differential equations of perturbation potential in Eq. (2-58a)
A_n	Fourier coefficient
A_0^*	reduced angle of attack of free field
A_1	wall perturbation of similarity parameter
b	wing semispan
b_0	far field constant derived in Ref. 29
b'_0	far field constant derived in Ref 29
B	body function, and body boundary operator in Eq. (2-100') scaled span $= \delta^{1/3}b =$ aspect ratio
B_n	Fourier coefficient
B_0	far field constant derived in Ref. 29 and defined before Eq. (2-47a)
c	characteristic length scale, local chord
C	undetermined constant in Eq. (2-18a)
C_p	pressure coefficient
COEF	defined in Eq. (2-57c)
C_0	undetermined constants in Eqs (2-18a,b)
$d(z)$	function related to aspect ratio correction in lifting line theory
D	drag
D_0	undetermined constant in Eqs. (2-18a,b)
D_1	doublet strength in Eq. (4-11b)
F	Eq. (2-1), $\phi_{0_{\bullet\bullet}}$
g	shock perturbation function
G	Green's function
G_0	shock shape perturbation function introduced before Eq. (2-43)
h	dimensional wall height or radius
H	scaled wall height or radius $= \delta h/c, \delta^{1/3}h$
I_v	integral defined in Eq. (3-10b)
I_{walls}	integral defined in Eq. (3-10c)
IMAX	refers to downstream boundary of computational domain
I_0, I_1	modified Bessel function of first kind
j_{nk}	zero satisfying $J_n(j_{nk}) = 0$
JMAX	refers to top of computational domain
$J_{0,1}$	Bessel functions of first kind
k	transform variable
K	transonic similarity parameter
K_0, K_1	modified Bessel functions of third kind
K_0^*	free field similarity parameter
K_1^*	wall perturbation of similarity parameter

L	length of body, TSD operator Eq. (2-32)
M	linear operator of interference flow
$\vec{n}$	surface normal
P_n	Fourier coefficient in Eq. (2-26a)
$P_{1,2}$	Legendre polynomial
Q_n	Fourier coefficient in Eq. (2-26a)
$\tilde{Q}_{1,2}$	functions to be determined by matching in Eqs. (2-26)
r	transverse radius
$\tilde{r}$	scaled transverse radius
R	polar radius defined in Figs. 2 and 9
RHS	right hand side defined in Eq. (2-57b)
$S(x)$	dimensionless area distribution
$\overline{S}(\overline{x})$	dimensional area distribution
$S_{1,2}$	intermediate quantities defined in Eqs. (3-21)
u	ϕ_x
u, v	horizontal and vertical velocity components
$u_{0,1}$	$\phi_{0,1_x}$
U	freestream velocity
v	$\phi_{\tilde{r}}$
$v_{0,1}$	$\phi_{0,1_{\tilde{r}}}$
W	interface pressure function Eq. (3-4)
$w(z)$	function related to wall correction in high aspect ratio theory
x^*, y^*, z^*	outer variables for lifting line theory defined in Eq. (3-6)
x', y', z'	dummy variables for x, y, z
x	streamwise coordinate
X	$x/\sqrt{K_0^*}$, and reduced streamwise coordinate defined after Eq. (2-48)
$\tilde{y}, \tilde{z}$	scaled variables for small disturbance theory for large aspect ratio formulation
$\hat{y}, \hat{z}$	scaled variables introduced in Eq. (3-9a)
$Y_{0,1}$	Bessel functions of second kind
Z	$z + iy$
Z'	$\zeta + i\eta$
$\mathcal{A}_i$	constants introduced in Eqs. (2-27)-(2-29) to be determined by matching in Fig. 5 ($i = 0, 1, 2, 3, 4$)
$\overline{\mathcal{A}}_i$	($i = 0 - 4$) constants determined by matching in Fig. 5
$\mathcal{A}_{00}$	constants introduced in Eqs. (2-27)-(2-29) to be determined by matching in Fig. 5 ($i = 0, 1, 2, 3, 4$)
$\mathcal{A}_{01}$	same as above
$\mathcal{B}_i$	same as above
$\mathcal{E}_0$	same as above
$\mathcal{E}_{01}$	same as above
$\mathcal{F}_0$	same as above
$\mathcal{F}_{01}$	same as above
$\mathcal{G}_0$	same as above

$\mathcal{H}_0$	same as above
α	angle of attack
$\alpha_{0,1,2}$	constants determined by matching in Eqs. (2-24)
γ	specific heat ratio, circulation
Γ	circulation
Γ_0	zeroth order flow circulation of high aspect ratio wing flow
Γ_1	interference flow circulation
δ	characteristic thickness ratio of body
Δ	Laplacian
ΔC_p	interference increment of pressure coefficient
ϵ_n	jump sum index, where $\epsilon_0 = 0$, $\epsilon_n = 2$, $n > 0$
$\epsilon_{1,\frac{1}{2},2}$	gauge functions appearing in Eq. (2-20)
ζ, η	dummy variables for z and y
θ	azimuthal angle in Fig. 2
θ', r'	dummy variables for θ and r
$\hat{\theta}, \hat{r}$	polar coordinates based on scaled variables
ϑ, ρ	dummy variables for θ and r
$\kappa_1(H)$	gauge function used in Eq. (2-6c)
λ_n	zero of secular equation $J_1(\lambda_n H) = 0$
λ_{nk}	scaled zero $= j_{nk}/\mu$
μ	H/B reciprocal of semispan to tunnel height ratio
μ_{ij}	switch parameter defined in Eq. (2-57d)
$\mu_{1,2}$	gauge functions appearing in Eq. (2-19)
$\nu_1(H)$	gauge functions used in Eq. (2-6b)
ξ, η, ζ	dummy variables for x, y, z
τ	body thickness ratio
ϕ	perturbation potential
$\hat{\phi}$	regularized potential
$\bar{\phi}$	intermediate representation of perturbation potential in Eq. (4-10a)
ϕ_{FF}	far field asymptotic for interference potential in Eq. (2-44); also in Eq. (3-102b)
ϕ_1	interference perturbation potential
Φ	velocity potential
φ	perturbation potential in wall deck, also outer representation of perturbation potential in confined lifting line theory
ω	polar angle shown in Fig. 2, relaxation parameter in Eqs. (2-57)
$\Omega^{(1,2)}$	special functions introduced in Eqs. (28)

Subscripts

In various locations in the manuscript, subscripts denote differentiation.

h	homogeneous

p particular
$0,1$ denotes order of approximation
∞ denotes freestream quantity

Superscripts

U immediately upstream of shock
D immediately downstream of shock
$\dagger$ Eq. (2–8b)
$+$ immediately downstream of shock
$-$ immediately upstream of shock

Special Symbols

$\overline{}$ overbar refers to dimensional quantity or Fourier transform
$\times$ vector cross product
∇ gradient operator
$\nabla\cdot$ divergence
$[\ ]$ jump across shock introduced after Eq. (2–33) or operator dependence
$\langle\ \rangle$ average across shock introduced before Eqs. (2–76)
$\cdot$ vector dot product
T_j cross flow operator in Eq. (2–62)
      bar across integral refers to principal value

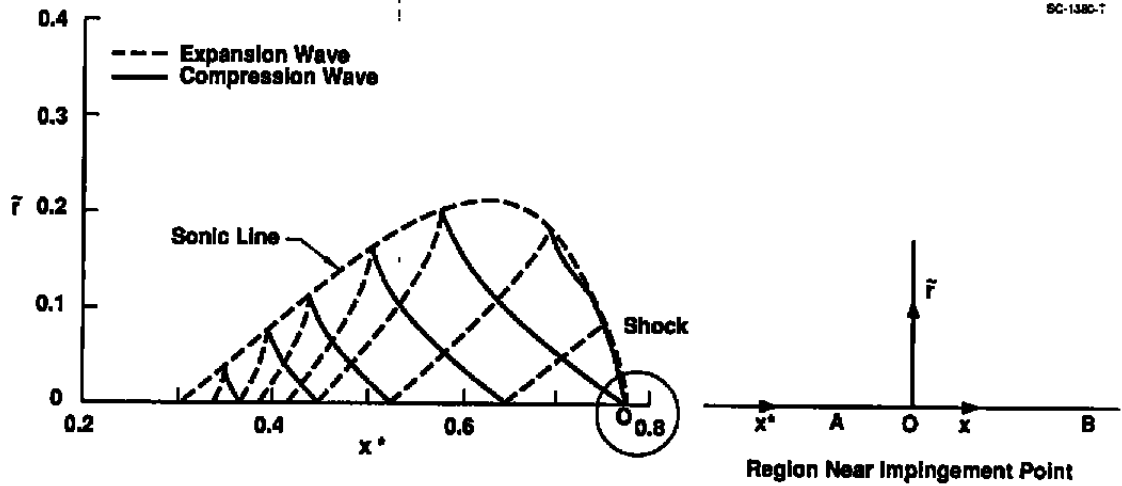## APPENDIX A — MODELS FOR INTERFERENCE FLOW NEAR SHOCKS

Fig. A1. Detail of shock region.

To obtain a qualitative understanding of the spikelike nature of the interference near the shock of the basic flow, certain model problems are of interest. Figure A1 is a schematic of the region near the shock wave in the wall interference flow for a slender body. The equation for the interference perturbation potential ϕ_1 given earlier in this report is

$$(K - (\gamma+1)\phi_{0_{x^*}})\phi_{1_{x^*x^*}} - (\gamma+1)\phi_{0_{x^*x^*}}\phi_{1_{x^*}} + \frac{1}{\tilde{r}}(\tilde{r}\phi_{1_{\tilde{r}}})_{\tilde{r}} = 0 \quad . \tag{A1}$$

In (A1), x^* refers to an origin displaced from the virtual intersection of the shock and x axis (body). For convenience in what follows, the translation

$$x = x^* - x_S^* \tag{A2}$$

is performed where x_S^* refers to the virtual intersection point O. Assuming that the shock is normal to the body at x_S^*, then the coefficient of the first term in (A1) changes sign in the small neighborhood of O. Approximate model equations for weak shock layer transitions near O are

$$(\text{sgn}(x)\phi_{1_x})_x + \frac{1}{\tilde{r}}(\tilde{r}\phi_{1_{\tilde{r}}})_{\tilde{r}} = 0 \tag{A3}$$

$$(x\phi_{1_x})_x + \frac{1}{\tilde{r}}(\tilde{r}\phi_{1_{\tilde{r}}})_{\tilde{r}} = 0 \quad . \tag{A4}$$

Equations (A3) and (A4) are generalizations of the Lavrentef–Bitsatze and Tricomi equations, respectively, for axisymmetric flow. These are, respectively

$$\text{sgn}(x)\phi_{1_{xx}} + \frac{1}{\tilde{r}}(\tilde{r}\phi_{1_{\tilde{r}}})_{\tilde{r}} = 0 \tag{A5}$$

214

$$x\phi_{1_{xx}} + \frac{1}{\tilde{r}}(\tilde{r}\phi_{1_{\tilde{r}}})_{\tilde{r}} = 0 \quad . \tag{A6}$$

Expanding the first term in (A3) yields a $\delta(x)\phi_{1_x}$ term. One possible set of conditions for a boundary value problem modeling the flow structure near the foot of the shock is

$$\phi_1 \quad \text{bounded as} \quad |x| \to \infty \quad . \tag{A7}$$

Other suitable matching conditions as $\tilde{r} \to \infty$ and 0 with x fixed are required for a properly posed formulation.

A full discussion of the appropriate boundary value problem for (A3) or (A5) is not intended here. However, the behavior of one class of solutions of (A3) will be discussed.

If separation of variables is used in (A3) by letting

$$\phi_1 = X(x)R(\tilde{r})$$

then

$$\frac{(\text{sgn}(x)X')'}{X} = -\frac{1}{\tilde{r}}\frac{(\tilde{r}R')'}{R} = -\lambda^2 \tag{A8}$$

or

$$\text{sgn}(x)X'' + 2\delta(x)X' + \lambda^2 X = 0 \tag{A9}$$

$$(\tilde{r}R')' - \lambda^2 \tilde{r}R = 0 \quad . \tag{A10}$$

Equation (A10) has

$$R = K_0(\lambda\tilde{r}) \tag{A11}$$

as one possible solution. Equation (A9) models the motion of a linear oscillator with impulsive positive damping for $x > 0$ and similar negative damping for $x < 0$. The delta function can be simulated by the square pulse

$$f(x) = \frac{1}{\epsilon} \quad , \quad -\frac{\epsilon}{2} \le x \le \frac{\epsilon}{2} \tag{A12a}$$

$$= 0 \quad , \quad |x| > \frac{\epsilon}{2} \quad . \tag{A12b}$$

Exponentially damped solutions can be used to match with the ϕ_1 field governed by (A1) as $\tilde{r} \to \infty$. The logarithmic behavior of (A11) as $\tilde{r} \to 0$ corresponds to a special singularity at the root of the shock at point O. Equation (A9) has been studied for the model delta function (A12). The second term in (A9) leads to spikes similar to that discussed earlier in this report.

Another simple plausibility argument for the spike behavior of ϕ_{1_x} near O is associated with the assumption that

$$\phi_{0_x} \simeq \text{sgn}(x) \quad \text{as } x \to 0 \quad .$$

If the interference perturbs ϕ_{0_x} to become

$$\phi_{0_x} \simeq (1 + \epsilon)\text{sgn}(x - \epsilon) \quad ,$$

then the dominant interference term behaves like

$$\text{sgn}(x - \epsilon) - \text{sgn}\,x \simeq 2\epsilon\delta(x)$$

which resembles our computed solutions.

APPENDIX B – REEXPANSION SINGULARITY DETAILS

Figure 97 shows an increase in the rate of reexpansion immediately downstream of the shock when the latter is weakened. This somewhat counterintuitive behavior can be understood in terms of the singularity of Transonic Small Disturbance Theory discussed in Ref. 30. The trends in Fig. 97 are supported by Figs. B1–B4. They represent experiments and other calculations. The relevance of the experiments is that if the Reynolds number is sufficiently high, the post–shock expansion resembles that obtained from inviscid predictions like ours. (Smaller Reynolds numbers will result in post–shock boundary layer separation and are not germane to this discussion.)

Figure B1 shows experimental data of Blackwell on a 12 percent thick airfoil. Here, a change in the Reynolds number gives an upstream shock displacement with an attendant weakening of the shock. Note the increased reexpansion tendency downstream of the weaker shock. Figure B2 shows so much increase in the reexpansion that a second shock forms. Figure B3 taken from E. Kraft's Ph.D. thesis[*], further confirms that weakening the shock exaggerates the reexpansion C_p blip.

Gadd, Oswatitsch, Zierep, and Cole have analyzed this behavior. Inviscidly, the reexpansion detail represents a logarithmic singularity immediately downstream of the point where the shock strikes the airfoil. If x denotes the distance in the freestream direction measured from the shock impingement point, b subscript represents conditions immediately behind the shock on the airfoil, M_∞ = freestream Mach number, δ = airfoil thickness ratio, $K = \frac{1-M_\infty^2}{\delta^{2/3}}$, and u is the perturbation velocity in the x direction, then if

$$w = (\gamma + 1)u - K, \qquad (B1)$$

the local behavior of the pressure coefficient C_p immediately downstream of the impingement point is given by

$$C_p = C_{p_b} + Ax\ln(x)\ldots, \qquad (B2)$$

where A is the strength of the singularity given by

$$A = -\frac{8F''(\tilde{x}_0)\delta^{2/3}}{\pi\sqrt{-w_b}}. \qquad (B3)$$

In Eq. (B3), $F''(\tilde{x}_0)$ is proportional to the curvature and $\tilde{x}_0$ represents the x coordinate of the impingement point, measured from the nose. The quantity w_b is proportional to the Mach number jump across the shock. Weakening the shock reduces w_b, increasing the reexpansion singularity strength A. For a NACA–0012 airfoil as well as other profiles, the weakened shock moves upstream and the magnitude of $F''(\tilde{x}_0)$ increases from its

[*] Kraft, E.M., "An Integral Equation Method for Boundary Interference in Perforated–Wall Wind Tunnels at Transonic Speeds," Ph.D. Thesis, U. of Tennessee, December, 1975.

downstream value. This has a compounding effect on the increase in A. Data from other profiles confirm this, but obviously it is an airfoil shape dependent phenomenon.

As an additional verification of these trends, Fig. B4 indicates a comparison of the singularity intensity A from our Mach .75 elliptic wing case for free field and pressure boundary conditions (circled points). Also shown are results from Kraft's thesis (square points derived from Fig. B3). They correspond to a NACA-0012 airfoil 2-D flow in the free field as well as between solid walls for the height to chord ratios shown in Fig. B3. The quantity A was determined from the numerical solution by a least squares fit of the solution using Eq. (B2) as the model to fit the solutions. Kraft's integral equation method simulates the shock as an instantaneous discontinuity, whereas the finite difference solution needs a few points to resolve the shock. These aspects as well as the shock fitting process used in the wall interference perturbation solution are factors affecting the comparison shown. Another is errors committed in digitizing the data near the impingement point. In this connection, at least four points were used for the least squares fit. Although these considerations lead to some minor discrepancies, there is a good correspondence between the numerically determined acceleration of the flow and the local asymptotic estimate.
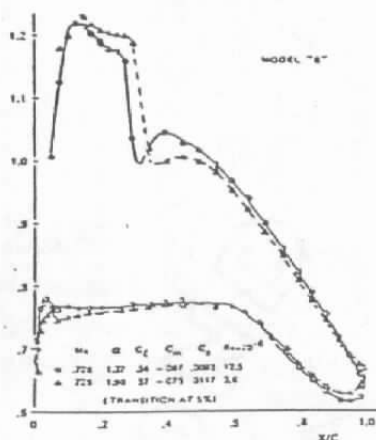

Fig. B1. Reynolds number effect on
pressure distribution —
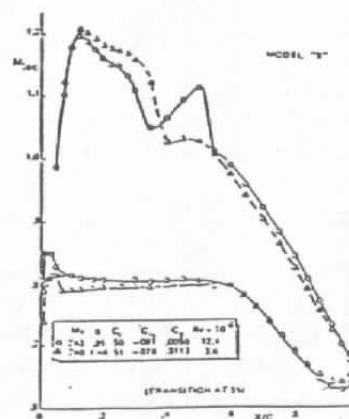example of upstream shock
displacement.

Fig. B2. Reynolds number effect on
pressure distribution —
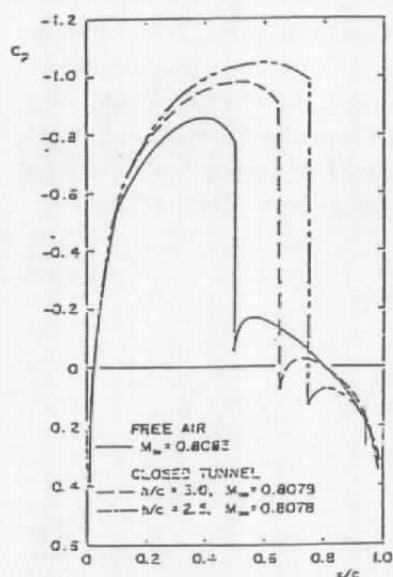example of change from
single to double shock system.

217

Fig. B3. Effect of a closed wind tunnel on the pressure distribution over an NACA–0012 airfoil.

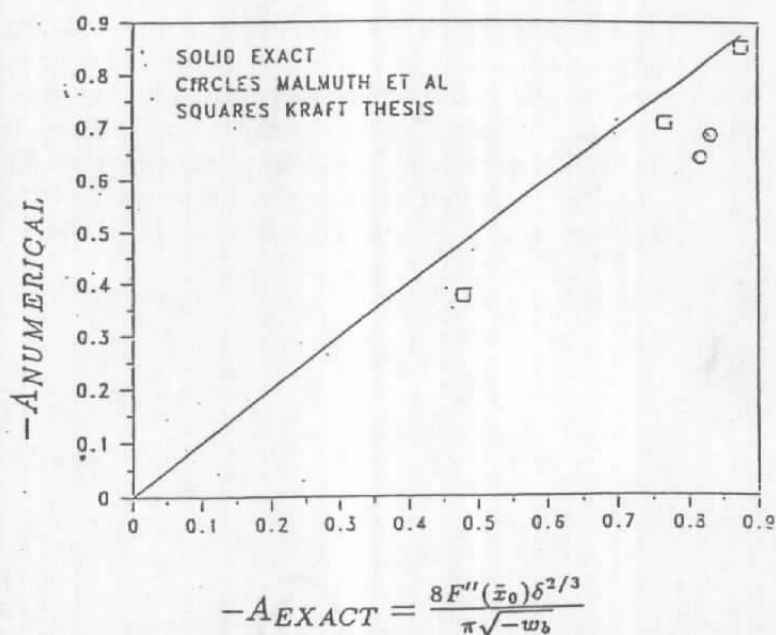$$-A_{EXACT} = \frac{8 F''(\bar{x}_0) \delta^{2/3}}{\pi \sqrt{-w_b}}$$

Fig. B4. Comparison of analytical reexpansion singularity with that from numerical solutions.

218